OBSERVATOIRE DE GRENOBLE
et
LABORATOIRE DE GÉOPHYSIQUE INTERNE ET TECTONOPHYSIQUE

THÈSE

présentée par

Ludovic MARGERIN

pour obtenir le titre de DOCTEUR de

L'UNIVERSITÉ JOSEPH FOURIER - GRENOBLE I
(Arrêtés ministériels du 5 juillet 1984 et du 30 mars 1992)

Specialité: **Géophysique - Géochimie - Géomécanique**

Diffusion multiple des ondes élastiques dans la lithosphère

Date de soutenance: 11 Décembre 1998

Composition du jury:

M. M. Campillo	Directeur de thèse	Professeur à l'Université Joseph Fourier, Grenoble
M. M. Fink	Rapporteur	Professeur à l'ESPCI, Paris
M. P. Gillet	Examinateur	Professeur à l'Ecole Normale Supérieure, Lyon
M. R. Madariaga	Rapporteur	Professeur à l'Ecole Normale Supérieure, Paris
M. B. Van Tiggelen	Examinateur	Chargé de Recherches, CNRS, Grenoble

Remerciements

Je remercie Michel Campillo pour tout ce qu'il m'a apporté depuis que nous nous connaissons (six ans déjà !), d'abord en qualité d'enseignant, puis de directeur de thèse. J'ai toujours apprécié son intuition, son sens physique et sa très grande ouverture d'esprit, sans laquelle ce travail n'aurait sans doute pas vu le jour. J'ai eu aussi beaucoup de plaisir à discuter de sujets extra-sismologiques avec lui.

Je remercie Bart van Tiggelen pour tout le temps qu'il a consacré à m'initier à la diffusion multiple, toujours avec beaucoup de pédagogie et de bonne humeur. J'ai beaucoup apprécié ses connaissances encyclopédiques et sa vision très claire des théories. Je le remercie aussi de l'intérêt enthousiaste qu'il a porté à la géophysique.

Je remercie Nicolas Shapiro pour l'attention constante qu'il a portée à mon travail depuis que je suis arrivé au laboratoire et qui n'a pas faibli même si nous sommes séparés de plusieurs milliers de kilomètres. J'ai appris beaucoup sur les méthodes de travail, l'informatique et la physique grâce à lui. Je le remercie, ainsi que Rosa, pour m'avoir acceuilli au Mexique et j'espère que nous pourrons travailler ensemble dans les années à venir.

Un grand merci à Catherine Pequegnat pour diriger l'informatique du LGIT avec beaucoup de compétence et d'efficacité.

Je remercie Mathias Fink pour l'intérêt qu'il a porté à mon travail et à la géophysique au sein du GDR POAN.

Je remercie Raúl Madariaga d'avoir accepté d'être rapporteur de mon travail de thèse et Philippe Gillet d'avoir présidé avec gentillesse et décontraction le jury de cette thèse.

Je remercie toutes les personnes du LGIT avec qui j'ai pu échanger des idées au cours de ces années. Merci à Céline, pour la relecture et la correction de mon manuscrit ... avec le sourire.

Je remercie Régine, Jean-Claude et Alex qui m'ont soutenu toutes ces années et qui m'ont permis de faire les choses qui me tenaient à coeur.

Je remercie tous mes ami(e)s qui de près ou de loin ont contribué à la réalisation de ce travail.

Un grand merci à Sabine pour tout.

Contents

Introduction.

Pourquoi étudier la diffusion multiple?

La diffusion multiple est un phénomène largement observé et étudié en physique. Elle concerne un grand nombre de domaines tels que la physique des semi-conducteurs, la physique atomique, l'astrophysique, l'optique, l'imagerie médicale, l'acoustique et ... la sismologie. En dépit des différences d'échelles -de l'Angström, jusqu'au kilomètre-, des différents types de particules -électrons, photons, phonons ...-, ou d'ondes -électromagnétiques, acoustiques, élastiques...- rencontrées, un formalisme et des théories communes à tous ces champs ont pu être développés. La diffusion multiple concerne la propagation d'ondes ou de particules dans des milieux où intervient une forme de désordre. Dans le cas des semi-conducteurs, le désordre peut provenir d'impuretés ou de défauts disposés aléatoirement sur le réseau atomique. Il a été démontré depuis 1958 par Anderson que la présence de désordre peut affecter dramatiquement les propriétés de transport des électrons, jusqu'à l'absence totale de diffusion. C'est ce qu'on a baptisé depuis la "localisation forte" et qui est de nos jours un domaine de recherches actives pour les ondes classiques, sur le plan théorique et expérimental. Dans le cas des milieux géophysiques - l'atmosphère, l'océan, la lithosphère, ou vivants - le corps humain-, le désordre est une manifestation naturelle, et l'interprétation des observations est fortement dépendante de notre compréhension de la propagation des ondes en présence de désordre. Soulignons brièvement quelques succès, qui ont été obtenus dans différents domaines grâce aux progrès de la physique des ondes en milieu aléatoire.

L'application de la théorie du transfert radiatif en astrophysique a permis par exemple de découvrir le composant chimique majoritaire de l'atmosphère de Jupiter, uniquement grâce aux informations fournies par les télescopes. En imagerie médicale se développe actuellement une tomographie optique par "ondes de densité de photon" (Yodh et Chance, 1995). Cette technique est basée elle aussi sur la théorie du transfert radiatif, mais dans une approximation dite de "diffusion". Les expériences ont en effet montré que les ondes électromagnétiques dans le corps humain se comportent de façon tout à fait similaire à des particules classiques subissant un mouvement brownien. Plus exactement, c'est la densité de photon qui suit une équation de diffusion. Il est bien connu, en théorie de la chaleur, qu'une source périodique placée en surface d'un milieu diffusant donne naissance à une onde de diffusion se propageant dans le milieu comme une onde "classique" . En effet, dans le cas d'une source périodique, l'équation de diffusion devient similaire à l'équation de Helmoltz. Une différence existe tout de même puisque le nombre d'onde d'une "onde de chaleur" est nécessairement complexe, la partie imaginaire traduisant son atténuation. L'onde de densité de photons présente toutes les propriétés des ondes classiques. En particulier, elle se diffracte sur les hétérogénéités du milieu. Précisons qu'une hétérogénéité se traduit ici par un contraste de constante de diffusion (ou de l'absorption) et non par un contraste de vitesse! Il vient donc l'idée naturelle d'utiliser les ondes diffusives pour faire une tomographie par diffraction du corps humain. En effet, la présence de tissus anormaux se traduit par une modification locale de la constante de diffusion. A l'aide d'une source laser modulée en fréquence et d'une caméra, on peut donc enregistrer le champ de densité de photon et essayer par inversion de reconstruire une image de l'organe. Ces deux applications montrent donc qu'il est possible d'extraire beaucoup d'information des ondes provenant de la diffusion multiple, avec éventuellement l'espoir de réaliser une tomographie telle qu'on la pratique sur les ondes directes en sismologie.

La diffusion multiple en sismologie.

Même si depuis longtemps (Aki 1969), on a reconnu l'existence d'ondes diffractées en sismologie, leur exploitation est resté limitée jusqu'au milieu des années 1980. En fait, un grand nombre d'informations très importantes sur la structure interne de la Terre ont été apportées par la sismologie grâce à l'utilisation de la théorie des rais. Elle a permis de fournir un modèle lisse mais fondamental de la Terre. L'intérêt des sismologues pour les problèmes de diffusion multiple a probablement été éveillé par Aki et Chouet en 1975, lorsqu'ils ont étudié la coda des séismes locaux courtes périodes ($< 1s$). Ils ont montré que dans une région donnée, la coda possédait des propriétés de décroissance énergétique remarquablement stables, indépendantes de la magnitude des séismes, de la position relative source-station et de l'effet de site. Ils ont défini le paramètre coda Q (Q_c), qui mesure la vitesse de décroissance énergétique des signaux. De plus, ils ont proposé deux modèles d'interprétation physique de la coda, l'un basé sur l'approximation dite de "single-scattering" (diffusion simple), et l'autre sur l'approximation de diffusion, dans un milieu infini uniforme. Depuis, le paramètre Q_c et le modèle de "single-scattering" ont acquis une popularité très grande, et la littérature sismologique contient de très nombreux articles rapportant la mesure de coda Q dans diverses régions du monde (Herraiz et Espinosa 1987). Néanmoins, l'interprétation de coda Q en terme de propriétés du milieu était (et demeure) une question largement ouverte. Le problème majeur du modèle de diffusion simple est qu'il est impossible de distinguer les processus anélastiques (absorption intrinsèque), des processus élastiques (diffraction).

C'est en 1985, que Wu et Aki ont proposé la première technique de séparation de l'absorption et de la diffraction basée sur la distribution spatiale de l'énergie sismique. Leur technique s'appuie sur la théorie du transfert radiatif acoustique, en régime stationnaire, dans un milieu infini uniforme. Ils ont montré qu'il était formellement possible de distinguer absorption et diffusion en régime de diffusion multiple. Il faut noter que cette séparation était déjà apparente dans le modèle diffusif de Aki et Chouet (1975), mais que peu d'auteurs l'ont utilisé comme modèle interprétatif. La première application sur des données sismologiques par Wu et Aki (1988) a donné lieu à l'estimation de l'albédo sismique $1/l_{sc}/(1/l_a + 1/l_{sc})$ et de la longueur d'extinction $1/l_e = 1/l_a + 1/l_{sc}$, où l_{sc} est le libre parcours moyen de "scattering" et l_a la longueur d'absorption telle que $l_a = Q_i v/\omega,$. Q_i est le facteur de qualité intrinsèque, ω la fréquence angulaire et v la vitesse moyenne des ondes. Leur résultat pour la région d'Hindu-Kush montre que l'atténuation est le facteur dominant pour expliquer la décroissance de la coda et que la longueur d'extinction est de l'ordre de 20-30 km. Par la suite, leur méthode a donné lieu à de nombreuses variantes, de plus en plus sophistiquées mais fondamentalement basées sur les mêmes hypothèses (Töksöz et al. 1988, Mayeda et al. 1991, Fehler et al. 1992, Hoshiba 1993). Suivant la région, l'importance de la diffraction et de l'absorption varient. D'autre part le lien entre Q_c et Q_i ne semble pas clair. Dans certaines régions Q_c et Q_i sont très proches (Japon, Est des Etats-Unis), alors qu'ils sont différents en Californie. Néanmoins toutes ces études montrent que Q_i augmente, parfois fortement, avec la fréquence. D'autre part, dans les régions dites "tectoniquement actives", on trouve des valeurs très faibles de Q_i entre 1 et 5 Hz de l'ordre de 100-300. Il apparaît alors une contradiction avec les résultats de mesure du facteur de qualité intrinsèque des ondes Lg. La comparaison entre la coda et les ondes L_g a du sens parce que toutes deux échantillonnent l'ensemble de la croûte et que leurs gammes de fréquence se chevauchent. Les ondes L_g semblent montrer que l'atténuation intrinsèque est faible dans les zones de tectonique active et qu'au contraire la diffraction joue un rôle très important (Campillo et Plantet 1991).

Objectifs et contenu de la thèse.

Confrontés à la contradiction évoquée au paragraphe précédent, il nous faut revenir sur les modèles. Les valeurs de Q_i et d'albédo proposées dans la littérature de la coda sont basées sur un modèle de transfert radiatif dans un milieu infini uniforme. Or, de nombreuses informations provenant de la géologie, de la géochimie et de la sismique réflexion nous montrent que la lithosphère n'est pas un milieu uniforme. En plus du contraste de vitesse bien connu au niveau du Moho, le caractère très hétérogène de la croûte, comparée au manteau, est manifeste.

Par conséquent, nous devons intégrer dans les modèles les conditions aux limites inhérentes à la structure de la lithosphère, et les variations de l'hétérogénéité avec la profondeur. Ceci nous amène à résoudre l'équation de transfert radiatif pour des milieux stratifiés (chapitre 2), le lien entre équation d'onde et équation de transfert radiatif étant évoqué au chapitre 1. Deux méthodes sont proposées: l'une numérique est basée sur la simulation de Monte-Carlo, l'autre analytique résoud l'équation de transfert dans l'approximation de diffusion. Le lien entre équation de transfert et de diffusion, ainsi qu'entre leurs conditions aux limites est discuté. L'étude montre le rôle fondamental de la stratification dans la Terre qui est un effet de premier ordre. Au chapitre 3, nous proposons un modèle conceptuel de la lithosphère continentale pour l'interprétation de la coda. Il consiste en une couche diffractante (la croûte), reposant sur un demi-espace homogène (le manteau). Le contraste de vitesse est également incorporé. Ce modèle est appliqué à des mesures de la dépendance fréquentielle de Q_c au Mexique. Une interprétation alternative de Q_c y est proposée (voir aussi le chapitre 5).

Le rôle des couplages entre ondes P et S a pour le moment été peu étudié en sismologie et nous a amené à modéliser la diffusion multiple des ondes élastiques incluant les conversions entre modes et une description rigoureuse de la polarisation des ondes S. Nous proposons une méthode de simulation Monte-Carlo de l'équation de transfert radiatif élastique obtenue indépendamment par Weaver (1990) et Ryzhik et al. (1996). Dans un premier temps, nous nous plaçons dans le cas d'un espace infini uniforme contenant des diffuseurs discrets. Nous étudions la vitesse de stabilisation des rapports d'énergie P et S en fonction de la taille relative des hétérogénéités et des longueurs d'onde. Lorsqu'elles sont de taille comparable, l'équilibre d'énergie entre les champs P et S est atteint rapidement. Une conclusion importante est que l'équilibration n'apparaît qu'en régime de diffusion multiple. Nous incorporons ensuite l'effet de la surface libre dans l'équation de transport élastique. Nous proposons une théorie de premier ordre pour calculer le rapport des énergies P et S à la surface. Cette théorie est appuyée par des simulations numériques qui montrent que le rapport d'énergie est inchangé à la surface libre. Le chapitre 5 constitue une synthèse de nos observations sur la coda. Une mesure de l'équilibration des modes P et S à partir de données d'un réseau de faible ouverture y est présentée (Shapiro et al. 1998). En relation avec l'étude numérique du chapitre 4, cette observation semble confirmer que les ondes dans la Terre sont en régime de diffusion multiple.

L'étude de la réflexion des ondes à la surface nous amène à discuter des possibles effets d'interférence en régime de diffusion multiple. Ces effets sont démontrés par l'existence du cône de rétrodiffusion cohérente qui a pu être mesuré en optique (Kuga et Ishimaru, 1984) et en acoustique (Tourin et al. 1997). Au chapitre 6, une étude théorique est présentée, basée sur des simulations numériques et un calcul analytique. Dans le cas de la sismologie, nous prédisons une largeur du cône de rétrodiffusion de l'ordre de la longueur d'onde.

Bibliographie

Aki, K., 1969. Analysis of the seismic coda of local earthquakes as scattered waves, J. Geophys. Res., 74, 615-618.

Aki, K. and B. Chouet, 1975. Origin of coda waves: Source, attenuation, and scattering effects, J. Geophys. Res., 80, 3322-3342.

Campillo, M. and J.L. Plantet, 1991. Frequency dependence and spatial distribution of seismic attenuation in France: experimental results and possible interpretations, Phys. Earth Planet. Inter., 67, 48-64.

Fehler, M., M. Hoshiba, H. Sato, and K. Obara, 1992. Separation of scattering and intrinsic attenuation for the Kanto-Tokai region, Japan using measurements of S-wave energy vs hypocentral distance, Geophys. J. Int., 787-800.

Herraiz, M. and A.F. Espinosa, 1987. Coda Waves: a review, Pure and Applied Geophysics 125, 499-577.

Hoshiba, M., 1993. Separation of scattering attenuation and intrinsic absorption in Japan using the multiple lapse time window analysis of full seismogram envelope, *Journal of Geophysical Research*, 98, 15 809-15 824.

Kuga, Y. and A. Ishimaru, 1984. Retroreflection from a dense distribution of particles, J. Opt. Soc. Am., A 1, 831-835.

Mayeda, K., Su. F. and K. Aki, 1991. Seismic albedo from the total seismic energy dependence on hypocentral distance in southern California, Phys. Earth planet. inter., 67, 104-114.

Ryzhik, L.V., G.C. Papanicolaou and J.B. Keller, 1996. Transport equations for elastic and other waves in random media, Wave Motion, 24, 327-370.

Shapiro, N.M., M. Campillo, L. Margerin, S.K. Singh, V. Kostoglodov and J. Pacheco, 1998. The energy partitioning between P and S waves and the diffusive character of the seismic coda. submitted to Bull. Seism. Soc. Am.

Töksöz, N., A.M. Dainty, E. Reiter, and R.S. Wu, 1988. A model for attenuation and scattering in the Earth's crust, Pure Appl. Geophys., 128, 81-100.

Tourin, A., A. Derode, P. Roux, B.A. van Tiggelen and M. Fink, 1997. Time-dependent coherent backscattering of acoustic waves, Phys. Rev. Let., 79, 3637-3639.

Weaver, R.L., 1982. On diffuse waves in solid media, J. acoust. Soc. Am., 71, 1608-1609.

Weaver, R.L., 1990. Diffusivity of ultrasound in polycrystals, J. Mech. Phys. Solids, 38, 55-86.

Wu, R.S., 1985. Multiple scattering and energy transfer of seismic waves: Separation of scattering effect from intrinsic attenuation, I, Theoretical Modelling, Geophys. J. R. Astr. Soc., 82, 57-80.

Wu R.S. and K. Aki, 1988. Multiple scattering and energy transfer of seismic waves: Separation of scattering effect from intrinsic attenuation, II, Application of the theory to Hindu Kush region, Pure Appl. Geophys. 128, 49-80.

Yodh A.G., and B. Chance, 1995. In *Physics Today*, 48, 34.

Chapter 1

Théorie du Transfert Radiatif

Dans la suite de cette thèse, nous allons utiliser l'équation de transfert radiatif afin de modéliser certaines observations sismologiques. La théorie phénoménologique développée par Chandrasekhar (1960) constitue une base suffisante pour la majeure partie de notre travail. Néanmoins, le cône de rétrodiffusion cohérente ne peut être correctement expliqué que si l'on tient compte d'interférences qui sont négligées dans l'approche phénoménologique. Ce phénomène d'interférence montre bien que même en régime de diffusion multiple, les ondes ne peuvent être traitées comme des particules classiques. Ceci pose naturellement la question des *connections* qui existent entre les propriétés statistiques du champ d'onde et l'intensité spécifique qui apparaît dans la théorie de transport. Nous allons donc essayer de montrer le lien entre l'équation d'onde et l'équation de transfert radiatif. Néanmoins, de nombreux détails calculatoires seront omis afin d'insister sur l'interprétation physique. On peut trouver la théorie complète dans les ouvrages de Frisch (1968), Ishimaru (1978), Rytov Kravstsov et Tatarski (1989), et Sheng (1995).

Il existe une grande variété de situations où l'expérimentateur doit interpréter des signaux très complexes et non reproductibles. En fait, c'est le cas dès que l'on a à faire face à des milieux naturels. Par exemple, en acoustique marine, on s'intéresse aux ondes sonores se propageant dans l'océan qui est un milieu dont les paramètres physiques fluctuent dans le temps et l'espace. Il en est de même en astrophysique, où les ondes électromagnétiques traversent un milieu turbulent tel que l'atmosphère. Enfin, en sismologie l'hétérogénéité de la croûte existe sur un grand nombre d'échelles. Lorsque le milieu est trop complexe, ou possède un trop grand nombre de degrés de liberté, il devient illusoire de caractériser le système étudié en termes classiques. Dans le cas de la Terre, par exemple, celà équivaudrait à connaître les valeurs des paramètres élastiques et de la densité en tout point, ce qui représente une quantité d'information énorme et de toute façon inaccessible. Il nous faut donc accepter dès le départ notre manque d'information et, par suite, l'imprédictibilité ou encore le caractère aléatoire des signaux sismiques. Nous allons justement exploiter ces propriétés afin de caractériser le milieu et le champ étudiés par leurs grandeurs *moyennes*, en espérant, bien sûr, que les fluctuations du champ réel autour de cette moyenne ne seront pas trop grandes. En fait, la statistique classique (Landau et Lifschitz) nous apprend que plus le sytème étudié comprend de particules (donc plus il a de degrés de liberté) et plus les fluctuations autour de la moyenne se réduisent. Dans la suite de ce chapitre, nous allons essayer de montrer le lien qui existe entre l'équation d'onde et l'équation de transfert radiatif, en insistant sur les résultats. Ceci est utile notamment pour connaître le contenu "ondulatoire" de l'équation de transfert radiatif.

1.1 Théorie du Champ Moyen: l'équation de Dyson

Le formalisme que nous adopterons sera directement emprunté à la théorie électromagnétique, qui provient lui-même de l'électrodynamique quantique. Tout le traitement sera effectué en régime permanent pour plus de simplicité.

1.1.1 Théorie des Perturbations

On considère l'équation de Helmoltz dans un milieu inhomogène aléatoire:

$$\Delta u(\boldsymbol{r}) + k_0^2 \epsilon(\boldsymbol{r}) u(\boldsymbol{r}) = 0, \tag{1.1}$$

où Δ est le laplacien, $\boldsymbol{r}$ le vecteur position, k_0 est le nombre d'onde dans le milieu homogène et ϵ est un paramètre adimensionnel traduisant les fluctuations de l'indice de refraction dans le milieu. L'équation (1.1) est écrite pour une réalisation particulière du champ aléatoire ϵ. On va décomposer ϵ en la somme de sa valeur moyenne et de ses fluctuations sous la forme:

$$\epsilon(\boldsymbol{r}) = \bar{\epsilon}(\boldsymbol{r}) + \tilde{\epsilon}(\boldsymbol{r}), \tag{1.2}$$

où $\bar{}$ siginifie que l'on a pris une moyenne d'ensemble, ce qui permet de mettre l'équation de Helmoltz sous la forme:

$$\Delta u(\boldsymbol{r}) + k_0^2 (\bar{\epsilon}(\boldsymbol{r}) + \tilde{\epsilon}(\boldsymbol{r})) u(\boldsymbol{r}) = 0. \tag{1.3}$$

Nous introduisons ensuite la fonction de Green du milieu en l'absence de fluctuations. Elle est solution de l'équation:

$$\Delta G(\boldsymbol{r}, \boldsymbol{r}_0) + k_0^2 \bar{\epsilon}(\boldsymbol{r}) G(\boldsymbol{r}, \boldsymbol{r}_0) = \delta(\boldsymbol{r} - \boldsymbol{r}_0), \tag{1.4}$$

où $\boldsymbol{r}_0$ est la position de la source dans le milieu. Nous remarquons qu'en plus de l'équation (1.4), on doit se donner des conditions de bord comme par exemple les conditions de radiation à l'infini. On note u_0 la solution de l'équation homogène associée:

$$\Delta u_0(\boldsymbol{r}) + k_0^2 \bar{\epsilon}(\boldsymbol{r}) u_0(\boldsymbol{r}) = 0, \tag{1.5}$$

avec les mêmes conditions de bord. Si l'on a une distribution quelconque de source $S(\boldsymbol{r})$ dans le milieu, la solution de l'équation de Helmoltz en l'absence de fluctuations s'écrit:

$$u(\boldsymbol{r}) = u_0(\boldsymbol{r}) + \int G(\boldsymbol{r}, \boldsymbol{r}_0) S(\boldsymbol{r}_0) d^3 r_0. \tag{1.6}$$

En réécrivant l'équation 1.3 sous la forme:

$$\Delta u(\boldsymbol{r}) + k_0^2 \bar{\epsilon}(\boldsymbol{r}) u(\boldsymbol{r}) = -k_0^2 \tilde{\epsilon}(\boldsymbol{r}) u(\boldsymbol{r}) \tag{1.7}$$

on remarque que la solution de l'équation d'Helmoltz en présence de fluctuations n'est rien d'autre que la solution de l'équation d'Helmoltz dans le milieu moyen (ou milieu de 'référence'), avec le terme de source $S(\boldsymbol{r}) = -k_0^2 \tilde{\epsilon}(\boldsymbol{r}) u(\boldsymbol{r})$. En accord avec l'équation (1.6), on obtient donc:

$$u(\boldsymbol{r}) = u_0(\boldsymbol{r}) - k_0^2 \int G(\boldsymbol{r}, \boldsymbol{r}_0) \tilde{\epsilon}(\boldsymbol{r}_0) u(\boldsymbol{r}_0) d^3 r_0. \tag{1.8}$$

Il faut noter que $u(\boldsymbol{r})$ respecte les conditions de bord via u_0 et G. Jusqu'à présent, nous n'avons fait aucune hypothèse restrictive sur ϵ, c'est à dire que l'équation (1.8) n'est qu'une reformulation de l'équation d'Helmoltz (1.1). Pour un ϵ quelconque, on est incapable de trouver une solution exacte. Néanmoins, si les fluctuations du champ ϵ sont suffisamment petites, on va pouvoir développer u sous forme d'une série en ϵ. Ce genre de méthode porte en mathématiques le nom de développement en série de Neumann et ses conditions d'application sont bien connues. En particulier, il est nécessaire que la norme du noyau de l'opérateur intégral de (1.8) soit très petite devant 1 afin d'assurer la convergence du développement en série. D'un point de vue physique, on comprend que si les fluctuations sont fortes, des phénomènes de résonance interne peuvent intervenir dans le milieu et rendre le problème non linéaire. Le principe d'établissement du développement de Neumann est très simple: Il consiste à écrire le champ en $\boldsymbol{r}_0$ en utilisant (1.8):

$$u(\boldsymbol{r}_0) = u_0(\boldsymbol{r}_0) - k_0^2 \int G(\boldsymbol{r}_0, \boldsymbol{r}_1) \tilde{\epsilon}(\boldsymbol{r}_1) u(\boldsymbol{r}_1) d^3 r_1 \tag{1.9}$$

puis à reporter cette expression dans (1.8):

$$\begin{aligned} u(\boldsymbol{r}) &= u_0(\boldsymbol{r}) - k_0^2 \int G(\boldsymbol{r},\boldsymbol{r}_0) u_0(\boldsymbol{r}_0) \tilde{\epsilon}(\boldsymbol{r}_0) d^3 r_0 \\ &\quad + k_0^4 \int G(\boldsymbol{r},\boldsymbol{r}_0) \tilde{\epsilon}(\boldsymbol{r}_0) d^3 r_0 \int G(\boldsymbol{r}_0,\boldsymbol{r}_1) \tilde{\epsilon}(\boldsymbol{r}_1) u_0(\boldsymbol{r}_1) d^3 r_1 \end{aligned} \tag{1.10}$$

En itérant ce procédé, on obtient la série perturbative:

$$\begin{aligned} u(\boldsymbol{r}) &= u_0(\boldsymbol{r}) - k_0^2 \int G(\boldsymbol{r},\boldsymbol{r}_0) \tilde{\epsilon}(\boldsymbol{r}_0) u_0(\boldsymbol{r}_0) d^3 r_0 \\ &\quad + k_0^4 \int G(\boldsymbol{r},\boldsymbol{r}_0) G(\boldsymbol{r}_0,\boldsymbol{r}_1) \tilde{\epsilon}(\boldsymbol{r}_0) \tilde{\epsilon}(\boldsymbol{r}_1) u_0(\boldsymbol{r}_1) d^3 r_0 d^3 r_1 \\ &\quad - k_0^6 \int G(\boldsymbol{r},\boldsymbol{r}_0) G(\boldsymbol{r}_0,\boldsymbol{r}_1) G(\boldsymbol{r}_1,\boldsymbol{r}_2) \tilde{\epsilon}(\boldsymbol{r}_0) \tilde{\epsilon}(\boldsymbol{r}_1) \tilde{\epsilon}(\boldsymbol{r}_2) u(\boldsymbol{r}_2) d^3 r_0 d^3 r_1 d^3 r_2 \\ &\quad + \cdots . \end{aligned} \tag{1.11}$$

L'interprétation physique de ce développement est claire: le premier terme du membre de droite correspond au champ dans le milieu de référence; le deuxième terme:

$$u_1(\boldsymbol{r}) = -k_0^2 \int G(\boldsymbol{r},\boldsymbol{r}_0) \tilde{\epsilon}(\boldsymbol{r}_0) u_0(\boldsymbol{r}_0) d^3 r_0 \tag{1.12}$$

correspond au champ diffusé une seule fois. En effet, on voit que le champ incident sur l'inhomogénéité $\tilde{\epsilon}$ est u_0 et qu'après diffusion, le champ est propagé jusqu'au point d'observation grâce à G. De même, le troisième terme peut être réécrit sous la forme:

$$u_2(\boldsymbol{r}) = -k_0^2 \int G(\boldsymbol{r},\boldsymbol{r}_0) \tilde{\epsilon}(\boldsymbol{r}_0) u_1(\boldsymbol{r}_0) d^3 r_0 \tag{1.13}$$

et correspond donc au champ diffusé au deuxième ordre. La série (1.11) contient donc tous les ordres de diffusion multiple. A ce point, si la fonction $\epsilon(\boldsymbol{r})$ est donnée, des solutions numériques sont possibles. Mais nous ne nous intéressons pas aux propriétés particulières du champ et c'est pourquoi nous allons introduire le calcul des moments du champ au premier et au deuxième ordre. Pour celà, la technique des expansions diagrammatiques est exposée.

1.1.2 Expansions diagrammatiques

La technique des expansions diagrammatiques a été développée par Feynman afin de traiter les problèmes d'electrodynamique quantique. Elle permet, dans notre cas de représenter de façon visuelle des intégrales multiples et de leur donner une interprétation physique. Pour calculer la fonction de Green moyenne dans le milieu, nous allons utiliser le développement en série (1.11) et calculer la valeur moyenne de chaque terme. On fait alors apparaître des termes de la forme $\langle \tilde{\epsilon}(\boldsymbol{r}_1)\tilde{\epsilon}(\boldsymbol{r}_2)\cdots\tilde{\epsilon}(\boldsymbol{r}_n)\rangle$. A ce point nous introduisons l'hypothèse importante que le champ est gaussien, ce qui implique que l'on peut exprimer tous ses moments d'ordre supérieur à partir des moments d'ordre 2. Plus précisément, on a:

$$\langle \tilde{\epsilon}(\boldsymbol{r}_1)\tilde{\epsilon}(\boldsymbol{r}_2)\cdots\tilde{\epsilon}(\boldsymbol{r}_{2n+1})\rangle = 0 \tag{1.14}$$

$$\langle \tilde{\epsilon}(\boldsymbol{r}_1)\tilde{\epsilon}(\boldsymbol{r}_2)\cdots\tilde{\epsilon}(\boldsymbol{r}_{2n})\rangle = \sum_{p.p.} \psi_{\tilde{\epsilon}}(\boldsymbol{r}_i,\boldsymbol{r}_j)\cdots\psi_{\tilde{\epsilon}}(\boldsymbol{r}_k,\boldsymbol{r}_l) \tag{1.15}$$

où $\sum_{p.p.}$ indique la somme sur toute les paires (i,j) distinctes, sans tenir compte de l'ordre dans lequel apparaissent les indices. On peut montrer que le nombre de ces paires est égal à $\frac{(2n)!}{2^n n!}$. Nous introduisons d'abord quelques notations. On appelle G et G_0 les solutions des équations suivantes:

$$\Delta G(\boldsymbol{r},\boldsymbol{r}_0) + k^2(1+\tilde{\epsilon}(\boldsymbol{r}))G(\boldsymbol{r},\boldsymbol{r}_0) = \delta(\boldsymbol{r}-\boldsymbol{r}_0) \tag{1.16}$$

$$\Delta G_0(\boldsymbol{r},\boldsymbol{r}_0) + k^2 G_0(\boldsymbol{r},\boldsymbol{r}_0) = \delta(\boldsymbol{r}-\boldsymbol{r}_0) \tag{1.17}$$

En utilisant les propriétés des variables gaussiennes et les résultats de la théorie des perturbations, on obtient pour la fonction de Green moyenne $\langle G(\boldsymbol{r},\boldsymbol{r}_0)\rangle$:

$$\begin{aligned}\langle G(\boldsymbol{r},\boldsymbol{r}_0)\rangle &= G_0(\boldsymbol{r},\boldsymbol{r}_0) + k^4\int G_0(\boldsymbol{r},\boldsymbol{r}_1)G_0(\boldsymbol{r}_1,\boldsymbol{r}_2)G_0(\boldsymbol{r}_2,\boldsymbol{r}_0)\psi_{\bar{\epsilon}}(\boldsymbol{r}_2,\boldsymbol{r}_1)d^3r_1d^3r_2 \\ &+ k^8\int G_0(\boldsymbol{r},\boldsymbol{r}_1)G_0(\boldsymbol{r}_1,\boldsymbol{r}_2)G_0(\boldsymbol{r}_2,\boldsymbol{r}_3)G_0(\boldsymbol{r}_3,\boldsymbol{r}_4)G_0(\boldsymbol{r}_4,\boldsymbol{r}_0) \\ &\quad\times[\psi_{\bar{\epsilon}}(\boldsymbol{r}_1,\boldsymbol{r}_2)\psi_{\bar{\epsilon}}(\boldsymbol{r}_3,\boldsymbol{r}_4)+\psi_{\bar{\epsilon}}(\boldsymbol{r}_1,\boldsymbol{r}_3)\psi_{\bar{\epsilon}}(\boldsymbol{r}_2,\boldsymbol{r}_4) \\ &+ \psi_{\bar{\epsilon}}(\boldsymbol{r}_1,\boldsymbol{r}_4)\psi_{\bar{\epsilon}}(\boldsymbol{r}_2,\boldsymbol{r}_3)]\,d^3r_1d^3r_2d^3r_3d^3r_4+\cdots\end{aligned} \tag{1.18}$$

Il est apparent que le calcul de la somme de la série (1.18) est compliqué. Afin de simplifier le calcul analytique, on introduit maintenant les notations de Feynmann. La fonction de Green du milieu non perturbé est représentée par un segment horizontal, dont les extrémités correspondent au point source et au point d'observation:

$$G_0(\boldsymbol{r}_1,\boldsymbol{r}_2) \sim \boldsymbol{r}_1 \overline{\qquad} \boldsymbol{r}_2 \tag{1.19}$$

De la même manière, le terme $k^4\psi_\epsilon(\boldsymbol{r}_1,\boldsymbol{r}_2)$ est remplacé par un trait en pointillé avec deux points aux extrémités:

$$k^4\psi_\epsilon(\boldsymbol{r}_1,\boldsymbol{r}_2) \sim \boldsymbol{r}_1 \bullet\text{------}\bullet \boldsymbol{r}_2 \tag{1.20}$$

On appelle ces points les vertex du diagramme. Afin de représenter les intégrales, on introduit la convention suivante: les points du diagramme n'étant pas situés aux extrémités (vertex internes du diagramme) correspondent à des variables d'espace muettes sur lesquelles on réalise l'intégration. Le nombre de vertex internes est appelé l'ordre du diagramme. Notons ici l'interprétation de la représentation diagrammatique: deux points reliés par des pointillés correspondent dans la réalité physique à deux points appartenant à *la même* inhomogénéité du milieu. En effet, pour deux points du milieu distants de plusieurs longueurs de corrélation la fonction $\psi_{\bar{\epsilon}}$ s'annule. Illustrons ceci en représentant le deuxième terme du développement 1.18:

$$k^4\int G_0(\boldsymbol{r},\boldsymbol{r}_1)G_0(\boldsymbol{r}_1,\boldsymbol{r}_2)G_0(\boldsymbol{r}_2,\boldsymbol{r}_0)\psi_\epsilon(\boldsymbol{r}_1,\boldsymbol{r}_2)d^3r_1d^3r_2 \sim \overset{\boldsymbol{r}_1}{\bullet}\!\cdots\!\overset{\boldsymbol{r}_2}{\bullet} \tag{1.21}$$

Pour la fonction de Green *moyenne* du milieu, on introduit la notation:

$$\bar{G}(\boldsymbol{r},\boldsymbol{r}_0) \sim \blacksquare \tag{1.22}$$

Nous allons maintenant représenter diagrammatiquement le développement en série (1.18), en dessinant tous les diagrammes jusqu'à l'ordre 6. Parmi ces diagrammes, on distingue ceux que l'on peut séparer en deux sans rompre de ligne en pointillé, et ceux pour lesquels cette dernière opération est impossible. Les premiers sont dits "réductibles" ou encore "faiblement connectés", alors que les seconds sont dits "irréductibles" ou encore "fortement connectés". Dans le développement (1.23), les diagrammes apparaissant en 3,6,7,8,10 et 11$^{\text{eme}}$ position sont du type faiblement connecté. Cette classification prend tout son sens lorsqu'on réalise que tous les diagrammes *réductibles* d'ordre 4 peuvent être construits en assemblant des diagrammes *irréductibles* d'ordre 2; les diagrammes réductibles d'ordre 6 sont construits à partir de diagrammes irréductibles d'ordre 2 et 4, etc.. Par exemple, en assemblant les 2$^{\text{eme}}$ et 5$^{\text{eme}}$ diagrammes, on obtient les 7$^{\text{eme}}$ et 8$^{\text{eme}}$. Plus précisément, on peut définir le degré de connectivité d'un diagramme par le nombre de coupures que l'on doit faire sur ce diagramme pour n'obtenir que des diagrammes irréductibles.

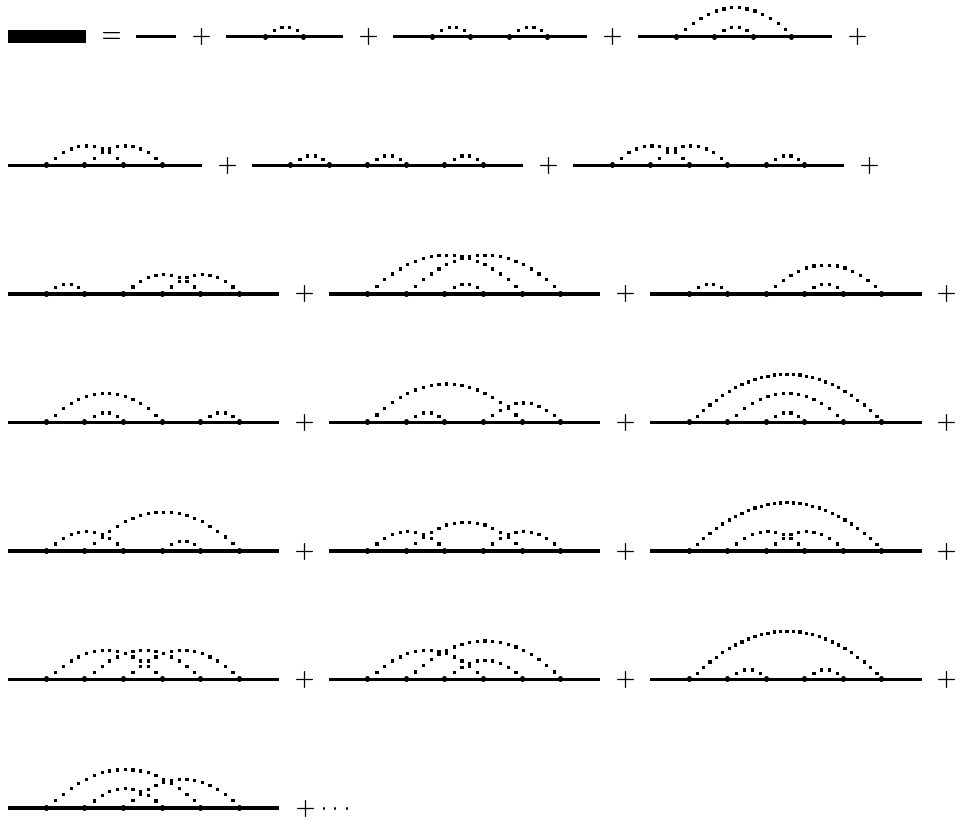

(1.23)

Par conséquent, on va pouvoir regrouper tous les termes irréductibles du développement en série (1.23), à tous les ordres. La somme de ces termes constitue une série infinie qui est notée:

(1.24)

Ci-dessous, nous représentons quelques termes de la série:

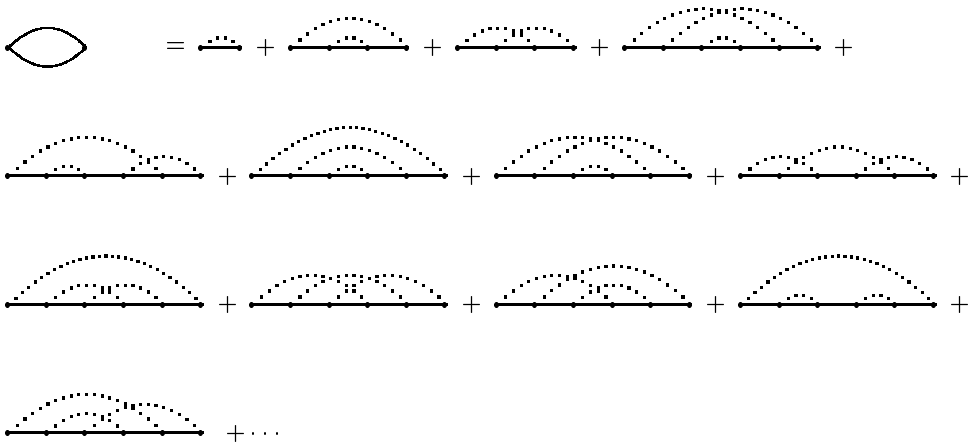

(1.25)

Comme on l'a expliqué plus haut, en connectant deux diagrammes du type 1.25, on obtient un diagramme faiblement connecté de degré 1. En connectant $(n+1)$ diagrammes irréductibles, on obtient

un diagramme réductible d'ordre n. Par exemple, pour $n = 2$ on obtient:

(1.26)

Maintenant, on va réarranger les termes du développement en série 1.23, comme somme de diagrammes irréductibles, et de diagrammes réductibles de degré croissant:

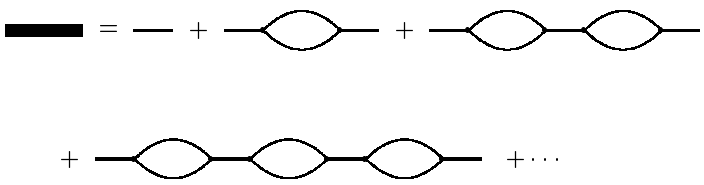

(1.27)

La dernière étape consiste à reconnaître que la somme de série (1.27) est solution de l'équation de Dyson régissant le champ moyen:

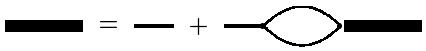

(1.28)

Pour s'en convaincre, il suffit de reporter l'expression du champ moyen donnée par l'équation de Dyson, dans l'équation de Dyson elle-même. En répétant cette opération à l'infini, on obtient le développement en série (1.27). Sous forme analytique, l'équation de Dyson s'écrit:

$$\bar{G}(\boldsymbol{r}, \boldsymbol{r}_0) = G_0(\boldsymbol{r}, \boldsymbol{r}_0) + \int d^3r_1 d^3r_2 G_0(\boldsymbol{r}, \boldsymbol{r}_1) M(\boldsymbol{r}_1, \boldsymbol{r}_2) G(\boldsymbol{r}_2, \boldsymbol{r}_0) \tag{1.29}$$

On peut noter l'analogie qui existe entre cette équation pour le champ moyen et l'équation (1.8) pour une réalisation du milieu aléatoire. En fait l'opérateur de masse est parfois défini comme une "super" diffusion simple. La résolution de l'équation de Dyson nécessite l'évaluation de la somme infinie de termes contenus dans M. En général, ce calcul n'est pas possible et on a recours à des approximations. La plus simple et la plus connue est celle introduite par Bourret. Elle consiste à ne retenir que le premier terme du développement (1.25). La fonction de Green moyenne s'écrit alors sous la forme diagrammatique:

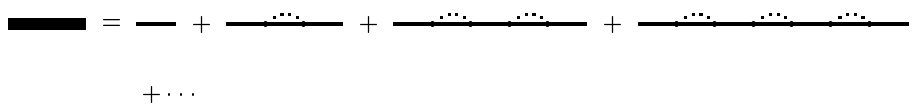

(1.30)

Lorsque cette approximation est adoptée, il est possible de résoudre l'équation de Dyson. Ce calcul peut être trouvé dans l'article de Frisch (1968) et les livres de Rytov et al. (1989) et Sheng (1995). Nous retiendrons seulement le résultat final qui s'écrit dans le cas d'un champ spatialement homogène et isotrope $\tilde{\epsilon}$:

$$\bar{G}(\boldsymbol{r}, \boldsymbol{r}_0) = -\frac{\exp(ik_{ef}|\boldsymbol{r} - \boldsymbol{r}_0|)}{4\pi\ |\boldsymbol{r} - \boldsymbol{r}_0|}. \tag{1.31}$$

Commentons d'abord ce résultat. On voit que la fonction de Green moyenne a exactement la même forme que la fonction de Green du milieu homogène. On a simplement substitué k_{ef} à k_0. La différence apparaît dans l'expression:

$$k_{ef} = k_1 + ik_2, \tag{1.32}$$

où l'on voit que le vecteur d'onde effectif se compose d'une partie réelle et d'une partie imaginaire. La partie réelle est telle que $\frac{k_1 - k}{k} \ll 1$ et $k_1 > k$. Le fait que la partie réelle de k_{ef} soit légèrement plus grande que k, le vecteur d'onde du milieu homogène traduit le fait que le trajet de l'onde dans le milieu

est allongé en raison de la rencontre avec les inhomogénéités du milieu. D'autre part, on peut montrer que la partie imaginaire du nombre d'onde effectif s'écrit:

$$k_2 = \frac{\pi^2 k^2}{2} \int_0^{2k} \Phi_{\tilde{\epsilon}}(\kappa)\kappa d\kappa \tag{1.33}$$

où $\Phi_{\tilde{\epsilon}}$ est relié à $\psi_{\tilde{\epsilon}}$ par la relation:

$$\psi_{\tilde{\epsilon}}(r) = \frac{4\pi}{r} \int_0^{\infty} \Phi_{\tilde{\epsilon}}(\kappa') \sin(\kappa' r)\kappa' d\kappa' \tag{1.34}$$

Autrement dit Φ est le "spectre" des inhomogénéités du milieu. Cette partie imaginaire traduit l'atténuation de l'onde dans le milieu aléatoire à cause de la diffusion. L'énergie initialement émise dans une direction est diffractée dans toutes les directions de l'espace, ce qui cause la décroissance exponentielle de la fonction de Green. Il est possible de montrer, qu'on a l'égalité :

$$k_2 = \frac{\gamma}{2} = \frac{1}{2l} \tag{1.35}$$

où γ est le coefficient d'atténuation de l'intensité calculé dans l'approximation de Born, comme on peut le trouver dans le livre de Aki et Richards (1981). Dans l'approximation de Born, on trouve:

$$\gamma = \frac{\pi k^4}{2} \int_0^{\pi} \int_0^{2\pi} \Phi_{\tilde{\epsilon}}(2k \sin\frac{\theta}{2}) \sin\theta d\theta d\phi \tag{1.36}$$

On s'aperçoit facilement en posant dans cette dernière équation: $\kappa = 2k \sin\frac{\theta}{2}$ que les expressions (1.33) et (1.36) sont cohérentes. l est le libre parcours moyen de l'onde dans le milieu, qui est la grandeur fondamentale dans toute cette thèse. On peut montrer que l'approximation de Bourret n'est valable que pour de faibles fluctuations du paramètre ϵ, plus précisément: $(ka)^2\sigma^2 \ll 1$, avec a la taille typique des inhomogénéités et σ^2, un paramètre adimensionnel qui définit l'intensité des fluctuations de $\tilde{\epsilon}$. Notons enfin que la fonction de Green moyenne vérifie le principe de réciprocité: $\bar{G}(\boldsymbol{r}, \boldsymbol{r}_0) = \bar{G}(\boldsymbol{r}_0, \boldsymbol{r})$.

1.2 Corrélation du Champ. Equations de Transport

Nous avons vu dans la partie précédente que dans un milieu aléatoire, le champ primaire perd de l'énergie à cause de l'interaction avec les inhomogénéités. Après que le champ se soit propagé sur une longueur supérieure à l, la majeure partie de l'énergie émise a été transférée depuis la partie dite "cohérente" du champ vers sa partie dite "incohérente". "Incohérent" signifie ici que les ondes diffusées ont perdu la direction initiale de l'onde émise. C'est sur la partie incohérente que nous allons obtenir des informations en calculant les moments d'ordre 2 du champ. Nous verrons notamment que l'énergie incohérente vérifie une équation de transport. On peut remarquer que pour le cas des ondes, comme pour le cas du marcheur aléatoire, les propriétés de transport sont contenues dans le moment d'ordre 2. En effet pour le marcheur aléatoire dont on mesure la position $\vec{r}(t)$ par rapport à l'origine, on a $\langle \vec{r}(t) \rangle = \vec{0}$, mais $\langle r^2(t) \rangle \sim 2dDt$ avec $t \to \infty$. d est la dimension de l'espace et D, la constante de diffusion. Cette analogie est soulignée par Sheng (1995).

1.2.1 Equation de Bethe-Salpeter.

Pour calculer le moment d'ordre 2 $\langle G(\boldsymbol{r}', \boldsymbol{r}_0'), G^\star(\boldsymbol{r}'', \boldsymbol{r}_0'') \rangle$, appelé aussi "fonction de cohérence", il faut d'abord calculer le produit des termes qui apparaissent dans le développement en série (1.11), puis calculer

leur valeur moyenne. Ceci est réalisé plus aisément en utilisant la représentation de (1.11) sous forme de diagrammes. Pour celà, nous introduisons les notations suivantes:

$$-k^2\tilde{\epsilon}(\boldsymbol{r}) \sim \times \qquad\qquad \langle \times \times \rangle = \quad \bullet\text{---}\bullet \tag{1.37}$$

La deuxième égalité n'est que la définition de la fonction de corrélation de $\tilde{\epsilon}$. Une fois ces notations adoptées, le développement en série 1.11 s'écrit sous la forme diagrammatique:

$$G(\boldsymbol{r}', \boldsymbol{r}_0') =$$ 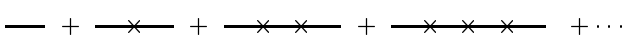 $$+\cdots$$ (1.38)

Nous allons maintenant considérer la valeur moyenne du produit de deux diagrammes contenant deux diffuseurs. Remarquons que lorsque le nombre de vertex apparaissant dans un produit est impair, ce terme disparaît car nous avons supposé que les champs sont gaussiens. On obtient:

$\langle$ 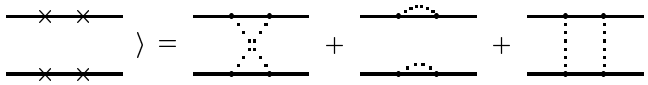 $\rangle =$ (1.39)

Par convention, les termes complexes conjugués apparaissent dans la partie inférieure du diagramme, mais cette distinction n'est pas fondamentale. Discutons la structure des diagrammes apparaissant dans le membre de droite. Nous allons introduire une classification basée sur les mêmes propriétés topologiques que pour l'équation de Dyson. Le deuxième diagramme est du type "non-connecté". C'est à dire qu'il correspond à un des termes du produit des deux fonctions de Green moyennes. En regroupant tous les termes de ce type, on obtiendra donc le produit :$\langle G(\boldsymbol{r}', \boldsymbol{r}_0')\rangle\langle G(\boldsymbol{r}'', \boldsymbol{r}_0'')\rangle$. Le troisième diagramme peut-être séparé par une coupure verticale en deux sous-diagrammes contenant chacun deux diffuseurs. C'est un diagramme connecté réductible (ici de degré 1). Le premier diagramme est par contre irréductible. Notons ici que dans la terminologie que nous utiliserons plus loin le troisième diagramme est dit en échelle ("ladder"), alors que le premier est dit cyclique ou "croisé maximum" ("maximally crossed").

Pour représenter la fonction de cohérence, nous utiliserons la notation:

$\langle G(\boldsymbol{r}', \boldsymbol{r}_0')G^\star(\boldsymbol{r}'', \boldsymbol{r}_0'')\rangle \sim$ 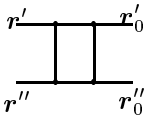

(1.40)

Cette fonction a deux canaux d'entrée $\boldsymbol{r}_0^{'}$ et $\boldsymbol{r}_0^{''}$ et deux canaux de sortie $\boldsymbol{r}'$ et $\boldsymbol{r}^{''}$. Elle est parfois appelée fonction de vertex à quatre points. Nous allons maintenant développer sous forme de série la fonction de cohérence (en nous limitant à quelques termes):

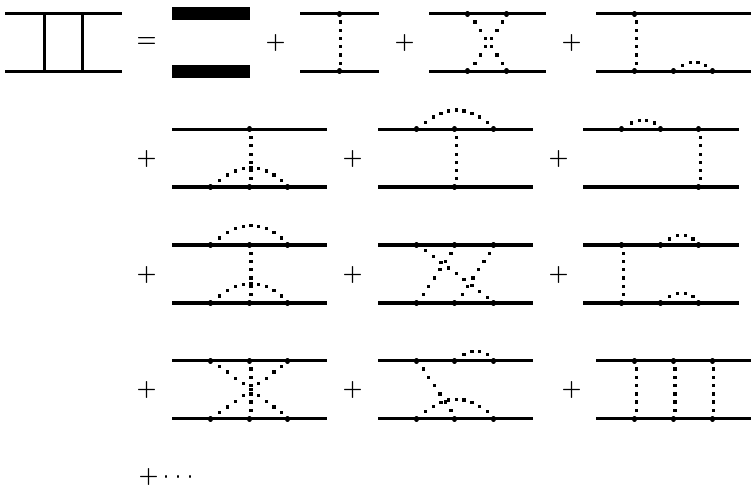 (1.41)

Le premier terme regroupe tous les diagrammes non connectés. On reconnaît également que les 4,7,10,12 et 13$^{\text{eme}}$ diagrammes sont du type réductible. Comme on l'a fait pour l'équation de Dyson, on va regrouper tous les termes de type irréductible à partir desquels on peut reconstruire tous les termes réductibles de degré (de connectivité) croissant. On définit ainsi le noyau de l'opérateur d'intensité $K(\boldsymbol{r}_1, \boldsymbol{r}_2; \boldsymbol{r}_3, \boldsymbol{r}_4)$:

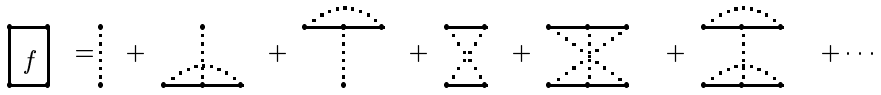

(1.42)

La lettre "*f*" au coeur du diagramme indique que le noyau de l'opérateur d'intensité n'est composé que de diagrammes *fortement* connectés. Afin de clarifier cette représentation, nous allons exprimer les premiers termes de l'opérateur d'intensité sous forme analytique:

$$\begin{aligned} K(\boldsymbol{r}_1, \boldsymbol{r}_2; \boldsymbol{r}_3, \boldsymbol{r}_4) &= k^4 \psi_{\bar{\epsilon}}(\boldsymbol{r}_1, \boldsymbol{r}_2)\delta(\boldsymbol{r}_1 - \boldsymbol{r}_3)\delta(\boldsymbol{r}_2 - \boldsymbol{r}_4) \\ &+ \int k^8 \psi_{\bar{\epsilon}}(\boldsymbol{r}_1, \boldsymbol{r}_5)\psi_{\bar{\epsilon}}(\boldsymbol{r}_2, \boldsymbol{r}_4) G_0^\star(\boldsymbol{r}_2, \boldsymbol{r}_5) G_0^\star(\boldsymbol{r}_5, \boldsymbol{r}_4)\delta(\boldsymbol{r}_1 - \boldsymbol{r}_3) d^3 r_5 \\ &+ \int k^8 \psi_{\bar{\epsilon}}(\boldsymbol{r}_1, \boldsymbol{r}_3)\psi_{\bar{\epsilon}}(\boldsymbol{r}_5, \boldsymbol{r}_2) G_0(\boldsymbol{r}_1, \boldsymbol{r}_5) G_0(\boldsymbol{r}_5, \boldsymbol{r}_3)\delta(\boldsymbol{r}_2 - \boldsymbol{r}_4) d^3 r_5 \\ &+ k^8 \psi_{\bar{\epsilon}}(\boldsymbol{r}_1, \boldsymbol{r}_4)\psi_{\bar{\epsilon}}(\boldsymbol{r}_2, \boldsymbol{r}_3) G_0(\boldsymbol{r}_1, \boldsymbol{r}_3) G_0^\star(\boldsymbol{r}_2, \boldsymbol{r}_4) \\ &+ \cdots \end{aligned} \tag{1.43}$$

Pour construire un diagramme de degré 1, il faut simplement mettre en entrée et en sortie de l'opérateur d'intensité des termes de la fonction de Green moyenne. Autrement dit, un diagramme faiblement connecté de degré 1 ne peut contenir qu'un seul diagramme fortement connecté. En sommant tous les diagrammes de ce type, on obtient:

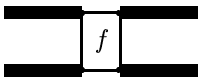

(1.44)

De la même manière, un diagramme faiblement connecté de degré 2 contient deux et seulement deux diagrammes fortement connectés. La somme de tous ces diagrammes s'écrit:

(1.45)

On constate donc que la fonction de cohérence peut s'écrire sous forme d'un développement en série diagrammatique de degré croissant:

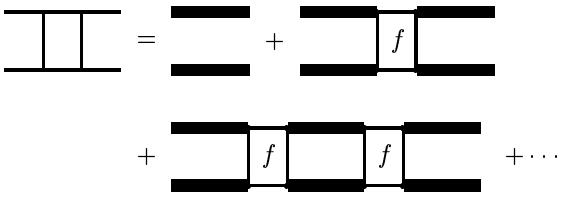

(1.46)

On peut montrer finalement que le développement en série (1.46) n'est autre que la solution de l'équation de Bethe-Salpether:

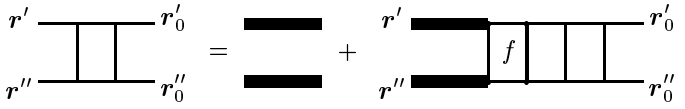

(1.47)

Cette équation s'ecrit sous la forme analytique:

$$\begin{aligned}\langle G(\boldsymbol{r}',\boldsymbol{r}_0')G^\star(\boldsymbol{r}^{''},\boldsymbol{r}_0^{''})\rangle &= \bar{G}(\boldsymbol{r}',\boldsymbol{r}_0')\bar{G}(\boldsymbol{r}^{''},\boldsymbol{r}_0^{''}) \\ &+\int \bar{G}(\boldsymbol{r}',\boldsymbol{r}_1)\bar{G}(\boldsymbol{r}^{''},\boldsymbol{r}_2)K(\boldsymbol{r}_1,\boldsymbol{r}_2;\boldsymbol{r}_3,\boldsymbol{r}_4)\langle G(\boldsymbol{r}_3,\boldsymbol{r}_0')G^\star(\boldsymbol{r}_4,\boldsymbol{r}_0^{''})\rangle dr_1 dr_2 dr_3 dr_4\end{aligned} \tag{1.48}$$

L'équation de Bethe-Salpeter est l'équation de transport la plus générale. Pourtant sous la forme 1.48, sa résolution est ardue. Le problème majeur étant que même en prenant une approximation simple pour le noyau de l'opérateur d'intensité K, l'équation de Bethe-Salpeter ne peut-être résolue exactement. Dans ce qui suit, nous allons mentionner sous quelles approximations on peut transformer l'équation de Bethe-Salpeter en équation de transfert radiatif.

1.2.2 Equation de Transfert Radiatif

Le passage de l'équation de Bethe-Salpeter à l'équation de transfert radiatif est loin d'être simple. Nous allons essayer de regarder les grands principes et laisserons de côté tous les aspects techniques et formels. Il faut d'abord noter qu'il existe une équation reliant le noyau de l'opérateur de masse, le noyau de l'opérateur d'intensité et la fonction de Green moyenne. Autrement dit sous forme implicite, on a:

$$F(M,K,\bar{G}) = 0, \tag{1.49}$$

où F doit être vu comme un opérateur. Il est physiquement compréhensible que ces trois quantités sont reliées. En effet, l'énergie perdue par le champ cohérent détermine l'atténuation de la fonction de Green moyenne, mais aussi alimente la partie "incohérente" de l'intensité dont nous avons dit que les propriétés de transport étaient déterminées par K. Par conséquent le respect de la conservation de l'énergie impose une relation entre K, M et $\bar{G}$. La relation 1.49 porte le nom de théorème optique. Elle existe sous une forme généralisée appelée "Identité de Ward". Il faut noter l'analogie entre le théorème optique et le théorème d'extinction. Le théorème d'extinction relie en effet la partie imaginaire de l'amplitude du champ diffusé vers l'avant par une inhomogénéité et la section efficace de cette inhomogénéité. Pour revenir à notre problème, les approximations faites sur K et M doivent vérifier le théorème optique, sinon l'énergie du système n'est pas conservée.

Nous allons discuter un second point important. Pour celà, on introduit la fonction de cohérence pour un champ u produit par une distribution (déterministe) de sources s. Par définition la fonction de cohérence de u s'écrit:

$$\Gamma_u(\boldsymbol{r}^{'},\boldsymbol{r}^{''}) = \int \langle G(\boldsymbol{r}',\boldsymbol{r}_0')G^\star(\boldsymbol{r}^{''},\boldsymbol{r}_0^{''})\rangle s(\boldsymbol{r}_0',\boldsymbol{r}_0^{''})dr_0' dr_0^{''} \tag{1.50}$$

C'est sur la fonction Γ_u que porte l'équation de transfert radiatif. Plus exactement, en passant en coordonnées barycentriques ou coordonnées du centre de masse $(\boldsymbol{R},\boldsymbol{r})$, on introduit une nouvelle fonction Γ telle que:

$$\Gamma(\boldsymbol{R},\boldsymbol{r}) = \Gamma_u(\boldsymbol{R}+\boldsymbol{r}/2,\boldsymbol{R}-\boldsymbol{r}/2) \tag{1.51}$$

avec $\boldsymbol{R} = (\boldsymbol{r}'+\boldsymbol{r}^{''})/2$ et $\boldsymbol{r} = \boldsymbol{r}^{''}-\boldsymbol{r}^{'}$. $\boldsymbol{R}$ représente la position moyenne, et $\boldsymbol{r}$ l'écart entre les deux points d'observation. Une hypothèse nécessaire au passage à l'équation de transfert radiatif est l'existence d'une *séparation d'échelle* entre les variations de Γ en $\boldsymbol{R}$ et en $\boldsymbol{r}$. Sur quelle base physique repose cette séparation d'échelle? Considérons d'abord les variations de Γ en $\boldsymbol{R}$. Lorsque $|\boldsymbol{R}|$ augmente et qu'on s'éloigne de la source, Γ varie en raison de la perte d'énergie diffusée par les inhomogénéités. Or, nous avons vu que l'échelle spatiale sur laquelle le champ moyen varie en raison de la diffusion est caractérisée par le libre parcours moyen l. Considérons ensuite les fluctuations de Γ en $\boldsymbol{r}$. Il est raisonnable de supposer (au moins lorsqu'on est éloigné d'un libre parcours moyen de la source) que les fluctuations du champ sont fortes. Par conséquent, lorsque les points d'observation sont éloignés de quelques longueurs de corrélations a, Γ fluctue fortement. On suppose dorénavant que les fluctuations de Γ sont rapides en $\boldsymbol{r}$ et lentes en $\boldsymbol{R}$.

Le troisième niveau d'approximation porte sur K. Nous avons vu qu'il était possible de résoudre l'équation de Dyson en utilisant une approximation de faibles fluctuations: l'approximation de Bourret.

D'autre part, nous avons mentionné la nécessité d'adopter un niveau d'approximation égal pour K et R. Ceci est réalisé lorsqu'on ne retient que le premier terme de l'équation 1.42. C'est l'approximation de Bourret qui permet de vérifier la conservation de l'énergie. On l'appelle aussi l'approximation d'échelle en raison de la ressemblance avec les diagrammes obtenus pour la fonction de cohérence dans ce cas:

(1.52)

Les lettres "*ld*" sont l'abbréviation de "ladder" en raison de la ressemblance entre les diagrammes ci-dessus et des échelles. Une fois que ces approximations sont adoptées, on obtient l'équation de transfert radiatif, qui s'écrit (en absence d'absorption) et dans le cas stationnaire:

$$\boldsymbol{\Omega} \cdot \boldsymbol{\nabla}_x I(\boldsymbol{x}, \boldsymbol{\Omega}) = -\frac{I(\boldsymbol{x}, \boldsymbol{\Omega})}{l} + \frac{1}{4\pi l} \int_{4\pi} d\Omega\, p(\boldsymbol{\Omega}, \boldsymbol{\Omega}') I(\boldsymbol{x}, \boldsymbol{\Omega}') + e(\boldsymbol{x}, \boldsymbol{\Omega}), \tag{1.53}$$

L'interprétation phénoménologique de cette équation est la suivante: le membre de gauche représente la variation de l'intensité dans la direction $\boldsymbol{\Omega}$ (vecteur unitaire) par unité de longueur. Le premier terme du membre de gauche représente l'ensemble des pertes d'énergie du faisceau en raison de la diffusion. Le deuxième terme représente les gains en énergie du faisceau en raison de la diffusion d'énergie de la direction $\boldsymbol{\Omega}'$ vers la direction $\boldsymbol{\Omega}$. Le troisième terme représente les sources internes. La fonction $p(\boldsymbol{\Omega}, \boldsymbol{\Omega}')$ décrit la dépendance angulaire de la diffusion simple. L'équation de transfert radiatif traduit donc la conservation de l'énergie dans le milieu. Son contenu ondulatoire nous est donné par le lien qu'il existe entre l'intensité spécifique $I(\boldsymbol{r}, \boldsymbol{\Omega})$ et la fonction de cohérence $\Gamma(\boldsymbol{R}, \boldsymbol{r})$ et par le lien entre $p(\boldsymbol{\Omega}, \boldsymbol{\Omega}')$ et le spectre des hétérogénéités $\Phi_{\tilde{e}}(k)$. Il est possible de montrer qu'il existe les relations suivantes:

$$\frac{p(\boldsymbol{\Omega}, \boldsymbol{\Omega}')}{l} = \frac{\pi k^4}{2} \Phi_{\tilde{e}}(k(\boldsymbol{\Omega} - \boldsymbol{\Omega}')) \tag{1.54}$$

$$\Gamma(\boldsymbol{R}, \boldsymbol{r}) = \oint I(\boldsymbol{R}, \boldsymbol{\Omega}) \exp(ik\boldsymbol{r} \cdot \boldsymbol{\Omega}) d\Omega. \tag{1.55}$$

$d\Omega$ représente un élément de surface de la sphère de rayon unité (élément d'angle solide). La relation (1.55) est très similaire à la transformation de Fourier entre $I(\boldsymbol{R}, \boldsymbol{\Omega})$ et Γ. Ainsi, $I(\boldsymbol{R}, \boldsymbol{\Omega})$ est parfois appelé spectre angulaire de Γ. Nous avons donc établi le lien entre équation d'onde et de transport. L'équation (1.54) est particulièrement utile puisqu'elle nous montre que la connaissance de la solution du problème de diffusion simple peut servir d'élément de base pour construire la diffusion multiple. Ces considérations seront importantes dans le cas élastique au chapitre 4. Dans le chapitre suivant nous allons résoudre l'équation de transfert radiatif dans le cas de milieux stratifiés.

Chapter 2

Transfert Radiatif et Diffusion en Milieu Stratifié

2.1 Principe de base des simulations Monte-Carlo.

Dans cette partie, nous allons rappeler les principes fondamentaux du calcul d'intégrales par méthode de Monte-Carlo. Nous montrerons ensuite comment la méthode peut-être appliquée à la résolution des problèmes de transfert radiatif, sous forme d'équations intégrales. Pour plus de clarté, nous nous placerons en régime stationnaire, l'extension au régime dynamique étant directe. Il faut noter que de nombreuses méthodes numériques ont été développées pour résoudre l'équation de transfert radiatif. Pour n'en citer que quelques-unes: développement en harmonique sphérique (Kourganoff 1964), "adding and doubling" (de Haan, Bosma et Hovenier 1987), la plus populaire étant la méthode des ordonnées discrètes (Chandrasekahr 1960). Pourquoi choisir la méthode de Monte-Carlo plutôt qu'une autre? La résolution de l'équation de transfert radiatif nécessite le calcul d'intégrales multi-dimensionnelles. Or, plus le problème comporte de degrés de liberté et plus les algorithmes Monte-Carlo se montrent efficaces par rapport à leurs concurrents tels l'intégration gaussienne (qui est à la base de la méthode des ordonnées discrètes par exemple). En fait, la plupart des méthodes développées en astrophysique considèrent des ondes planes et des systèmes unidimensionnels. Dans le cas de la sismologie où les problèmes sont tri-dimensionnels et dépendants du temps, l'utilisation des méthodes que nous avons citées plus haut devient très prohibitif.

2.1.1 Théorème fondamental.

La méthode de Monte-Carlo permet de calculer des intégrales multi-dimensionnelles de la façon suivante: On appelle I l'intégrale d'une fonction $f(\boldsymbol{x})$ sur un domaine D:

$$I = \int_D d\boldsymbol{x} f(\boldsymbol{x}), \tag{2.1}$$

où $\boldsymbol{x}$ est un vecteur à plusieurs dimensions. Npus pouvons réécrire l'intégrale sous la forme suivante:

$$I = \int_D h(\boldsymbol{x}) g(\boldsymbol{x}) d\boldsymbol{x}, \tag{2.2}$$

avec $g(\boldsymbol{x}) \geq 0$ et $\int_D g(\mathbf{x}) = \mathbf{1}$. La méthode de Monte Carlo repose sur le théorème suivant: Si N echantillons indépendants $\boldsymbol{x}_i$ du domaine D sont tirés aléatoirement selon la distribution de probabilité donnée par la fonction $g(\boldsymbol{x})$ alors:

$$\hat{I} = \frac{1}{N} \sum_{i=1}^{N} h(\boldsymbol{x}_i) \tag{2.3}$$

est un estimateur non biaisé de l'intégrale I. La preuve peut être trouvée dans le livre de Lux et Koblinger (1991). Dans le paragraphe suivant, nous allons montrer comment ce théorème s'applique directement sur l'équation de transfert radiatif.

2.1.2 Application aux équations de transport.

Considerons le cas le plus simple de la diffusion multiple par des diffuseurs isotropes dans un milieu infini et uniforme, en régime indépendant du temps. On souhaite calculer la fonction de Green de l'équation de transfert radiatif pour une source isotrope située à l'origine du système de coordonnées. Dans ce cas, l'équation de transfert radiatif peut être facilement transformée en une équation intégrale de la forme (Liu et Ishimaru 1974):

$$I(\boldsymbol{r}) = \frac{1}{l}\int I(\boldsymbol{r}')\frac{\exp -\frac{|\boldsymbol{r}-\boldsymbol{r}'|}{l}}{4\pi|\boldsymbol{r}-\boldsymbol{r}'|^2}d^3r' + \frac{S_0 \exp -\frac{|\boldsymbol{r}|}{l}}{4\pi r^2} \tag{2.4}$$

avec les notations suivantes:

- I est l'intensité, solution de l'équation de transfert radiatif.
- l est le libre parcours moyen,
- S_0 caractérise l'énergie totale libérée à la source,
- enfin l'intégrale est prise sur tout l'espace.

Le premier terme représente l'énergie des ondes diffusées et le second terme, l'énergie provenant directement de la source. Pour résoudre cette équation intégrale, nous utilisons le développement en série de Neumann de $I(\boldsymbol{r})$, aussi appelé développement de Born en optique:

$$I = I^{(0)} + I^{(1)} + \cdots + I^{(i)} + \cdots. \tag{2.5}$$

$I^{(0)}$ est l'énergie provenant directement de la source, $I^{(1)}$ est la solution de l'équation obtenue en supposant que $I = I^{(0)}$ dans l'intégrale; $I^{(i)}$ est obtenu en supposant que $I = I^{(i-1)}$ dans l'intégrale et ainsi de suite. Chaque terme correspond physiquement à un ordre de diffusion. Nous pouvons, par exemple, expliciter le terme de deuxième ordre:

$$I^{(2)}_{incoh}(\boldsymbol{r}) = \int\int \frac{\exp -\frac{|\boldsymbol{r}'|}{l}d^3r'}{l4\pi r'^2}\frac{\exp -\frac{|\boldsymbol{r}''-\boldsymbol{r}'|}{l}d^3r''}{l4\pi|\boldsymbol{r}''-\boldsymbol{r}'|^2}\frac{\exp \frac{|\boldsymbol{r}-\boldsymbol{r}''|}{l}}{4\pi|\boldsymbol{r}-\boldsymbol{r}''|^2}. \tag{2.6}$$

Chaque intégrale est prise sur tout l'espace et on a supposé que $S_0 = 1$. En introduisant la nouvelle variable $\boldsymbol{r}_2 = \boldsymbol{r}'' - \boldsymbol{r}'$ et en utilisant ensuite les coordonnées sphériques, nous obtenons:

$$I^{(2)}(\boldsymbol{r}) = \int\int \overbrace{\frac{\exp -\frac{r_1}{l}}{l}\frac{sin\theta_1}{4\pi}\frac{\exp -\frac{r_2}{l}}{l}\frac{sin\theta_2}{4\pi}}^{g(r_1,\theta_1,\phi_1,r_2,\theta_2,\phi_2)}\overbrace{\frac{\exp -\frac{|\boldsymbol{r}-\boldsymbol{r}_1-\boldsymbol{r}_2|}{l}}{4\pi|\boldsymbol{r}-\boldsymbol{r}_1-\boldsymbol{r}_2|^2}}^{h(r_1,\theta_1,\phi_1,r_2,\theta_2,\phi_2)} d\theta_1 d\phi_1 dr_1 d\theta_2 d\phi_2 dr_2, \tag{2.7}$$

avec $r_i \in [0,\infty], \theta_i \in [0,\pi], \phi_i \in [0,2\pi]$. De plus, nous distinguons dans cette intégrale les fonctions h et g introduites au paragraphe précédent. On peut facilement vérifier que g satisfait bien aux hypothèses d'application du théorème (2.3). A partir de cette expression, on peut retrouver l'image physique classique de la marche aléatoire:
Tirer aléatoirement la variable aléatoire r_1 selon une loi exponentielle, simule un "pas" de la marche aléatoire. Tirer les variables θ_1 et ϕ_1 selon la loi $\frac{\sin(\theta_1)}{4\pi}$, simule une source isotrope. Le tirage de r_2 simule le deuxième pas de la marche, et le tirage de θ_2 et ϕ_2 simule la diffusion isotrope. La quantité $\frac{\exp -(|\boldsymbol{r}-\boldsymbol{r}_1-\boldsymbol{r}_2|/l)}{4\pi|\boldsymbol{r}-\boldsymbol{r}_1-\boldsymbol{r}_2|^2}$ représente le flux d'énergie atteignant le détecteur lors de la deuxième diffusion. Il y a donc correspondance 1 pour 1 entre méthode de Monte-Carlo et processus physique de transport. L'extension de la formule à la diffusion multiple d'ordre supérieur est directe. Dans l'article qui suit, nous présentons une méthode Monte-Carlo pour des milieux où le libre parcours moyen et la vitesse dépendent de la profondeur.

Radiative transfer and diffusion of waves in a layered medium: new insight into coda Q

L.Margerin, M. Campillo, B. Van Tiggelen

Geophys. J. Int., 134, 596-612, 1998.

This paper is devoted to the study of the seismic coda in inhomogeneous media exhibiting a discontinuity of physical properties at a given depth. We focus on the problem of a layer overlying a half-space and analyze the precise effect of a contrast of wave velocities and/or scattering strength between both. In order to model S-coda wave envelopes, we solve the radiative transfer equation (Radiative Transfer Equation) by the Monte Carlo method, thereby neglecting the polarization (i.e. acoustic approximation). We pay special attention to the transition towards the diffusion regime. Under the assumption of an almost isotropic intensity field, a diffusion equation (Diffusion Equation) can be derived from the Radiative Transfer Equation and we accurately determine the boundary conditions associated with our models. Analytical solutions of the Diffusion Equation have been obtained and systematically compared to the numerical solutions of the Radiative Transfer Equation. We identify the domain of validity of the diffusion approximation which provides a simple analytical form for the decay in the late coda.

We apply our theoretical investigations to the continental lithosphere. If the scattering strength of the mantle and the crust are supposed to be of the same order, a velocity contrast at the Moho will - according to our theory - amplify the coda signal, since part of the energy is trapped in the crust. An amplification factor is defined and given explicitly as a function of the reflection coefficients and the velocity contrast at the Moho. The shape of the long time decay is of the algebraic form $t^{-\frac{3}{2}}$ like for the one of a uniform half-space.

On the other hand, if the scattering strength of the mantle is small with respect to the one of the crust, the decay in the diffusive regime is predicted to be of the form $t^{-1}\exp(-\frac{2\pi ft}{Q_c^\star})$ where $Q_c^\star$ is a functio of reflection coefficients at the Moho, mean free path of waves in the crust, and frequency f. The coefficient $Q_c^\star$ quantifies the rate at which the partially trapped energy leaks from the crust into the mantle. This formula has the same form as the one proposed by Aki and Chouet (1975) to fit coda observations, which has since then been widely used to deduce the Q_c parameter. With realistic model parameters, we find that $Q_c^\star$ roughly equals the parameter Q_c deduced from observations. It shows that the effect of partial trapping of energy in the crust may be significant. Consequently, seismic albedos of the crust may have been underestimated in previous studies. In our theory, the energy decay of seismic coda waves is determined by the layered structure of the Earth, that is, a highly heterogeneous crust overlying a rather homogeneous mantle. Such structure is confirmed by geological and geochemical studies.
Key words: scattering, seismic coda, Q, layered media

2.2 Introduction

Observations show that the waves forming the tail of the seismograms follow complicated paths in the Earth's lithosphere. Aki and Chouet (1975) demonstrated that the time decay of these so-called coda waves is a characteristic of the underlying medium, independent of the source or the site conditions at the station. By interpreting these arrivals as scattered waves on randomly distributed heterogeneities in the lithosphere, and using two different approximations (single-scattering and diffusion) they proposed an expression of the coda decay in terms of the attenuating properties of the Earth's lithosphere.

The existence of a coda has been recognized on different time and length scales in various areas of physics where multiple scattering occurs. Although the typical wave lengths for optics, acoustics and seismology are microns, centimeters, and hundred meters respectively, a similar theoretical framework can be used for all these fields. Especially in optics, the coda is widely accepted as the result of multiple scattering in a disordered medium. More than forty years ago, Chandrasekhar (1950) developed the phenomenological theory of radiative transfer (Radiative Transfer), solving the problem of energy propagation in a random medium, using the basic assumption that the phase of scattered waves is randomized by the many scattering events, so that no interference occurs. Since then, several authors successfully

established the link between the wave and Radiative Transfer equations (Burridge & Papanicolaou 1975, Turner & Weaver 1994, Ryzhik Papanicolaou & Keller 1996).

When $ka \ll 1$ (k is the wave number and a a typical correlation length of the fluctuations), perturbation theory provides an expansion of the Green function G of the inhomogeneous medium. Averaging G and GG^* over all realizations of the random medium, the so-called Dyson equation governing the mean field and the so-called Bethe-Salpeter equation governing its covariance can be obtained (Frisch 1968). The latter is basically equivalent to a radiative transfer equation (Radiative Transfer Equation), once the so-called "ladder approximation" (Rytov Kravtsov & Tatarskii 1989, Sheng 1995) is adopted The theory turns out to be applicable for a wide range of parameters, only excluding the regime of localization (Ryzhik *et al* 1996).

Several solutions of the Radiative Transfer Equation pertaining to seismic waves have been published and their relevance to seismology has been realized (Abubakirov & Gusev 1990, Hoshiba 1991, Zeng 1991, Sato 1995). They have been used in attempts to estimate the seismic albedo and the scattering mean free path from seismic data. So far, in the interpretation of the data, the underlying assumption has been that the Earth can be considered as an infinite medium with homogeneous wave velocities and statistical properties. Yet, several authors have suggested that the scattering and absorption properties of the Earth may vary with depth (Rautian & Kalthurin 1978, Abubakirov & Gusev 1990, Hoshiba 1994, Gusev 1995).

In this paper, we would like to get some insight into the time decay of coda waves in continental domains for local as well as regional earthquakes. To this end, we solve the acoustic Radiative Transfer Equation by the Monte-Carlo method, taking into account two major boundary conditions: the surface of the Earth which perfectly reflects energy and an angle-dependent reflection coefficient at the Moho interface, due to the difference of wave velocities in the crust and the mantle. No P to S or S to P mode conversions have been taken into account in our scalar analysis. In addition, we assume that earthquakes occur just below the surface, which is in agreement with the observed shallow seismogenic zone in continental areas. Another question we want to address is the convergence of the multiple scattering towards the diffusion limit. We systematically compare our numerical solutions to analytical solutions of the diffusion equation (Diffusion Equation). This enables us to define the domain of validity of the diffusion approximation (Diffusion Approximation). It is important to note that inside the Earth, the causes for multiple scattering are numerous : random velocity fluctuations, cracks, cavities. Each scattering process has its own mean free path. Quite conveniently the Diffusion Equation characterizes the entire scattering process with only two parameters, the diffusion constant D of the waves and the transport mean free path ℓ^* (related by $D = v\ell^*/3$, where v is the shear wave speed), and we do not need to know the microscopic details of the Earth structure.

2.3 Radiative Transfer in a Layered Medium

In this section we present the geometries and physical properties of our different models, and explain our numerical scheme to solve the Radiative Transfer Equation.

2.3.1 Description of the Models

To a first-order approximation, the continental lithosphere can be regarded as a horizontally stratified medium, with depth-dependent properties. A well-known feature of continental areas is the Moho which separates the low-velocity crust from the high-velocity mantle. To understand how a plane structure affects the decay of coda signals, we apply the Radiative Transfer theory to a simplified layered medium. In such a medium physical properties can be different in upper and lower part of the medium as explained below.

Let us recall the parameters relevant to the description of multiple scattering. The acoustic Radiative

Transfer Equation for a statistically isotropic medium without absorption reads,

$$\frac{1}{v}\frac{\partial I(\boldsymbol{x},\boldsymbol{\Omega},t)}{\partial t} + \boldsymbol{\Omega}\cdot\boldsymbol{\nabla}_x I(\boldsymbol{x},\boldsymbol{\Omega},t) = -\frac{I(\boldsymbol{x},\boldsymbol{\Omega},t)}{l} + \frac{1}{4\pi l}\int_{4\pi} d\Omega\, p(\boldsymbol{\Omega},\boldsymbol{\Omega}')I(\boldsymbol{x},\boldsymbol{\Omega}',t) + e(\boldsymbol{x},\boldsymbol{\Omega},t), \qquad (2.8)$$

(e.g. Chandrasekhar, 1950).
Our notations are:

I is the specific intensity, which is the amount of energy flowing across a surface in a specified direction per unit time, per unit solid angle and per unit surface. It is a function of:
$\boldsymbol{x}$, the position in some reference frame,
$\boldsymbol{\Omega}$, a unit vector in the direction of propagation,
and t, the time of observation.

∇_x denotes derivatives are performed on the position variable $\boldsymbol{x}$.

$\int_{4\pi} d\Omega$ denotes integration over all directions of space.

$p(\boldsymbol{\Omega},\boldsymbol{\Omega}')$ is the phase function which describes the angular dependence of the scattering process.

e is the source term,

v, the S-wave velocity, and

l, the scattering mean free path.

All are functions of depth as explained below. It is customary to define the mean free time $\tau = l/v$ denoting the average time between two scattering events. In seismology, the observable quantity is the local, time-dependent energy density at the surface of the Earth:

$$\rho(\boldsymbol{x},t) = \frac{1}{v}\int_{4\pi} I(\boldsymbol{x},\boldsymbol{\Omega},t)d\Omega. \qquad (2.9)$$

The left hand side of equation (2.8) is the intensity variation of a beam of energy during propagation along $\boldsymbol{\Omega}$. The first term on the right hand side is the loss of the incident beam in all directions due to scattering. The second term represents the reinforcement of the incident beam due to the scattered energy from direction $\boldsymbol{\Omega}'$ to direction $\boldsymbol{\Omega}$. The last term denotes sources of intensity. This equation expresses the local conservation of energy. In infinite uniform media the dimensionless parameters which control the physics of the problem are $\frac{r}{l}$ and $\frac{t}{\tau}$ where r is the distance between the point source and the detector.

Let us focus on the problem of a layer on top of a half-space and discuss the physical implications. In the following, the subscripts 1 and 2 will refer to top layer and underlying half-space respectively. The upper layer is bounded from above by a free surface that perfectly reflects energy. We suppose that the earthquake occurs at shallow depths and that the detectors are located just below the free surface. We distinguish four types of models, which differ in their relative values of the velocities v_1 and v_2 and of the mean free path l_1 and l_2; H is the thickness of the layer (see Figure 2.1 and Table I). We distinguish two cases:

Media where scattering occurs in the whole space (models 1 and 2);

Media where scattering is confined to the subsurface layer of thickness H (models 3 and 4). This corresponds to the limiting case $l_2 \to \infty$. An infinite value of the mean free path physically means that no scattering occurs and that waves propagate along straight lines.

Subsequently, we distinguish media with and without a wave-velocity discontinuity at depth H. Together this leads to four different categories summarized in Table I. The numbers in Table I will be explained later. Note that model 1 corresponds to the classical uniform half-space used by Hoshiba (1993) for data interpretation and will be considered by us as a reference model. Below, we discuss major differences with the three other cases.

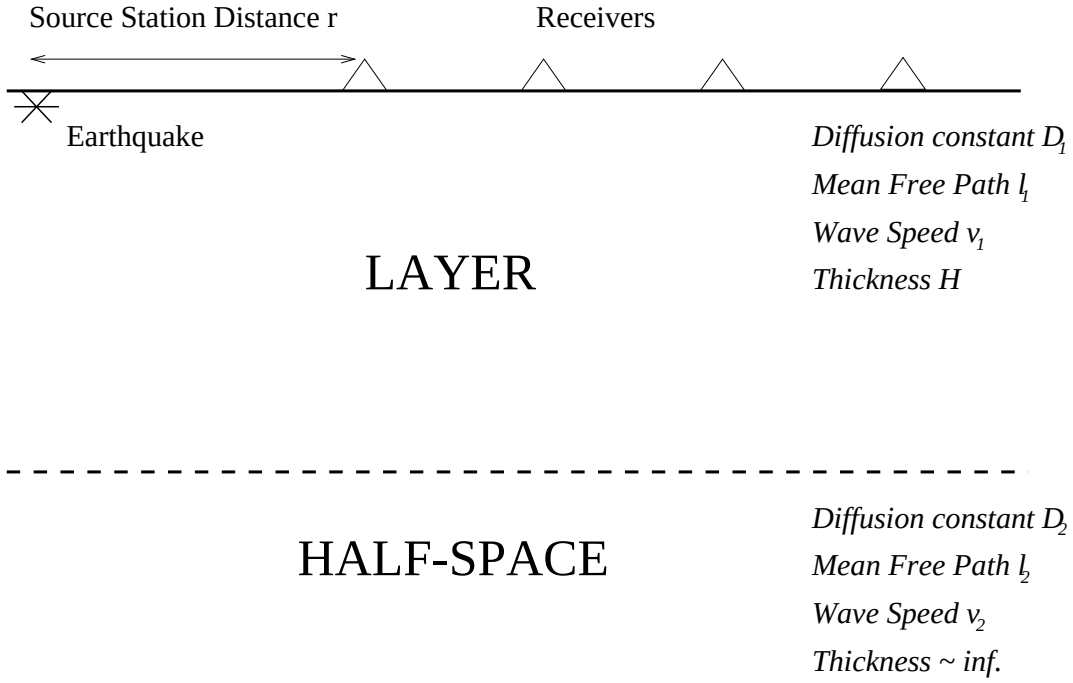

Figure 2.1: Geometry and physical parameters of the models. The earthquakes and receivers are supposed to be located just below the free surface. Numerical values of the physical constants can be found in Table I.

Table I: Classification and Physical Properties of the Models.

	Model 1	Model 2	Model 3	Model 4
velocity contrast $\frac{v_1}{v_2}$	no $\frac{3.5}{3.5} = 1.$	yes $\frac{3.5}{4.7} = 0.74$	no $\frac{3.5}{3.5} = 1.$	yes $\frac{3.5}{4.7} = 0.74$
mean free path contrast $\frac{l1}{l2}$	no $\frac{10}{10}, \frac{30}{30} = 1.$ $\frac{70}{70}, \frac{150}{150} = 1.$	no $\frac{10}{10}, \frac{30}{30} = 1.$ $\frac{70}{70}, \frac{150}{150} = 1.$	yes $\frac{10}{\infty}, \frac{30}{\infty} = 0.$ $\frac{70}{\infty}, \frac{150}{\infty} = 0.$	yes $\frac{10}{\infty}, \frac{30}{\infty} = 0.$ $\frac{70}{\infty}, \frac{150}{\infty} = 0.$
relative layer thickness $\frac{H}{l_1}$				
$H = 40$ km	∞	$0.27, 0.57$ $1.33, 4.$	id.	id.
$H = 30$ km	∞	$0.2, 0.43$ $1., 3.$	id.	id.

Due to the addition of a sharp velocity contrast between the top layer and the half-space, reflection and transmission of waves at the base of the layer must be taken into account. Hence, part of the emitted energy will be guided in the upper layer and another part will leak into the half-space.

For models 3 and 4 the thickness H is the crucial length scale.

In addition to the space and time variables, the solutions of the Radiative Transfer Equation depend on the following ratios :

$\frac{l_1}{l_2}, \frac{v_1}{v_2}$ for model 2.

$\frac{H}{l_1}, \frac{v_1}{v_2}$ for model 3 and 4.

The many degrees of freedom make our model - though largely simplified - rather complex. In the next section, we discuss how the boundary conditions at the top and bottom of the layer are taken into account.

2.3.2 Solution of the Radiative Transfer Equation by Monte Carlo simulations

The basic procedure we use has been described in great detail by Hoshiba (1991, 1995). So, we will only summarize the method and mention some important modifications we have added to deal with the interfaces. The Monte Carlo scheme is a discretized version of the Radiative Transfer process (see Lux & Koblinger 1991) and requires three main steps :

Construction of the i^{th} random walk of a so-called acoustic "energy particle" in a medium with a specified geometry, where $i = 1, \cdots, N$; N is the total number of random walks we wish to simulate. The particle starts at a point source and changes its direction of propagation each time it encounters either an interface or a scatterer.

We define a lapse time window of observation such that the time origin is the energy emission in the medium and the end time is at 420 seconds, which is enough to study the coda of regional earthquakes. This window is divided in intervals $]n\Delta t, (n+1)\Delta t[$, where $\Delta t = \frac{1}{30}$ s is a constant time increment small with respect to the mean free times, and $n = 0, \cdots, 12600$. $\rho_i(O, n)$ denotes the time-discretized version of the energy density at a subsurface receiver, located at point O. For the m^{th} scattering event, we calculate all energy contributions $E_i^m(pp)$ of the current particle and their associated travel times $t_i^m(pp)$ from source to detector. pp denotes all paths from the last scatterer to the detector, including multiple reflections on the interfaces, but excluding other scattering events, and such that $t_m^i(pp) < 420s$. These contributions are stored in $\rho_i(O, n_i^m(pp))$ where $t_i^m(pp) \in]n_i^m(pp)\Delta t, (n_i^m(pp)+1)\Delta t[$. When the travel time of the particle exceeds the length of the observation window, the random walk is stopped and a new particle is launched at the source.

The process is repeated in order to explore all realizations of the random variables. Finally, all random walk results are averaged to obtain the energy density :

$$\rho(O, n) = \frac{1}{N} \sum_i \rho_i(O, n). \tag{2.10}$$

We now explain how we have taken into account interfaces during the random walk. Consider a layer (medium 1) overlying a half-space (medium 2) as shown in Figure 2.1. They may have different scattering mean free paths, densities and wave speeds. In our analysis, mode conversions are neglected and shear waves are treated as acoustic waves. v_j, d_j, l_j are respectively the shear wave velocity, density, and mean free path of layer j. When a wave is incindent in medium 1 on the velocity discontinuity with medium 2, it may be either reflected or refracted from the boundary, according to Snell's law. Let us call θ_1, θ_1', θ_2, the angles of incidence, reflection and refraction respectively. For $v_1 < v_2$, a critical angle $\theta_c = \arcsin \frac{v_1}{v_2}$ exists that requires special care.

Below the critical angle ($\theta_1 < \theta_c$), we have:

$$\cos\theta_2 = \sqrt{1 - \left(\frac{v_1}{v_2}\right)^2 \sin^2\theta_1} \text{ and } \theta_1 = \theta_1'. \tag{2.11}$$

Introducing $\zeta = \dfrac{d_2 v_2 \cos\theta_2}{d_1 v_1 \cos\theta_1}$, we define:

$$R_{12} = \left(\frac{1-\zeta}{1+\zeta}\right)^2 \tag{2.12}$$

and

$$1 - R_{12} = T_{12} = \frac{4\zeta}{(1+\zeta)^2}, \tag{2.13}$$

where one recognizes R_{12} as the energy reflection coefficient and T_{12} as the energy transmission coefficient, for an acoustic plane wave, incident in medium 1 on the boundary between media 1 and 2. Accordingly, when a particle in medium 1 encounters the boundary between media 1 and 2, it remains in medium 1 with probability R_{12} and continues its walk in medium 2 with probability T_{12}. The new direction of propagation of the particle is determined by equation (2.11).

In the case where $\theta_1 > \theta_c$, one has $R_{12} = 1$, $T_{12} = 0$ and the particle will stay in medium 1. Note that contributions from evanescent waves are neglected in the present analysis. The phase change of the reflected wave at the interface is unimportant since, as stated earlier in the introduction, the intensity is defined as $\langle GG^\star \rangle$, average of the product of two conjugates values. When the particle reaches the free surface it is always reflected with probability 1.

To determine the free path length FPL of a particle between two consecutive scattering events in the layered medium, we proceed as follows. Let us define $SP^m_{i_1}, SP^m_{i_2}, \cdots, SP^m_{i_k}, \cdots$ the lengths of straight paths (that is with a constant direction of propagation) of the particle i in the layered medium between the m^{th} and $(m+1)^{th}$ scatterings (see Figure 2.2). If the particle encounters a velocity discontinuity, its direction of propagation changes according to the reflection/refraction laws defined above. If not, the direction of propagation of the particle is kept constant. We select a uniformly distributed random number $\epsilon \in]0,1[$ and determine the integer q such that :

$$\sum_{k=1}^{k=q} \frac{SP^m_{i_k}}{l^m_{i_k}} = -\ln\epsilon, \tag{2.14}$$

where $l^m_{i_k}$ is the value of the mean free path on the k^{th} straight path. The free path length between two consecutive scattering events is therefore:

$$FPL = \sum_{k=1}^{k=q} SP^m_{i_k} \tag{2.15}$$

and the corresponding travel time T is easily calculated as :

$$T = \sum_{k=1}^{k=q} \frac{SP^m_{i_k}}{v^m_{i_k}}, \tag{2.16}$$

where $v^m_{i_k}$ is the value of the S-wave speed on the k^{th} straight path. Figure 2.2a illustrates the case where the particle remains trapped in the layer; Figure 2.2b illustrates the case where the particle is reflected several times from the boundaries of the layer before it is finally transmitted into the half-space. In each case, we have $q = 4$. Note that the value $m = 0$ corresponds to the emission at the source and is treated

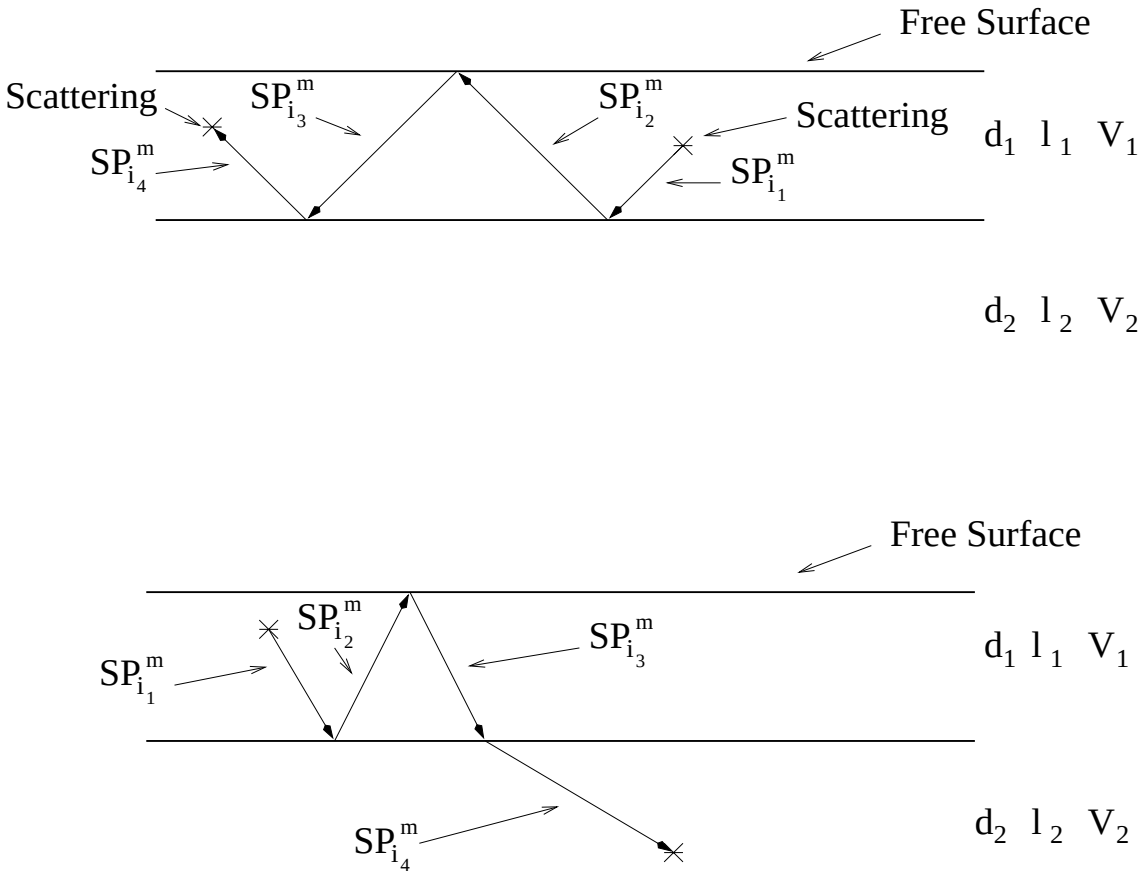

Figure 2.2: Determination of the free path between two successive scattering events in the layered medium. The direction of propagation of the particle changes according to Snell's law when it encounters a boundary and is kept constant otherwise.a) The particle remains in the layer, b) it is transmitted in the lower half-space.

exactly in the same way, since an isotropic radiation is assumed. When the mean free path in the half-space is very large, that is $l_2 \to \infty$, the particle transmitted in the lower medium will travel downward and cannot be backscattered. Its random walk is therefore stopped and a new particle is launched at the source.

The next modification concerns the energetic contents of a particle after scattering. In principle, we have to account for all possible paths from the scatterer to the detector. But let us begin with the simplest path:

We consider a beam of energy emitted in a solid angle $(\theta_2, \theta_2 + d\theta_2; \phi_2, \phi_2 + d\phi_2)$ from a scatterer S located in the half-space, where θ and ϕ are the angular spherical coordinates (see Figure 2.3). Once the beam has crossed the interface separating the layer and the half-space its direction of propagation has changed to $(\theta_1, \theta_1 + d\theta_1; \phi_1, \phi_1 + d\phi_1)$ because of the refraction and it directly reaches a point-like detector O in the layer. If we call dS_2 and dS_1 the cross section of the beam at I (the intersection point at the Moho) and at O respectively, the ratio $\dfrac{dS_1}{dS_2}$ is different from the one for the uniform case because the geometrical spreading of the beam is modified by the refraction. This is the fundamental modification compared to a model with uniform velocity. The energy density contribution of the particle is calculated in the following way :

The probability to be scattered in the right cone of direction is : $p(\cos\chi)\dfrac{dS_2}{4\pi SI^2}$, where χ is the cosine of the scattering angle, and p is the phase function.

The probability to be transmitted is : $T_{21}(\theta_2)$, where T_{21} is the transmission coefficient for a plane wave incident from medium 2 on the boundary between media 1 and 2.

The probability that no other scattering event occurs on the path from S to O is $\exp(-\dfrac{SI}{l_2} - \dfrac{IO}{l_1})$.

We impose the following angular relations :

$$d\phi_1 = d\phi_2 \qquad \text{and} \qquad \frac{\cos\theta_1 d\theta_1}{v_1} = \frac{\cos\theta_2 d\theta_2}{v_2} \tag{2.17}$$

Geometrical considerations show that :

$$dS_2 = SI^2 \sin\theta_2 d\theta_2 d\phi_2 \tag{2.18}$$

$$dS_1 = (SI\sin\theta_2 + IO\sin\theta_1)\left(IO d\theta_1 + SI d\theta_2 \frac{\cos\theta_1}{\cos\theta_2}\right) \tag{2.19}$$

The volume swept by the energy beam during the time interval dt is : $dS_1 v_1 dt$

Finally we obtain the energy contents of the direct beam:

$$E_0 = \frac{p(\cos\chi)T_{21}(\theta_2)\exp\left(-\frac{SI}{l_2} - \frac{IO}{l_1}\right)}{v_1 dt\left(SI\dfrac{\cos\theta_1}{\cos\theta_2} + IO\dfrac{v_1\cos\theta_2}{v_2\cos\theta_1}\right)\left(SI + IO\dfrac{v_1}{v_2}\right)} \tag{2.20}$$

Other paths from the scatterer to the receiver are possible. They involve multiple reflections between top and bottom of the layer, excluding other scattering events. Accounting carefully for the reflection and transmission coefficients, a straightforward modification of the formula (2.20) enables us to calculate the energy contributions of all these paths. A similar Monte Carlo scheme has been developed by Hoshiba (1997) to study the effect of the focal depth, in depth-dependent velocity structures. We checked the validity of our code by comparing our results with published solutions for simple configurations. The agreement is perfect with the results presented by Hoshiba (1995, 1997).

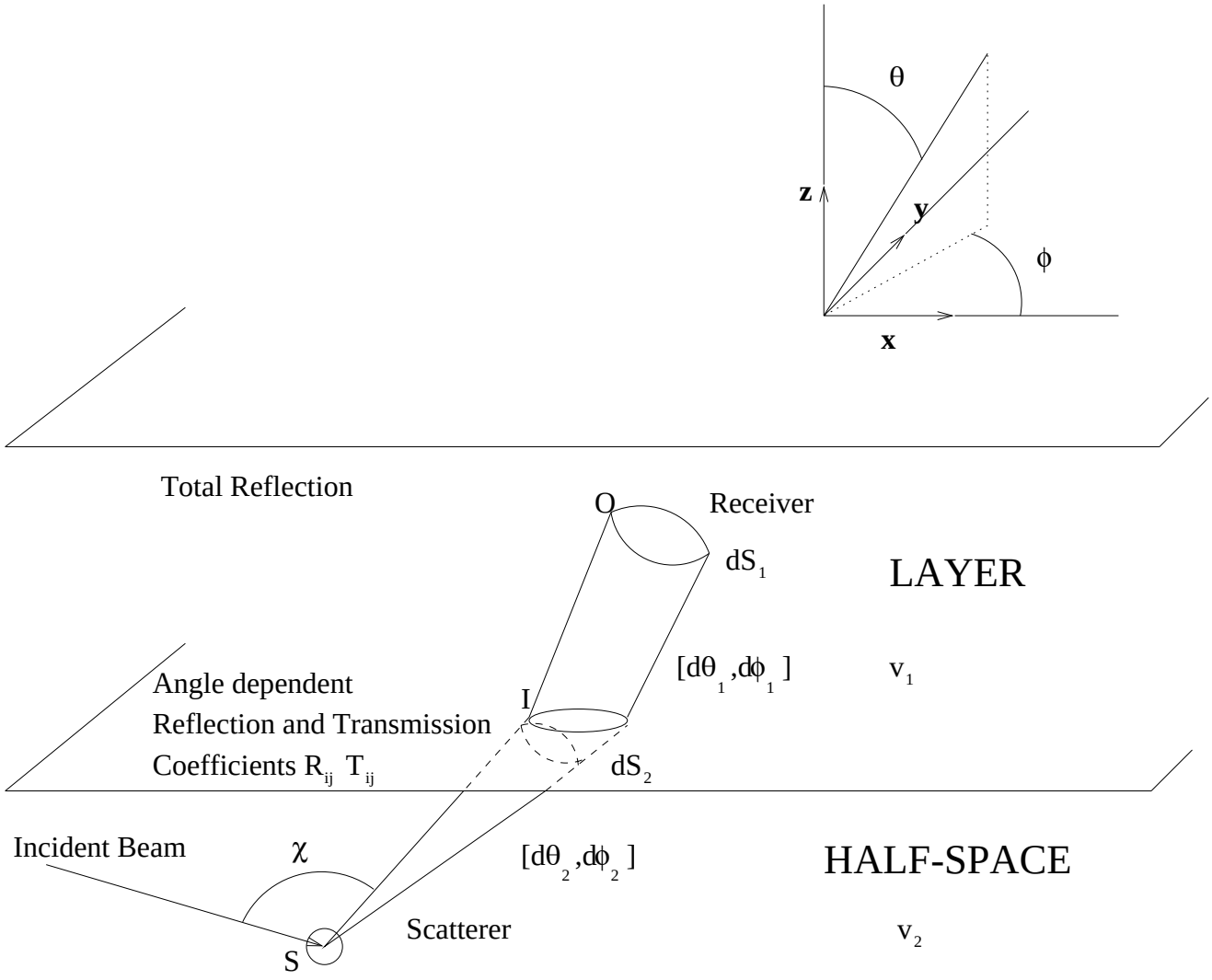

Figure 2.3: Transmission of a scattered energy beam at an interface separating two media with different wave speeds. S is the location of the scattering event. I is a point on the intersection surface between scattered beam and interface. O is the location of the detector. χ denotes the angle between incident and scattered direction. The beam is composed of scattered energy in the solid angle of measure $(d\theta_2, d\phi_2)$ from the point S, where θ and ϕ represent angular spherical coordinates. At the point I, cross section of the beam is dS_2. Once the beam crosses the interface, the new solid angle is $(d\theta_1, d\phi_1)$. At the point O, cross section of the beam is dS_1.

2.4 Diffusion Approximation

2.4.1 Derivation of the Diffusion Equation

Multiple scattering processes will tend to uniformize the angular dependence of the intensity because each scattering event distributes energy in all directions of space. Hence, after a sufficiently large number of scattering events, the intensity will only slightly differ from isotropy. In the theory of Radiative Transfer it is customary to introduce the current vector $\boldsymbol{J}(\boldsymbol{x},t) = \int_{4\pi} I(\boldsymbol{x},t)\boldsymbol{\Omega}d\Omega$ so that $\boldsymbol{J}(\boldsymbol{x},t)\cdot\boldsymbol{n}dS$ gives the rate of flow of energy across the surface dS with normal $\boldsymbol{n}$. At each point $\boldsymbol{x}$, the current vector gives the direction of maximum energy flow. The physical idea of the Diffusion Approximation is to write the intensity as a sum of two terms: first its angularly averaged value, and second a term which takes into account the slight deviation from isotropy expressed by the current vector. Mathematically, this implies that at each point the intensity is only a function of the cosine of the angle $(\boldsymbol{J},\boldsymbol{\Omega})$. In term of $\boldsymbol{J}$ and ρ the intensity is

$$I(\boldsymbol{x},\boldsymbol{\Omega},t) = \frac{\rho v}{4\pi}(\boldsymbol{x},t) + \frac{3}{4\pi}\boldsymbol{J}(\boldsymbol{x},t)\cdot\boldsymbol{\Omega} + \cdots, \tag{2.21}$$

(e.g. Kourganoff 1967). One recognizes here the two first terms of an expansion of the intensity in a Legendre series. The Diffusion Approximation ignores terms of higher order. We shall now derive two equations, by integrating the Radiative Transfer Equation over all solid angles. We first apply the following operator : $\int_{4\pi}(.)d\Omega$ and we also assume that the source is isotropic and point-like (which will be the case in all our simulations). We get the following expression sometimes called the "continuity equation" due to its similarity with that of fluid mechanics:

$$\frac{\partial\rho(\boldsymbol{x},t)}{\partial t} + \boldsymbol{\nabla}\cdot\boldsymbol{J}(\boldsymbol{x},t) = \delta(\boldsymbol{x}-\boldsymbol{x_0})\delta(t) \tag{2.22}$$

An exact consequence of eq. (2.22) is that the variation of the energy amount in a volume V is due to the flow across its boundaries plus the local production. Next we apply to the Radiative Transfer Equation the vectorial operator $\int_{4\pi}(.)\boldsymbol{\Omega}d\Omega$, make use of eq. (2.21) to evaluate the second term of the left hand side:

$$\frac{v}{3}\boldsymbol{\nabla}\rho(\boldsymbol{x},t) + \frac{1}{v}\frac{\partial\boldsymbol{J}(\boldsymbol{x},t)}{\partial t} = -\frac{\boldsymbol{J}(\boldsymbol{x},t)}{l}(1-\langle\cos\theta\rangle), \tag{2.23}$$

where brackets denote averaging over all solid angles,

$$\langle\cos\theta\rangle = \frac{1}{4\pi}\int_{4\pi} p(\cos\theta)\cos\theta\ d\Omega, \tag{2.24}$$

and p is the phase function that describes the angular dependence in single-scattering. By neglecting the derivative of the current vector with respect to time, we obtain the so-called Fick's law :

$$\boldsymbol{J}(\boldsymbol{x},t) = -\frac{vl^*}{3}\boldsymbol{\nabla}\rho(\boldsymbol{x},t) \tag{2.25}$$

$$l^* = \frac{l}{1-\langle\cos\theta\rangle}. \tag{2.26}$$

Equation (2.25) shows that the diffusion process tends to smooth the inhomogeneous distribution of energy in the medium, since current flows from region of high to low energy density.
Equation (2.26) defines the transport mean free path which we shall discuss below.
The final step consists in replacing $\boldsymbol{J}(\boldsymbol{x})$ in eq. (2.22) by its expression given in (2.25). It results in:

$$\frac{\partial\rho(\boldsymbol{x},t)}{\partial t} - D\nabla^2\rho(\boldsymbol{x},t) = \delta(t)\delta(\boldsymbol{x}-\boldsymbol{x_0}) \tag{2.27}$$

$$D = \frac{vl^*}{3} \tag{2.28}$$

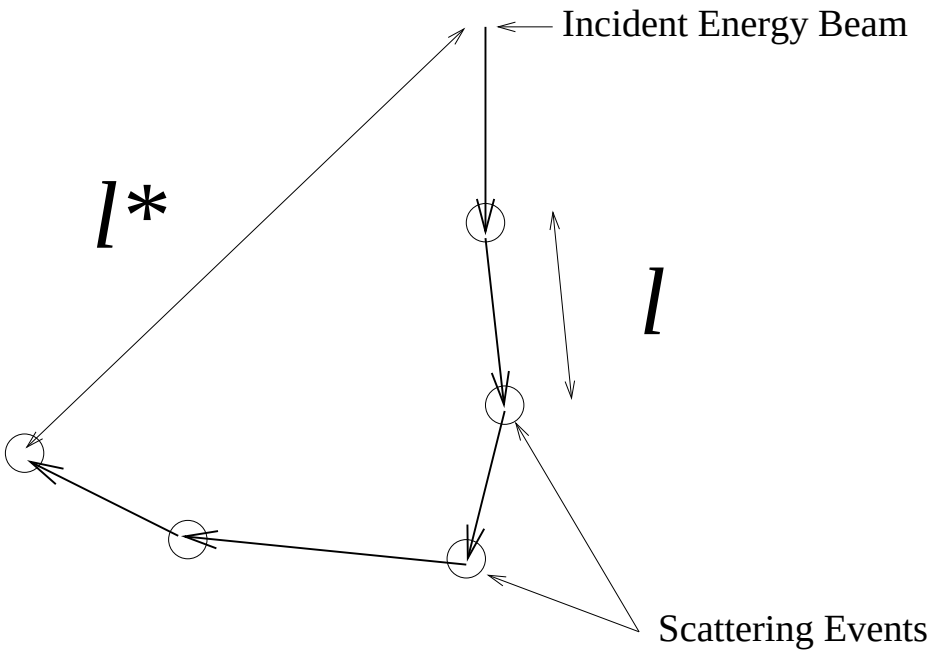

Figure 2.4: l is the scattering mean free path of waves. It represents the average distance between two scattering events. $l^\star$ is the transport mean free path. It is the length scale necessary for a wave packet to loose memory of its initial direction. In the case of isotropic scattering, both are equal.

D is the diffusion constant of waves in the medium. We should note that when single scattering is isotropic $l^* = l$. When scattering is anisotropic, several scattering events are necessary for the direction of a scattered beam to become independent from the one of the initial beam (see Figure 2.4). Hence l^* can be interpreted as the length scale required for a beam to loose "memory" of its initial direction when scattering is anisotropic. For a full derivation of all equations above in the steady state case, we refer to Kourganoff (1967).

2.4.2 Boundary conditions of the Diffusion Equation

We follow a method initiated by Zhu et al. (1991). First, we suppose that the approximation (2.21) is also valid at the interface of two media. The basic procedure consists in writing a balance of energy for an element of surface dS of the boundary. We treat three cases that are relevant to our applications and detail the calculations in one case. *Case a:* A perfectly flat interface separating two scattering media with different wave speeds and diffusion constants (see Figure 2.5). We use the same notations for the reflection and transmission coefficients and in addition introduce D_i the diffusion constant of medium i.

The energy amount J^+ flowing per second in the $+\boldsymbol{z}$ direction at a point P of the boundary can be explicited in two different ways. First, by merely applying the definition of the specific intensity, we get:

$$J^+ = \int_0^{2\pi} d\phi_1 \int_0^{\frac{\pi}{2}} I_1(\boldsymbol{P}, \boldsymbol{\Omega_1}, t) \cos\theta_1 \sin\theta_1 d\theta_1 \tag{2.29}$$

The integration is performed over the upper hemisphere of space directions ($\boldsymbol{\Omega}.\boldsymbol{z}$ is positive). This quantity should equal the flux of medium 1 incident on the interface and reflected back in medium 1,

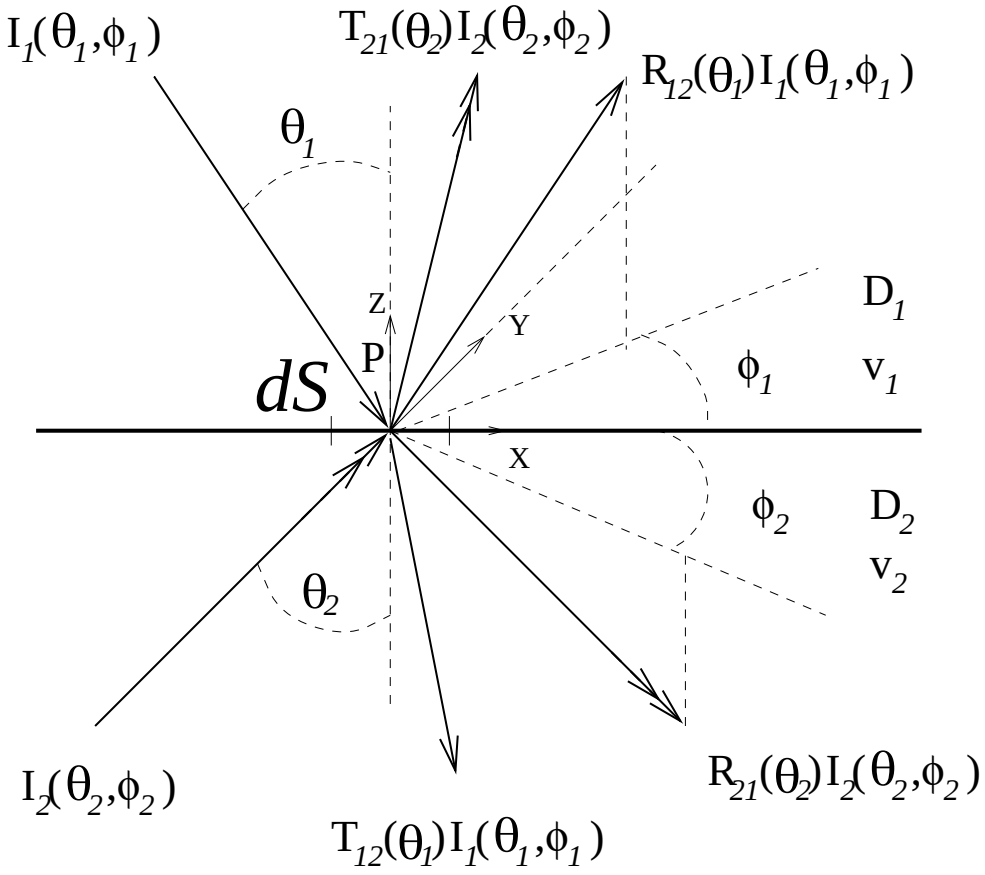

Figure 2.5: Energy balance at the interface between media 1 and 2. The beam 1 (resp. 2) has a single (resp. double) arrow. A beam of intensity $I_i(\theta_i, \phi_i)$ is incident from medium i on a small surface element dS of the boundary of media i and j ($i, j = 1, 2$ and $i \neq j$). θ_i and ϕ_i are the angles of incidence of the beam i in spherical coordinates, the orthonormal reference frame being $(\vec{x}, \vec{y}, \vec{z})$. The part of the beam i reflected in medium i is $R_{ij}I_i$. The part of the beam i transmitted in medium j is $T_{ij}I_i$

plus the flux of medium 2 incident on the boundary and transmitted into medium 1. Hence ,

$$\begin{aligned} J^+ &= \int_0^{2\pi} d\phi_1 \int_\pi^{\frac{\pi}{2}} R_{12}(\theta_1) I_1(\boldsymbol{P}, \boldsymbol{\Omega_1}, t) \cos\theta_1 \sin\theta_1 d\theta_1 \\ &+ \int_0^{2\pi} d\phi_2 \int_0^{\frac{\pi}{2}} T_{21}(\theta_2) I_2(\boldsymbol{P}, \boldsymbol{\Omega_2}, t) \cos\theta_2 \sin\theta_2 d\theta_2 \end{aligned} \tag{2.30}$$

where $\boldsymbol{\Omega_1}, \boldsymbol{\Omega_2}$ are the unit vectors of directions $(\theta_1, \phi_1), (\theta_2, \phi_2)$ respectively. We express the intensity as specified by the approximation (2.21) and replace the current vector by its expression (2.25) and perform the integration over the variable ϕ. Two integrals have to be calculated. The first one is evident :

$$\int_0^{2\pi} \frac{\rho v}{4\pi} d\phi = \frac{1}{2}\rho v \tag{2.31}$$

and the second one is :

$$\frac{3}{4\pi} \int_0^{2\pi} \boldsymbol{J}(\boldsymbol{x}).\boldsymbol{\Omega} d\phi = -\frac{v l^*}{2} \frac{\partial \rho}{\partial z}, \tag{2.32}$$

The integration over θ yields, substituting T_{21} for $(1 - R_{21})$:

$$\rho_1 v_1 (\frac{1}{2} - C_1) - D_1 \frac{\partial \rho_1}{\partial z}(1 + 3\widetilde{C_1}) = \rho_2 v_2 (\frac{1}{2} - C_2) - D_2 \frac{\partial \rho_2}{\partial z}(1 - 3\widetilde{C_2}) \tag{2.33}$$

where:

$$C_j = \int_0^{\frac{\pi}{2}} R_{ji}(\theta) \cos\theta \sin\theta d\theta \tag{2.34}$$

$$\widetilde{C_j} = \int_0^{\frac{\pi}{2}} R_{ji}(\theta) \cos^2\theta \sin\theta d\theta \tag{2.35}$$

We must also impose that the component of the current normal to the surface is conserved so that :

$$D_1 \frac{\partial \rho_1}{\partial z} = D_2 \frac{\partial \rho_2}{\partial z} \tag{2.36}$$

Note that if we write the amount of energy flowing in the $-z$ direction across dS, together with equation (2.33), we check the conservation of normal flux, so that everything is consistent. Upon introducing,

$$\alpha = \frac{(\frac{1}{2} - C_2)}{(\frac{1}{2} - C_1)}, \tag{2.37}$$

$$\beta = 3\frac{(\widetilde{C_1} + \widetilde{C_2})}{\frac{1}{2} - C_1}, \tag{2.38}$$

we obtain the following set of boundary conditions:

$$D_1 \frac{\partial \rho_1}{\partial z} = D_2 \frac{\partial \rho_2}{\partial z} \equiv -J \tag{2.39}$$

$$\rho_1 v_1 + \beta J = \alpha \rho_2 v_2 \tag{2.40}$$

Also for a random surface, rather than a flat surface, exact boundary conditions of this type can be written down.

Case b. A perfectly flat interface separating medium 1 having finite diffusion constant from medium 2 with infinite diffusion constant. This is the case when scattering is infinitely weak in medium 2. In such a medium, waves follow straight ray paths, so that we have only the Diffusion Equation defined in medium 1. In this case the boundary condition only requires that the incoming flux (the amount of energy flowing across the surface dS in the $+z$ direction) be equal to the internally reflected energy. With :

$$\gamma = \frac{2l_1^\star}{3}\frac{(1+3\widetilde{C_1})}{1-2C_1}, \tag{2.41}$$

one has :

$$\rho_1 v_1 + \gamma J = 0. \tag{2.42}$$

Case c. The free surface corresponds to an interface across which no energy can flow. So the boundary condition reads :

$$J = 0. \tag{2.43}$$

For all models of table I we are able to completely describe the diffusion of acoustic energy, since we know the governing equation and its boundary conditions. This equation is simpler to solve than the Radiative Transfer Equation because only derivatives are involved. The solutions of Radiative Transfer Equation should match the Diffusion Equation ones in the limit of large lapse times. The comparison of both helps us to characterize time and length scales necessary to be in the diffusive regime and will be discussed in the next section.

2.4.3 Analytical Solution of the Diffusion Equation.

In this section we briefly describe how analytical solutions of the Diffusion Equation have been obtained for the models 1 to 4 and leave final formulas to the Appendix. In these two models, one always has the same boundary condition (case c) at the top, and two possible boundary conditions (case a or b) at the base of the layer. The latter depends on the finite or infinite value of the diffusion constant in the half-space. The case of a uniform half-space simply corresponds to $v_1 = v_2$, $D_1 = D_2$, $l_1 = l_2$. The following steps have been undertaken: We calculated the Laplace transform with respect to time of the Diffusion Equation and its boundary conditions. We take advantage of the symmetry of the problem by employing cylindrical coordinates. The separation of the variables leads to two Sturm-Liouville differential equations with a delta like source term in both. The homogeneous differential equations are solved with their boundary conditions matched. Next, the source terms are introduced which gives the solution of the problem in the complex frequency (Laplace) domain. Finally, the inverse Laplace transform is calculated. It is expressed in terms of a closed contour integral involving a branch cut. The use of the residue theorem enables us to find the solution in closed form. The technique described above is quite general and powerful and used in various domains of physics to solve partial differential equations (Morse & Feshbach 1953). We do not reproduce the tedious calculations but keep them available to the interested reader.

2.5 Comparison of Diffusion and Radiative Transfer models

In this section, we analyze the results obtained from analytical solutions of the Diffusion Equation and numerical solutions of the Radiative Transfer Equation. We focus on the characteristics of the diffusion regime and define the domain of validity of the Diffusion Approximation. We assume that the scattering is isotropic in both the half-space and the layer. In all calculations, the source is assumed instantaneous, point-like, isotropic, and located just below the free surface. Without loss of generality we assume it to have unit strength. We present tests of convergence of the Radiative Transfer Equation and Diffusion

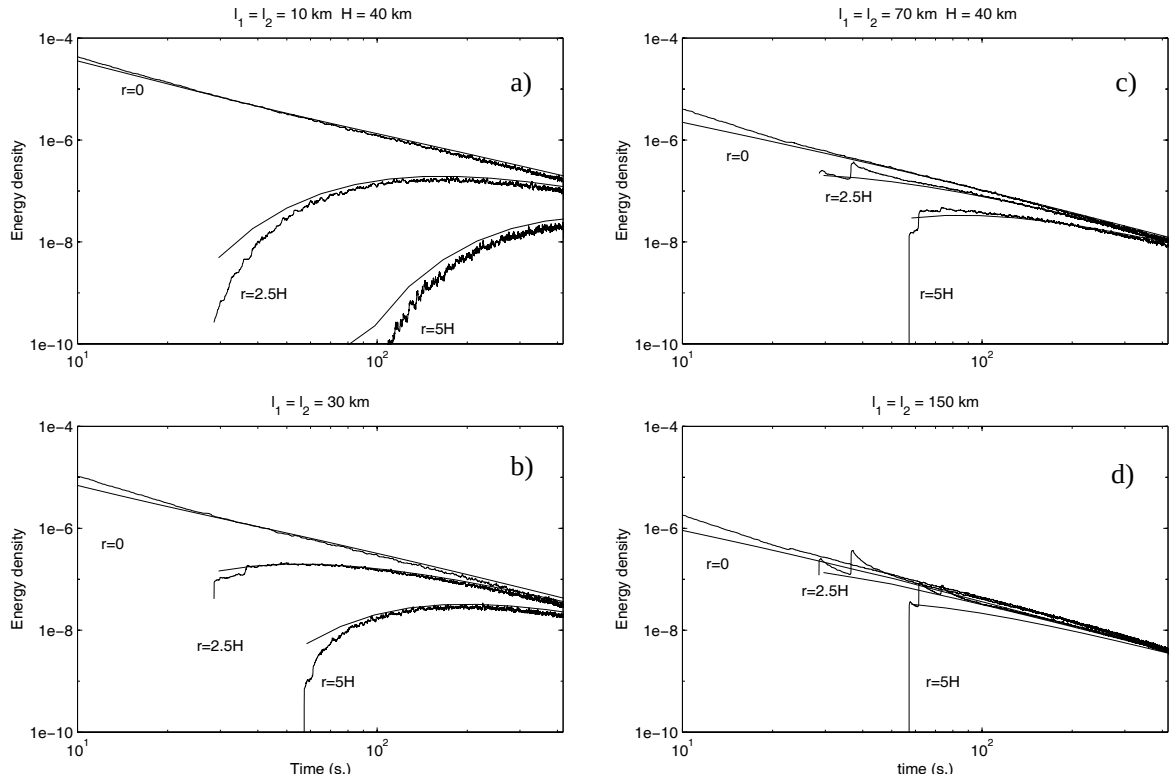

Figure 2.6: Comparison of the solutions of the Diffusion and Radiative Transfer Equations for model 2, with a layer thickness $H = 40$ km. The Radiative Transfer Equation solution curves exhibit characteristic ripples. The mean free path values l_1 (in the upper layer) and l_2 (in the underlying half-space) are indicated on top of each figure. The source is isotropic, point-like, instantaneous and has unit strength. Source and receivers are located just below the free surface. The time origin corresponds to the energy release at source. For each curve the source station distance r is indicated in terms of the upper layer thickness H.

Equation solutions for models 2 and 4. In both models, we have a fixed velocity contrast ($v_1/v_2 = 0.74$) and hence energy is partially reflected and transmitted at the base of the layer. This is a fundamental change with respect to the uniform half-space (model 1). This ratio of 0.74 corresponds to $v_1 = 3.5\,\mathrm{kms}^{-1}$ and $v_2 = 4.7\,\mathrm{kms}^{-1}$ which are realistic values for the shear wave velocities in the continental crust and the upper mantle respectively. We recall that in model 2, the mean free path is depth-independent (no mean free path contrast), while in model 4, the mean free path takes a very large (in the limit, infinite) value below the layer, that is the ratio $\dfrac{l_1}{l_2}$ is equal to zero. This enables us to check our results for two entirely different configurations.

The Diffusion Equation and Radiative Transfer Equation solutions for models 2 have been plotted in Figure 2.6. The Radiative Transfer curves can easily be recognized because they exhibit the characteristic ripples caused by an incomplete averaging. The source detector distance r varies over the broad range 0-200 km. We consider mean free path values ranging from 10 to 150 km in order to explore different scattering regimes. The diffusion theory predicts the asymptotic behavior of the Radiative Transfer Equation solutions with a very good accuracy. Since both calculations are completely independent, this agreement demonstrates the correctness of our calculations.

For the smallest mean free path value ($l_1 = l_2 = 10$ km), one can note the particular shape of the envelopes computed at large distances which do not exhibit the familiar monotonic decay shown in

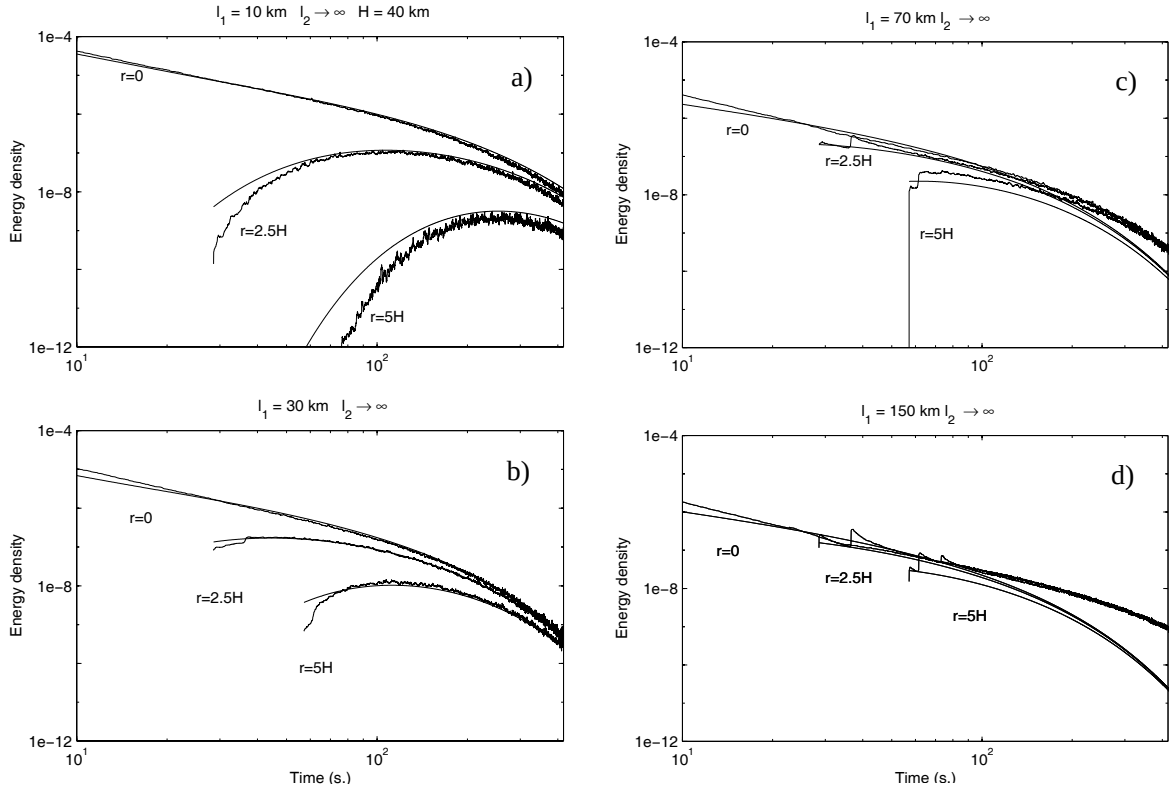

Figure 2.7: Same as figure 6 for model 4.

previous studies (eg Abubakirov & Gusev 1990, Hoshiba 1995). This difference is explained by the fact that previous theoretical studies of the coda decay concentrated on much smaller epicentral distances ($r \leq 100$ km) and larger mean free paths. In addition, we did not take into account any intrinsic absorption of rocks at all, which would evidently lead to a faster decay. Our method does not have any limitation to incorporate an intrinsic attenuation, but in this study we wanted to separate the influence of the mean free path from the one of velocity contrast on the coda decay. For small mean free path ($l = 10$ km) and large epicentral distances ($r > 100$ km), the Radiative Transfer curves show the passage of a diffusion front (Figure 2.6 a), characteristic of the diffusion regime (eg Sheng 1995). We present, in Figure 2.7, the envelopes obtained for model 4. When we consider relatively small values of the mean free path (10 km in Figure 2.7a, and 30 km in Figure 2.7b), the solutions of the Diffusion Equation coincide very well with the solutions of the Radiative Transfer Equation. On the contrary, for somewhat larger mean free path (70 km in Figure 2.7c, 150 km in Figure 2.7d), we found a significant disagreement between the decay of the Radiative Transfer Equation and the one predicted by the Diffusion Equation, especially for large lapse times when the diffusion regime is reached. We need to discuss these results in detail to define the domain of validity of the solutions of the Diffusion Equation.

We introduce the dimensionless parameter H/l_1 in order to keep the discussion as general as possible. We recall that in the derivation of the boundary conditions of the Diffusion Equation, we have assumed the intensity field to be almost isotropic even at the boundaries of the layer. The limitation of this assumption is of particular importance for model 4, where scattering is restricted in a layer of depth H, in particular when $H \approx l_1$. The conditions necessary to reach the diffusion regime at the boundaries will be fulfilled if $H/l_1 \gg 1$ but will be violated if $H/l_1 \ll 1$. Between these two extreme cases, it is not *a priori* obvious that the diffusion model will lead to a correct approximation to the Radiative Transfer Equation solutions. The numerical simulations help us in precising the actual limits of the Diffusion Approximation.

For $H/l_1 = 4$ and $H/l_1 = 1.3$ (Figures 2.7a,b), the convergence toward the Diffusion Equation is confirmed, independent of the mean free path contrast, and for various source station distances. Yet, for $H/l_1 = 0.6$ and $H/l_1 = 0.25$ the solutions start to diverge (Figures 2.7c and d). In the last two cases, the decay predicted by the Diffusion Approximation is clearly faster than the one observed for the Radiative Transfer Equation solutions. The explanation for this discrepancy is found in the assumption that the intensity field is isotropic at the boundary between the layer and the half-space. For $H/l_1 = 0.6$ or 0.25, a significant part of the energy emitted by the source follows straight ray paths and directly encounters the inner boundary. This is illustrated in Figure 2.7c and 7d by the existence of jumps in the coda amplitude on the Radiative Transfer curves at postcritical distances. Moreover, part of the direct energy incident at the bottom of the layer at precritical angles will be irreversibly lost. Therefore, the energy balance at the bottom of the layer is inaccurately described by the Diffusion Approximation, leading to an incorrect asymptotic decay. These arguments do not hold for model 2 because in this model scattering takes place in whole space. Although some energy is directly transmitted into the half-space, it suffers other scatterings and will be backscattered to the receiver. Hence, the diffusion in the lower half-space, which is well described in our approximation will finally be the dominant process.

Finally, if $l_1/l_2 = 1$ (no mean free path contrast), the Diffusion Approximation always turns out to provide a reliable approximation to the Radiative Transfer for large lapse times, while for $l_1/l_2 = 0$ (strong mean free path contrast), the Diffusion Approximation is valid only when the layer thickness is larger than the mean free path ($H/l_1 > 1$). In the following sections, we focus on some applications of the above results to the observation of coda in continental domains. Scattering has been assumed to be isotropic in all calculations.

2.6 Effect of the velocity structure on the coda.

In this section we study the effect of a velocity contrast in a medium where the mean free path is independent of depth. To this end, we consider the models 1 and 2. The source is located at the surface and scattering is assumed to be isotropic. Our reference model (model 1) has a uniform speed $v_1 = 3.5$ km/s, while in model 2 the velocity jumps to the value $v_2 = 4.7$ km/s at depth H. Model 2 and model 4 present a simplified model of the continental crust on top of the mantle. The interface between both layers is identified with the Moho. We consider different mean free path values and epicentral distances and show the comparison between models 1 and 2 in Figure 2.8a-c. In each case, for short lapse times, the envelopes are very close for both velocity models since the different structure can only be felt after some energy beams reached the depth H and are reflected back to the free surface. For larger lapse times, the curves start to split up: The coda amplitude is bigger in model 2. This amplification is due to the trapping of a part of the energy in the low velocity layer, which acts as a wave guide. A comparison of Figure 2.8a to Figure 2.8b illustrates that the amplification is independent of the distance, while a comparison of Figure 2.8a to Figure 2.8c shows the amplification to be independent of the mean free path as well. In Figure 2.8b, we remark a jump of the coda amplitude for model 2. This jump is created by the total reflection of waves at the Moho beyond the critical angle. Such a discontinuity in the coda decay has already been observed by Obara and Sato (1988) who related it to the existence of a dipping reflector beneath the southern Kanto district in Japan. In each case the curves obtained for the two velocity models finally become parallel and decay as $t^{-\frac{3}{2}}$. This algebraic decay is characteristic of the diffusion regime in a uniform half-space.

The use of the Diffusion Approximation makes it possible to give closed form formulas for the asymptotic decay of the synthetic codas. These analytical solutions of the Diffusion Equation are given in appendix. Under the following assumptions:

$$\frac{H}{\sqrt{D_2 t}} \ll 1 \text{ and } \frac{r}{\sqrt{D_2 t}} \ll 1, \tag{2.44}$$

we obtain:

$$\rho_1(t) \sim \frac{1}{4(\pi D_1 t)^{1.5}} \qquad \text{for model 1, whereas} \tag{2.45}$$

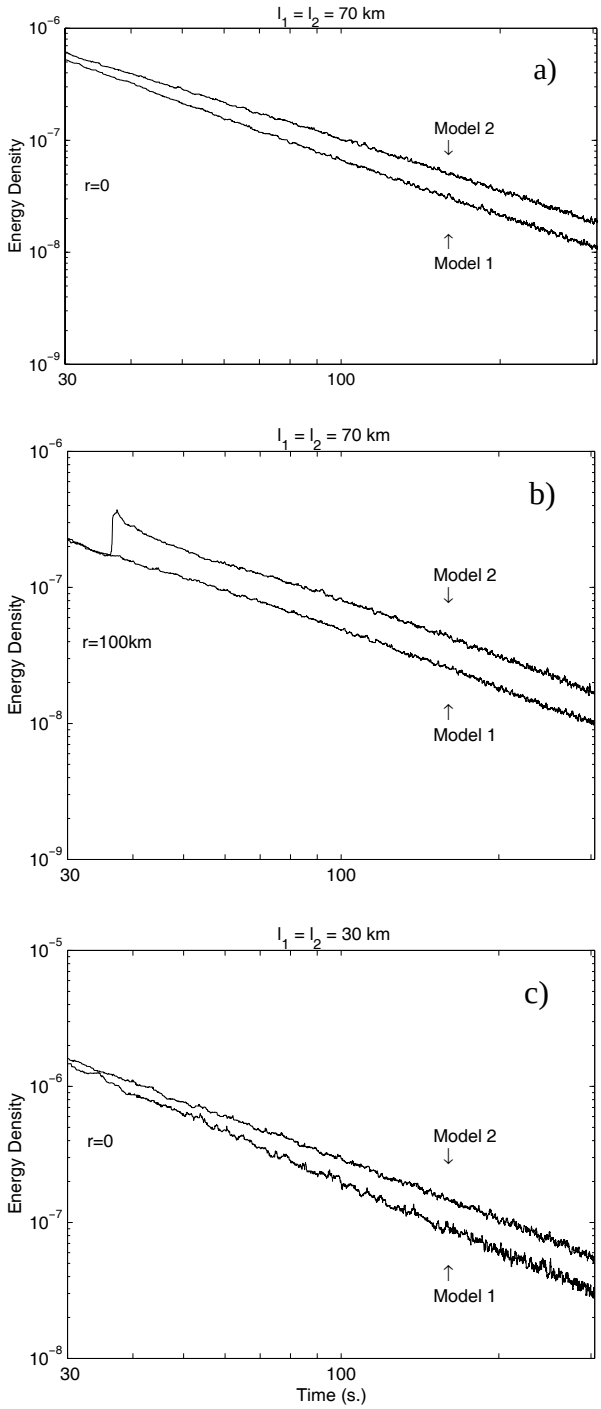

Figure 2.8: Comparison of the coda for models 1 and 2. The epicentral distance r is given in the figure. In both models, the mean free path is uniform and its value is indicated on top of each figure. For model 2 the upper layer thickness is $H = 40$ km and the velocity contrast is $\frac{v_1}{v_2} = \frac{3.5}{4.7}$. The time origin is the energy release at source.

$$\rho_2(t) \sim \frac{\alpha v_2}{4v_1(\pi D_2 t)^{1.5}} \qquad \text{for model 2,} \tag{2.46}$$

where α depends only on the reflection coefficients at the Moho (see equations $2.34 - 2.38$). The coda amplification induced by a velocity contrast is defined by $A = \rho_2/\rho_1$. This yields,

$$A = \frac{\alpha v_2}{v_1}(\frac{D_1}{D_2})^{\frac{3}{2}} \tag{2.47}$$

In the present case, with $l_1 = l_2$, A simply reads:

$$A = \alpha\sqrt{\frac{v_1}{v_2}} \tag{2.48}$$

This amplification factor is a function of the velocity contrast only, as indicated by the numerical Radiative Transfer Equation solutions. In the examples shown in Figure 2.8, we found $A \simeq 1.55$ in complete agreement with equation (2.48). We have therefore shown that a low velocity upper layer increases the coda level in a medium where the source is located at the surface and the mean free path is independent of depth. Yet, in models with jumps in velocity, the asymptotic decay remains of the form $t^{-\frac{3}{2}}$ as is the case for a homogeneous half-space without intrinsic absorption.

The Radiative Transfer Equation solutions for models with equal mean free path in the crust and mantle might give us a first estimate for the shape of the coda decay in continental areas. However, owing to the different mechanical and chemical properties, crust and mantle are unlikely to have the same mean free path values. The model considered in the next section will give us a more realistic estimate for the possible range of variation in coda decay.

2.7 Effect of a strong mean free path contrast on the coda

We want to investigate the changes in coda decay induced by a jump of the mean free path at depth H. Several observations indicate that the mantle may be less heterogeneous than the crust. This suggests that the mean free path of the mantle is larger than the one of the crust. From the geological viewpoint (see for example Fowler 1990), the crust components (sediments, metamorphic rocks ...) have very inhomogeneous chemical and mechanical properties, in sharp contrast with the mantle, which is believed to have an almost uniform composition.

From a seismological viewpoint, at least two independent observations tend to confirm our assumption of a weak scattering mantle: Deep seismic reflection experiments have established a strong reflectivity of the crust whereas almost no energy is backscattered by the upper mantle. The absence of seismic reflectors in the mantle supports the relative homogeneity of its mechanical properties (Marthelot & Bano 1991).

Secondly, the direct S-wave pulse emitted by local earthquakes exhibits a characteristic broadening as a function of the source station distance. Abubakirov and Gusev (1990) calculated the pulse duration of direct S waves, using a Monte Carlo simulation for multiple anisotropic scattering in a medium with uniform wave velocities and uniform scattering properties. From a comparison of their simulations to observations, they inferred some estimates for the scattering mean free path of waves. They noticed large deviations in their estimates that seem to indicate that a uniform scattering strength does not apply in the Earth's lithosphere. A careful analysis showed that the mean free path seems to increase with the exploration depth of the seismic waves. This made them conclude that the scattering strength is probably strongly decreasing with depth. Other studies by Gusev (1995) and Hoshiba(1994) more or less confirm this.

These arguments have led us to investigate the extreme case where scattering in the mantle can be entirely neglected with respect to scattering in the crust. In Figure 2.9 we consider models 1,3 and 4. We recall that model 1 is a half-space with uniform velocities and mean free path which is used as a reference model. In model 3, scatterers are confined to a layer of thickness $H = 40$ km, while the velocity

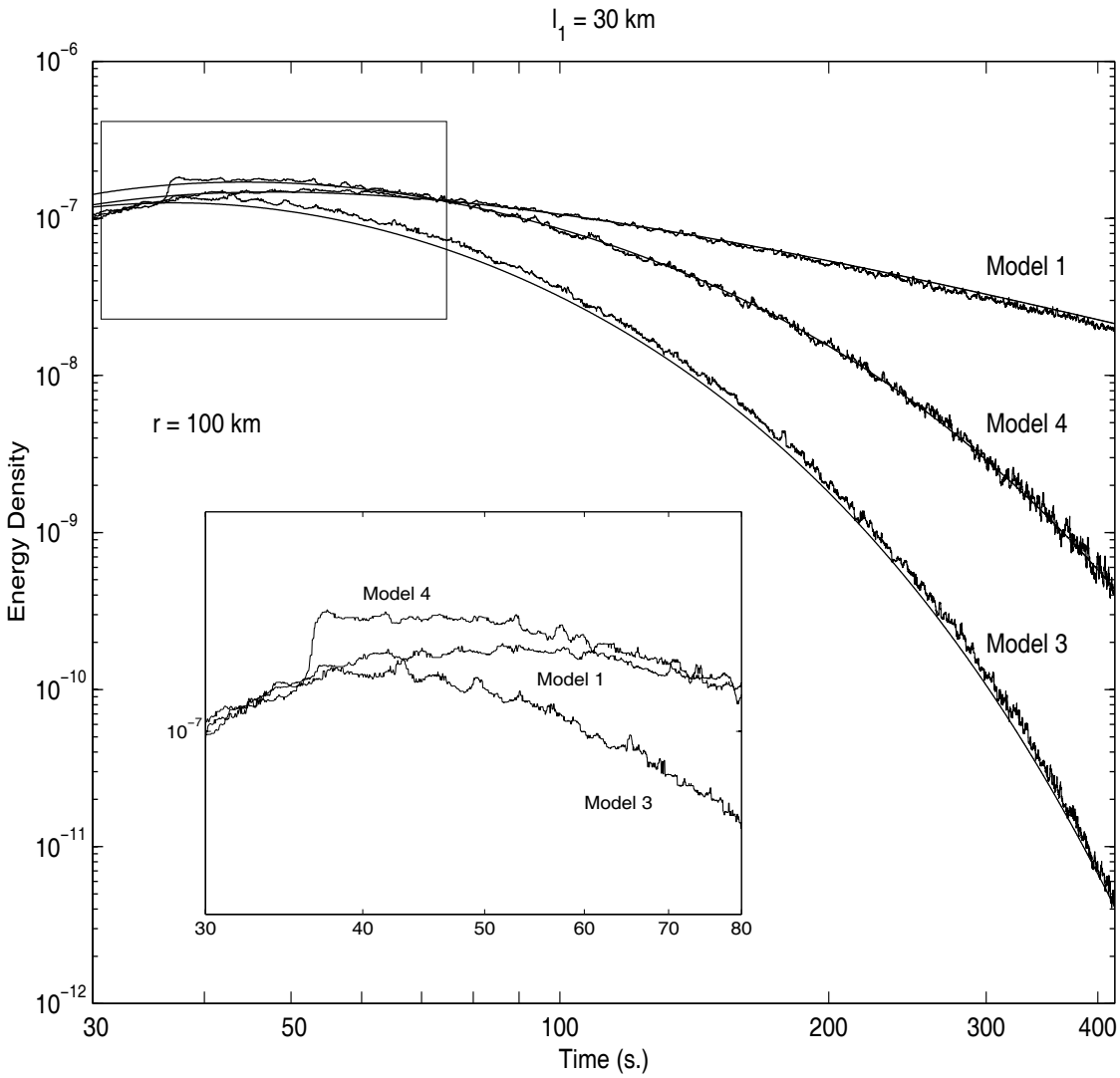

Figure 2.9: Comparison of models 1, 3 and 4. The Radiative Transfer and Diffusion Equation solutions are plotted. The Radiative Transfer Equation solution curves exhibit characteristic ripples. For models 3 and 4 , the scattering is confined to an upper layer of thickness $H = 40$ km. In models 1 and 3 , the S wave velocity is $v_1 = 3.5$ km/s, whereas in model 4 a velocity contrast $\frac{v_1}{v_2} = \frac{3.5}{4.7}$ has been added. The source station distance is $r = 100$ km and the mean free path value is $l_1 = 30$ km for all models. The time origin is the energy release at source. The beginning of the signals has been magnified in order to distinguish the evolution of the coda for the three models.

is kept constant. In model 4, also the velocity mismatch at the Moho is incorporated. The top layer - the heterogeneous crust - overlying a non scattering half-space -the mantle- is a crude model for the lithosphere. In these models, any wave transmitted into the mantle propagates downward and has a zero probability to go back to the receiver.

2.7.1 Analysis of Synthetic Codas

In the following we assume that codas are computed for waves with a central frequency $f = 1$ Hz. We consider mean free paths ranging from 30 up to 150 km, that is, covering almost one order of magnitude. In figure 2.9, we present the coda envelopes computed for models 1, 3 and 4 detected at 100 km from the source and for a mean free path $l_1 = 30$ km. The early coda is magnified in order to differentiate the curves. For lapse times smaller than the travel time of the reflection at the Moho (approximately 37 seconds), the coda amplitudes are the same for the three models because the medium explored by the waves is the same. For model 4, we observe a slight jump in the coda level, due to the energy reflected at post-critical angles on the Moho. Apart from these details, one must note that the dependences of the energy density with respect to time in models 3 and 4 are very different from the one of our reference model 1. Clearly, the decay rate of the envelopes for strong mean free path jumps is much bigger than the one in the uniform model. This is a direct consequence of the energy losses at the base of the crust in models 3 and 4, as has already been noticed by Korn (1990) for energy flux models. In our case, scattering in the mantle is neglected and the mean free path in the crust is of the order of the layer thickness. After a few scatterings, most energy escaped from the crust and disappeared into the mantle. In view of the relatively fast decay rate of model 3 compared to model 4, it is important to consider a velocity jump at the Moho in the modeling.

After about fifty seconds, the Radiative Transfer solutions have converged towards their diffusion asymptotics (Figure 2.9). Therefore, we can use the analytical solutions of the Diffusion Equation to give an approximation for the shape of the coda. From the solution of the Diffusion Equation given in the appendix - retaining the leading term at large times - we obtain for model 4:

$$\rho_4(r,t) \quad \sim \quad \exp\left(-\frac{r^2}{4D_1 t}\right) \frac{\exp(-D_1 \frac{\xi_0^2}{H^2} t)}{H D_1 t} \tag{2.49}$$

where ξ_0 denotes the smallest root of the equation:

$$\xi \tan \xi = \frac{\gamma}{H}, \tag{2.50}$$

γ is determined by the reflection coefficient at the Moho (equation 2.41), and D_1 is the diffusion constant of waves. When the source and the station are close, the first exponential term will rapidly tend to 1 and formula (2.49) can be rewritten as:

$$\rho(t) \quad \sim \quad \frac{1}{t} \exp(-\frac{2\pi f t}{Q_c^\star}), \tag{2.51}$$

where we have introduced :

$$Q_c^\star = \frac{2\pi H^2 f}{D_1 \xi_0^2}\,. \tag{2.52}$$

The expression (2.51) has the form proposed by Aki and Chouet (Aki & Chouet 1975, formula 9) and will be discussed below. By $Q_0^\star$ we denote the value of $Q_c^\star$ at a frequency of 1 Hz.

We can give a simple physical interpretation to equation (2.51). The t^{-1} dependence corresponds to the asymptotic decay associated with a diffusion process without absorption in a two-dimensional medium. Actually, when t is large, the finite thickness of the crust becomes negligible with respect to the large distance traveled by the waves so that the layer can be approximated by a two-dimensional medium. The exponential factor expresses the energy loss into the mantle, due to the waves that reach

the Moho below the critical angle. Since each time a scattering event occurs, a fraction of the energy initially emitted in the crust is lost in the mantle, the energy density decays exponentially. The decay rate will depend on the reflection coefficient R_{12} since the fraction of energy lost at each scattering is determined by the width of the cone of directions below the critical angle.

Although formula (2.52) applies only under the restrictive conditions of the Diffusion Approximation discussed earlier, we will now show that the formula (2.51) still is an excellent approximation for the decay in our computations. Outside the domain of validity of the Diffusion Approximation, $Q_0^\star$ is evaluated numerically by a simple regression. In Figure 2.10 the solid lines show the numerical solutions of the Radiative Transfer Equation and the broken lines show the curves of regression obtained using formula (2.51). The mean free path, thickness of the crust and corresponding $Q_0^\star$ values are given in the Figure 2.10. After a delay of about 30 seconds, the approximate expression (2.52) fits the numerical solution very closely. Therefore, it is possible to give a simple analytical expression of our synthetic codas (2.51), even outside the domain of validity of the Diffusion Approximation. In Figure 2.10, with $H = 40$ km and $l_1 = 30$ km, the conditions of application of the Diffusion Approximation are fulfilled and one may check that the $Q_0^\star$ evaluated numerically is the same as the one obtained from the analytical formula (2.52).

2.7.2 Comparison of Synthetic Codas to Observations

It is worth noting that the formula (2.49) with $r = 0$ has exactly the same form as the one proposed by Aki and Chouet (1975) (formula 9), to fit the observed codas:

$$\rho(t) \quad \sim \quad \frac{1}{t^n} \exp(-\frac{2\pi f t}{Q_c}), \tag{2.53}$$

where $n \in [1, 2]$. While originally derived from simple models, namely, single-scattering and diffusion in a homogeneous infinite space (Aki & Chouet 1975), this expression has been used extensively to describe the coda decay of actual seismograms because this simple formula fits remakably well the observed codas (eg Herraiz & Espinosa 1987 for a review). Therefore Q_c (coda Q) emerged as a very useful parameter that measures the decay rate of observed codas in a defined area. Globally, the Q_c measurements can be summarized as:

$$Q_c = Q_0 f^\nu, \tag{2.54}$$

where $50 < Q_0 < 1000$ and $0 < \nu < 1$. Hereafter, we will not discuss the frequency dependence of Q_c but rather focus on its value around 1 Hz. The lower bound for Q_0 is probably of the order of $Q_0 = 50$, as found in Mexico by Rodriguez, Havskov and Singh (1983). The upper bound is probably larger than 1000 as measured in central China by Jin & Aki (1988). Several extensive studies of Q_0 can be found in literature (eg Singh & Herrmann 1983, Jin & Aki 1988, Oancea Bazacliu & Mihalache 1991), that show large variations on Q_0 with respect to the geological environment.

The physical interpretation of Q_c and its relation to scattering and intrinsic absorption of the lithosphere is still actively debated. Among recent papers, one can cite those by Abubakirov & Gusev (1990), Hoshiba (1993,1994), and Gusev (1995). In the previous section, we have shown that a formula similar to (2.53) is expected in a layered elastic model with a strong mean free path contrast. Since the observed and synthetic coda decay have the same expression, we can directly compare Q_0 and $Q_0^\star$ in order to evaluate the importance of the leakage effect we have described. We note that, depending on the authors, the value of the exponent n used in Q_c measurements ranges from 1 to 2. But as already pointed out in Rautian & Khalturin (1978) and Jin & Aki (1988), the choice of n has a minor effect on the Q_c value, since in equation (2.53), the exponential factor dominates over the algebraic one. Let us compare the observations with our results for a mean free path larger than the thickness of the crust, that is a reasonable assumption for short period waves in the Earth crust. We found that $Q_0^\star$ is increasing for increasing values of the mean free path. With a layer thickness $H = 40$ km, $Q_0^\star$ ranges from 450 to 860, while for $H = 30$ km, $Q_0^\star$ ranges from 360 to 840. The quality factor $Q_0^\star$ which describes the leakage of energy in a purely elastic model is of the same order as the ones measured. This demonstrates that the leakage effect has to be considered as a real physical origin for the observed decays. Yet, the existence of a velocity jump at some depth has to be incorporated as evident from Figure 2.9.

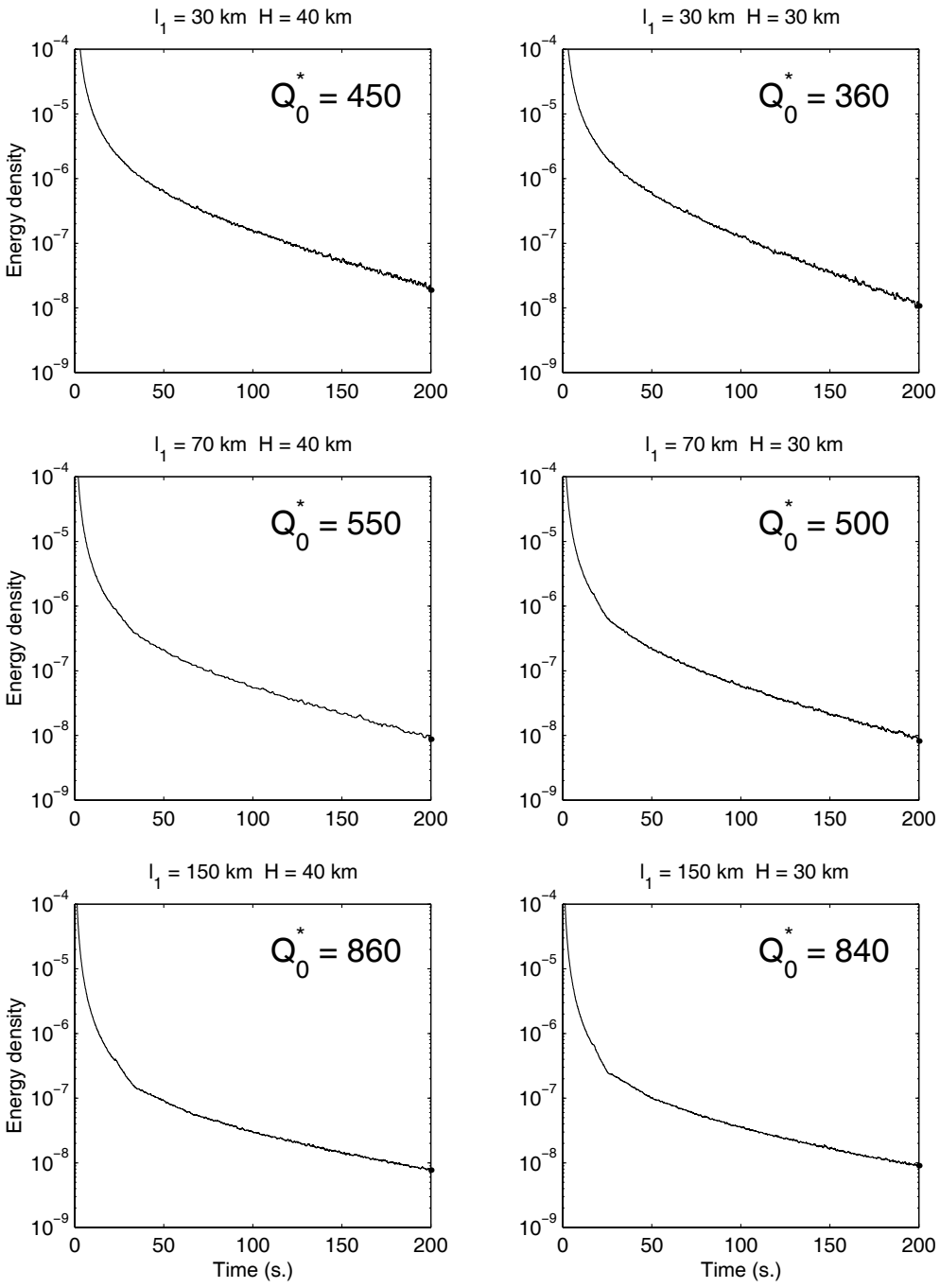

Figure 2.10: Coda decay obtained for model 4 with $H = 30$ km, $H = 40$ km, and the mean free path of the upper layer l_1 ranging from 30 km to 150 km. Solid lines show the numerical solution of the Radiative Transfer Equation, while broken lines show the best approximation obtained with the formula $\frac{1}{t}\exp(-\frac{2\pi t}{Q_0^*})$. The $Q_0^\star$ value corresponding to the best approximation is given in the figures. The standard deviation of the $Q_0^\star$ is $\Delta Q_0^\star \approx 15$.

When the mean free path is much larger in the mantle than in the crust, the leakage of energy into the mantle has some important implications for the interpretation of Q_c. Hoshiba (1993), for instance, applying the results of the Radiative Transfer theory to a lithosphere model with uniform mean free path, absorption and wave speed, inferred the seismic albedo values for Japan. The albedo measures the relative importance of the two processes responsible for the wave attenuation: anelasticity on one hand, and scattering on the other. From his models Hoshiba deduced that in the 1-2 Hz frequency band, the albedo values should be as small as 0.3 to 0.7. Values of the albedo smaller than 0.5 indicate that anelasticity dominates over scattering. Yet, Gusev (1995) pointed out that, in uniform and purely elastic lithosphere models, the discrepancy between observations and models can only be ascribed to anelastic absorption. The consideration of the loss of scattered energy into the mantle offers a rather attractive alternative to resolve this discrepancy. To our knowledge, such partial leakage has always been neglected in previous analyses of the coda decay, leading to an overestimation of anelastic absorption.

2.8 Conclusions

We have used both Monte Carlo simulations of the Radiative Transfer Equation and analytical solutions of the Diffusion Equation to model multiple scattering of seismic waves in media including a surficial layer. In models with uniform mean free path, the solution of the Diffusion Equation turns out to be a good approximation to the Radiative Transfer model and gives the exact asymptotic solution. If scattering is confined to a layer, the validity of the solution of the Diffusion Equation proposed is limited to the case where the thickness of the layer is larger than the mean free path of waves.

In media with constant mean free path, a low velocity top layer amplifies the coda signal with respect to a half-space with uniform wave speed. The amplification factor is a function of the velocity contrast and the reflection coefficient of waves only. Nevertheless, the energy density still decays asymptotically as $t^{-\frac{3}{2}}$ as the diffuse waves in a homogeneous half-space. We have considered media where scattering is confined to a layer, which is not unrealistic for the Earth. The synthetic coda decays like $\frac{1}{t}\exp(-\frac{2\pi ft}{Q_c^\star})$. In the regime of the Diffusion Approximation one obtains the simple relation $Q_c^\star \approx \frac{H^2 2\pi f}{D t_0^2}$, that establishes a link between coda $Q_c^\star$ in our model and the diffusion constant of waves. $Q_c^\star$ is also a function of the reflection coefficient at the base of the layer, the frequency of waves and the layer thickness. In our model, the Earth's crust is responsible for trapping the scattered energy near the surface, which enables the formation of a coda, even in the absence of scattering in the mantle. Neglecting the possibility of an energy leakage into the mantle in the interpretation of the coda decay may lead to a serious underestimation of the seismic albedo. The model proposed here, based on the assumption of a heterogeneous and scattering crust overlying a rather homogeneous mantle offers a new alternative physical interpretation of coda Q.

We are indebted to F. Roch and C. Pequegnat for the parallelization of the C code. Fruitful discussions with N. Shapiro, J. Turner and R. Maynard are greatly appreciated. We thank K. Aki, M. Hoshiba, M. Korn and G. Müller, for their helpful and critical comments on an earlier version of the manuscript. The numerical simulations have been performed on the SP-1 computer at the "Institut de Mathématiques Appliquées de Grenoble" and at the "Centre de Calcul Intensif de l'Observatoire de Grenoble". This work has been supported by the GDR "POAN" in France.

Références

Abubakirov, I.R. & Gusev, A.A., 1990. Estimation of scattering properties of lithosphere of Kamchatka based on Monte-Carlo simulation of record envelope of a near earthquake, *Physics of the Earth and Planetary Interior*, **64**, 52-67.

Aki, K., & Chouet, B., 1975. Origin of coda waves: source, attenuation and scattering effects, *Journal of Geophysical Research*, **80**, 3322-3342.

Burridge, R. & Papanicolaou G.C., 1975. Transport equations for Stokes' parameters from Maxwell's equations in a random medium, *Journal of Mathematical Physics*, **16**, 2074-2085.

Chandrasekhar, S., *Radiative Transfer* (Van Nostrand, New Jersey, 1950).

Fowler, C.M.R., *The Solid Earth*, (Cambridge University Press, 1990).

Frisch, U., "Wave Propagation in Random Media," in *Probabilistic Methods in Applied Mathematics,* edited by A.T. Bharucha-Reid (Academic, New York, 1968), Vol.1, pp. 75-198.

Gusev, A., 1995. Vertical profile of turbidity and coda Q, *Geophysical Journal International*, **123**, 665-672.

de Haan,J.F., P.B. Bosma and J.W. Hovenier, 1987. The adding method for multiple scattering calculations of polarized light, Astron. Astrophys., 183, 371-391.

Herraiz, M. & Espinosa, A.F., 1987. Coda Waves: a review, *Pure and Applied Geophysics*, **125**, 499-577.

Hoshiba, M., 1991. Simulation of multiple scattered coda wave excitation based on the energy conservation law, *Physics of the Earth and Planetary Interiors*, **67**, 123-136.

Hoshiba, M., 1993. Separation of scattering attenuation and intrinsic absorption in Japan using the multiple lapse time window analysis of full seismogram envelope, *Journal of Geophysical Research*, **98**, 15 809-15 824.

Hoshiba, M., 1994. Simulation of coda wave envelope in depth dependent scattering and absorption structure, *Geophysical Research Letters*, **21**, 2853-2856.

Hoshiba, M., 1995. Estimation of nonisotropic scattering in western Japan using coda waves envelopes: Application of a multiple nonisotropic scattering model, *Journal of Geophysical Research*, **100**, 645-657.

Hoshiba, M., 1997. Seismic coda wave envelope in depth dependent S-wave velocity structure, *to appear in Physics of the Earth and Planetary Interior.*

Jin, A., & Aki, K., 1988. Spatial and temporal correlation between coda Q and seismicity in China, *Bulletin of the Seismological Society of America,* **78**, 741-769.

Korn, M., 1990. A modified energy flux model for lithospheric scattering of teleseismic body waves, *Geophysical Journal International*, **102**, 165-175.

Kourganoff, V., 1963. *Basic methods in transfer problems-Radiative equilibrium and neutron diffusion.* Dover, New-York, 1963.

Kourganoff, V., *Introduction à la Théorie Générale du Transfert des Particules* (Gordon and Breach, 1967).

Liu, J.C. and A. Ishimaru, 1974. Multiple scattering of waves by a uniform random distribution of discrete isotropic scatterers, J. Acoust. Soc. Am., 56, 1695-1700.

Lux, I. & Koblinger, L., *Monte Carlo Particle Transport Methods : Neutron and Photon Calculations* (CRC Press, 1991).

Marthelot, J.M. & Bano, M., 1991. Lateral variations in crustal reflectivity beneath the Paris Basin, *Tectonophysics*, **173**, 425-434.

Morse, P.M., & Feshbach, H., *Methods of Theoretical Physics, vol.1,2* (McGraw Hill, New-York, 1953).

Oancea, V., Bazacliu & O., Mihalache, G., 1991. Estimation of the coda quality factor for the Romanian territory, *Physics of the Earth and Planetary Interior,* **67**, 87-94.

Obara, K. & Sato, H., 1988. Existence of an S wave reflector near the upper plane of the double seismic Zone beneath the southern Kanto district, Japan, *Journal of Geophysical Research,* **93**, 15037-15045.

Rautian, T.G. & Khalturin, V.I., 1978. The use of coda for determination of the earthquake source spectrum, *Bulletin of the Seismological Society of America,* **68**, 923-948.

Rodriguez, M., Havskov, J., Singh, S.K., 1983. Q from coda waves near Petatlan, Guerrero, Mexico, *Bulletin of the Seismological Society of America,* **73**, 321-326.

Rytov, S.M., Kravtsov, Yu.A. & Tatarskii, V.I., "4 Wave Propagation Through Random Media" in *Principle of Statistical Radiophysics* (Springer-Verlag 1989).

Ryzhik, L.V., Papanicolaou, G.C. & Keller, J.B., 1996. Transport equation for elastic and other waves in random medium, *Wave Motion*, **24**, 327-362.

Sato, H., 1995. Formulation of the multiple non-isotropic scattering process in 3-D space on the basis of the energy transport theory, *Geophysical Journal International,* **121**, 523-531.

Sheng, P. *Introduction to Wave Scattering, Localization, and Mesoscopic Phenomena* (Academic Press, 1995).

Singh, S., & Herrmann, R.B., 1983. Regionalization of crustal coda Q in the continental United States, *Journal of Geophysical Research,* **88**, 527-538.

Turner, J.A. & Weaver, R. L., 1994. Radiative Transfer and multiple scattering of diffuse ultrasound in polycristalline media, *Journal of the Acoustical Society of America*,**96**, 3675-3683.

Zeng, Y., Su, F. & Aki, K., Scattering wave energy propagation in a random isotropic scattering medium –I theory, *Journal of Geophysical Research*, **96**, 607-619, 1991.

Zhu, J.X., Pine, D.J. & Weitz, D.A., 1991. Internal reflection of diffusive light in random media, *Physical Review A*, **44**, 3948-3959, 1991.

Appendix: Solutions of the Diffusion Equation We briefly recall the diffusion equation and the boundary conditions associated to our models. We note that the energy flux always vanishes at the free surface ($z = 0$).

$$\frac{\partial \rho(\boldsymbol{x},t)}{\partial t} - D\nabla^2\rho(\boldsymbol{x},t) = \delta(t)\delta(\boldsymbol{x}-\boldsymbol{x_0}) \tag{2.55}$$

$$J = 0 \qquad \text{at } z = 0, \tag{2.56}$$

where J denotes the energy flux. In what follows, we assume that the focal depth is $z_0 = 0$ and denote by r the epicentral distance.

Model 1 (Half-Space): The solution is easily deduced from the infinite space solution by the method of images.

$$\rho(r,t) = \frac{1}{4(\pi D_1 t)^{\frac{3}{2}}}\exp(-\frac{r^2}{4D_1 t}) \tag{2.57}$$

Model 2 with $D_2 > D_1$:
The boundary conditions required at the interface of two media differing in their diffusion constant is:

$$\text{at } z = H \left\{ \begin{array}{lcl} D_1\frac{\partial\rho_1}{\partial z} = D_2\frac{\partial\rho_2}{\partial z} & = & -J \\ \rho_1 v_1 + \beta J = \alpha\rho_2 v_2 & , & \end{array} \right. \tag{2.58}$$

α and β are defined in (2.37) and (2.38) respectively. The solution is composed of a double integral and a simple integral over an infinite sum of residues. Note that the number of residues depends on the x variable and becomes infinite as x goes to infinity.

$$\rho(r,t) = \frac{1}{\pi}\int_0^\infty dx x^2 J_0(xr)(A(x) + \frac{v_2}{2\pi v_1}B(x)) \tag{2.59}$$

where J_0 denotes the Bessel function of order 0.

$$A(x) = \sum_{n(x)} \frac{\left[(\frac{s_n}{\delta}-1)Q_n^2 + l^2(1-s_n)\right]\sqrt{1-s_n}\exp(-D_2x^2s_nt)}{l(1-\delta)Q_n + \left(xd\left[(\frac{s_n}{\delta}-1)Q_n^2 + l^2(1-s_n)\right] - \frac{1}{3}\beta l_2^\star\delta l(\frac{s_n}{\delta}-1)\right)\sqrt{1-s_n}} \tag{2.60}$$

$$B(x) = \int_1^\infty ds \frac{\alpha\sqrt{s-1}\exp(-D_2x^2st)}{C(x,s)} \tag{2.61}$$

$$\begin{aligned} C(x,s) &= \frac{\alpha^2}{l^2}(\frac{s}{\delta}-1)\sin^2\left(xd\sqrt{\frac{s}{\delta}-1}\right) \\ &\quad +(s-1)\left[\cos\left(xd\sqrt{\frac{s}{\delta}-1}\right) - \frac{x\beta l_2^\star}{3l}\sqrt{\frac{s}{\delta}-1}\sin(xd\sqrt{\frac{s}{\delta}-1})\right]^2, \end{aligned} \tag{2.62}$$

where the following notations have been introduced:

$$\delta = \frac{D_1}{D_2} \qquad\qquad l = \frac{l_2^\star}{l_1^\star} \tag{2.63}$$

$$Q(s) = \alpha + \frac{l_2^\star x\beta}{3}\sqrt{1-s} \tag{2.64}$$

$$Q_n = Q(s_n) \tag{2.65}$$

The s_n are the roots of the following equation :

$$\tan\left[xd\sqrt{\frac{s}{\delta}-1}\right] = \frac{l}{Q(s)}\sqrt{\frac{1-s}{\frac{s}{\delta}-1}} \qquad \delta < s < 1. \tag{2.66}$$

The summation for a given x is indicated by $\sum_{n(x)}$. The number of residues that contribute to the simple integral increases with x. For $xd\sqrt{\frac{1}{\delta}-1} < \frac{\pi}{2}$, one has only one solution s_1, but for $xd\sqrt{\frac{1}{\delta}-1} \gg 1$ many solutions $s_1, s_2, \cdots, s_n, \cdots$ exist.

Models 3 and 4 : These models correspond to the limiting case $D_2 \to \infty$. The boundary conditions at the interface of a diffusing and a non-diffusing medium are:

$$\rho_1 v_1 + \gamma J = 0 \qquad \text{at } z = H, \tag{2.67}$$

γ is defined in equation (2.41). The final formula simplifies to a sum of residues.

$$\rho(r,t) = \frac{\exp(-\frac{r^2}{4D_1 t})}{2\pi H D_1 t} \sum_n \frac{\sin\xi_n + \frac{t_n\gamma}{H}\cos\xi_n}{(1+\frac{\gamma}{H})\sin\xi_n + \frac{t_n\gamma}{H}\cos\xi_n} \exp(-D_1\frac{\xi_n^2}{H^2}t) \tag{2.68}$$

where the ξ_n are the roots of the equation :

$$\xi_n \tan\xi_n = \frac{H}{\gamma}, \qquad \xi_n \in \left]n\pi, n\pi + \frac{\pi}{2}\right[\qquad n \in \mathbb{N}. \tag{2.69}$$

Chapter 3

Inteprétation Physique de Coda Q

Residence time of diffuse waves in the crust as a physical interpretation for coda Q. Application to seismograms recorded in Mexico.
L.Margerin, M. Campillo, N.M. Shapiro, B. Van Tiggelen
Geophys. J. Int., en révision, 1999.

Abstract

We consider a simple model for elastic wave propagation in the Earth lithosphere consisting of a heterogeneous and scattering crust overlying a homogeneous mantle, that is, we neglect the back-scattering from the upper mantle. The free parameters describing the wave propagation are the mean free path of the waves and the intrinsic absorption in the crust. We assume a constant S-wave speed of 3.5 km/s in the crust, 4.7 km/s in the upper mantle and a crustal thickness ranging from 20 to 30 km. In the framework of the radiative transfer theory, we treat, accurately, the jumps of S-wave speed and mean free path at the Moho. Without intrinsic absorption, this configuration yields a synthetic coda decay $1/t \exp(-2\pi f t/Q_c^\star)$, a form similar to that proposed by Aki and Chouet (1975) to parametrize the observations. The exponential decay in our purely elastic model is due to the partial leakage of diffuse energy into the mantle.

In order to test the applicability of our model, we have determined the coda Q parameter (Q_c) in the 1-15 Hz frequency band, from data recorded at the Cayaco station, Mexico. In the low frequency regime (around 1 Hz), we find that the energy leakage significantly affects the coda Q, while at higher frequencies (around 10 hz), the anelastic attenuation dominates. A weak intrinsic absorption expressed by a frequency-independent parameter Q_i of 1100 or 1200 accounts satisfactorily for the observed Q_c values in the whole frequency range. Our very simple model has only two free parameters and offers an alternative physical interpretation of coda Q. In Mexico, Q_c represents mostly the leakage effect at low frequency, and the intrinsic absorption at high frequency.

In regions where the mean free path is much larger than the crustal thickness, we find that the leakage effect is small and that the observed Q_c is mainly due to the intrinsic absorption. On the contrary, when the mean free path is of the order of the crustal thickness, we predict a strong sensitivity of the decay rate of the coda with the crustal thickness, which has to be incorporated in the interpretation of the regional variations of coda Q. We propose to introduce a new parameter τ_d, the residence time of diffuse energy in the crust, which is physically more meaningful than a quality factor to quantify the leakage effect.
Keywords: Multiple Scattering, Radiative transfer, Diffusion, Coda, Q.

3.1 Introduction

Since coda waves have been recognized as scattered waves on randomly distributed inhomogeneities in the lithosphere (Aki 1969, Aki and Chouet 1975), seismologists have tried to deduce a statistical parameter describing the scattering in the lithosphere from coda records (that is the mean free path of the waves l), as well as the intrinsic absorption of rocks Q_i. Due to the complexity of elastic wave propagation in the lithosphere, some simplifications had to be introduced regarding the physical processes and/or the mechanical and scattering properties of the Earth. The early interpretation of the coda as singly-scattered waves in a uniform infinite space led to several estimates of the mean free path of waves (see Herraiz and Espinosa (1987) for a review). But higher scattering orders may not be negligible and several attempts were made to include multiple-scattering. For example, Wu and Aki (1988), Fehler et al. (1992), Hoshiba (1993) developed different methods, all based on radiative transfer theory in a uniform half-space, to estimate the mean free path of waves and seismic albedos. Yet, as pointed out several times in the literature (e.g. Abubakirov and Gusev 1990, Fehler et al. 1992, Hoshiba 1993), the underlying assumption that the Earth is homogeneous with regard to wave speeds and mean free paths is known to be inaccurate. In the following, we present a new simplified model of scattering in the Earth that incorporates the well-known existence of the Moho at depth, the free surface and a heterogeneity contrast between crust and mantle. By analyzing a specific set of data from Mexico, we demonstrate that the present model accounts for the frequency dependence of coda Q in this region.

3.2 Presentation of the Model

We consider a conceptual model consisting of a heterogeneous and scattering crust with low S-wave velocity, overlying a homogeneous and weak scattering mantle with high S-wave velocity. The velocity constrast between crust and mantle is obviously well documented. The heterogeneous character of the crust is known from geological observations as well as from deep seismic soundings. Deep reflection seismology offers direct access to the depth dependence of the reflection/diffraction properties in the crust and mantle beneath the continents. The frequency band used in these experiments (typically 5-20Hz) is widely overlapping with the one of coda studies (1-20Hz). The results of the deep reflection experiments are therefore relevant to the description of the structures associated with the scattering in the lithosphere. A considerable effort has been invested worldwide to provide seismic images of the deep crust. Among others, the programs COCORP in USA, BIRPS in Britain, DEKORP in Germany, LITHOPROBE in Canada, BABEL in Fennoscandia or ECORS in France confirmed the generality of the main features of the seismic signature of the continental lithosphere (see for example Allmendinger et al., 1987; Meissner, 1989 and the contributions to the Proceedings of the 4th International Symposium on Deep Reflection Profiling of the Continental Lithosphere (Meissner et al., editors, 1990)). A striking characteristics of the continental lithosphere revealed by deep reflection experiments is the strong variation of the seismic reflectivity at a depth corresponding to the Moho that was observed in different regions of the world. Above the Moho, the lower crust is reflective while below the Moho the upper mantle is generally almost transparent. The Moho can even be defined on these sections as the deepest limit of the reflective crust. The crustal reflectivity strongly depends on the geological setting (Allmendinger et al., 1987; Meissner, 1989). There are some examples of reflectors below the Moho (McGeary and Warner, 1985; Cloves et al., 1996; Krishna et al. 1996) but they are exceptional. Nevertheless these sub-Moho reflections demonstrate the capability of the soundings to probe the upper mantle. The huge amount of observations that was obtained by the deep reflection programs cannot be neglected in the construction of simple models of heterogeneity in the lithosphere.

Based on results on the study of pulse broadening (Abubakirov and Gusev (1990)) and the analysis of coda decay, Gusev (1995) invoked a strong variation of scattering strength with depth and claimed the potential importance of this layering for the interpretation of coda Q. Consequently, our model, the characteristics of which are given in Figure 3.1, is not just an ad-hoc model since numerous seismological and non-seismological arguments lead to study such a simple configuration . This model is indeed not expected to represent the actual structure of the lithosphere in every region of the world but we study it to emphasize the properties of scattered waves associated with the layering. While simple, this model introduces new features in the study of coda waves, namely the existence of a velocity and mean free path contrast at a certain depth. We model multiple-scattering using an acoustic radiative transfer equation supplemented by appropriate boundary conditions. In our analysis, mode conversions are neglected, and isotropic scattering is assumed but the angular dependence of transmission and reflection coefficients of acoustic energy at the Moho is taken into account. We consider mean free path values covering one order of magnitude, from 10 to 100 km. The relevance of these values will be justified in this paper, when we consider data interpretation. The way to deal with a reflective interface as well as depth dependent mean free path values has been described in a previous paper (Margerin et al., 1998, referred to as paper A in the following, and also Hoshiba 1997). An important feature of this model is the existence of partial leakage of energy at the base of the crust into the mantle which gives a functional form of the synthetic coda decay very different from the decay obtained in uniform models. This point is discussed in detail in the next section.

3.3 Description of Synthetic Codas

First, we consider a model without intrinsic absorption. In paper A, we have presented a series of Monte-Carlo solutions of the radiative transfer equation for the lithospheric model discussed above. These numerical tests have shown that for a large range of mean free path values (from 10 to 100 km), the

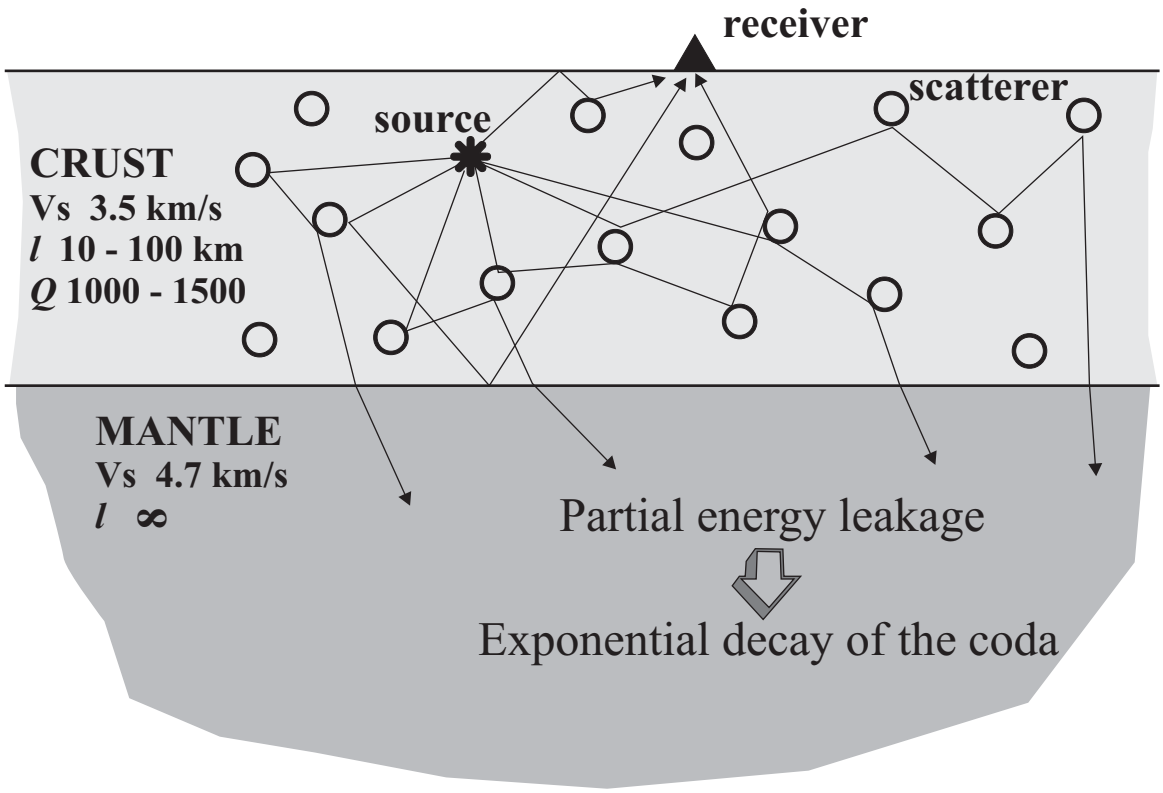

Figure 3.1: Geometry and physical parameters of the model.

envelope of the synthetic codas in the multiple scattering follows the formula:

$$\rho(t) = \frac{1}{t}\exp(-\frac{t}{\tau_d}), \text{ and} \tag{3.1}$$

$$\tau_d = \frac{Q_c^\star}{2\pi f}, \tag{3.2}$$

where ρ is the energy density in the coda, t the time elapsed since the energy release at the source, f the wave frequency, $Q_c^\star$ the parameter that describes the decay rate of our model, and τ_d the characteristic residence time of diffuse waves in the crust, which measures the rate of leakage into the mantle.

We denote by $Q_0^\star$ the value of $Q_c^\star$ at the frequency $f = 1$ Hz. Formula (3.1) shows the same functional form as the one proposed by Aki and Chouet (1975) to measure coda Q, a parameter extensively used to describe the decay rate of actual seismogram envelopes. This analogy with the classical quality factor is somehow arbitrary, but justified by its wide application in seismology. Physically, we believe that a residence time of energy is more meaningful to characterize the leakage effect. This will be discussed in the last section.

The physical interpretation of equation (3.1) is the following (paper A): The t^{-1} dependence corresponds to the asymptotic decay associated with a diffusion process without absorption in a two-dimensional medium. The exponential factor expresses the energy loss into the mantle, due to the waves that reach the Moho below the critical angle. We have shown in paper A that for mean free paths smaller than the crustal thickness and sufficiently large lapse times, the radiative transfer equation is basically equivalent to a diffusion equation that can be solved analytically. This provides closed form expressions of $Q_0^\star$ in terms of the physical parameters of the model:

$$l < H \begin{cases} Q_0^\star \simeq \frac{2\pi H^2}{D\xi^2} \simeq \frac{6\pi H^2}{vl\xi^2} \text{ and} \\ \tau_d \simeq \frac{H^2}{D\xi^2} \simeq \frac{3H^2}{vl\xi^2}, \end{cases} \tag{3.3}$$

where H is the thickness of the crust, D, the diffusion constant of waves, v, the S-wave speed, ξ, a parameter representing the effect of internal reflection at the Moho. The mean free path l, and D are related by $D = vl/3$. Note that $\xi \in]0, \frac{\pi}{2}[$. This formula, while restricted to the domain of validity of our diffusion approximation, helps to clarify the physics of the leakage process. Obviously, the larger the diffusion constant, the faster the diffuse energy leaks into the mantle. We note that the crustal thickness H affects the leakage rate even more than the mean free path, since $Q_0^\star$ and τ_d increase with the square of H (see eq. (3.3)). Nevertheless, we emphasize that the analytical relation between $Q_0^\star, l$ and H is restricted to the domain of validity of the diffusion approximation ($l < H$). In particular, one should not extrapolate equation (3.3), for mean free paths larger than the crustal thickness.

Outside the domain $l < H$, the diffusion approximation no longer describes the partial trapping of waves in the crust, mainly because it assumes a nearly isotropic field and angularly averaged values of the reflection coefficient at the Moho. As the mean free path in the crust increases, post-critical reflections at the Moho contribute more and more to the energy trapped in the crust, which is not described in our diffusion approximation. Therefore to quantify the leakage effect for $l > H$, we must rely on the radiative transfer theory which provides a complete framework, where the angular dependence of the internal reflection at the Moho is accurately taken into account. Surprisingly, it turns out that expression (3.1) is valid outside of the restrictive domain where our analytical solution of the diffusion equation is justified. In Figure 3.2, we present the numerical solutions of the radiative transfer equation. Earthquakes are assumed to be very shallow and the receivers are located on the free surface near the source. These assumptions are made for simplicity but are by no mean necessary. In particular, the leakage rate does not depend on the source position in the crust, as long as the source station distance is smaller than a few mean free paths. In Figure 3.2, we also plotted the approximations of the numerical solutions, given by expression (3.1), where the value of $Q_0^\star$ were determined by a simple regression. For the different crustal thicknesses and mean free path values considered, we note that for lapse times larger than twenty seconds

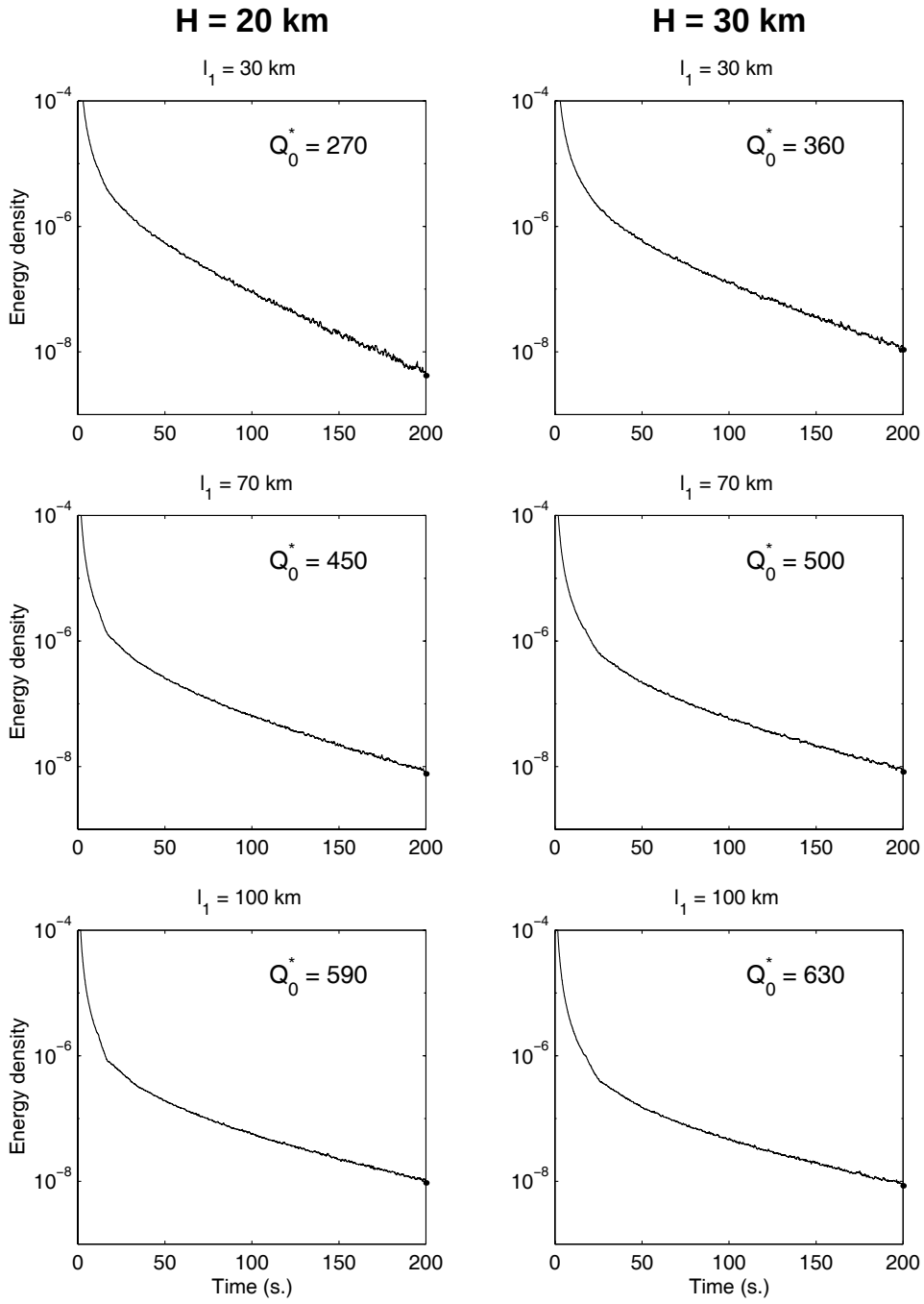

Figure 3.2: Coda decay obtained for our model with $H = 20$ km, $H = 30$ km, and the mean free path of the crust l ranging from 30 km to 100 km. Solid lines show the numerical solution of the Radiative Transfer Equation, while dotted lines show the best approximation obtained with the formula $\frac{1}{t}\exp(-\frac{2\pi t}{Q_0^*})$. The $Q_0^\star$ value corresponding to the best approximation is given in the figures. The maximum standard deviation of the $Q_0^\star$ is $\Delta Q_0^\star \approx 30$.

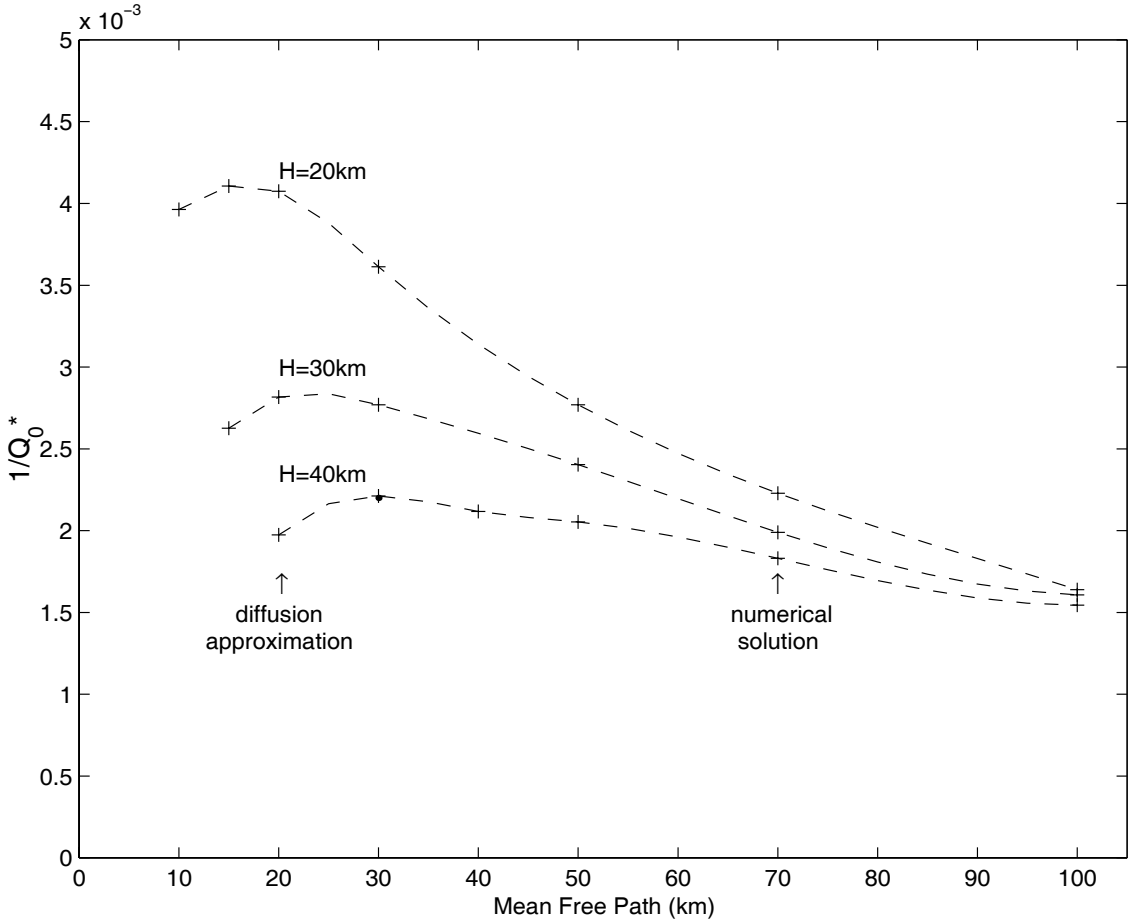

Figure 3.3: Dependence of the parameter $1/Q_0^\star$ on the mean free path l for three crustal thicknesses $H = 20, 30, 40$ km. Dots correspond to the values calculated with the diffusion approximation, while crosses denote the values estimated numerically with the radiative transfer theory. Both coincide for $l < H$. The dashed line interpolates between the crosses.

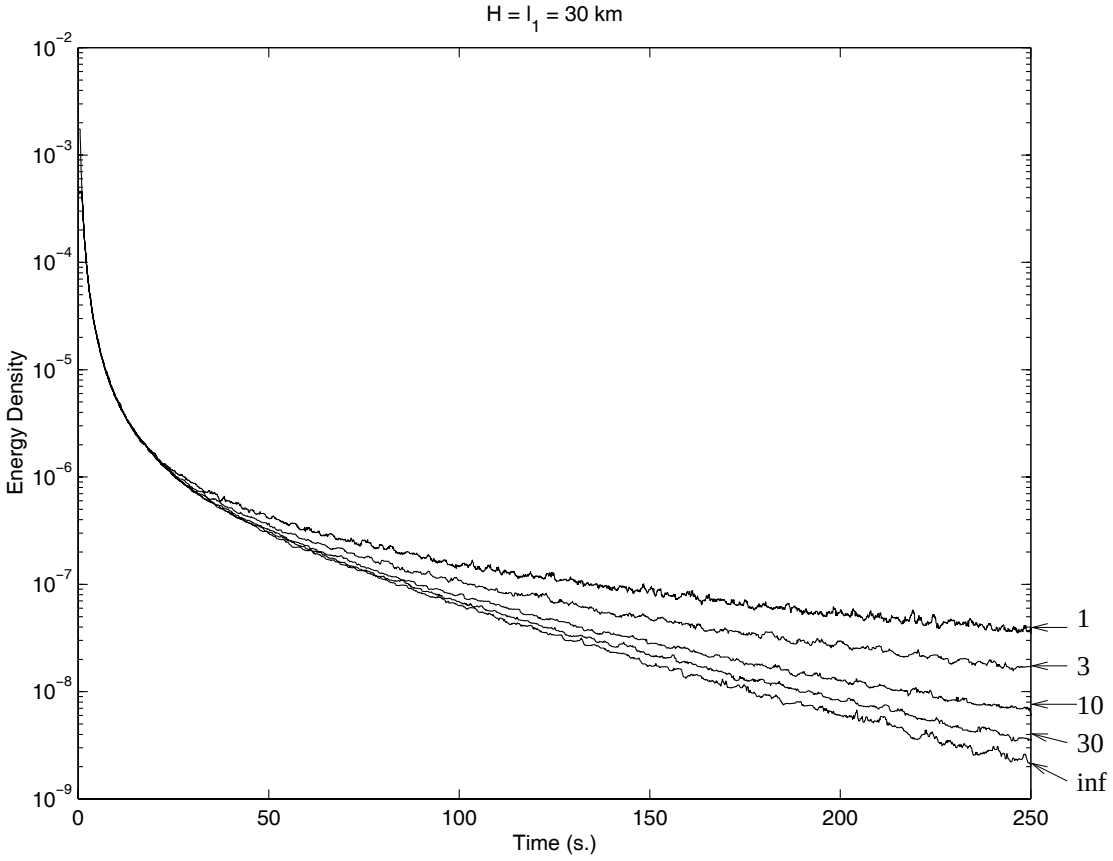

Figure 3.4: Effect of the mean free path contrast on the shape of the synthetic codas. The ratio of the crustal to the mantle mean free path is indicated in front of each curve. One can observe the steady transition from the algebraic decay $t^{-3/2}$, when there is no contrast, to the exponential decay $1/t \exp(-t/\tau_d)$, when the mantle is transparent.

the formula (3.1) fits the numerical solution very closely. We conclude that when $l > H$, the functional dependence (3.1) is still accurate but $Q_0^\star$ has to be evaluated numerically.

Calculations have been performed for three different thicknesses, $H = 20, 30$ and 40 km and mean free paths ranging from 10 to 100 km. The dependence of $1/Q_0^\star$ is plotted as a function of the mean free path in Figure 3.3, for the three different values of H. We note that when $l < H$, $1/Q_0^\star$ (or $1/\tau_d$) increases with l according to formula (3.3). When l is of the order or larger than H, $1/Q_0^\star$ decreases as l increases, because in this case, the leakage rate is governed by the number of scatterings per unit time. Scattering causes the loss of trapped energy into the mantle, but with increasing l, the number of scattering events decreases. We note that in the two cases $l \ll H$ and $l \gg H$, the leakage effect becomes small ($Q_0^\star > 800$) as shown in Figure 3.3. As a consequence, when l is much larger than H, $Q_0^\star$ is large and almost independent of the value of H. On the contrary, when l is of the order of H, $Q_0^\star$ is strongly decreasing with H (see Figure 3.3).

Although extreme, our assumption of a transparent mantle does not represent a singular case with respect to models where the mean free path is much larger in the mantle than in the crust. We present in Figure 3.4 the results of simulation of the radiative transfer equation in stratified models with increasing values of mean free paths in the mantle. These computations show the progressive evolution of the shape of the curves from the uniform case to the case of a transparent mantle.

The question we want to address next is the importance of the leakage for the interpretation of

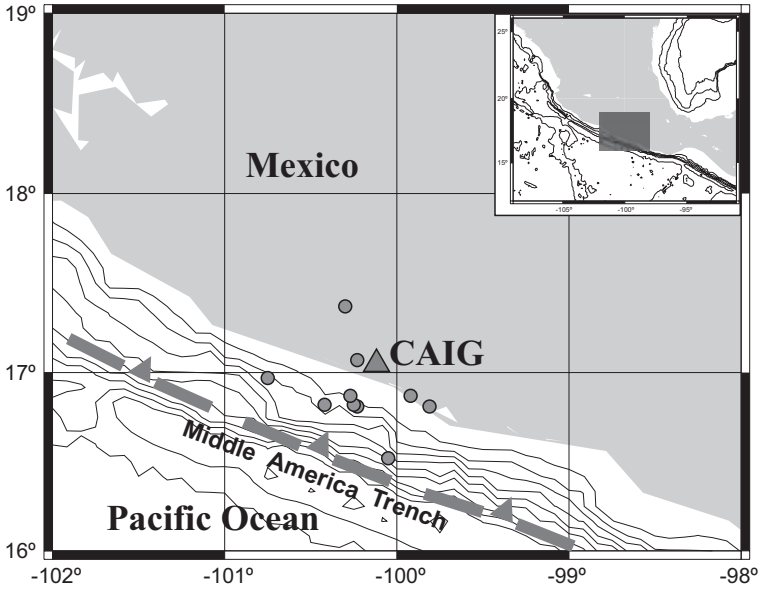

Figure 3.5: Map of location of epicenters and station.

Table I: Location and magnitude of earthquakes used in this study.

Latitude	Longitude	Depth (km)	Magnitude
16.81	-100.23	7.0	4.6
16.82	-100.25	1.0	4.6
16.87	-100.27	15.0	4.7
17.37	-100.30	7.0	4.8
16.81	-99.81	6.0	4.9
16.82	-100.42	21.0	4.6
16.87	-99.92	9.0	4.2
16.97	-100.75	20.0	4.5
17.07	-100.23	23.0	4.2
16.52	-100.05	22.0	4.6

observed codas and the estimation of the mean free path and intrinsic absorption in the crust. This will be studied by applying our model to account for the frequency dependence of the coda Q measured in Mexico.

3.4 Observations

We consider a data set of 10 local earthquakes (maximum epicentral distance less than 50 kilometers) recorded at the station CAIG of the Servicio Sismologico Nacional in Mexico. The earthquake locations and magnitudes are given in Table 1 and epicenters are plotted in Figure 3.5. CAIG is located in the Guerrero state where the crust is about 30 km thick (Kostoglodov & al. 1996). We measure the time decay of the coda using the procedure outlined by Aki and Chouet (1975). The noise level is observed before the onset of the first arrival. We end the coda analysis when the signal becomes smaller than four times the noise level. The analysis starts about twenty seconds after the first S-wave arrival, which roughly corresponds to the time when the signals exhibit a steady decay. The signal is band-pass filtered

in a frequency window with a width of 2/3 the central frequency. The energy of the signal is calculated in half-overlapping time windows of duration three times the central period of the signal. By squaring the amplitude time series and then summing the values in a time window, an intensity time series E_k^i is obtained, where i denotes the i^{th} record and k the k^{th} point in time, and the origin time is the energy release at the source.

The envelopes have been assumed to follow the relation:

$$\log(E_k^i {t_k^i}^n) = A^i - \frac{2\pi f t_k^i}{Q_c}. \tag{3.4}$$

The A_i are individual amplitudes of the envelopes, Q_c is the coda Q parameter common to the set of envelopes, and n is an exponent depending on the model used for interpretation. It equals 2 for single-scattering of body waves (see Aki & Chouet 1975), and 1 in our model. The best solution in the least-squares sense of the system of linear equations (3.4), has been determined by the singular value decomposition method. The statistics on 10 events gives stable Q_c values that are not significantly modified by adding or suppressing one event to the set we have used. The fit was made for both $n = 1$ and $n = 2$. The exponent $n = 1$ gives the smallest relative error (about 2 %) on the Q_c values while the error reaches 4 % for $n = 2$. The measurements of $1/Q_c$ with respect to the frequency are plotted in Figure 3.6, with the corresponding error bars. In the same Figure, the dashed curves limit the domain of $1/Q_c^\star$ obtained in our purely elastic model for thicknesses of 20 and 30 km. Since we cannot say a priori how l varies with frequency, we assume that for $1 \leq f \leq 15$, we have $20 < l(f) < 100$ km. We exclude smaller mean free path values because they would lead to unrealistic attenuation of the primary S-wave. The use of the value $H = 20$ km for the comparison with data will be discussed in the next section.

When l is assumed to be frequency independent, the parameter $Q_c^\star$ is of the form $Q_0^\star f$ (i.e. τ_d is independent of the frequency) because l is the only parameter potentially depending on frequency in our model. In some simple cases, it may be possible to determine the frequency dependence of the mean free path. For example, let us introduce the correlation length of the fluctuations in the medium a, and the wavelength λ. In the low frequency limit ($\lambda \ll a$), the mean free path varies like f^4, whereas in the high frequency limit ($\lambda \gg a$), l tends to a constant. If the medium is self-similar and contains all length scales of inhomogeneities, one also expects l to be frequency independent. It is beyond the scope of this paper to discuss more complicated cases that may occur in the lithosphere. When $1/Q_c^\star$ is plotted as a function of frequency for the two limiting values $l = 20, 100$ km, one obtains the two branches of hyperbola in Figure 3.6 limiting the estimated variation of the parameter $1/Q_c^\star$.

Around 1 Hz, the values of coda decay predicted for a purely elastic model are of the same order as the ones measured on actual data. This shows that the value of $1/Q_c$ measured at 1 Hz can possibly be explained by the leakage effect without invoking any intrinsic absorption. If we had neglected the leakage effect, as it is the case in uniform half-space models, we would have ascribed the value of $1/Q_c$ to the intrinsic attenuation in the crust around 1 Hz. At higher frequencies, we see in Figure 3.6 that the leakage effect becomes negligible with respect to the anelastic absorption. We can expect that, in the high frequency limit, Q_c gives an estimation of the anelastic absorption in the crust. We also point out that, when the leakage is dominant, the notion of 'coda quality factor' tends to loose its physical meaning. We find more natural to use a characteristic time $\tau_d^\star$ such that the coda decays like $1/t \exp(-t/\tau_d^\star)$. This new parameter $\tau_d^\star$ represents the typical time, necessary for the diffuse energy partially trapped in the crust to escape into the mantle.

In order to fit the frequency dependence of Q_c on the entire frequency band, we have to take into account the intrinsic attenuation of rocks. Thus, we introduce in the model an intrinsic quality factor Q_i. In a first step, Q_i is assumed to be frequency independent. We will discuss the implications of this assumption in the case of the mexican data. We note that frequency independent Q of about 1500 has been measured for L_g waves in the 1-20 Hz frequency band in stable shield areas, where scattering is expected to be very weak (Hasegawa 1985). We use this measurement as a typical order of magnitude of the intrinsic quality factor for dry crustal rocks. We define the total attenuation predicted by the model as $1/Q_m^\star = 1/Q_i + 1/Q_c^\star$. We present, in Figure 3.7, a comparison between the observations at CAIG and the model predictions including intrinsic absorption. For crustal thicknesses of 20 km and 30 km,

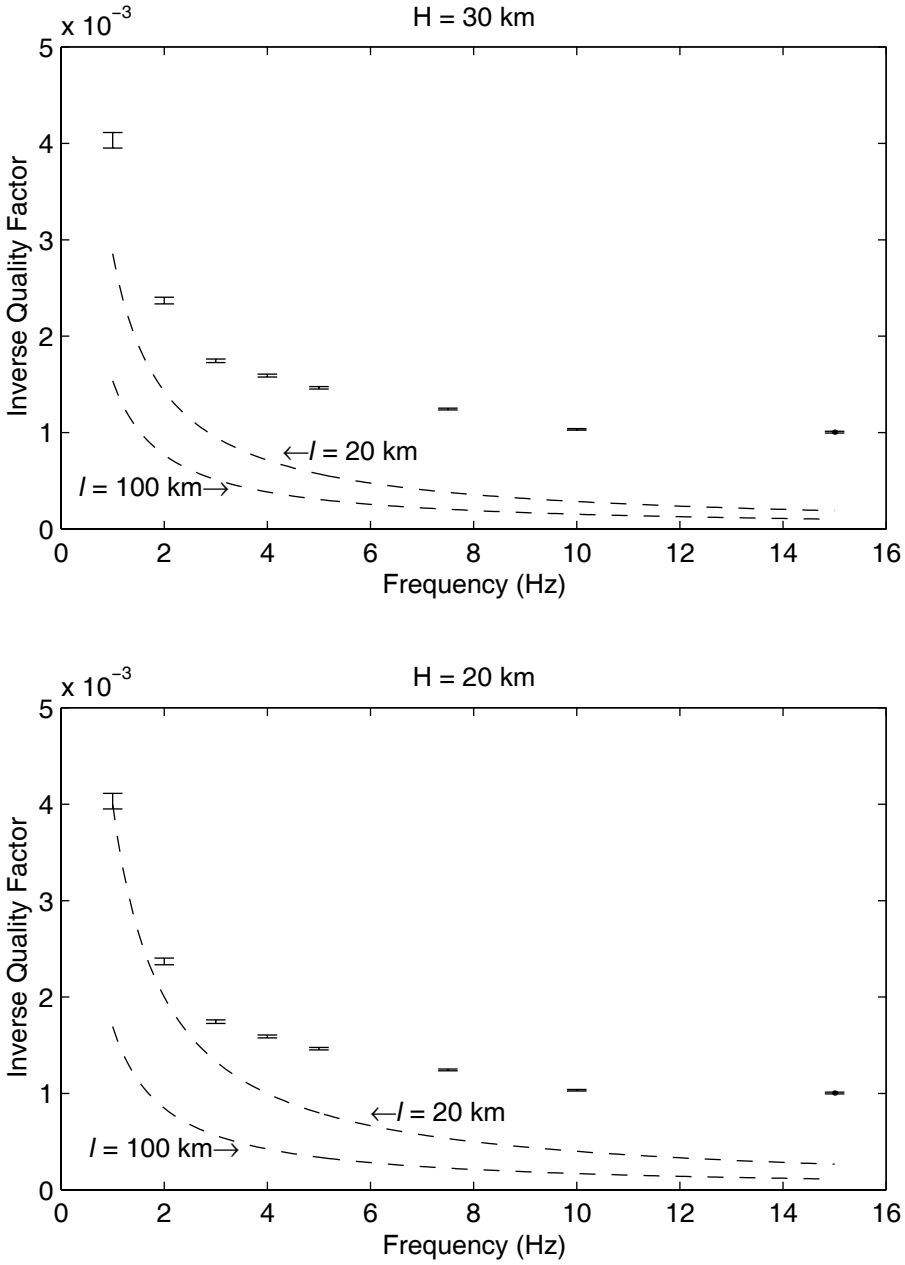

Figure 3.6: Dots with error bars show the values of $1/Q_c$ between 1 and 15 Hz at CAIG. In the same graph, the dashed curves delimit the domain of variation of $1/Q_c^\star$ predicted by the model for the crustal thicknesses $H = 20, 30$ km, assuming that $20 < l < 100$ km in the 1-15 Hz frequency band. Arrows show the value of l for each limiting hyperbola.

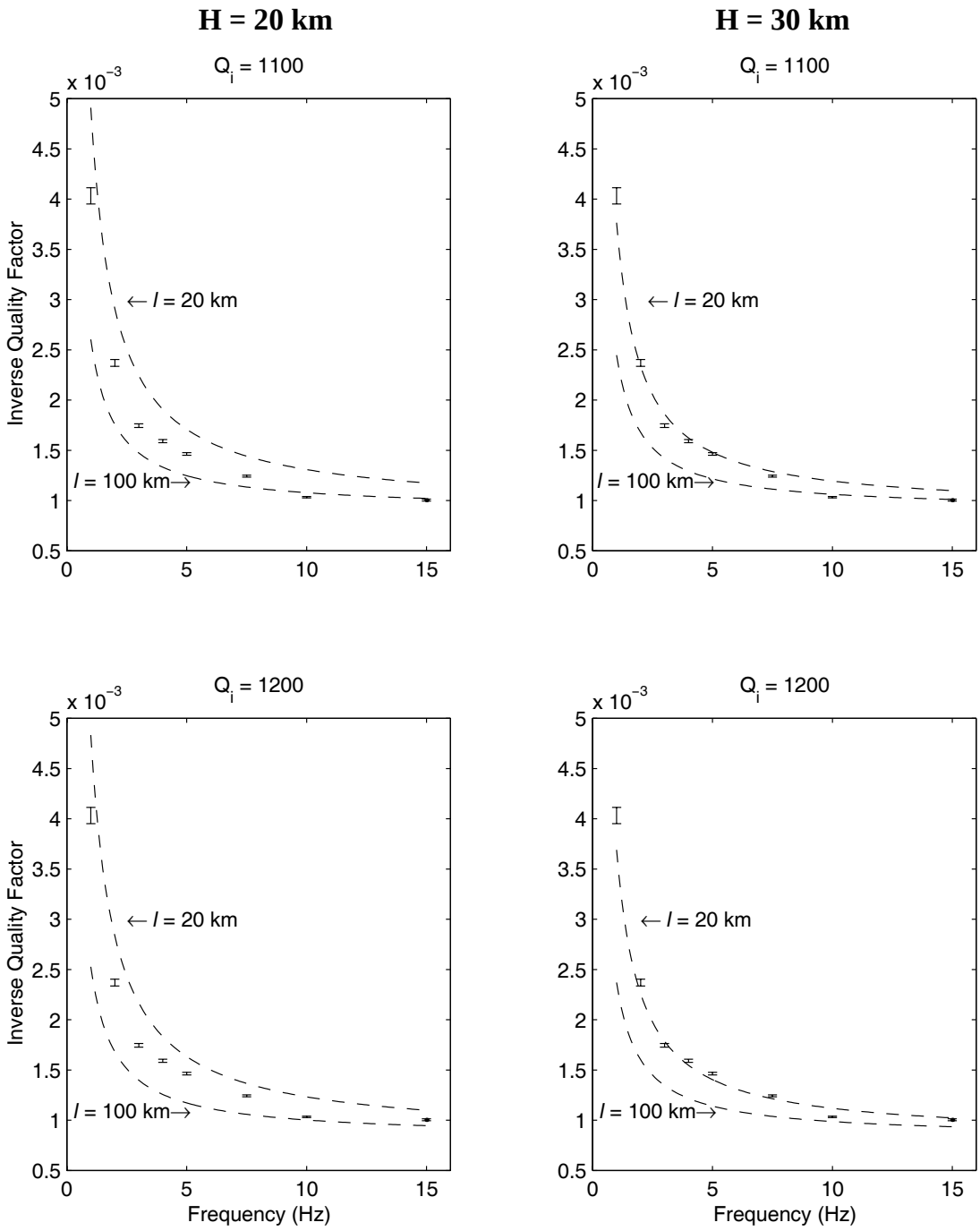

Figure 3.7: Same as figure 3.6 except that a constant intrinsic absorption Q_i has been incorporated in the model. The dashed curves limit the domain of $1/Q_m^\star$ predicted by the model for $20 < l < 100$ km.

and intrinsic Q of 1100 and 1200, the model expectations are in good agreement with the observations in the whole frequency range. We do not aim at finding a "best" set of model parameters but rather to capture the relative importance of the physical processes at work. The data are fitted satisfactorily with only two free parameters, l and Q_i, both with very reasonable values. It is therefore not required by our data set to introduce an ad-hoc frequency dependence of Q_i. The results of our study indicate the need for taking into account the depth dependence of mean free path and velocity for the interpretation of coda decay in terms of statistical parameters. An interpretation of this data set using a half-space with uniform scattering properties would have led to infer a large intrinsic absorption at low frequency.

3.5 Discussion and Conclusion

In the preceding analysis, we have used the two crustal thicknesses 20 and 30 km, while the actual local crustal thickness is about 30 km. We emphasize that the values of H used in the model cannot be directly compared to the actual crustal thickness at the station. What matters is the existence of the velocity contrast to create a wave guide and the *effective* thickness H_e of the scattering layer. In the continental crust, the heterogeneity is often concentrated in the lower part (see e.g. Fuchs et al. 1987, Bois et al. 1988). Therefore, in such a case, the thickness of the lower crust could be preferred as the value of H_e. On the other hand, we stress that it is not possible to neglect the velocity mismatch at the Moho. Even at high frequencies, post-critical reflections at the base of the crust can always be identified in seismograms. We have shown in paper A that the absence of reflection at the base of the scattering layer would imply a leakage effect much bigger than observed.

In previous coda studies based on radiative transfer in a uniform half-space, a separation of scattering and intrinsic absorption was proposed. Fehler at al. (1992) and Hoshiba (1993) found that Q_i tends to increase with frequency. This would have also been our conclusion if we had based our interpretation on a half-space with constant properties. But, it has been shown that, for mexican data, the frequency dependence of Q_i is not required when considering a stratified model including the leakage effect. This shows that the intrinsic Q and the seismic albedo may be underestimated at low frequency (around 1 Hz), when data interpretation is based on uniform half-space models. On the other hand, Fehler et al. (1992) and Hoshiba (1993) pointed out that Q_c and Q_i do not differ much at higher frequency (around 10 Hz), which is in agreement with our interpretation. Therefore, we propose that the intrinsic quality factor of the crust Q_i, can be estimated from the value of Q_c at frequencies larger than a tens of Hz.

When l is of the order of H as it may be the case in Mexico, the leakage effect more strongly affected by the variations of H than the variations of l. This is clear from Figure 3.3 and from equation (3.3). This is not true when l is much larger than H. As shown in Figure 3.3, for $l = 100$ km, the value of $Q_0^\star$ is large and almost independent of the crustal thickness. In regions where the actual structure of the crust corresponds to the case where l is of the order of H, Q_c around 1 Hz may be the result of the effect of partial leakage of diffuse energy from the scattering crust into the mantle. In regions where l is much larger than H, the leakage effect is negligible and we expect in this case that Q_c is mostly measuring the absorption. These points can be related to the observations of Singh and Herrman (1983). They showed that in the stable shield areas of North America, where l is supposed to be large, Q_c has high values and is almost frequency independent, as expected when leakage is negligible. On the other hand, in the tectonically active regions, where l and H may be of the same order, Q_0 is of the order of 100-300, and Q_c strongly depends on frequency as is expected when leakage is prominent.

Our conclusion concerning the physical properties of the crust beneath Mexico is that the interpretation of the coda decay does not require a strong intrinsic attenuation since we found Q_i larger than 1000. The frequency dependence of Q_c is explained by scattering in a stratified model. Indeed, the scattering effects tend to dominate at low frequency. A similar conclusion was reached from the study of L_g wave attenuation by Campillo and Plantet (1991). We found a strong sensitivity of the decay rate of the coda with the ratio l/H and with the crustal thickness itself. Again, we point out that when l is of the order of H, the coda decay is more sensitive to a variation of the crustal thickness than of the mean free path. This suggests that the crustal thickness has to be taken into account to interpret the regional variations

of coda Q.

The authors thank Shri Krishna Singh, Javier Pacheco and Christopher Bean for helpful discussions. We thank M. Hoshiba, G. Müller and an anonymous reviewer for their comments and suggestions to improve the manuscript. The data from station CAIG were kindly provided by Servicio Sismologico Nacional, Instituto de Geofisica, UNAM, Mexico. This work was supported by Program "Intérieur de la Terre" of INSU/CNRS and "Groupement de Recherches POAN" of CNRS.

Abubakirov, I.R. and A.A. Gusev, 1990. Estimation of scattering properties of lithosphere of Kamchatka based on Monte-Carlo simulation of record envelope of a near earthquake, Phys. Earth and Planet. Inter. 64, 52-67.

Aki, K., 1969. Analysis of the seismic coda of local earthquakes as scattered waves, J. Geophys. Res., 74, 615-618.

Aki, K. and B. Chouet, 1975. Origin of coda waves: Source, attenuation, and scattering effects, J. Geophys. Res., 80, 3322-3342.

Allmendinger, R.W., K.D. Nelson, C.J. Otter, M. Barazangi, L.D. Brown and J.E. Oliver, 1987. Deep seismic reflection characteristics of the continental crust, Geology, 15, 304-310.

Bois, C., M. Cazes, A. Hirn, A. Mascle, P. Matte, L. Montadert, and B. Pinet, 1988. Contribution of deep seismic profiling to the knowledge of the lower crust in France and neighbouring areas, Tectonophysics, 145, 253-275.

Campillo, M. and J.L. Plantet, 1991. Frequency dependence and spatial distribution of seismic attenuation in France: experimental results and possible interpretations, Phys. Earth Planet. Inter., 67, 48-64.

Cloves, R.M., A.J. Calvert, D.W. Eaton, Z. Hajnal, J. Hall and G.M. Ross, 1996. LITHOPROBE reflection studies of archean and proterozoic crust in Canada, Tectonophysics, 264, 65-88.

Fehler, M., M. Hoshiba, H. Sato, and K. Obara, 1992. Separation of scattering and intrinsic attenuation for the Kanto-Tokai region, Japan using measurements of S-wave energy vs hypocentral distance, Geophys. J. Int., 787-800.

Fuchs, K., K.P. Bonjer, D. Gajewski, E. Lüschen, C. Prodehl, K.J. Sandmeier, F. Wenzel, and H. Wilhelm, 1987. Crustal evolution of the Rhinegraben rift by unified geophysical experiments, Tectonophysics, 141, 261-275.

Gusev, A.A., 1995. Vertical profile of turbidity and Coda Q, Geophys. J. Int. 123, 665-672.

Hasegawa, H. S., 1985. Attenuation of *Lg* waves in the canadian shield, Bull. Seismol. Soc. Am. 75, 1569-1582.

Herraiz, M. and A.F. Espinosa, 1987. Coda Waves: a review, Pure and Applied Geophysics 125, 499-577.

Hoshiba, M., 1993. Separation of scattering attenuation and intrinsic absorption in Japan using the multiple lapse time window analysis of full seismogram envelope, J. Geophys. Res. 98, 15809-15824.

Hoshiba, M., 1997. Seismic coda wave envelope in depth dependent S-wave velocity structure, Phys. Earth and Planet. Inter. 104, 15-22.

Kostoglodov, V., Bandy, W., Dominguez, J., and Mena, M., 1996. Gravity and seismicity over the Guerrero seismic gap, Mexico, Geoph. Res. Lett. 23, 3385-3388.

Krishna, V.G., R. Meissner and S.A. Thomas, 1996. Unusual sub-Moho events near Bornholm, Baltic Sea: modelling of BABEL seismic wide angle data and a tectonic interpretation, Geophys. J. Int. 125, 193-198.

Margerin, L., M. Campillo, B.A. Van Tiggelen, 1998. Radiative transfer and diffusion of waves in a layered medium: new insight into coda Q, Geophys. J. Int., 134, 596-612.

McGeary, S. and M. R. Warner, 1985. Seismic profiling the continental lithosphere, Nature 317, 795-797.

Meissner, R., 1989. Rupture, creep, lamellae and crocodiles: happenings in the continental crust, Terra Nova 1, 17-28.

Meissner, R., L. Brown, H.J. Durbaum, W. Franke, K. Fuchs, F. Seifert (editors), 1990. Continental Lithosphere: deep seismic reflections, Geodynamics Series vol 22, American Geophysical Union, Washington DC, USA.

Singh, S., & Herrmann, R.B., 1983. Regionalization of crustal coda Q in the continental United States, *Journal of Geophysical Research,* **88**, 527-538.

Wu R.S. and K. Aki, 1988. Multiple scattering and energy transfer of seismic waves: Separation of scattering effect from intrinsic attenuation, II, Application of the theory to Hindu Kush region, Pure Appl. Geophys., 128, 49-80.

Chapter 4

Diffusion Multiple en Elasticité Complète

Monte-Carlo simulation of multiple scattering of elastic waves.
Ludovic Margerin, Michel Campillo, Bart Van Tiggelen
article soumis à Journal of Geophysical Research, 1999.

Résumé

We study multiple scattering of elastic waves with a Monte-Carlo method. We take into account the mode conversions and the polarization of the S waves. Some important physical parameters relevant to the description of the polarization are recalled, such as the definition and properties of the elastic Stokes vector. We briefly derive the scattering and Mueller matrices, as well as the differential and total scattering cross-sections for one spherical inclusion embedded in a homogeneous matrix. The results of the single-scattering problem are used as a building block for multiple-scattering. A Monte Carlo method to simulate the propagation of full elastic waves is presented. We pay a special attention to the convergence towards the diffusive regime which exhibits the equilibration of the P and S energy densities. Our simulations show the shear energy to become very rapidly dominant in the coda, and the S to P energy density ratio to tend to 10.4 for a Poisson solid, as predicted by the equipartition theorem. However, the typical time and length scales to reach equipartition heavily depend on the scattering parameter $k_P a$, where k_P is the P wave number and a the sphere radius. For Rayleigh scatterers ($k_P a \ll 1$), we find a smooth evolution of energy density with time and a slow convergence towards the equilibration, mainly because of the large difference between the P and S scattering mean free paths in this case. On the other hand, for Rayleigh-Gans scatterers ($k_P a \sim 1.2, 1.6$), a peak of energy associated with the forward scattered waves is observed, followed by a slow decay according to the diffusion approximation. We find that after a few mean free times only, the equipartition is reached in spite of the strong anisotropy of the scattering in this regime. As the scattering parameter $k_P a$ increases, we find that the equipartition is again delayed because the transport mean free paths become quite large. We find that a large source-station distance favors a rapid equilibration. This effect is seen to be very pronounced for Rayleigh scatterers. When a source of P-waves is considered, the equipartition time can be twice as long as compared with a shear source. The time evolution of the E_P/E_S ratio could be used as a marker for the different scattering mechanisms.

4.1 Introduction

The propagation of high-frequency elastic waves in the Earth's crust is a complex problem that has been addressed many times in recent years [*Sato,* 1994; *Zeng,* 1993, *Shapiro and Hubral,* 1996; *Sato and Fehler,* 1998]. The complexity stems from the heterogeneity of the crust which involves numerous physical phenomena like reflection and refraction from velocity discontinuities, and multiple scattering. One specific feature of elastic wave propagation is that the energy can be transported by compressional (P) and shear (S) waves that are coupled. Each time a seismic wave encounters boundaries or heterogeneities of the medium, it gives rise to scattered P and S waves which, in turn, will give rise to new scattered P and S waves. This makes the interpretation of high-frequency seismograms rather complex, because the coherent P and S wave arrivals from the source are followed by numerous incoherent arrivals which are called coda waves. Most often, the coda is modeled with the acoustic radiative transfer equation. This approximation relies on certain observational and theoretical evidences that the transport of scattered energy should be rapidly dominated by the shear mode [*Dainty and Töksöz,* 1990; *Aki,* 1992; *Papanicolaou et al.*, 1996a,b]. But even if shear waves are dominant, the P-S mode conversions lead to results different from the acoustic approximation. For example, *Turner* [1998] has shown that, in the long wavelength limit, the elastic diffusivity is about 1/3 higher than the pure shear diffusivity.

Several efforts have been made to include mode conversions in the modeling of the seismic coda [*Zeng,* 1993; *Sato,* 1994] relying on some assumptions. Yet, as pointed out several times in the literature [*Ryzhik et al.,* 1996; *Turner,* 1998], some of these assumptions are never fulfilled in practice. For example, scattering of elastic waves is always anisotropic, whatever the value of a/λ, where a is the correlation length of the fluctuations, and λ the wavelength. Like in optics, the elastic scattering problem is intrinsically dependent on the state of polarization of the waves, especially for S waves which are similar to transverse electromagnetic waves. Complete modeling of the multiple scattering of elastic waves should incorporate

a description of the polarization. An additional difficulty of elasticity is the interaction of longitudinal and transverse modes. Recently, the radiative transfer (or transport) equations for elastic waves have been obtained independently by *Weaver* [1990] and *Ryzhik et al.* [1996]. These equations can be derived from the wave equation by a rigorous statistical analysis. The conditions of validity of the transport theory are summarized in the papers by *Papanicolaou et al.* [1996a,b]. The main condition is that the mean free paths are much larger than the wavelengths, making it possible to neglect interference effects. However, no particular restriction on the a/λ ratio exists and therefore strong interactions of the waves with the heterogeneities are allowed. The transport equations describe the space and time evolution of the elastic energy as well as the state of polarization of the waves. It has been shown that the evolution of the seismic energy in the coda is ruled by an equilibration law, which states that the ratio of the P to S energy density tends to a constant ratio as time tends to infinity [*Weaver* 1982, 1990; *Ryzhik et al.* 1996; *Papanicolaou et al.* 1996a,b]. In the case of a full space, this ratio equals $2\alpha^3/\beta^3$ where α and β are the P and S waves velocities respectively. This result appears immediately by realizing that, in the diffusion regime, all the volumes of the phase space are equally occupied, consistent with the equipartition theorem. The factor 2 comes from the existence of two degrees of freedom for the S waves and only one for the P wave. The ratio of the P to S wave speeds cubed comes from the counting of the P and S modes in a given volume of the phase space.

A central question addressed in this paper concerns the required time and length scales to reach the diffusion regime in the Earth. In this regime, the description of coda waves is greatly simplified. A similar problem has already been studied in acoustics by *Turner and Weaver* [1994a,b,c]. They showed that the time necessary to reach equipartition heavily depends on the scattering mechanism. Only a few mean free times suffice for Rayleigh scatterers while many mean free times are necessary for Mie scatterers. Unfortunately the pioneering results of Turner and Weaver obtained for incident plane waves cannot be transposed directly to seismology. We have to take into account the fact that small earthquakes are almost point-like sources in both space and time. The statistical description of fluctuations in the Earth can be accessed from well-log data [Wu et al., 1994] or from geological maps [*Holliger and Levander,* 1992]. For the sake of simplicity, we consider discrete spherical inclusions embedded in a homogeneous matrix.

In this paper, we will explain how multiple scattering of elastic waves can be simulated with a Monte Carlo method. For simplicity, only infinite and statistically uniform media are considered, but anisotropy of scattering, polarization, mode conversions and point like sources are accurately described. When scattering problems are considered, a complete description of the polarization of the S waves is necessary. Indeed, initially depolarized S waves can become partially polarized by scattering. Moreover the interaction of S waves with heterogeneities in turn depend on their polarization. In the next section, these problems will be examined.

4.2 Description of Polarization

4.2.1 Definition of the Stokes parameters.

In optics, polarized light is represented by a four element vector, called the Stokes vector, whose components are intensities [*Chandrasekhar* 1960]. In view of the transverse nature of S waves and electromagnetic waves, the definition of the Stokes parameters can readily be transposed from optics to elasticity. To be complete, one additional Stokes parameter is necessary to represent the P waves. Our definition of the elastic Stokes parameters follows the one given by *Turner and Weaver* [1994a]. Let us define a Cartesian reference frame $(\vec{x}, \vec{y}, \vec{z})$ where $\vec{z}$ denotes the propagation direction and let us call ω the central frequency of the waves. The wave displacements can be written at $x = 0, y = 0, z = 0$ (without loss of generality) as:

$$\left\{ \begin{array}{lcl} P(t) & = & A_P(t) \exp\left(i\omega t + i\eta(t)\right) \\ S_x(t) & = & A_x(t) \exp\left(i\omega t\right) \\ S_y(t) & = & A_y(t) \exp\left(i\omega t + i\delta(t)\right), \end{array} \right. \tag{4.1}$$

where δ is the phase difference between the y and x component of the S wave, η a phase shift for the P-wave, and $i^2 = -1$. In typical experiments, A_x, A_y, A_z and δ fluctuate with time t. These fluctuations should obviously be slow compared to the central frequency of the signal. If the wave is polarized, certain constant relations, or *correlations* should persist between the phase and amplitude terms of the displacements. This will be expressed mathematically through the Stokes vector:

$$S = (I_P, I_{S_x}, I_{S_y}, U, V) \tag{4.2}$$

where:

$$I_P = \langle \frac{\rho\omega^2\alpha}{2} A_P^2 \rangle \tag{4.3}$$

$$I_{S_x} = \langle \frac{\rho\omega^2\beta}{2} A_x^2 \rangle \tag{4.4}$$

$$I_{S_y} = \langle \frac{\rho\omega^2\beta}{2} A_y^2 \rangle \tag{4.5}$$

$$U = \langle \rho\omega^2\beta A_x A_y \cos\delta \rangle \tag{4.6}$$

$$V = \langle \rho\omega^2\beta A_x A_y \sin\delta \rangle \tag{4.7}$$

ρ is the density of the medium, and α and β are the P and S wave velocities respectively. The brackets indicate that the time average is taken over a large number of periods. The parameters defined in equations (4.3) – (4.5) are just the intensities carried by the wave when measured along the three axes of the reference frame. The last two parameters U and V measure the cross-correlations between the x and y components of the shear wave. We note that the four parameters (4.4) – (4.7) contain information about the total intensity, the degree of polarization, the ellipticity, and the plane of polarization of of S-waves, like in optics. For future developments, we will give the relation between the Stokes parameter and the ellipticity and azimuth of the polarization plane in the simple case of elliptical polarization. The azimuth $-\pi/2 < \chi < +\pi/2$ is defined as the angle between the major axis of the ellipse and the x axis. The ellipticity $\tan|\epsilon| < 1$ is defined as the ratio of length of the major to the minor axis. $\epsilon > 0$ corresponds to a right-handed ellipse and $\epsilon < 0$ to a left-handed one. We have

$$\tan 2\chi = \frac{U}{I_{S_x} - I_{S_y}} \tag{4.8}$$

$$\sin 2\epsilon = \frac{V}{I_{S_x} + I_{S_y}} \tag{4.9}$$

4.2.2 Properties of the Stokes parameters.

A useful property is that independent Stokes vectors are additive. 'Independent' here means that the waves, whose Stokes parameters are added do not obey any phase relations [*Chandrasekhar,* 1960]. The Stokes parameters are subject to the inequality:

$$(I_{S_x} + I_{S_y})^2 \leq (I_{S_x} - I_{S_y})^2 + U^2 + V^2 \tag{4.10}$$

The equality applies when the wave is elliptically polarized. In this case, only three parameters are necessary to characterize the polarization ellipse. Another relation that we will need is the transformation of the Stokes parameters when the coordinate system is rotated an angle ϕ around the z axis. One can show that the Stokes vector S in the new coordinate system is related to the Stokes vector S_0 in the old coordinate system by the matrix relation:

$$S = LS_0, \tag{4.11}$$

(see *Turner and Weaver* [1994a]). The expression of the 5×5 matrix L can be found in appendix A.1. It is worth noting that V, I_P, and $I_S = I_{S_x} + I_{S_y}$ are invariant under this rotation. Indeed, V corresponds to the decomposition of the wave on the basis of the right and left circular polarization.

4.3 Scattering by one sphere

To study the multiple scattering of elastic waves, we consider a very simple model composed of randomly distributed spherical inclusions in a homogeneous matrix. The spherical inclusions are of the same nature and show a small contrast of wave speeds and density with the reference medium. We assume that the wave speeds and the density are equally perturbed. The choice of spherical scatterers introduces symmetry relations that greatly simplify the problem. The first step is to calculate all the physical quantities relevant to the description of scattering by a single sphere. Then, these results will be used as a building-block for multiple scattering. The scattering of elastic waves by one sphere has been largely studied and many references exist in the literature [*Ying and Truell,* 1956; *Einspruch, Witterholt and Truell,* 1960; *Wu And Aki,* 1985a; *Korneev and Johnson,* 1993a, 1993b, 1996]. For the sake of simplicity, we shall follow the approach of *Wu and Aki* [1985a] who calculated the field scattered by one sphere using the Born approximation. In this approximation, the elastic inclusion is decomposed in infinitesimal volumes which are considered as independent Rayleigh scatterer. The total scattered field is written a sum of partial waves emitted by each fraction of the whole inclusion. Thereby, the Born approximation neglects interactions between infinitesimal volumes and holds good as long as $k_{P,S}a|m-1| \ll 1$, where $k_{P,S}$ is the P or S wave number, a the radius of the sphere and $m = \alpha/\alpha_0$ or $m = \beta/\beta_0$ is the value of the ratio of the wave speeds inside and outside the sphere. Like in the electromagnetic literature [*Van de Hulst,* 1981], we will term this scattering mechanism 'Rayleigh-Gans' scattering. The results of *Wu and Aki* [1985a,b] will be our starting point to derive some physical quantities of interest like the scattering and Mueller matrices, and the differential and integrated scattering cross sections.

4.3.1 Scattering and Mueller Matrices

We consider a plane wave propagating in the $\vec{z}$ direction, incident on a sphere centered at the origin of the Cartesian reference frame $(\vec{x}, \vec{y}, \vec{z})$. The scattered wave propagates in the $\vec{z'}$ direction, at an angle Θ with $\vec{z}$. The plane containing $\vec{z}$ and $\vec{z'}$ is called the scattering plane. To derive the scattering matrix, we choose the following convention (see Figure 4.1): the incident Stokes parameters are expressed in the $(\vec{r}, \vec{l}, \vec{z})$ Cartesian frame where $\vec{r}$ and $\vec{l}$ denote, respectively, the directions perpendicular and parallel to the scattering plane. Similarly, the Stokes parameters of the scattered wave are expressed in the $(\vec{r'}, \vec{l'}, \vec{z'})$ Cartesian frame where the same convention is assumed. We find that the incident and scattered Stokes vectors S_{inc}, S_{sc} are related by:

$$S_{sc} = \frac{1}{R^2} F S_{inc}, \tag{4.12}$$

where R is the distance from the center of the inclusion to the observer, and F the scattering matrix:

$$\frac{1}{16\pi^2} \begin{pmatrix} k_P^4\gamma_1^2(\Theta)f_{PP}^2(\Theta) & 0 & \frac{\alpha}{\beta}k_P^4\gamma_3^2(\Theta)f_{SP}^2(\Theta) & 0 & 0 \\ 0 & k_S^4\gamma_4^2(\Theta)f_{SS_r}^2(\Theta) & 0 & 0 & 0 \\ \frac{\beta}{\alpha}k_S^4\gamma_2^2(\Theta)f_{PS}^2(\Theta) & 0 & k_S^4\gamma_4^2(\Theta)f_{SS_l}^2(\Theta) & 0 & 0 \\ 0 & 0 & 0 & k_S^4\gamma_4^2(\Theta)f_{SS_l}(\Theta)f_{SS_r}(\Theta) & 0 \\ 0 & 0 & 0 & 0 & k_S^4\gamma_4^2(\Theta)f_{SS_l}(\Theta)f_{SS_r}(\Theta) \end{pmatrix} \tag{4.13}$$

where k_p and k_s are the P and S wave numbers respectively. The functions $f_\star(\Theta)$ and $\gamma_\star(\Theta)$ come out of the Born approximation, the subscript $\star$ denoting any of these functions. The functions $f_\star$ correspond to Rayleigh scattering and the functions $\gamma_\star$ are shape factors that appear for scatterers of finite size [*Wu and Aki,* 1985a]. These functions are given in appendix A.2. The matrix F depends on Θ only as required by the rotational symmetry (see *Van de Hulst* [1981] for details). From the structure of the matrix F, it can be inferred that for an elliptically polarized incident wave, the scattered wave will remain elliptically polarized. This means that depolarization can occur in multiple scattering only.

The scattering matrix is not convenient to deal with multiple scattering, since it is referred to a *local* frame. For the purpose of our simulation, we will find it convenient to know how a beam of energy propagating in a direction of space (θ', ϕ') contributes to a beam propagating in an other direction of

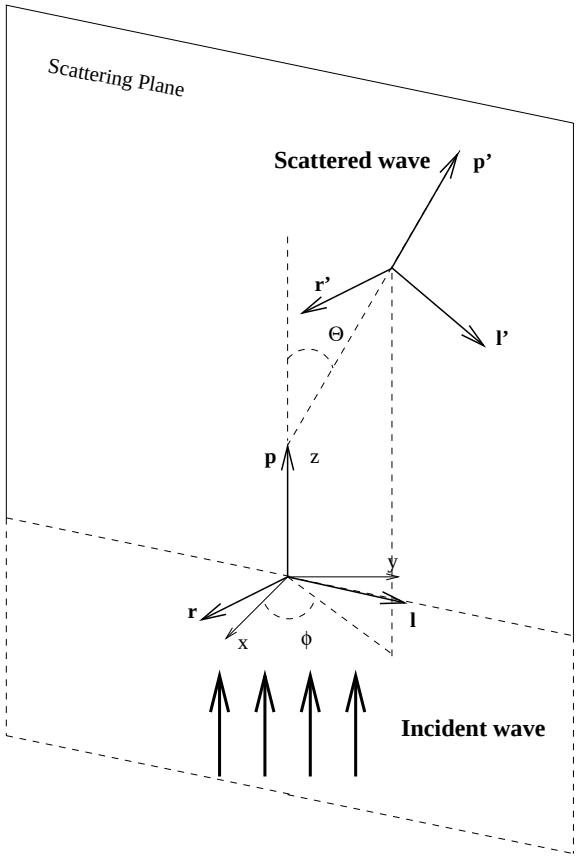

Figure 4.1: Sketch of the convention used to derive the scattering matrix.

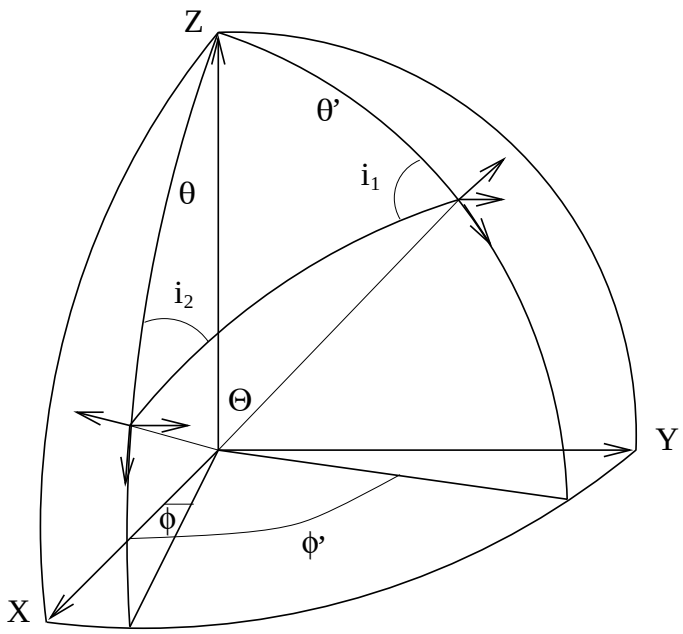

Figure 4.2: Sketch of the convention used to derive the Mueller matrix. i_1 denotes the dihedral angle between the incident and scattering planes, while i_2 denotes the dihedral angle between the scattering and outgoing planes. Θ is the scattering angle.

space(θ, ϕ), where $(\theta^{(\prime)}, \phi^{(\prime)})$ refer to the usual definition of polar coordinates in a *global* reference frame $(O, \vec{x}, \vec{y}, \vec{z})$. Moreover, a convention must be adopted for the analysis of the polarization of S waves. Following *Turner and Weaver* [1994a], the Stokes vector will be written in the basis $(\vec{u_\theta}, \vec{u_\phi}, \vec{p})$ composed of three unit vectors in the direction of increasing θ, increasing ϕ and in the propagation direction respectively (see Figure 4.2). With these conventions the incident and scattered Stokes vectors S_{inc} and S_{sc} are related by $S_{sc} = PS_{inc}$ where the Mueller matrix P can be deduced from the scattering matrix F after carrying out the necessary rotations (see *Chandrasekhar* [1960] for electromagnetic waves and *Turner and Weaver* [1994a] for elastic waves). Upon introducing i_1, the dihedral angle between the plane containing the directions Oz and (θ', ϕ') and the scattering plane, i_2, the dihedral angle between the scattering plane and the plane containing the directions Oz and (θ, ϕ) (see Figure 4.2), the Mueller matrix reads:

$$P(\theta, \phi; \theta', \phi') = L(i_2 - 3\pi/2)F(\Theta)L(i_1 + \pi/2) \tag{4.14}$$

The rotation through i_1 brings the incident basis in the scattering plane and enables us to use the relation (4.12). The rotation through i_2 ensures that the outgoing Stokes vector is referred to the basis $(\vec{u}_\theta, \vec{u}_\phi, \vec{p})$. The expression of the Mueller matrix for a spherical elastic inclusion is left to Appendix A.3. From the structure of this matrix, we see that the parameter V decouples and that linearly polarized S waves give rise to scattered waves that are still linearly polarized. This property will be helpful when considering the numerical simulation.

4.3.2 Scattering Cross-Sections

We shall first consider the differential cross-sections which contain all the information about the angular dependence of the scattered flux. They are defined as the ratio of the energy scattered in the space direction (Θ, Φ) (see Figure 4.1) per unit time and per unit solid angle by the spherical inclusion to the energy per unit area and unit time carried by the incident wave [*Sato and Fehler,* 1998]. These cross-sections clearly depend on the polarization of incident and scattered waves. In the following, we will consider linearly polarized S waves only for simplicity, but our results can easily be generalized to any

type of polarization. From the solution of the scattering problem given by *Wu and Aki* [1985a], we find:

$$\frac{d\sigma_{PP}}{d\Omega} = \frac{k_P^4}{16\pi^2}\gamma_1^2(\Theta)f_{PP}^2(\Theta) \tag{4.15}$$

$$\frac{d\sigma_{PS}}{d\Omega} = \frac{k_S^4\beta}{16\pi^2\alpha}\gamma_2^2(\Theta)f_{PS}^2(\Theta) \tag{4.16}$$

$$\frac{d\sigma_{SP}}{d\Omega} = \frac{k_P^4\alpha}{16\pi^2\beta}\gamma_2^3(\Theta)f_{SP}^2(\Theta)\cos^2\Phi \tag{4.17}$$

$$\frac{d\sigma_{SS}}{d\Omega} = \frac{k_S^4}{16\pi^2}\gamma_4^2(\Theta)(f_{SS_l}^2(\Theta)\cos^2\Phi + f_{SS_r}^2(\Theta)\sin^2\Phi). \tag{4.18}$$

In equations (4.15) – (4.18), Θ denotes the angle between the incident and scattered directions and Φ the angle between the scattering plane and the polarization plane of the S wave, which contains both the propagation and wave displacement directions. For incident S wave polarized in the x direction, the polarization plane is merely $(\vec{x},\vec{z})$ and Φ denotes the usual azimuthal angle. As has already been noted by *Papanicolaou et al.* [1996a,b] and *Turner* [1998], the angular distribution of scattered energy is never isotropic, even in the low frequency limit $k_{P,S}a \ll 1$ or Rayleigh regime.

The integrated scattering cross-sections Σ_{MN} with $M,N = S,P$, are obtained by integrating the differential cross-sections over the solid angle. In the case of incident S waves the total cross-sections for a spherical inclusion do not depend on the polarization because of the symmetry of the scatterer [*Van de Hulst,* 1981]. In the intermediate frequency regime $ka \simeq 1$, the cross sections can be evaluated numerically. The accuracy of our computations has been checked, using the results presented in the paper by *Korneev and Johnson* [1993b]. In the Rayleigh regime, the scattering cross-sections can be computed analytically and are given in Appendix A.4. It is important to note that according to the definition of the scattering cross-sections and the symmetry of the function f_{SP} and f_{PS}, a relation exists between Σ_{SP} and Σ_{PS}:

$$\Sigma_{PS} = 2\frac{\alpha^2}{\beta^2}\Sigma_{SP}, \tag{4.19}$$

independent of the scattering mechanism. As has been explained by *Aki* [1992], this relation finds its origin in the reciprocity of the Green functions. The same relation has been obtained by *Papanicolaou et al.* [1996a,b] for a continuous random medium. The reciprocity argument of Aki also holds for scatterers of more complicated shape, making equation (4.19) a fundamental relation.

4.4 Diffusion of Elastic waves

In a recent paper, *Turner* [1998] made a summary of theoretical work done on multiple scattering of elastic waves. For our purpose, it is important to recall some results concerning the diffusion of elastic waves. It has first been shown by *Weaver* [1990] that the propagation of elastic waves in inhomogeneous media could be described by a radiative transfer equation, which is a coupled equation for the five Stokes parameters described above. For large lapse times, the equation of radiative transfer can be turned into a simple diffusion equation for the total energy density (E) of the P and S modes. It is remarkable that such a simple scalar equation is able describe the evolution of the seismic energy. Since the diffusion theory is much easier to use than the full radiative transfer equation, it would be very interesting to know what are the typical time and length scales necessary to reach the diffusive regime. In this regime, the total energy density E for a point source in both space and time in an infinite medium reads:

$$E(r,t) = \frac{1}{(2\sqrt{\pi D t})^3}\exp\left(-r^2/4Dt\right), \tag{4.20}$$

where t is the lapse time, r the source station distance, and D the diffusion constant of elastic waves:

$$D = \frac{1}{1+2K^3}\left(\frac{\alpha l_P^\star}{3} + 2K^3\frac{\beta l_S^\star}{3}\right), \tag{4.21}$$

The variables α, β are respectively the P and S wave speeds, and $K = \alpha/\beta$ is the P to S wave speed ratio. A crucial point is the definition of the transport mean free paths $l_P^\star$ and $l_S^\star$ appearing in formula (4.21). In order to cope with discrete scatterers, we have to modify slightly the definitions given by *Turner* [1998] and obtain:

$$l_P^\star = \frac{1}{n} \frac{\Sigma_S - \Sigma_{SS}^\star + \Sigma_{PS}^\star}{(\Sigma_P - \Sigma_{PP}^\star)(\Sigma_S - \Sigma_{SS}^\star) - \Sigma_{PS}^\star \Sigma_{SP}^\star} \tag{4.22}$$

$$l_S^\star = \frac{1}{n} \frac{\Sigma_P - \Sigma_{PP}^\star + \Sigma_{SP}^\star}{(\Sigma_P - \Sigma_{PP}^\star)(\Sigma_S - \Sigma_{SS}^\star) - \Sigma_{PS}^\star \Sigma_{SP}^\star} \tag{4.23}$$

where the following notations have been introduced:

$$\Sigma_{MN}^\star = \int_{4\pi} \frac{d\sigma_{MN}(\cos\Theta)}{d\Omega} \cos\Theta d\cos\Theta d\phi \qquad M, N = P, S \tag{4.24}$$

and n is the density of scatterers. The $\Sigma_{M,N}^\star$ are the averages of the cosine of the scattering angle, weighted by the differential cross-section. The definition of the transport mean free paths in terms of the $\Sigma_{M,N}^\star$ are more complicated than in the acoustic case. The exact results of the diffusion theory will be useful in checking the accuracy of our numerical simulations.

Another relation of importance is the value of the equilibration ratio of the P to S energy density, shown to be independent of the details of the scattering [*Ryzhik et al.,* 1996],

$$\frac{E_P}{E_S} = \frac{1}{2} \left(\frac{\beta}{\alpha} \right)^3 \tag{4.25}$$

We finally comment on the definitions of the wave speeds appearing in the diffusion theory. It is now well established that in the case of very strong scattering, we have to distinguish between the phase and group velocities of a pulse and the transport velocity appearing in the definition of the diffusion constant [*Lagendijk and Van Tiggelen,* 1996]. It has been shown that for resonant scatterers, the transport velocity can be reduced by a factor of ten, compared to the group velocity. Since we consider scatterers away from resonances, the difference between the phase, group and transport velocity becomes immaterial.

4.5 Monte Carlo Simulation

In recent years, the Monte Carlo method has been used to model the propagation of high frequency seismic waves in the Earth's lithosphere. Starting from infinite space models [*Gusev and Abubakirov,* 1987; *Abubakirov and Gusev,* 1990; *Hoshiba,* 1991], the most recent models [*Hoshiba,* 1997; *Margerin et al.* 1998] have also included depth dependence of wave velocity and scattering mean free path, yet retaining the acoustic approximation. In this section, we will generalize the method to include mode conversions. The problem of boundary reflections and non-uniform mean free path will not be discussed in this paper. Instead, we will emphasize the elastic aspects and the time dependent propagation.

4.5.1 Outline of the simulation

The Monte Carlo method requires three steps, which are schematically depicted in Figure 4.3. First, the random walk of "particles" representing seismic wave packets is simulated. The path length distribution is given by an exponential probability law. Second, at each scattering event the energy contribution of the particle is calculated in terms of probability at different receivers. Finally, the average of all the random walk results is calculated to obtain the time evolution of the seismic energy at different positions of space (see eg *Hoshiba* [1991] for a clear description of the basic method).

Our treatment follows the one used for anisotropic scattering of acoustic waves [*Hoshiba,* 1995]. To describe the particle, we use the following quantities:

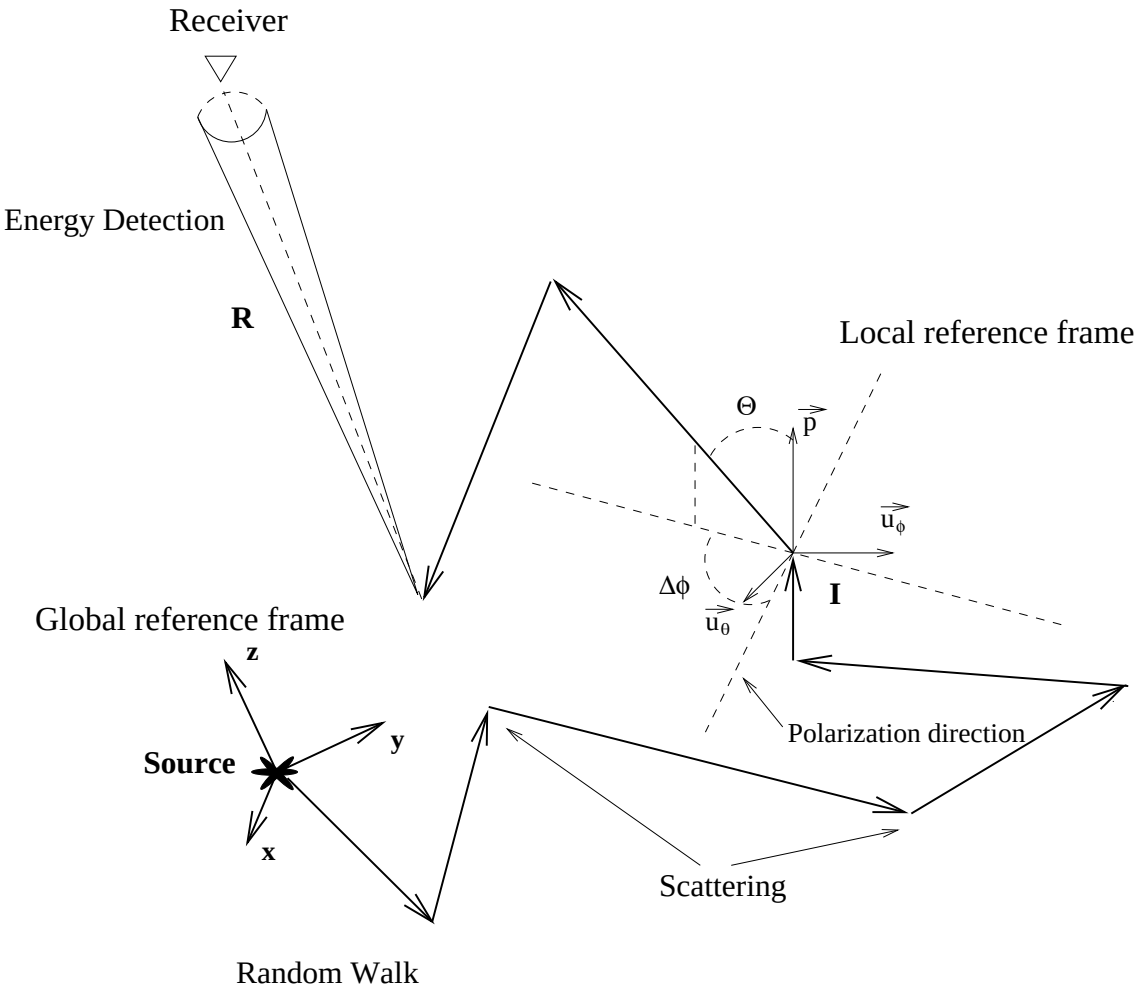

Figure 4.3: Schematic picture of the Monte Carlo simulation. The particle starts at a point source and makes a random walk in the medium. At each scattering, the choice of the new mode, propagation direction, path length is made; the energy contribution of the particle is also calculated at the receiver

vectors $\vec{I} = (x_I, y_I, z_I)$ and $\vec{p} = (p_x, p_y, p_z)$ to determine respectively the position and propagation direction in a Cartesian global reference frame $(\vec{x}, \vec{y}, \vec{z})$

The travel time of the particle since the emission at the source is stored in a scalar T.

To allow for absorption in the medium, a weight $w \leq 1$ can be assigned to the particle. In the following, we will consider non dissipative media only.

For elastic waves, additional information is required:

the polarization M of the wave (P or S),

for S waves, the Stokes vector $\vec{S} = (I_{S_1}, I_{S_2}, U, V)$ that describes the polarization. In our simulation, the Stokes vector is written with the same convention as the one used for the Mueller matrix. For example, if a particle propagates in the direction $\vec{p}$, the shear components of the displacement are analyzed in the basis $(\vec{u_\theta}, \vec{u_\phi}, \vec{p})$, where $\vec{u_\theta}$ and $\vec{u_\phi}$ denote unit vectors in the direction of respectively increasing θ and ϕ in the global reference frame (see Figures 4.2 and 4.3).

4.5.2 Random walk

During its random walk, the particle changes its direction of propagation and may also change polarization. We will assume an isotropic and point-like source radiation in both space and time of either P or S waves. For S waves, we make the additional assumption that they are initially linearly polarized. Since both P and linearly polarized S waves scatter into linearly polarized S wave as explained earlier, our last assumption implies that the particle is fully linearly polarized during all the propagation in the medium. Thus, the depolarization of S waves can only occur when summing the contributions of many independent particles. This fact greatly simplifies the selection of the propagation direction after scattering since we will have to consider the scattering of P waves or linearly polarized S waves only.

Distance between collisions

Between two collisions, the wave will propagate ballistically on a length L which is determined by the exponential probability distribution $(1/l_M) \exp(-L/l_M)$ where $M = P, S$ denotes the polarization of the wave.

Scattering of elastic waves

When a collision occurs, one must determine the new polarization and propagation direction after scattering, according to the scattering cross-sections. We use the methods developed by *Collins et al.* [1972] to study the propagation of light through the atmosphere and the methods of *Heiderich* [1995] and *Heiderich et al.* [1997], to cope with light scattering in nematic liquid crystals. Light propagation in nematics bears some important resemblances with elastic wave propagation. Among these similarities, one can cite the existence of two modes of propagation (ordinary and extraordinary) with two different wave speeds, and the anisotropy of the differential scattering cross-sections. In the elastic case, the joint probability distribution of the polarization M_{sc} and of the propagation direction (Θ, Φ) after scattering reads:

$$P(M_{inc}|M_{sc}, \Theta, \Phi) = \frac{\frac{d\sigma}{d\Omega}(M_{inc}|M_{sc}, \Theta, \Phi)}{\sum\limits_{M_{inc}} \int\limits_{4\pi} \frac{d\sigma}{d\Omega}(M_{inc}|M_{sc}, \Theta, \Phi) d\cos\Theta d\Phi}. \tag{4.26}$$

$P(M_{inc}|M_{sc}, \Theta, \Phi)$ denotes that the probability distribution is parameterized by the incident polarization M_{inc}. The core of the Monte-Carlo simulation consists in simulating accurately this probability distribution. As in the case of anisotropic scattering of scalar waves, the polar and azimuthal angles (Θ, Φ) are selected in a local frame (see Figure 4.3). A rotation of coordinates provides the new propagation directions in the global coordinate system. In the case of incident P waves, the angle Φ is equidistributed

over $[0, 2\pi]$. In the case of incident S waves, Φ denotes the angle between the plane of polarization and the scattering plane. From the definition of the probability distribution (4.26), we conclude that the variables M_{sc}, Θ and Φ are not independent. This is an additional complication of the Monte Carlo simulation for elastic waves. To overcome this difficulty, we will rewrite expression (4.26) as a product of conditional probability distributions:

$$P(M_{inc}|M_{sc}, \Theta, \Phi) = P(M_{inc}|M_{sc})P(M_{inc}, M_{sc}|\Theta)P(M_{inc}, M_{sc}, \Theta|\Phi), \tag{4.27}$$

where the following notations have been introduced:

$$P(M_{inc}|M_{sc}) = \frac{\int_{4\pi} \frac{d\sigma}{d\Omega}(M_{inc}|M_{sc}, \Theta, \Phi) d\cos\Theta d\Phi}{\sum_{M_{sc}} \int_{4\pi} \frac{d\sigma}{d\Omega}(M_{inc}|M_{sc}, \Theta, \Phi) d\cos\Theta d\Phi} \tag{4.28}$$

is the conditional probability of the mode M_{sc},

$$P(M_{inc}, M_{sc}|\Theta) = \frac{\int \frac{d\sigma}{d\Omega}(M_{inc}, M_{sc}|\Theta, \Phi) d\Phi}{\int_{4\pi} \frac{d\sigma}{d\Omega}(M_{inc}, M_{sc}|\Theta, \Phi) d\cos\Theta d\Phi} \tag{4.29}$$

is the conditional probability of the angle Θ,

$$P(M_{inc}, M_{sc}, \Theta|\Phi) = \frac{\frac{d\sigma}{d\Omega}(M_{inc}, M_{sc}, \Theta|\Phi)}{\int_{4\pi} \frac{d\sigma}{d\Omega}(M_{inc}, M_{sc}, \Theta|\Phi) d\Phi}, \tag{4.30}$$

is the conditional probability of the angle Φ. Note that in these equations, the vertical bar | separates the known parameters from those that have to be randomly selected. Equation (4.27) decomposes the joint probability distribution as a product of conditional probability distributions. At this point, three independent numbers $\epsilon_1, \epsilon_2, \epsilon_3$, uniformly distributed between $]0, 1[$ are randomly generated. First, we select the mode of the scattered wave M_{sc} which depends on the mode of the incident wave. For example, in the case of an incident S wave, the probability to be converted is $P_{conv} = \Sigma^{SP}/(\Sigma^{SS} + \Sigma^{SP})$ and the probability to keep the same mode is $1 - P_{conv} = \Sigma^{SS}/(\Sigma^{SS} + \Sigma^{SP})$ consistent with equation (4.28). Thus, if ϵ_1 is smaller than P_{conv}, the wave is converted, otherwise it keeps its original mode. Once the mode of the scattered wave is known, we select the value of $\cos\Theta$ with the usual inverse distribution function method [*Lux and Koblinger* 1991]:

$$\epsilon_2 = \int_0^{\cos\Theta} P(M_{inc}, M_{sc}|\Theta') d\cos\Theta' \tag{4.31}$$

Since the angular dependence is too complicated to find $\cos\Theta$ as an explicit function of ϵ_2, we divide the $[-1, 1]$ interval into sub-intervals of equal probability such that

$$\int_{\cos\Theta_{i-1}}^{\cos\Theta_i} P(M_{inc}, M_{sc}|\Theta') d\cos\Theta' = \frac{1}{q}, \tag{4.32}$$

where q denotes the number of intervals, and $i \in [0, q]$. These values are stored in a table which is calculated once at the beginning of the simulation, from which we can select randomly the value of $\cos\Theta$. Finally the angle Φ is selected with the same method:

$$\epsilon_3 = \int_0^{\Phi} P(M_{inc}, M_{sc}, \Theta|\Phi') d\Phi' \tag{4.33}$$

Once the propagation direction of the scattered wave is known in the local coordinate system, a rotation provides the propagation direction of the particle $(\vec{p_x}, \vec{p_y}, \vec{p_z})$ in the global coordinate system . Then, using the Mueller matrix, the Stokes vector of the scattered wave can be calculated, enabling us to keep track of the orientation of the polarization in the global reference frame too. For further details, we refer to *Heiderich et al.* [1997]. It is worth mentioning that using a very similar method for polarized light, *Collins et al.* [1972] have shown good agreement between the Monte-Carlo computations and solutions of the radiative transfer equation obtained with other numerical methods.

4.5.3 Energy detection

The step of the simulation dealing with energy detection is very similar to the acoustic case except that the particle contributes to the P and S modes at each scattering event. We refer to *Hoshiba* [1995] for the details of the Monte Carlo simulation for anisotropic scattering and just give the expressions of the probabilities for the elastic case:

$$E_{M_{sc}} = \frac{P(M_{inc}|M_{sc}, \Theta, \Phi) \exp\left(-R/l_{M_{sc}}\right)}{4\pi R^2 v_{M_{sc}} dt} \tag{4.34}$$

where $v_{M_{sc}}$ denotes the wave speed of the scattered mode M_{sc}. R is the distance between the scattering site and the detector, and dt is the discretization step of time. The energy contributions of the particle at each scattering event are stored in a vector $\rho_M(t)$, which is the discrete version of the energy density as a function of time. Finally all random walks results are averaged to provide an estimate of the energy density of each mode.

4.6 Numerical Tests

We expect our numerical solutions to lie between the single-scattering (SSc) and diffusion approximations. The SSc approximation for elastic waves has been studied in detail by *Sato* [1984] and *Wu and Aki* [1985a,b]. Using the formulas of *Sato* [1984] (equations 68 a-d) and the diffusion theory outlined in this paper, we have compared the decay of the total energy density in the SSc and diffusion approximations, against our numerical results. This comparison is plotted in Figure 4.4 a,b for an isotropic source of linearly polarized shear waves because seismic sources mainly release shear energy. In Figure 4.4 a, we consider Rayleigh scatterers i.e. with size much smaller than the wavelength ($k_{P,S}a \ll 1$). In Figure 4.4 b, we consider Rayleigh-Gans scatterers whose size is comparable to the wavelength ($k_P a = 2$). As will be explained latter, these two regimes strongly differ in their scattering characteristics. For both size of scatterers, at short times, we find that our solution perfectly matches the SSc asymptotic and as time increases, our solution approaches the solution of the diffusion equation. In addition, our Monte-Carlo simulation describes the intermediate multiple-scattering regime. After one mean free time, the single-scattering and full numerical solutions start to diverge strongly, which shows that multiple scattering effects become important. It is also clear that, after a few mean free times, the diffusion approximation is much closer to the full numerical solution than the SSc approximation.

Another strong constraint on our numerical results is the equilibration ratio of the P to S energy densities, as given in equation (4.25). We have performed a series of simulations in the Rayleigh regime with $\alpha/\beta = 1.5,\ \sqrt{3},\ 2$. In Figure 4.5, the ratio of the P to S energy densities E_P/E_S is plotted as a function of time, in terms of the mean free time of the shear waves $\tau_S = l_S/\beta$. The results are shown for an isotropic source of shear waves and a source station distance of two P mean free paths. After a transition regime, we find that the P and S energies equilibrate with exactly the expected ratio. Our numerical simulations show some oscillations caused by an incomplete averaging. The characteristic time required to reach equipartition is about 25 shear mean free times, which is rather large. One should note that as the ratio α/β changes, the angular dependence of the differential cross-sections is modified. This clearly shows that the details of the scattering are unimportant and that only the P and S speeds affect the ratio E_P/E_S at equilibrium. Scattering just ensures the coupling between P and S modes, and

(a) (b)

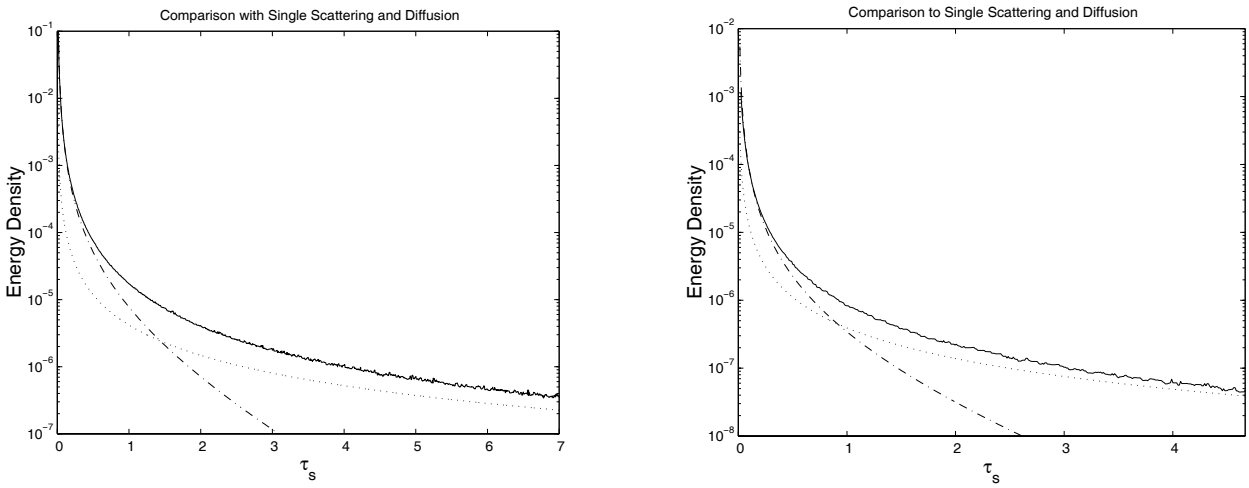

Figure 4.4: Comparison of the Monte Carlo simulation (solid) with the single-scattering (dash-dotted) and diffusion approximation (dotted) for an isotropic source of S waves close to the receiver. (a) Rayleigh Regime, (b)Rayleigh-Gans Regime.

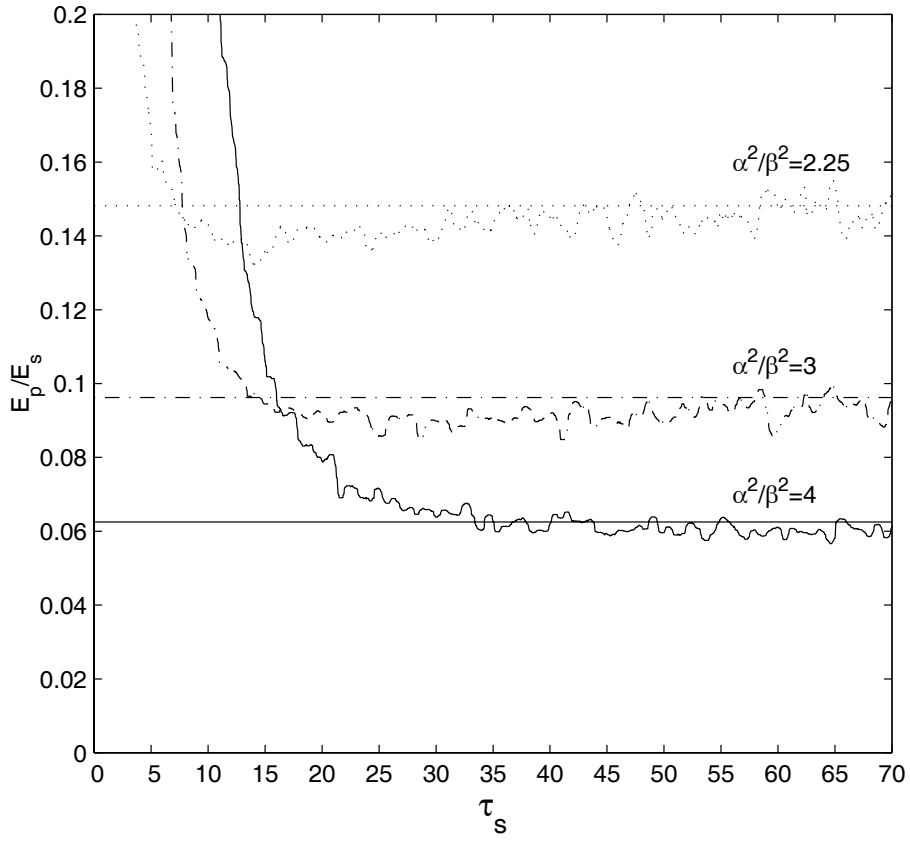

Figure 4.5: P to S energy ratio as a function of time for different values of the ratio of wave speeds α/β. The Monte Carlo solutions exhibit characteristic ripples. The theoretical asymptotic value of the equilibration ratio is also plotted. Time unit is the mean free time of the shear waves.

Table 4.1: Scattering parameters in different regimes

	$\frac{\Sigma_{PP}}{\Sigma_{PS}}$	$\frac{\Sigma_{SS}}{\Sigma_{SP}}$	$\frac{l_P}{l_S}$	$\frac{l_S^\star}{l_S}$	$\frac{l_P^\star}{l_P}$	$\frac{\Sigma_{PP}^\star}{\Sigma_{PP}}$	$\frac{\Sigma_{PS}^\star}{\Sigma_{PS}}$	$\frac{\Sigma_{SS}^\star}{\Sigma_{SS}}$
Rayleigh Regime	0.3	19.6	2.6	0.7	0.8	-0.4	-0.4	-0.3
Rayleigh-Gans Regime								
$k_P a = 1.2$	0.7	14.1	1.5	1.7	0.9	-0.1	-0.1	0.4
$k_P a = 1.6$	1.2	21.2	1.67	3.1	1.5	0.2	0.5	0.7
$k_P a = 2.0$	1.2	28.4	2.0	4.6	2.5	0.6	0.7	0.8

equipartition in the whole phase space. We stress that the ratio of the P to S energy densities calculated with the SSc approximation does not tend to a constant. Therefore, if the equilibration could be observed, the SSc approximation may be discarded as a physical explanation for the coda, leaving the alternative of a coda composed of diffuse waves.

4.7 Comparison of the Rayleigh-Gans and Rayleigh regimes.

4.7.1 Scattering characteristics

In Figures 4.6a-d, we show the polar diagrams of the differential scattering cross-sections for one sphere in the Rayleigh-Gans and Rayleigh regimes. For S-S scattering, we averaged over the azimuthal angle Φ, which corresponds to incident depolarized waves. In the Rayleigh regime, scatterers are taken to be significantly smaller than the wavelength ($k_P a \ll 1$). In this case, most part of the energy is scattered in the backward direction as shown in Figure 4.6 a. In multiple scattering, this feature tends to keep the energy close to the source. A typical consequence of this situation is that the transport mean free paths $l_P^\star$ and $l_S^\star$ are smaller than the scattering ones. We note that the ratio l_P/l_S of the mean free paths is rather large (2.6), which means that scattering is much stronger for S waves than for P waves.

In the Rayleigh-Gans Regime (4.6 b-d), the scatterers are supposed to be of a size that is comparable to the wavelength ($k_P a \sim 1$). As $k_P a$ increases, the angular dependence of the scattering becomes more and more anisotropic, and the P-P and S-S differential cross sections start to exhibit a peak in the forward direction, as also known to occur for acoustic waves [*Chernov,* 1960]. The ratio l_P/l_S varies from 1.5 to 2 but the enhanced forward scattering causes the transport mean free paths to become much larger than the scattering mean free paths. For example, for $k_P a = 2$, we find $l_S^\star \simeq 4.6 l_S$ and $l_P^\star \simeq 2.5 l_P$. Most of the scattered energy is concentrated in a small solid angle in the forward direction and therefore several scatterings are required before the scattered waves loose memory of their initial direction. All the characteristics of the Rayleigh and Rayleigh-Gans scatterers have been summarized in Table 1.

For all values of ka, S-P or P-S conversions are forbidden in the exact forward and backward directions. From this brief description, we conclude that the scattering mechanism heavily depends on the size of the scatterers as compared to the wavelength, and therefore expect different behaviors regarding the shape of the envelopes and the convergence to diffusion and energy equilibration. These topics will be discussed in the next section.

4.7.2 Analysis of the synthetic codas

In Figure 4.7, we present the results of our numerical simulations in the Rayleigh regime. Each Figure is composed of three parts. On top, we show the P (solid lines) and S (dashed lines) energy densities as a function of time. On each horizontal axis, time is expressed in terms of the shear mean free time.

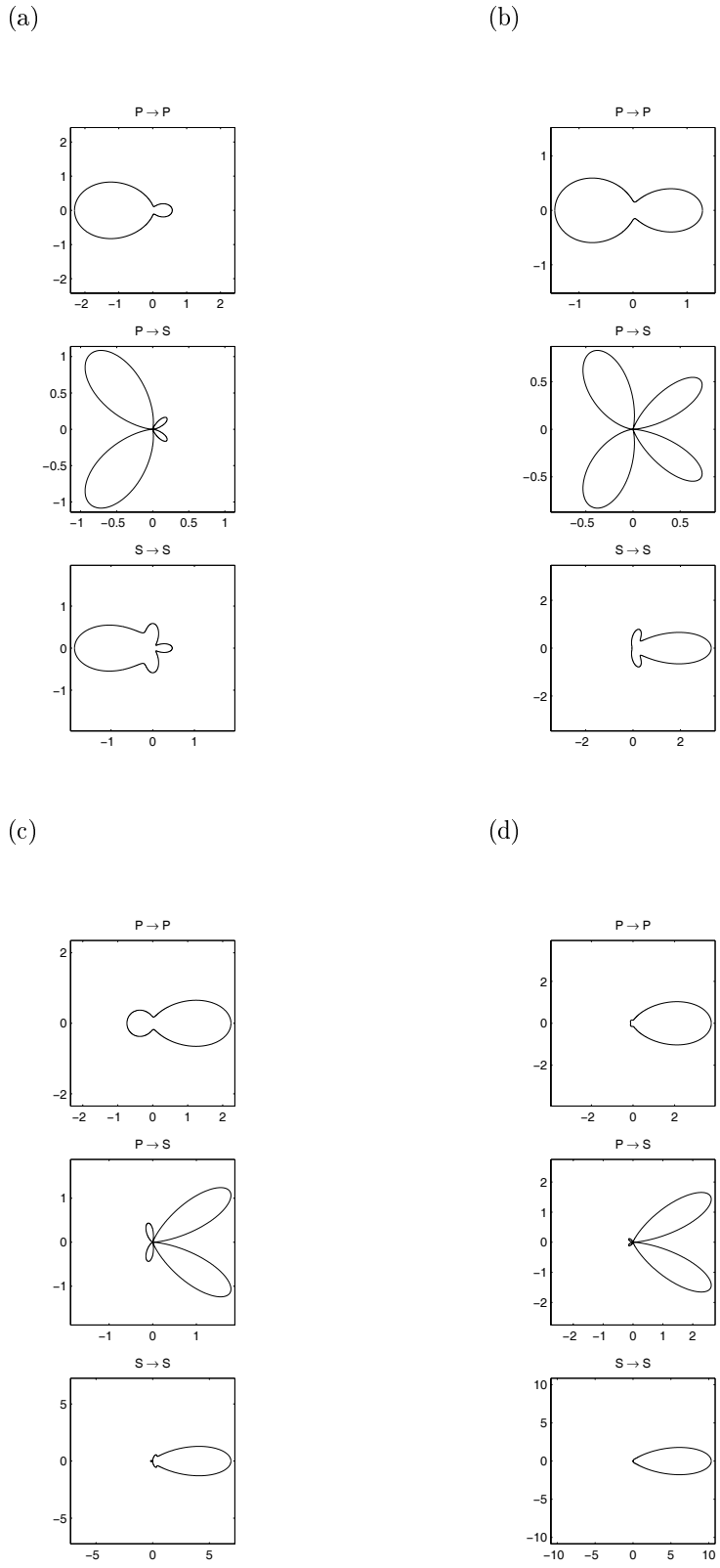

Figure 4.6: Polar plot of the differential scattering cross-sections for the mode conversions P-P, P-S and S-S. (a) Rayleigh Regime $k_P a \ll 1$ (b)Rayleigh-Gans (R-G) Regime $k_P a = 1.2$ (c)R-G $k_P a = 1.6$ (d)R-G $k_P a = 2$

$k_P a \ll 1$

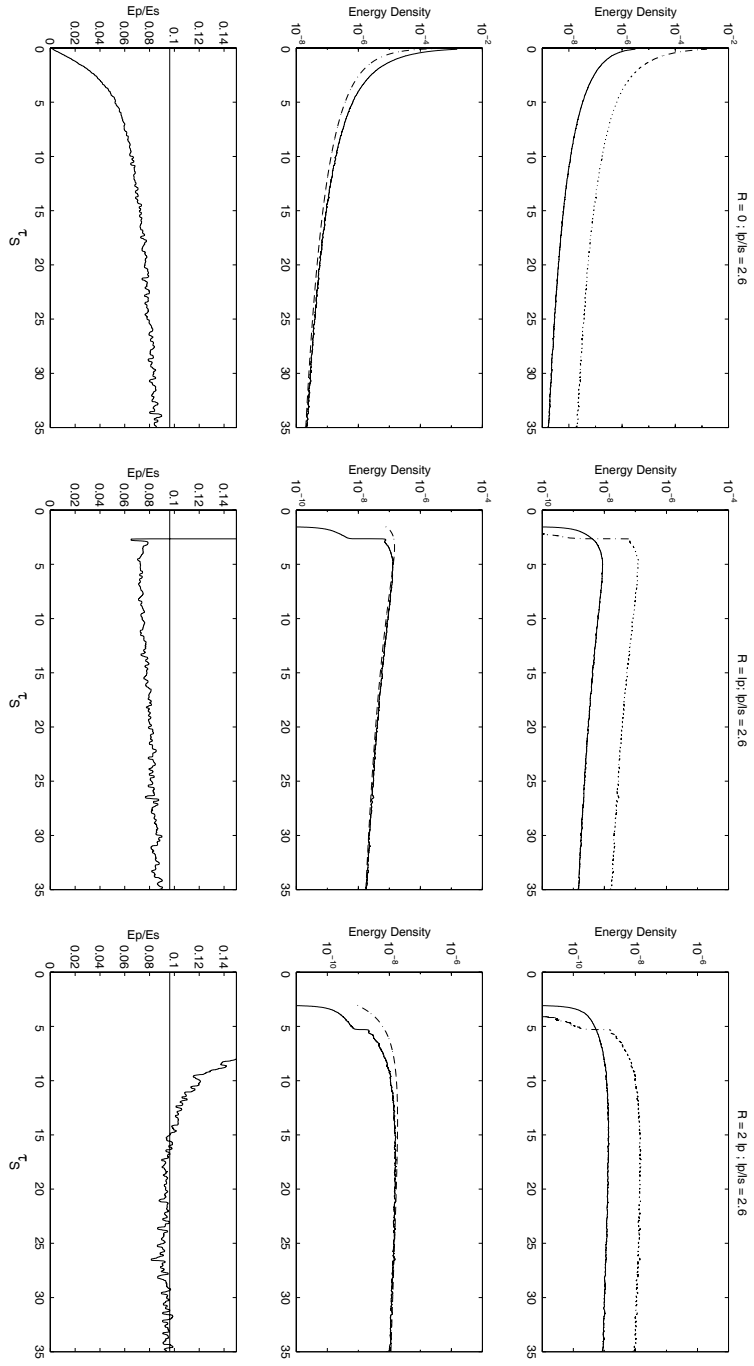

Figure 4.7: Results of the Monte-Carlo simulation for an isotropic and point-like source of S waves in a medium with Rayleigh scatterers. The ratio l_P/l_S and the source-station distance R (in terms of P mean free path) are indicated on top of the figure. Time is indicated on the horizontal axis in term of the S mean free time. Top: Energy density of the S-waves (dashed) and of the P-waves (solid). Middle: Comparison of the total energy density (solid) with the diffusion approximation (dashed). Bottom: Plot of the E_P/E_S ratio. The theoretical asymptotic value is also indicated.

In the middle, the total energy density $E_P + E_S$ is plotted in solid lines and compared to the solution of the diffusion equation in dash-dotted lines. This enables us to discuss the accuracy of the diffusion approximation. At the bottom, the ratio of S to P energy densities is plotted. Note that this part of the Figure has no logarithmic scale, which makes easier the evaluation of the equilibration time. In the Rayleigh regime $k_P a \ll 1$, most of the energy is backscattered (see Figure 4.6 a). Except when source and receivers are close (typically less than one transport mean free path), the synthetic codas are rather smooth, showing a slow evolution of the energy density with time. The smoothness of the curves reflects that in the Rayleigh regime ($k_P a \ll 1$), the angular dependence of the scattering is only slightly anisotropic as compared to the Rayleigh-Gans regime. At a few mean free paths from the source, the maximum of the total energy density occurs after the arrival time of the primary waves. Beyond this maximum, the energy of the coda is almost flat. A similar behavior is observed in the acoustic case for isotropic scatterers [*Margerin et al.,* 1998] and shows the formation of a diffusion front. This is confirmed by the very good agreement between the diffusion approximation and the simulation. We note that for elastic waves, the transport mean free paths can be smaller than the scattering one. This can never be achieved for acoustic waves. In particular, in the Rayleigh regime of acoustic waves, scattering becomes isotropic.

In Figure 4.8, we show the results of our computations for Rayleigh-Gans scatterers with ($k_P a = 1.6$). The energy arrival associated with the forward scattered waves can clearly be identified. Just after this peak, the energy falls by one order of magnitude and then decays slowly, exactly as predicted by the diffusion approximation. The analytical form ($\sim t^{-3/2}$) of the coda in the diffusion regime is very simple. By comparing Figures 4.7 and 4.8 we can observe that the diffusive regime is reached much more rapidly for Rayleigh-Gans scatterers than for Rayleigh scatterers. Several reasons can be invoked to explain this result. As has already been pointed out by *Turner* [1998], a large value of the ratio l_P/l_S tends to delay the diffusion regime. This statement is confirmed by our computations. In spite of the larger P-wave velocity, the shear mean free time is smaller than the compressional one. This means that the time required to achieve isotropy and equipartition for P waves is expected to be larger than for S waves. In addition, we note that for Rayleigh scatterers, P waves are preferentially converted into S waves (see table 1). This means that the P mode is rather unstable which prevents the onset of a rapid equilibration between the P and S energies. This is illustrated by the slow evolution of the ratio E_P/E_S in Figure 4.7, where equipartition is reached after 15 mean free times at least. For Rayleigh-Gans scatterers (Figure 4.8), only five mean free times or less are required. In this case there is a very efficient coupling between the P and S modes.

A remarkable result is the effect of the source station distance R on the equilibration time. In Figure (4.7-4.8), we note that the largest time scale occurs when the source and the receiver are close. This is particularly evident in the Rayleigh case where the onset of equilibration takes no less than 35 mean free times. In Figure 4.7, we see that it takes quite a long time for the total energy density to be described very accurately by the diffusion approximation when $R = 0$. This means that most of the energy leaves the source region before it is diffuse. The part which remains corresponds to the energy which propagates slowly, far behind the diffusion front, and that is not equilibrated. This effect is more pronounced in the Rayleigh case, because of the difference in the P and S scattering mean free paths. As the source station distance increases, the energy that arrives at the receiver rapidly exhibits a diffusive behavior as has been described above. Therefore, the time evolution of the E_P/E_S ratio could be used to discriminate different scattering mechanisms, which are determined by the size of the scatterers compared to the wavelength. Although equipartition can be in some cases quite long to achieve, we find that the solution of the diffusion equation approximates rather well the full solution. This suggests that the coda could be accurately described in the framework of the diffusion theory, as has already been proposed by *Campillo et al.* [1999]. It is also noticeable that the value of equipartition is completely independent of the scattering mechanism and only depends on the ratio α/β

$k_P a = 1.6$

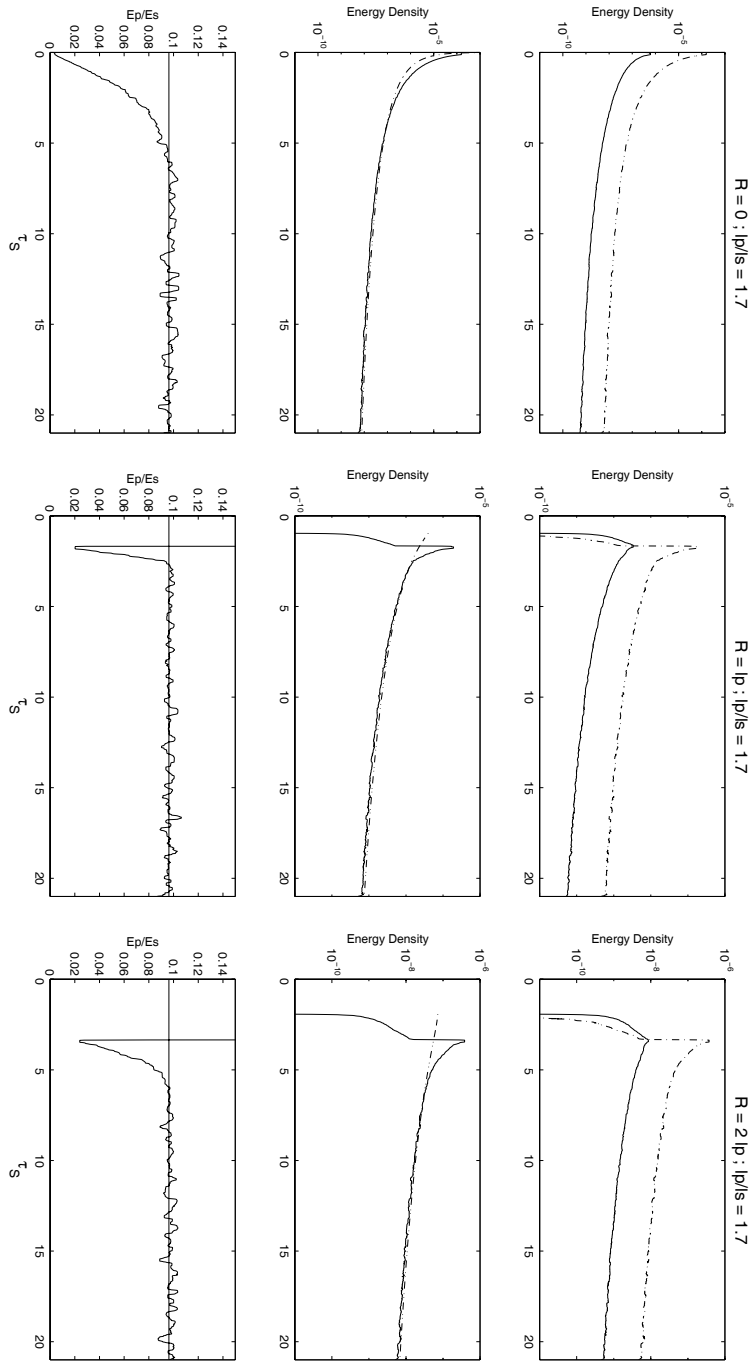

Figure 4.8: Same as figure 4.7 with R-G scatterers ($k_P a = 1.6$)

$k_P a = 1.2$

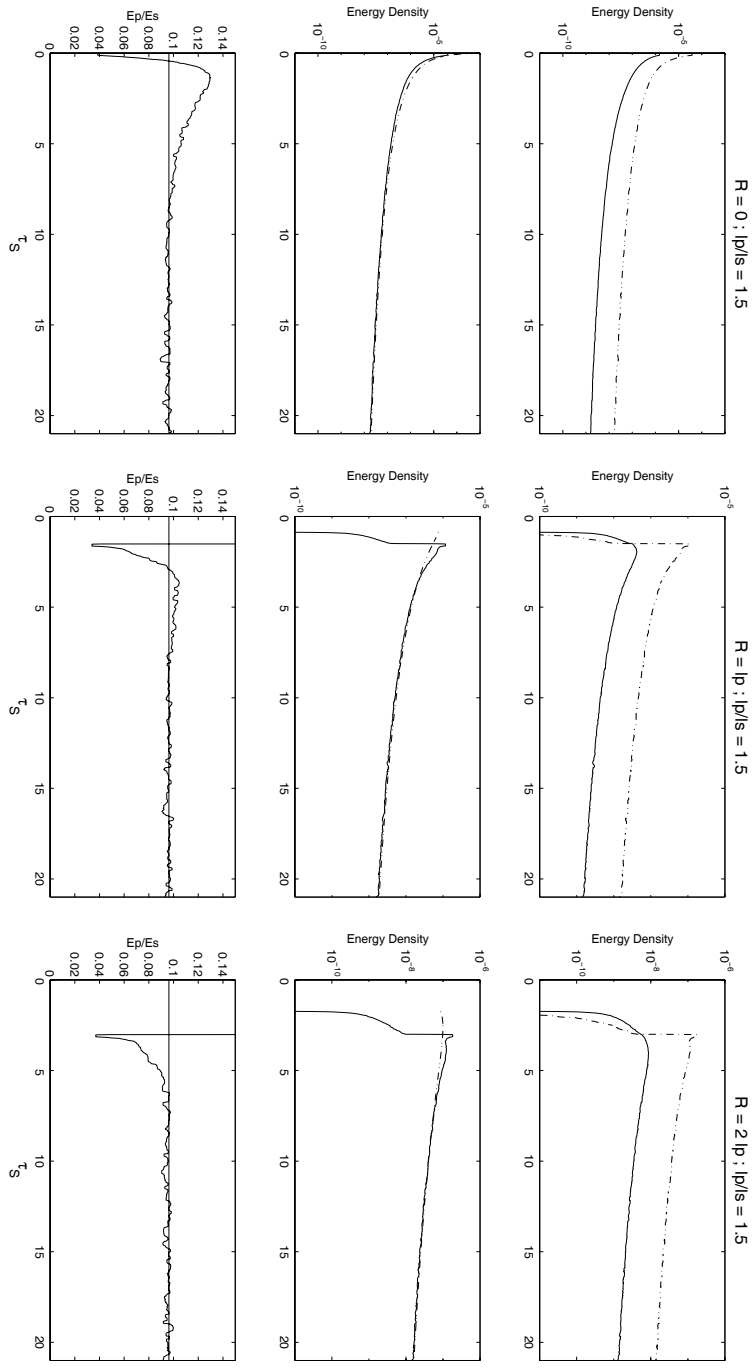

Figure 4.9: Same as Figure 4.7 with $k_P a = 1.2$

$k_P a = 2$

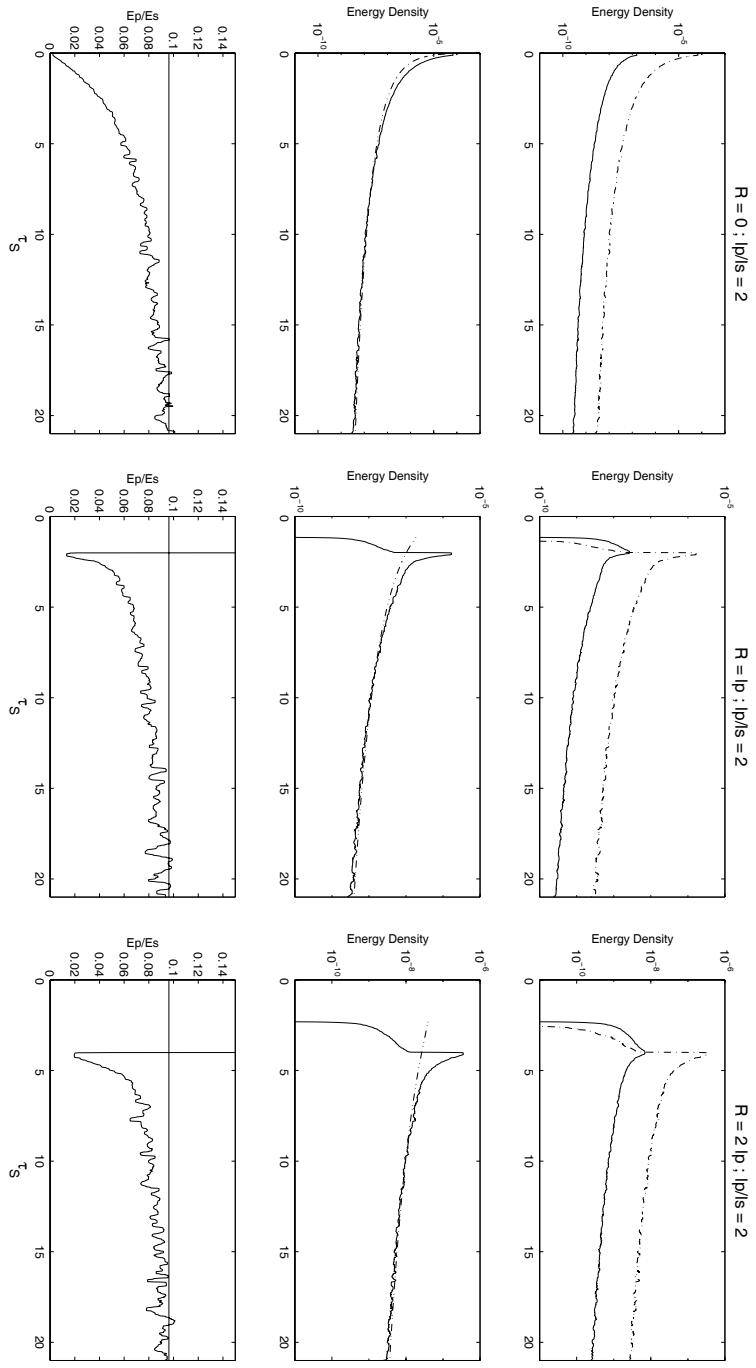

Figure 4.10: Same as Figure 4.7 with $k_P a = 2$

4.8 Diffusion and equilibration

In this section, we discuss the parameters that can affect the equilibration time. In Figures 4.9 and 4.10, we present the results of the Monte Carlo simulations in the Rayleigh-Gans Regime ($k_P a = 1.2$ and $k_P a = 2$) for a source of linearly polarized shear waves. We recall that as $k_P a$ increases the scattering becomes more and more anisotropic and forwardly peaked as illustrated by the polar plots of the differential scattering cross-sections in Figure 4.6. The case $k_P a = 2$ is very similar to $k_P a = 1.6$ except that the equilibration time is largely delayed. This follows from the increase of the ratio l_P/l_S as discussed above, and from the highly anisotropic angular dependence of the scattering. When l_P is much larger than l_S, the P energy can propagate on large distances without being scattered. Moreover, when the angular dependence of the scattering is highly anisotropic, the transport mean free paths are much larger than the scattering mean free paths. Thus, complete isotropy of the field will take a long time to set in.

The case $k_P a = 1.2$ is rather interesting because the scattering is preferentially forward for P waves and backward for S waves. Although the l_P/l_S ratio is smaller (about 1.5) in this case, the equilibration time is somewhat larger than for $k_P a = 1.6$, especially at short offsets. This suggests that the ratio l_P/l_S is not the only parameter that controls the equilibration time. In Figure 4.9, we note that the time variation of the ratio E_P/E_S exhibits an overshoot which disappears as the receiver is moved away from the source. This can be explained by the fact that the P wave energy tends to remain close to the source, while the S wave energy is scattered away. Once again, we note that the study of the E_P/E_S ratio could provide useful information concerning the scattering mechanism in the Earth.

A final comment will be on the effect of the source. In Figure 4.11, we show the results of the numerical simulation for $k_P a = 1.2$ and $k_P a = 1.6$, with an isotropic source of P energy. The situation is now the opposite to the one with an S source. Equipartition is reached more rapidly for $k_P a = 1.2$ than for $k_P a = 1.6$ where the equilibrium between the P and S energies is delayed by a factor of two. This has also been observed for ultrasounds by *Turner and Weaver* [1994c]. To explain the effect of the source, we must consider the higher value of the l_P/l_S ratio for $k_P a = 1.6$ which enables the P energy to propagate on larger length without being significantly scattered. Also in this case, $\Sigma_{PP} > \Sigma_{PS}$ (see table 1) implies that P waves are preferentially scattered into P waves which is unfavorable for the equilibration of the energy. The numerical simulations for P sources in the Rayleigh regime have shown no influence on the equilibration time, because in this case the P energy is almost completely converted into shear energy after a few scatterings.

4.9 Conclusion and Outlook

Our numerical simulations have shown that in the coda, S energy rapidly dominates, independent of the nature of the source and consistent with the equipartition principle. With our choice of scattering parameters, the single-scattering approximation leads to exactly the opposite statement. Another fundamental difference concerns the evolution of the ratio E_P/E_S with time. When multiple scattering is taken into account, the energy density ratio E_P/E_S stabilizes in a universal way, as theoretically predicted by *Weaver* [1990] and *Ryzhik et al.* [1996]. An observation of the time evolution of the E_P/E_S ratio would help to identify the physical process responsible for the formation of the coda. Although the E_P/E_s ratio tends to a constant, the equilibration time heavily depends on the scattering mechanisms. With our choice of model parameters, we find that for Rayleigh scatterers, no less than fifteen mean free times are required to reach equipartion. The main reason for this is the large value of the P mean free path. P energy propagates on rather large distances without having scattered significantly. This conclusion is in agreement with *Turner and Weaver* [1994b,c]. On the other hand, in the Rayleigh-Gans regime, equipartition can be reached very rapidly, within a few mean free times. Although the differential cross-section is more anisotropic in this case, the l_P/l_S ratio is closer to 1, which ensures an efficient coupling between the two modes. As $k_P a$ increases, the scattering becomes more and more anisotropic, which tends to postpone the equilibration. The effect of the source station distance has also been studied. When source and receivers are close, equilibration is also delayed. On the other hand, as the source station distance

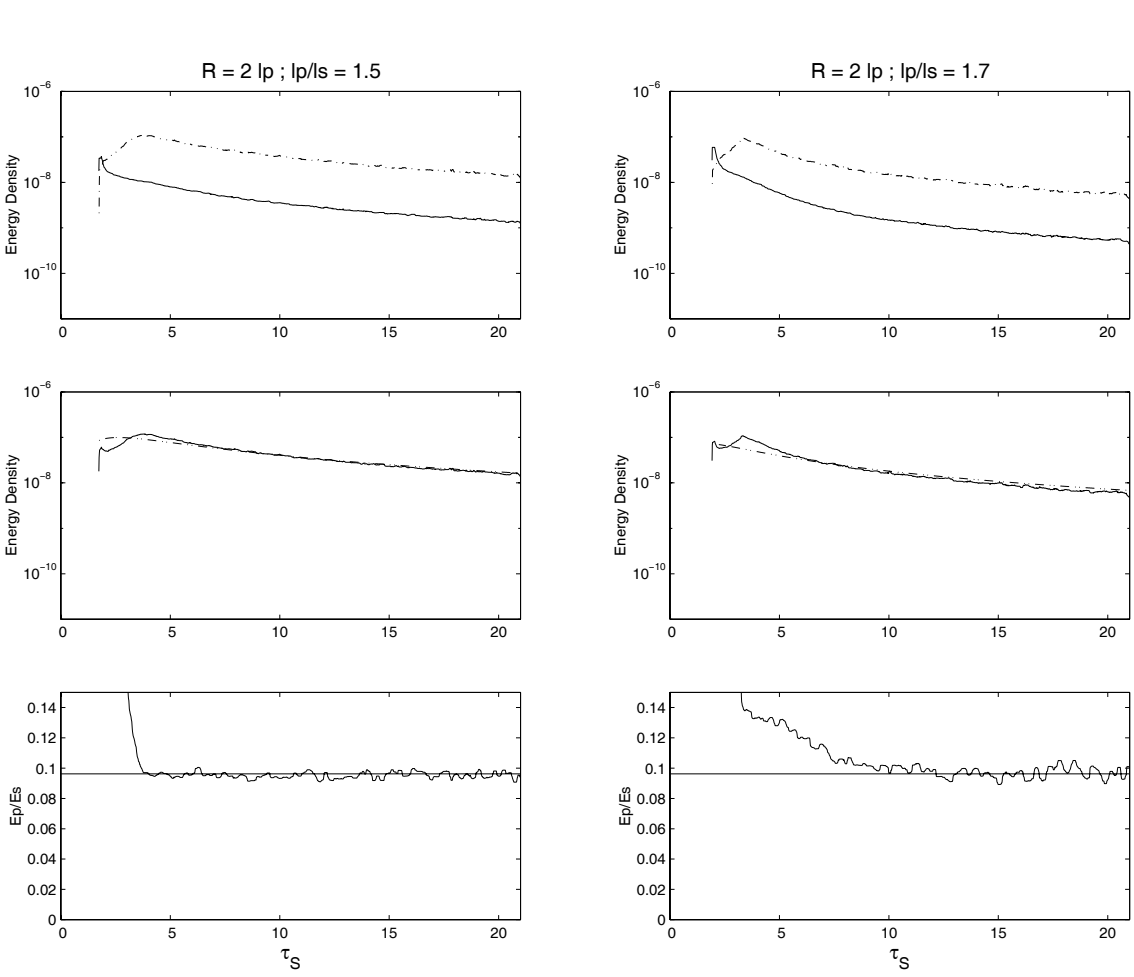

Figure 4.11: Same as 4.7 with a P wave source emitting in a medium with Rayleigh-Gans scatterers.

increases, the field becomes rapidly diffuse after the arrival of the primary waves. Therefore, if the offset amounts a few mean free paths, the equilibration of the P and S modes could be observed. The use of a P source also delays the equilibration time, especially in the Rayleigh-Gans regime, but this effect is weaker than the one of the source station distance. The measurement of the E_P/E_S ratio could be used as a marker of the scattering mechanisms in the Earth.

Additional difficulties have to be overcome to model the propagation of high-frequency waves in the lithosphere. First, we have to take into account the boundary reflections at the free surface and the Moho, which will introduce conversions of the P and S modes. Second, most seismic experiments are set up at the free surface of the Earth. The reflection at the surface introduces deterministic interferences between the incident and reflected waves, which are neglected in the classical theory of radiative transfer. An important task for future studies will be to incorporate the mode conversions and deterministic interference effects.

4.10 Appendix

4.10.1 Rotation of the Stokes parameters.

Let us define a Cartesian reference frame $(\vec{x_0}, \vec{y_0}, \vec{z_0})$. If this frame is rotated an angle ϕ in the positive sense around the z_0 axis, one obtains the new reference frame $(\vec{x}, \vec{y}, \vec{z_0})$. Simple geometrical relations and the application of the definition of the Stokes parameters (4.3) – (4.7) leads to the matrix L given in equation (4.11), that relates original and rotated Stokes vectors.

$$L(\phi) = \begin{pmatrix} 1 & 0 & 0 & 0 & 0 \\ 0 & \cos^2\phi & \sin^2\phi & \frac{1}{2}\sin 2\phi & 0 \\ 0 & \sin^2\phi & \cos^2\phi & -\frac{1}{2}\sin 2\phi & 0 \\ 0 & -\sin 2\phi & \sin 2\phi & \cos 2\phi & \\ 0 & 0 & 0 & 0 & 1 \end{pmatrix} \tag{4.35}$$

4.10.2 The functions f and γ in the Rayleigh-Gans approximation.

Let us introduce the perturbation of the Lamé parameters $\delta\lambda$, $\delta\mu$ and of the density $\delta\rho$ with respect to the homogeneous reference medium; α and β refer respectively to the P-wave and S-wave speeds. It can be shown that the functions f introduced in equation (4.13) describing the angular dependence of the scattered field in the Rayleigh scattering read:

$$f_{PP}(\Theta) = -\frac{\delta\lambda}{\lambda+2\mu} + \frac{\delta\rho}{\rho}\cos\Theta - \frac{2\delta\mu}{\lambda+2\mu}\cos^2\Theta \tag{4.36}$$

$$f_{PS}(\Theta) = (\frac{2\beta}{\alpha})\frac{\delta\mu}{\mu}\sin\Theta\cos\Theta - \frac{\delta\rho}{\rho}\sin\Theta \tag{4.37}$$

$$f_{SP}(\Theta) = \frac{\delta\rho}{\rho}\sin\Theta - (\frac{2\beta}{\alpha})\frac{\delta\mu}{\mu}\sin\Theta\cos\Theta \tag{4.38}$$

$$f_{SS_l}(\Theta) = \frac{\delta\rho}{\rho}\cos\Theta + \frac{\delta\mu}{\mu}(1-2\cos^2\Theta) \tag{4.39}$$

$$f_{SS_r}(\Theta) = -\frac{\delta\rho}{\rho} + \frac{\delta\mu}{\mu}\cos\Theta \tag{4.40}$$

For acoustic waves, Rayleigh scattering would be isotropic. In the Rayleigh-Gans approximation, finite size heterogeneities are considered as Rayleigh scatterers distributed in a volume V. The resulting scattered wave is the superposition of the partial waves produced by each small portion of the scattering volume. The phase difference between these partial waves is taken into account. To describe the angular dependence of the scattered wave, new functions γ are required. If the inclusion is a sphere of radius a

with correlated homogeneous variations of the elastic parameters λ, μ, ρ, one has:

$$\gamma_n(\Theta) = \frac{4\pi a^3}{(\omega S_n a)^2}\left[\frac{\sin \omega S_n a}{\omega S_n a} - \cos \omega S_n a\right] \tag{4.41}$$

$$S_1(\Theta) = \frac{2}{\alpha}\sin\frac{\Theta}{2} \tag{4.42}$$

$$S_2(\Theta) = \sqrt{\left(\frac{1}{\alpha}\right)^2 + \left(\frac{1}{\beta}\right)^2 - \frac{2}{\alpha\beta}\cos\Theta} \tag{4.43}$$

$$S_3 = S_2 \tag{4.44}$$

$$S_4 = \frac{2}{\beta}\sin\frac{\Theta}{2} \tag{4.45}$$

In the acoustic case, the functions γ_1 and S_1 suffice to derive the shape factor.

4.10.3 The Mueller matrix for a spherical scatterer.

Consider a plane wave incident on a scatterer in the direction (θ', ϕ') and scattered into the direction (θ, ϕ), where the directions are given in usual polar coordinates. The angle between both directions will be denoted Θ. The relation between the Scattering matrix F and the Mueller matrix P is:

$$P = L(i_2 - \frac{3\pi}{2})FL(i_1 + \frac{\pi}{2}), \tag{4.46}$$

where L is the rotation matrix given in Appendix A.1 and i_1 and i_2 are defined by the following trigonometric relations:

$$\cos i_1 = \frac{1}{\sqrt{1-\cos^2\Theta}}\left[\cos\theta\sqrt{1-\cos^2\theta'} - \cos\theta'\sqrt{1-\cos^2\theta}\cos(\phi'-\phi)\right] \tag{4.47}$$

$$\sin i_1 = \sqrt{\frac{1-\cos^2\theta}{1-\cos^2\Theta}}\sin(\phi'-\phi) \tag{4.48}$$

$$\cos i_2 = \frac{1}{\sqrt{1-\cos^2\Theta}}\left[\cos\theta'\sqrt{1-\cos^2\theta} - \cos\theta\sqrt{1-\cos^2\theta'}\cos(\phi'-\phi)\right] \tag{4.49}$$

$$\sin i_2 = \sqrt{\frac{1-\cos^2\theta'}{1-\cos^2\Theta}}\sin(\phi'-\phi) \tag{4.50}$$

We recall that:

$$\cos\Theta = \sqrt{1-\cos^2\theta}\sqrt{1-\cos^2\theta'}\cos(\phi-\phi') + \cos(\theta)\cos(\theta')$$

In order to simplify the final expressions, we introduce the following functions:

$$\begin{aligned} F_{PP}(\Theta) &= f_{PP}(\Theta)\gamma_1(\Theta) \\ F_{PS}(\Theta) &= f_{PS}(\Theta)\gamma_2(\Theta) \\ F_{SP}(\Theta) &= f_{SP}(\Theta)\gamma_3(\Theta) \\ F_{SS_l}(\Theta) &= f_{SS_l}(\Theta)\gamma_4(\Theta) \\ F_{SS_r}(\Theta) &= f_{SS_r}(\Theta)\gamma_4(\Theta) \end{aligned}$$

Except for a constant prefactor, the terms P_{ij} where $i, j \in [1, 5]$ of the matrix P read:

$$P_{11} = k_P^4 F_{PP}^2(\Theta) \tag{4.51}$$

$$P_{12} = \frac{\alpha}{\beta}k_P^4 F_{SP}^2(\Theta)\cos^2 i_1 \tag{4.52}$$

$$P_{13} = \frac{\alpha}{\beta} k_P^4 F_{SP}^2(\Theta) \sin^2 i_1 \tag{4.53}$$

$$P_{14} = \frac{\alpha}{2\beta} k_P^4 F_{SP}^2(\Theta) \sin 2i_1 \tag{4.54}$$

$$P_{15} = 0 \tag{4.55}$$

$$P_{21} = \frac{\beta}{\alpha} k_S^4 F_{PS}^2(\Theta) \cos^2 i_2 \tag{4.56}$$

$$P_{22} = k_S^4 r^2 \quad \text{with } r = F_{SS_r}(\Theta) \sin i_1 \sin i_2 - F_{SS_l}(\Theta) \cos i_1 \cos i_2 \tag{4.57}$$

$$P_{23} = k_S^4 s^2 \quad \text{with } s = F_{SS_r}(\Theta) \cos i_1 \sin i_2 + F_{SS_l}(\Theta) \sin i_1 \cos i_2 \tag{4.58}$$

$$P_{24} = -k_S^4 rs \tag{4.59}$$

$$P_{25} = 0 \tag{4.60}$$

$$P_{31} = \frac{\beta}{\alpha} k_S^4 F_{PS}^2(\Theta) \sin^2 i_2 \tag{4.61}$$

$$P_{32} = k_S^4 t^2 \quad \text{with } t = F_{SS_r}(\Theta) \sin i_1 \cos i_2 + F_{SS_l}(\Theta) \cos i_1 \sin i_2 \tag{4.62}$$

$$P_{33} = k_S^4 u^2 \quad \text{with } u = F_{SS_r}(\Theta) \cos i_1 \cos i_2 - F_{SS_l}(\Theta) \sin i_1 \sin i_2 \tag{4.63}$$

$$P_{34} = k_S^4 tv \quad \text{with } v = F_{SS_l}(\Theta) \sin i_1 \sin i_2 - F_{SS_r}(\Theta) \cos i_1 \cos i_2 \tag{4.64}$$

$$P_{35} = 0 \tag{4.65}$$

$$P_{41} = -\frac{\beta}{\alpha} k_S^4 F_{PS}^2(\Theta) \sin 2i_2 \tag{4.66}$$

$$P_{42} = 2k_S^4 rt \tag{4.67}$$

$$P_{43} = 2k_S^4 su \tag{4.68}$$

$$P_{44} = k_S^4 (rv - st) \tag{4.69}$$

$$P_{45} = 0 \tag{4.70}$$

$$P_{51} = 0 \tag{4.71}$$

$$P_{52} = 0 \tag{4.72}$$

$$P_{53} = 0 \tag{4.73}$$

$$P_{54} = 0 \tag{4.74}$$

$$P_{55} = k_S^4 F_{SS_r}(\Theta) F_{SS_l}(\Theta) \tag{4.75}$$

One may check that this matrix has all the symmetry properties discussed by *Sekera* [1966] and *Turner and Weaver* [1994a].

4.10.4 Scattering Cross Sections in the Rayleigh regime.

The scattering cross-section are defined by

$$\Sigma^{MN} = \int_{4\pi} \frac{d\sigma_{MN}}{d\Omega} d\Omega, \tag{4.76}$$

where 4π denotes the whole sphere of space directions and $d\Omega$ is an element of solid angle.

$$\Sigma^{PP} = \frac{V^2 k_P^4}{4\pi} \left[(\frac{\delta\lambda}{\lambda + 2\mu})^2 + \frac{4}{5} (\frac{\delta\mu}{\lambda + 2\mu})^2 + \frac{1}{3} (\frac{\delta\rho}{\rho})^2 + \frac{4}{3} \frac{\delta\lambda \delta\mu}{(\lambda + 2\mu)^2} \right] \tag{4.77}$$

$$\Sigma^{PS} = \frac{V^2 k_S^4 \beta}{2\pi\alpha} \left[\frac{4}{15} (\frac{\beta}{\alpha})^2 (\frac{\delta\mu}{\mu})^2 + \frac{1}{3} (\frac{\delta\rho}{\rho})^2 \right] \tag{4.78}$$

$$\Sigma^{SP} = \frac{V^2 k_P^4 \alpha}{4\pi\beta} \left[\frac{4}{15} (\frac{\beta}{\alpha})^2 (\frac{\delta\mu}{\mu})^2 + \frac{1}{3} (\frac{\delta\rho}{\rho})^2 \right] \tag{4.79}$$

$$\Sigma^{SS} = \frac{V^2 k_S^4}{4\pi} \left[\frac{2}{3} (\frac{\delta\rho}{\rho})^2 + \frac{2}{5} (\frac{\delta\mu}{\mu})^2 \right] \tag{4.80}$$

Acknowldegements.
The authors would like to thank J. Turner, G. Papanicolaou, L. Ryzhik, G. Bal and R. Maynard for helpful disccusions.

4.11 Effet de la surface libre

La simulation numérique que nous avons développée nous permet de mieux appréhender les échelles de temps et d'espace requises pour observer l'équipartition. Pourtant, ces résultats numériques ne peuvent être directement comparés aux résultats expérimentaux. En effet, les sismogrammes sont toujours enregistrés à la surface libre (à quelques exceptions près). Or l'existence des bords introduit des difficultés d'ordre théorique et expérimental que nous allons essayer de détailler.

On peut en premier lieu s'interroger sur la validité de la relation d'équilibre entre les ondes P et S près de la surface, pour deux raisons:

> Le théorème d'équipartition est basé sur le fait que la diffusion est un processus aléatoire qui donne la même probabilité d'occupation à chaque volume de l'espace des phases. Or, en raison de l'anisotropie du coefficient de réflexion, l'équidistribution angulaire de l'intensité est certainement brisée près du bord. Il n'est donc pas possible d'appliquer directement ce théorème près de la surface libre.
>
> L'interaction des ondes incidentes avec un bord donne également lieu à des conversions, échanges d'énergie entre polarisations différentes. Ceci signifie que même si l'équipartition est atteinte loin de la surface, le rapport des énergies P et S peut-être fortement modifié lorsqu'on s'en rapproche.

Un autre point à souligner est que la théorie du transport n'est pas rigoureusement applicable à la surface car elle est précisément le lieu d'interférences entre les ondes incidentes et réflechies. En particulier, comme il existe des relations déterministes entre la phase des ondes incidentes et réflechies, on ne peut plus additioner leurs paramètres de Stokes respectifs. Bien entendu, dès que l'on s'éloigne du bord d'une longueur d'onde, les interférences disparaissent et la théorie de transport est à nouveau applicable.

Dans ce qui suit, nous allons essayer d'apporter quelques réponses aux problèmes que nous venons de soulever. Notre première tâche sera d'écrire les conditions de bord de la théorie du transfert radiatif à la surface libre. Ensuite, nous proposerons une correction de premier ordre à la valeur du rapport des densités d'énergie E_P/E_S au voisinage de la surface libre. Ces résultats seront comparés à des simulations Monte-Carlo dans un demi-espace, où l'on fera toutefois l'hypothèse que les ondes S sont initialement dépolarisées. Enfin, nous proposerons ume méthode possible pour étendre la théorie de transport près des bords.

4.11.1 Réflexion des paramètres de Stokes à la surface libre

Le problème posé est le suivant. Etant donné le vecteur de Stokes des ondes incidentes $S^0(I_P^0, I_{S_V}^0, I_{S_H}^0, U^0, V^0)$, quel est le vecteur de Stokes réfléchi $S^1(I_P^1, I_{S_V}^1, I_{S_H}^1, U^1, V^1)$. Plus précisément, on va chercher à établir une relation du type $S_1 = RS_0$ où R est une matrice de réflexion 5×5. L'expression des paramètres de Stokes, et donc de la matrice de réflexion nécessite le choix une convention. On adopte la même que celle utilisée pour obtenir l'expression de la matrice de Mueller pour une sphère (voir figure 4.12)

Le repère cartésien global (X, Y, Z) est orienté de telle sorte que l'axe Z soit normal à la surface libre. On suppose que le plan d'incidence des ondes est le plan (X, Z). Pour une onde S incidente se propageant dans la direction $\vec{p}$, la polarisation est analysée sur la base orthonormée $(\vec{u}_\theta, \vec{u}_\phi, \vec{p})$. De même, pour l'onde réfléchie se propageant selon $\vec{p'}$, la polarisation est analysée sur la base orthonormée $(\vec{u}_{\theta'}, \vec{u}_\phi, \vec{p'})$. Les coefficients de réflexion pour une onde plane SH,SV,P sont calculés avec les mêmes conventions. On peut trouver l'expression de ces coefficients dans de nombreux ouvrages (Aki et Richards, Ben-Menahem et Singh, Brekhosvkikh).

Pour calculer les coefficients de réflexion des paramètres de Stokes, on doit tenir compte des conversions possibles des ondes d'une part, et des modifications de la polarisation des ondes S d'autre part. En

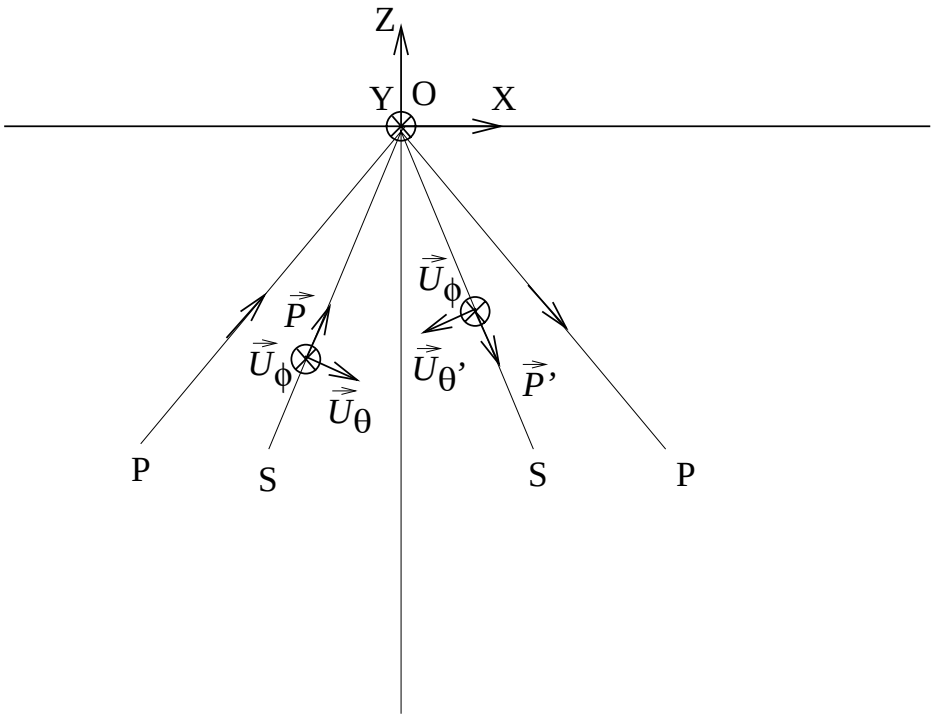

Figure 4.12: Conventions pour l'expression des vecteurs de Stokes incidents et réfléchis. Les conversions possibles sont également indiquées.

effet, supposons qu'une onde S polarisée linéairement arrive sur la surface libre, au delà de l'angle de réflexion critique des ondes SV: l'onde SH est découplée et se réfléchit totalement. L'onde SV subit, en plus de la réflexion totale, un déphasage car le coefficient de réflexion est complexe. Ainsi, une onde initialement polarisée linéairement devient polarisée elliptiquement après réflexion à la surface. D'autre part, l'intensité spécifique est une grandeur définie par unité d'angle solide. Or, en raison du changement de vitesse de propagation et des lois cinématiques de réflexion, les angles solides peuvent être modifiés ce qui est montré schématiquement sur la figure 4.13.

Pour quantifier ces effets, nous rappelons la définition de l'intensité spécifique. Pour les ondes P et SV, on a:

$$I_P = \frac{dE_P}{\cos\theta_P dS d\Omega_P dt} \tag{4.81}$$

$$I_{SV} = \frac{dE_{SV}}{\cos\theta_{SV} dS d\Omega_{SV} dt}. \tag{4.82}$$

θ_P (θ_{SV}) est l'angle d'incidence du faisceau, dS représente l'élément de surface à travers lequel on mesure le flux d'énergie, dt est l'intervalle de temps, et dE_P (dE_{SV}), la quantité d'énergie du mode P (SV). Supposons, qu'on ait un faisceau P incident (voir figure (4.13)). Le rapport des intensités spécifiques s'ecrit:

$$\frac{I_P}{I_{SV}} = \frac{dE_P}{dE_{SV}} * \frac{\cos\theta_{SV} d\Omega_{SV}}{\cos\theta_P d\Omega_P} \tag{4.83}$$

En utilisant les lois de Descartes sous forme différentielle:

$$\frac{\cos\theta_{SV} d\theta_{SV}}{\beta} = \frac{\cos\theta_P d\theta_P}{\alpha} \qquad \text{et } d\phi_{SV} = d\phi_P, \tag{4.84}$$

ainsi que la définition des éléments d'angle solide:

$$d\Omega_{P(SV)} = \sin\theta_{P(SV)} d\theta_{P(SV)} d\phi_P, \tag{4.85}$$

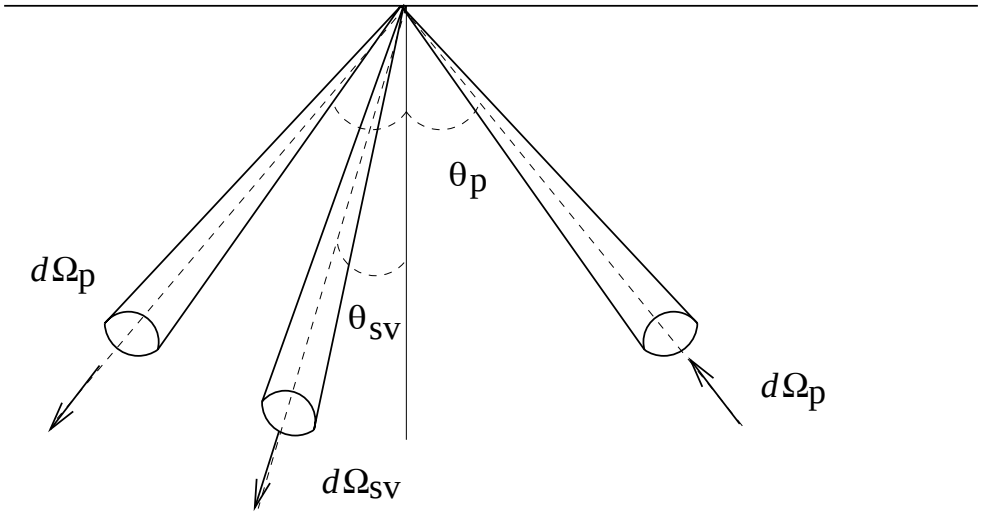

Figure 4.13: Modification de l'angle solide d'un faisceau d'énergie P lors de la réflexion à la surface

On obtient le rapport des intensités spécifiques sous la forme:

$$\frac{I_P}{I_{SV}} = \frac{dE_P}{dE_{SV}} * \left(\frac{\beta}{\alpha}\right)^2 \tag{4.86}$$

On voit donc que le changement d'expansion géométrique du faisceau fait intervenir le rapport des vitesses au carré des ondes P et S. Il reste maintenant à calculer le rapport des énergies. Pour cela, nous allons utiliser la définition du vecteur densité de courant pour des ondes planes:

$$\vec{J} = \frac{\rho v \omega^2 |A_{P(SV)}|^2}{2} \vec{p}, \tag{4.87}$$

où v est la vitesse de propagation de l'onde (α ou β) et $A_{P(SV)}$ désigne l'amplitude de l'onde P (resp. SV). On obtient pour le rapport des énergies:

$$\frac{dE_P}{dE_{SV}} = \frac{\rho\alpha\omega^2 |A_P|^2 dS dt \cos\theta_P}{\rho\beta\omega^2 |A_{SV}|^2 dS dt \cos\theta_{SV}} \tag{4.88}$$

qui se simplifie en:

$$\frac{dE_P}{dE_{SV}} = \frac{\sin 2\theta_P}{|R^2_{P-SV}| \sin 2\theta_{SV}}, \tag{4.89}$$

où l'on a introduit le coefficient de réflexion (en déplacements) R_{P-SV} à la surface libre. Si l'on note R^E_{P-SV} le coefficient de réflexion pour l'énergie $|R_{P-SV}|^2 \frac{\sin 2\theta_{SV}}{\sin 2\theta_P}$, on obtient l'expression de I_{SV} en fonction de I_P:

$$\frac{I_{SV}}{I_P} = R^I_{P-SV} \text{ avec} \tag{4.90}$$

$$R^I_{P-SV} = \frac{\alpha^2}{\beta^2} R^E_{P-SV} \tag{4.91}$$

De la même manière, on établit le coefficient de réflexion pour une conversion d'intensité spécifique SV-P:

$$R^I_{SV-P} = \frac{\beta^2}{\alpha^2} R^E_{SV-P} \tag{4.92}$$

Les réflexions de type P-P, SV-SV, et SH-SH, ne posent pas de difficultés et on obtient:

$$R^I_{PP} = R^E_{PP} \quad (4.93)$$
$$R^I_{SV} = R^E_{SV} \quad (4.94)$$
$$R^I_{SH} = R^E_{SH}. \quad (4.95)$$

Les $R^E\star$ désignent les coefficients de réflexion en énergie, qui sont égaux au module carré des coefficients en déplacement. Il faut noter que dans le cas d'angles d'incidences post-critiques, des ondes se propageant le long de la surface sont générées. Dans le cas d'une onde plane, on peut montrer que l'onde évanescente se propageant le long de l'interface ne transporte pas d'énergie (Aki et Richards, Ben-Menahem et Singh). Dans le cadre de la théorie du transport, nous négligerons l'existence des ondes d'interface. Nous allons maintenant calculer les coefficients de réflexion pour les paramètres U et V déterminant l'état de polarisation des ondes S. Par définition, on a pour une onde S plane :

$$U^0 = \langle \frac{\rho\omega^2\beta}{2} 2\Re(A_{SV}A^\star_{SH})\rangle \quad (4.96)$$
$$V^0 = \langle \frac{\rho\omega^2\beta}{2} 2\Im(A_{SV}A^\star_{SH})\rangle. \quad (4.97)$$

A_{SV} et A_{SH} désignent l'amplitude des composantes SV et SH de l'onde S incidente, et le symbole $X^\star$ représente le complexe conjugué de X. Les brackets $\langle\rangle$ indiquent que l'on s'intéresse à la valeur moyenne. Il faut noter que l'amplitude des ondes incidentes peut comporter une partie imaginaire qui tient compte du déphasage entre les deux composantes. Pour l'onde S réfléchie, les paramètres de Stokes s'écrivent:

$$U^1 = \langle \frac{\rho\omega^2\beta}{2} 2\Re(R_{SV}A_{SV}R^\star_{SH}A^\star_{SH})\rangle \quad (4.98)$$
$$V^1 = \langle \frac{\rho\omega^2\beta}{2} 2\Im(R_{SV}A_{SV}R^\star_{SH}A^\star_{SH})\rangle. \quad (4.99)$$

On a introduit les coefficients de réflexion en déplacement R_{SV} et R_{SH}. Les paramètres de Stokes U^1 et V^1 réfléchis s'expriment donc en fonction des paramètres incidents de la façon suivante:

$$U^1 = R_{UU}U^0 + R_{VU}V^0 \quad (4.100)$$
$$V^1 = R_{UV}U^0 + R_{VV}V^0 \quad (4.101)$$

avec

$$R_{UU} = R_{VV} = \Re(R_{SV}R^\star_{SH}) \quad (4.102)$$
$$R_{UV} = -R_{VU} = \Im(R_{SV}R^\star_{SH}) \quad (4.103)$$

Nous avons donc établi la matrice réflexion pour les paramètres de Stokes:

$$R = \begin{pmatrix} R^I_{PP} & R^I_{SV-P} & 0 & 0 & 0 \\ R^I_{P-SV} & R^I_{SV-SV} & 0 & 0 & 0 \\ 0 & 0 & 1 & 0 & 0 \\ 0 & 0 & 0 & R_{UU} & R_{VU} \\ 0 & 0 & 0 & R_{VU} & R_{VV} \end{pmatrix} \quad (4.104)$$

Nous allons utiliser ces résultats pour essayer de prédire une valeur approchée du rapport d'énergie $\frac{E_P}{E_S}$ à la surface libre.

4.11.2 Bilan d'énergie à la surface libre

Nous pouvons raisonnablement supposer qu'à un libre parcours moyen de transport de la surface libre en profondeur, le rapport d'énergie $\frac{E_S}{E_P}$ atteint celui prévu dans le milieu infini. En effet, dans le cas

d'un milieu inhomogène fini de volume $V \sim L^3$, l'approximation de diffusion n'est applicable que lorsque $L > l^\star$, où $l^\star$ est le libre parcours moyen de transport. D'autre part, on peut également supposer que le champ d'intensité est faiblement anisotrope à une profondeur plus grande que $l^\star$.

Pour faire le bilan d'énergie, nous allons maintenant écrire que la densité d'énergie P (S) près de la surface libre est la somme de trois termes:

un terme d'énergie P (S) incidente depuis la profondeur atteignant directement le détecteur,

un terme d'énergie P (S) atteignant le détecteur après réflexion à la surface,

un terme d'énergie P (S) correspondant à la conversion d'onde S (P)

De plus nous allons supposer que le rapport des énergies incidentes est le rapport théorique dans le milieu infini, que l'anisotropie de la distribution angulaire d'énergie peut-être négligée et que les ondes S sont dépolarisées. Ceci revient à supposer que la diffusion multiple dans le volume domine sur l'effet des conversions à la surface. On rappelle que la densité d'énergie est liée à l'intensité spécifique par la relation:

$$E = \frac{1}{v} \int_{4\pi} I(\vec{\Omega}) d\Omega, \tag{4.105}$$

où l'intégrale est prise sur l'angle solide. Par conséquent le rapport des densités d'énergie à la surface s'écrit:

$$\frac{E_S}{E_P} = \frac{\alpha \int_0^{\pi/2} \sin\theta d\theta \left[I_S^{inc}(\theta) + (R^I_{SV} I^{inc}_{SV})(\theta) + R^I_{SH} I^{inc}_{SH}(\theta) + (R^I_{P-SV} I^{inc}_P)(\theta) \right]}{\beta \int_0^{\pi/2} \sin d\theta \left[I_P^{inc}(\theta) + (R^I_{PP} I^{inc}_P(\theta)) + (R^I_{SV-P} I^{inc}_{SV})(\theta) \right]} \tag{4.106}$$

En raison de la symétrie du problème l'intégrale sur ϕ disparaît. Nous allons maintenant utiliser nos hypothèses pour simplifier cette expression:

Ondes S dépolarisées : $I^{inc}_{SV} = I^{inc}_{SH}$

Le champ incident est quasi isotrope : $I^{inc}_P \simeq \frac{\alpha E^{inc}_P}{4\pi} + \cdots$, et $I^{inc}_S \simeq \frac{\beta E^{inc}_S}{4\pi} + \cdots$,

Le champ incident est à l'équilibre: $\frac{E^{inc}_S}{E^{inc}_P} = 2(\frac{\alpha}{\beta})^3$

Pour simplifier l'équation (4.106), nous allons transformer les termes faisant intervenir des conversions. L'énergie SV provenant de la réflexion d'ondes P s'écrit:

$$\int I^{conv}_{SV}(\theta_{SV}) \sin\theta_{SV} d\theta_{SV} = \frac{\alpha^2}{\beta^2} \int I^{inc}(\theta_P) R^E_{P-SV}(\theta_P \to \theta_{SV}) \sin\theta_{SV} d\theta_{SV}, \tag{4.107}$$

où *conv* indique qu'il s'agit d'énergie S provenant d'une conversion. Or, il existe entre les coefficients de réflexion en énergie la relation de symétrie:

$$R^E_{P-SV}(\theta_P \to \theta_{SV}) = R^E_{SV-P}(\theta_{SV} \to \theta_P) \tag{4.108}$$

La densité d'énergie des ondes S provenant de la conversion P-SV s'écrit donc:

$$\frac{E^{inc}_P \alpha^3}{4\pi\beta^3} \int_0^{\pi/2} R^E_{SV-P}(\theta_{SV} \to \theta_P) \sin\theta_{SV} d\theta_{SV}.$$

En procédant de même manière pour la conversion d'ondes SV en ondes P, puis en mettant en facteur E_S^{inc} au numérateur et E_P^{inc} au dénominateur, on obtient:

$$\frac{E_S}{E_P} = \frac{E_S^{inc}}{E_P^{inc}} \frac{\int_0^{\pi/2} \sin\theta d\theta \left[1 + \frac{1}{2} R_{SH}^E(\theta) + \frac{1}{2}(R_{SV}^E + R_{SV-P}^E)(\theta)\right]}{\int_0^{\pi/2} \sin\theta d\theta \left[1 + R_{PP}^E(\theta) + R_{P-SV}^E)(\theta)\right]} \tag{4.109}$$

On fait maintenant intervenir les relations de conservation de l'énergie:

$$R_{SH}^E = 1, \qquad R_{PP}^E + R_{P-SV}^E = 1 \qquad \text{et} \qquad R_{SV}^E + R_{SV-P}^E = 1 \tag{4.110}$$

On établit finalement:

$$\frac{E_P}{E_S} = \frac{E_P^{inc}}{E_S^{inc}}. \tag{4.111}$$

Ceci signifie, avec nos approximations, que la surface libre ne modifie pas le rapport d'énergie dans le milieu infini. Nous nous sommes basés sur des lois fondamentales telles que la conservation de l'énergie et la symétrie des coefficients de réflexion. La critique la plus évidente sur notre calcul est le fait que la surface libre brise l'isotropie du champ et qu'on ne peut donc pas rigoureusement supposer que l'intensité spécifique est indépendante de l'angle d'incidence. L'étape suivante consiste naturellement à tenir compte de la possible anisotropie du champ, ce que nous avons fait dans le cadre de simulations de type Monte-Carlo.

4.11.3 Simulation Monte-Carlo dans un demi-espace

Dans la partie précédente, nous avons décrit un schéma Monte-Carlo permettant de simuler la diffusion multiple des ondes élastiques. Nous allons maintenant mentionner les modifications à incorporer pour tenir compte de la surface libre. Pour simplifier le problème, nous nous placerons dans le cas d'ondes S dépolarisées, de telle sorte que l'on a toujours: $I_{SV} = I_{SH}$.

Modification de la marche aléatoire. Lors de la construction de la marche aléatoire d'une particule, nous devons tenir compte des conversions et des changements de direction de propagation. Considérons le cas d'une particule de mode S se propageant vers la surface selon le vecteur $\vec{p}$. La distribution de la longueur de pas L est donnée par la loi:

$$\begin{cases} \ln\epsilon = \frac{L}{l_S} & L < SO \\ \ln\epsilon = \frac{L}{l_S} & L > SO \quad \text{si Réflexion S} \to \text{S} \\ \ln\epsilon = \frac{SO}{l_S} + \frac{L - SO}{l_P} & L > SO \quad \text{si Réflexion S} \to \text{P} \end{cases} \tag{4.112}$$

SO désigne la distance entre la dernière diffusion et la surface libre mesurée selon la direction $\vec{p}$ et ϵ est un nombre équidistribué entre 0 et 1. Ce résultat découle directement du cas acoustique. Il nous faut cependant préciser les probabilités de conversion. Dans le cas d'une onde S incidente, il faut tenir compte du fait que seule la partie SV intéragit avec le mode P. Par conséquent, les probabilités de réflexion S-S et S-P sont données respectivement par:

$$Prob(S \to S) = \frac{1}{2}(1 + R_{SV}^E) \tag{4.113}$$

$$Prob(S \to P) = \frac{1}{2} R_{SV-P}^E \tag{4.114}$$

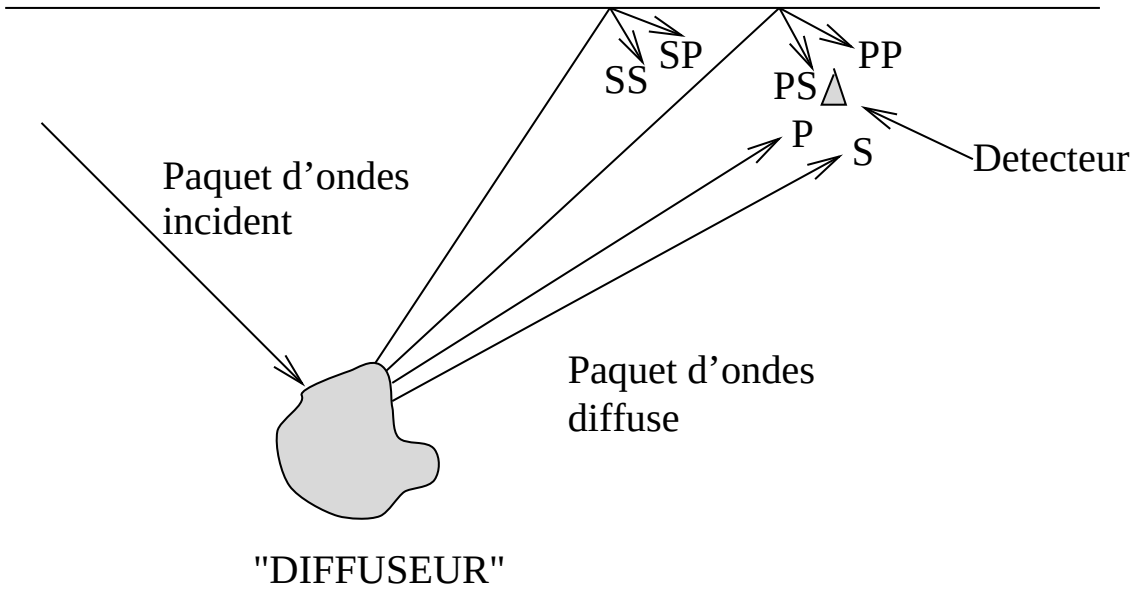

Figure 4.14: Représentation schématique des différentes probabilités pour l'énergie d'atteindre le détecteur.

et on peut vérifier que $Prob(S \to S) + Prob(S \to P) = 1$. De la même manière, on définit les probabilités de conversion pour les ondes P. D'autre part, on tient compte des changements de direction de propagation à la surface en appliquant les lois de Descartes. En pratique, les coefficients de réflexion sont discrétisés en fonction de l'angle d'incidence, et les valeurs sont stockées dans des tableaux. La valeur du coefficient pour un angle d'incidence quelconque est approchée par une interpolation linéaire entre deux valeurs du tableau.

Contribution énergétique. Nous allons maintenant calculer les contributions énergétiques d'une particule à chaque diffusion en termes de probabilité. Les différents chemins de l'énergie entre la dernière diffusion et le détecteur sont représentés schématiquement sur la figure 4.14. Les trajets directs ne posent aucune difficulté et ont déjà été détaillés dans la partie précédente. Pour les conversions, il faut pondérer les probabilités avec les coefficients de réflexion en énergie, mais aussi tenir compte du changement d'expansion géométrique du faisceau d'énergie émis par le diffuseur après réflexion à la surface libre. Ce problème est rigoureusement analogue à celui que nous avons résolu pour les ondes acoustiques dans le cas d'un milieu où la vitesse de propagation dépend de la profondeur. Dans le cas où le détecteur est très proche de la surface libre, on obtient:

$$E_{P\to S} = \frac{\frac{\sigma_{PS}}{\sigma_{PP}+\sigma_{PS}} F_{PS}(\Theta) R^E_{P-SV}(\theta_P) \exp -R/l_P}{\beta dt R^2 \frac{\cos\theta_S V}{\cos\theta_P}} \tag{4.115}$$

$$E_{S\to P} = \frac{\frac{\sigma_{SP}}{\sigma_{SS}+\sigma_{SP}} F_{PS}(\Theta) R^E_{SV-P}(\theta_{SV}) \exp -R/l_S}{\alpha dt R^2 \frac{\cos\theta_P}{\cos\theta_S V}} \tag{4.116}$$

On appelle R la distance dernier diffuseur-détecteur, les fonctions F_{SP} et F_{PS} sont les fonctions de phase normalisées tenant compte de l'anisotropie de la diffusion simple:

$$\int_{4\pi} F_{SP}(\vec{\Omega}) d\Omega = 1$$

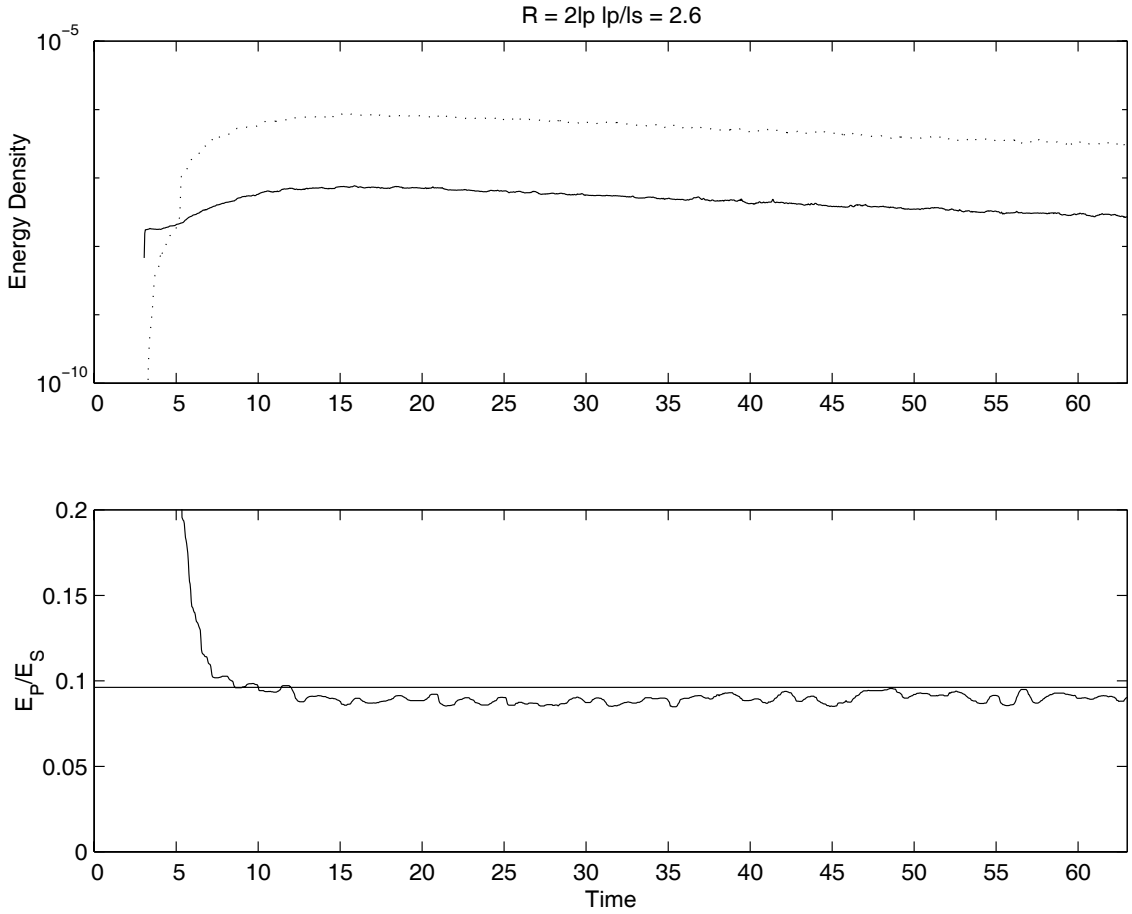

Figure 4.15: Résultat de la simulation Monte-Carlo pour une source d'ondes S et un détecteur situés au voisinage de la surface. La distance source-station R ainsi que le rapport l_P/l_S sont indiqués sur la figure. En abscisse, l'unité de temps est le temps libre moyen des ondes S. En haut, évolution temporelle de la densité d'énergie des ondes P (trait plein) et des ondes S (pointillé). En bas, évolution du rapport des densités d'énergie E_P/E_S. La valeur "théorique" du rapport d'énergie est indiquée.

Θ est l'angle entre les directions des paquets d'ondes incident et diffusé. θ_{SV} et θ_P sont les angles entre la normale à la surface et les directions d'incidence et d'émergence des ondes SV et P. dt est l'intervalle de discrétisation du temps utilisé dans la simulation Monte-Carlo. Les σ_{xy} sont les sections efficaces pour la diffusion simple, les l_P et l_S sont les libres parcours moyens des ondes P et S, grandeurs définies dans la partie précédente. Durant la simuation numérique les différents types de contributions: PP et SS directs, PP et SS réflechis, PS et SP réfléchis seront stockés dans des vecteurs différents. On pourra donc tester directement la validité de la théorie développée plus haut.

Résultats de la simulation. Nous nous plaçons dans le cas du régime de Rayleigh. Une source située juste sous la surface émet de l'énergie S dépolarisée dans le milieu diffusant. Cette source est instantanée, isotrope et ponctuelle (fonction δ pour les variables de temps et d'espace). Le détecteur est placé au voisinage de la surface libre à deux libres parcours moyens P de la source. Sur la figure 4.15, nous représentons l'évolution temporelle de la densité d'énergie des ondes P et S, et de leur rapport. Comme pour le milieu infini, on observe une lente évolution des densités d'énergie en fonction du temps. D'autre part, on observe le maximum d'énergie après l'arrivée des ondes balistiques, ce qui est caractéristique

du comportement diffusif (cf discussion du milieu infini). Après une dizaine de temps libres moyens des ondes S, le rapport des énergies se stabilise autour d'une valeur très proche de celle que nous prédisons théoriquement. Nous pouvons donc conclure qu'il existe bien un phénomène d'équilibration du rapport d'énergie des ondes P et S au voisinage de la surface. Comme nous l'avons dit, ce résultat n'est à-priori pas évident puisqu'en raison de la réflexion, l'isotropie du champ est brisée à la surface et le théorème d'équipartition n'est plus applicable.

Nous allons maintenant comparer les résultats de la simulation avec les prédictions de la théorie. Nous allons procéder de la façon suivante:
Grâce à la simulation, nous avons accès aux valeurs exactes (dans la limite des incertitudes numériques) des densités d'énergie P et S incidentes à la surface, réfléchies et converties. Or, notre calcul de la valeur du rapport E_P/E_S repose sur l'hypothèse que l'on peut négliger l'anisotropie du champ incident (qui existe toujours, y compris dans le milieu infini). Dans ce cas, nous avons montré que si l'on connaît les densités d'énergies *incidentes*, on peut en déduire les densités d'énergie *réfléchies et converties*. Plus précisément, on a vu que l'on déduit les premières des secondes via multiplication par la valeur moyenne des coefficients de réflexion (voir l'équation (4.109)). Nous allons appliquer cette même approximation ici et comparer le résultat avec le calcul numérique. Précisons ceci sur un exemple: Nous calculons dans la simulation la valeur de la densité d'énergie P, E_{PP}, provenant de la réflexion d'énergie P incidente. Nous allons comparer cette valeur avec $\tilde{R}_{PP}E_P^{inc}$, où $\tilde{R}_{PP}$ désigne la moyenne angulaire du coefficient de réflexion et E_P^{inc}, la densité d'énergie P incidente, calculée numériquement. Il faut noter que la comparaison est intéressante car la simulation numérique tient compte de l'anisotropie du champ. Sur la figure 4.16, nous pouvons observer qu'après quelques temps libres moyens, la différence entre les valeurs de densité d'énergie P calculées sans approximation et celles obtenues en supposant l'isotropie du champ est très petite. Par conséquent, la simulation numérique nous apporte la preuve que la surface ne perturbe pas la valeur d'équilibre du milieu infini. Bien sûr, cela ne signifie pas que le champ à la surface est isotrope, mais que l'écart à l'isotropie est suffisamment faible pour être négligé. La figure 4.17 nous amène à la même conclusion. On peut noter en plus que dans le cas de la réflexion SS (dépolarisées), la surface libre se comporte pratiquement comme un miroir parfait. En effet, on peut calculer que le coefficient de réflexion en énergie moyenné sur l'angle solide atteint environ 0.93.

Conclusions et perspectives Dans cette partie, nous avons étudié l'effet de la surface libre dans le cadre de la théorie du transfert radiatif. Nous avons montré qu'en dépit de l'anisotropie du coefficient de réflexion, il existe bien un phénomène d'équilibration du rapport d'énergie E_P/E_S et que la valeur de ce rapport est la même que celle prédite dans le milieu infini. Ainsi, les échanges d'énergie à la surface préservent l'équilibre entre les modes P et S. Il s'agit d'un résultat important puisqu'il montre qu'en régime de diffusion multiple, on doit pouvoir observer un rapport d'énergie constant, y compris lorsque les mesures sont faites à la surface libre.

Nous suggérons maintenant quelques voies de continuation de ce travail sur le plan théorique et expérimental. Il a été proposé par Turner et Weaver (1995) que l'effet des bords était d'accélérer la convergence vers l'équilibre. A ce stade, nos résultats numériques ne permettent pas encore de confirmer leur affirmation. Néanmoins, si l'on compare les résultats des simulations en présence et en l'absence de bords, il apparaît, dans un cas au moins, que l'équilibre d'énergie soit atteint dans un délai inférieur de 1/3 lorsqu'on ajoute un bord. Cette observation doit être confirmée par de nouvelles simulations numériques dans différents régimes de diffusion. L'équilibration des rapports d'énergie des composantes rotationnelles et divergentes du champ de déplacement a pu être observée (voir chapitre suivant). Afin de pouvoir comparer directement les simulations avec la mesure expérimentale, nous devons tenir compte de l'existence des effets d'interférences à la surface libre. Il doit être possible d'incorporer ces effets en faisant intervenir les fonctions de Green du champ moyen entre le dernier diffuseur et le détecteur, exactement comme cela est fait pour le calcul du cône de rétro-diffusion cohérente. Enfin, nous n'avons pas traité rigoureusement la polarisation des ondes S. Néanmoins, de nombreux travaux d'optique (par exemple Van de Hulst) ont montré que les effets de polarisation sont rapidement négligeables en régime de diffusion multiple.

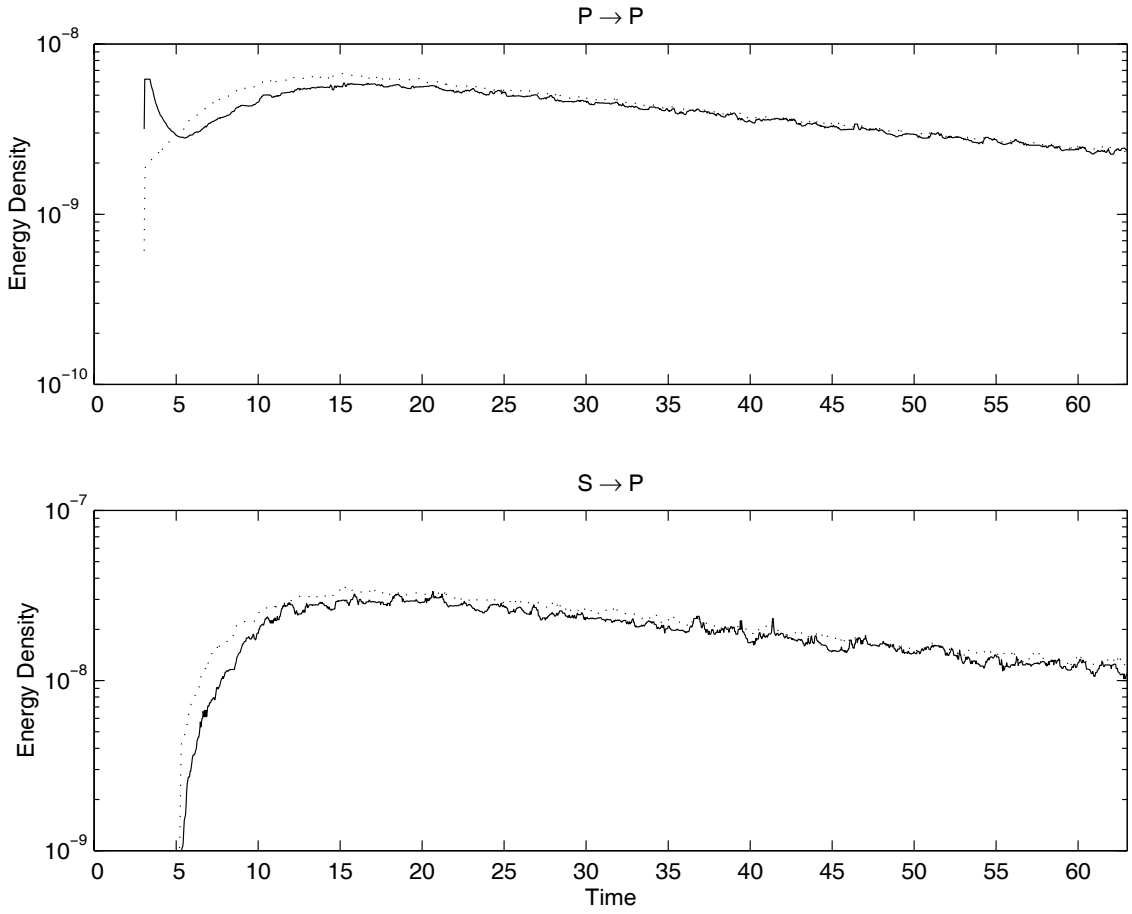

Figure 4.16: Densité d'énergie P correspondant à la réflexion d'ondes P incidentes (en haut), ou d'ondes S incidentes (en bas). La valeur prédite en négligeant l'anisotropie du champ incident est indiquée en pointillé; le trait plein correspond à la valeur obtenue en tenant compte de l'anisotropie.

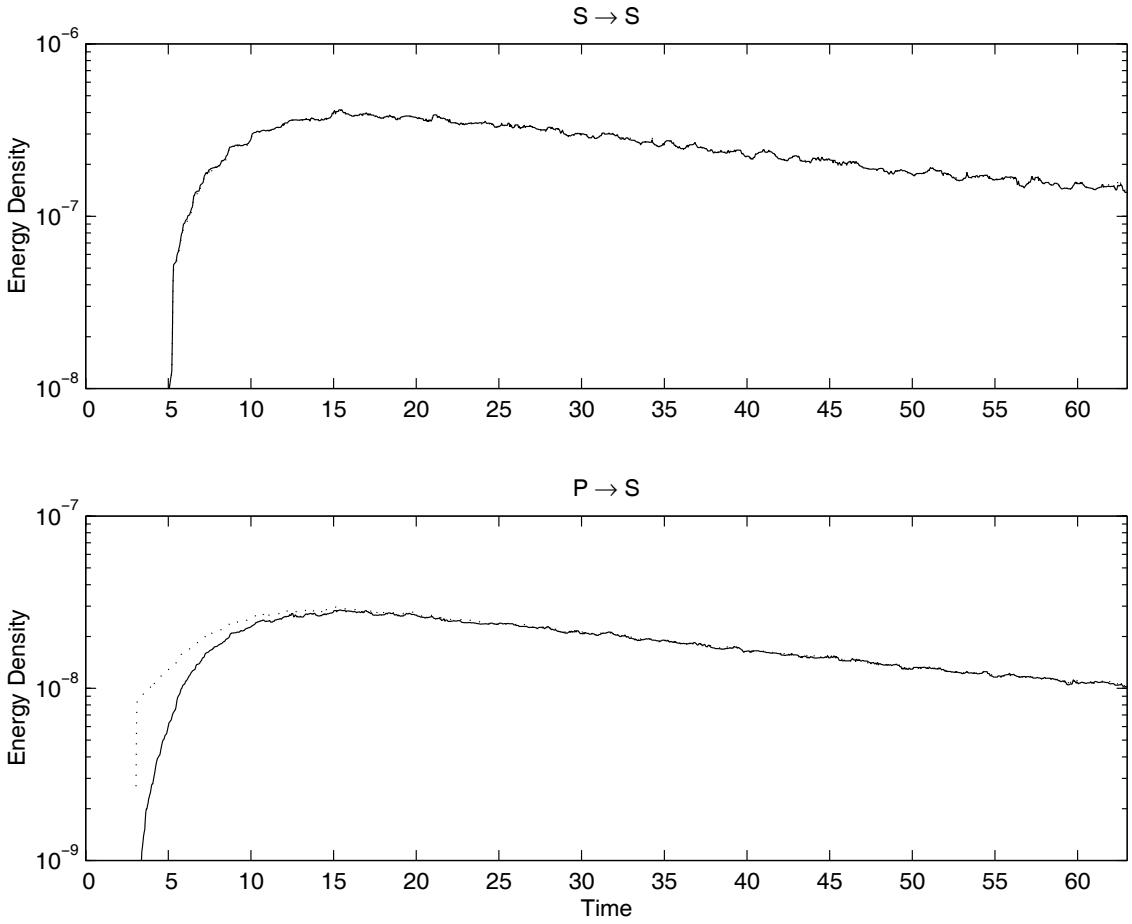

Figure 4.17: Densité d'énergie S correspondant à la réflexion d'ondes S incidentes (en haut), ou d'ondes P incidentes (en bas). La valeur prédite en négligeant l'anisotropie du champ incident est indiquée en pointillé; le trait plein correspond à la valeur obtenue en tenant compte de l'anisotropie.

Références.

Aki, K., 1992. Scattering conversions P to S versus S to P, Bull. Seism. Soc. Am., 82, 1969-1972.

Aki, K. and P.G. Richards, 1980. *Quantitative seismology: Theory and Methods*, W.H. Freeman, San Francisco.

Ben Menahem, A. and S.J. Singh, 1981. *Seismic Waves and Sources*, Springer-Verlag, New-York, 1981.

Brekhovskikh, L.M., 1980. *Waves in layered media*, Academic Press, San Diego.

Campillo, M., L. Margerin, N.M. Shapiro, Seismic wave diffusion in the earth lithosphere, in *Diffuse waves in complex media*, edited by J.P. Fouque, *NATO Advance Series Studies, in press*, 1999.

Chandrasekhar, S., 1960. *Radiative Transfer*, Dover, New-York.

Chernov, L.A., 1960. *Wave propagation in a Random Medium*, Mc Graw-Hill, New-York, 1960.

Collins, D.G., W.G. Blättner, M.B. Wells, H.G. Horak, Backward Monte Carlo calculations of the polarization characteristics of the radiation emerging from spherical-shell atmospheres, *Appl. Opt.* , 11, 2684-2696, 1972.

Dainty, A. M., and M.N. Töksöz, 1990. Array analysis of seismic scattering, Bull. Seism. Soc. Am., 80, 2248-2260.

Einspruch, N.G., E.J. Witterholt and R. Truell, 1960. Scattering of a plane transverse wave by a spherical obstacle in an elastic medium, J. Appl. Phys., 31, 806-818.

Heiderich, A., *Diffusion multiple en milieu non linéaire ou anisotrope*, Ph. D. thesis, Univ. Joseph Fourier, Grenoble, 1995.

Heiderich, A., R. Maynard and B.A. Van Tiggelen, Multiple light scattering in oriented nematic liquid crystals: Monte-Carlo simulations, *Journal de Physique II (France),* 7, 765-792, 1997.

Holliger, K. and A. Levander, A stochastic view of lower crustal fabric based on evidence from the Ivrea zone,*Geophys. Res. Lett.,* 19, 1153-1156, 1992.

Hoshiba, M., 1991. Simulation of multiple scattered coda wave excitation based on the energy conservation law, Physics of the Earth and Planetary Interiors, 67, 123-136.

Hoshiba, M., 1995. Estimation of nonisotropic scattering in western Japan using coda waves envelopes: Application of a multiple nonisotropic scattering model, J. Geophys. Res., 100, 645-657.

Hoshiba, M., 1997. Seismic coda wave envelope in depth dependent S-wave velocity structure, Phys. Earth Planet. Inter., 104, 15-22.

Korneev, V.A. and L.R. Johnson, 1993a. Scattering of elastic waves by a spherical inclusion-I. Theory and numerical results, Geophys. J. Int., 115, 230-250.

Korneev, V.A. and L.R. Johnson, 1993a. Scattering of elastic waves by a spherical inclusion-II. Limitations of asymptotic solutions, Geophys. J. Int., 115, 251-263.

Korneev, V.A. and L.R. Johnson, Scattering of elastic waves by a spherically symmetric inclusion, *Pure Appl. Geophys.*, 147, 675-718, 1996.

Lagendijk, A. and B.A. Van Tiggelen, Resonant multiple scattering of light, *Physics Reports*, 270, 143-215, 1996.

Lux, I. and L. Koblinger, 1991. *Monte Carlo Particle Transport Methods: Neutron and Photon Calculations*, CRC Press, Paris.

Margerin, L., M. Campillo and B. Van Tiggelen, 1998. Radiative transfer and diffusion of waves in a layered medium: new insight into coda Q, Geophys. J. Int., 134, 596-612.

Papanicolaou, G.C., L.V. Ryzhik, and J.B. Keller, 1996a. Stability of the P-to-S energy ratio in the diffusive regime, Bull. Seism. Soc. Am., 86, 1107-1115.

Papanicolaou, G.C., L.V. Ryzhik, and J.B. Keller, 1996b. Stability of the P-to-S energy ratio in the diffusive regime, *Erratum*, Bull. Seism. Soc. Am., 86.

Ryzhik, L.V., G.C. Papanicolaou and J.B. Keller, 1996. Transport equations for elastic and other waves in random media, Wave Motion, 24, 327-370.

Sato, H., 1984. Attenuation of body waves and envelope formation of three-component seismograms of small local earthquakes in randomly inhomogeneous lithosphere, J. Geophys. Res., 89, 1221-1241.

Sato, H., 1994. Multiple isotropic scattering model including P-S conversions for the seismogram envelope formation, Geophys. J. Int., 117, 487-494.

Sato, H. and M. Fehler, *Wave propagation and scattering in the heterogeneous Earth*, Springer-Verlag, New York, 1998.

Sekera, Z., 1966. Scattering matrices and reciprocity relationships for various representations of the state of polarization, J. Opt. Soc. Am., 56, 1732-1740.

Shapiro, S.A. and P. Hubral, 1996. Elastic waves in finely layered sediments: The equivalent medium and generalized O'Doherty-Anstey formulas, Geophysics, 1996, 1282-1300.

Turner J.A. and R.L. Weaver, 1994a. Radiative transfer of ultrasound, J. Acoust. Soc. Am., 3654-3674.

Turner J.A. and R.L. Weaver, 1994b. Radiative transfer and multiple scattering of diffuse ultrasound in polycrystalline media, J. Acoust. Soc. Am., 96, 3675-3683.

Turner J.A. and R.L. Weaver, 1994c. Time dependence of multiply scattered diffuse ultrasound in polycrystalline media, J. Acoust. Soc. Am., 97, 2639-2644.

Turner J.A. and R.L. Weaver, 1995. Ultrasonic radiative transfer in polycrystalline media: Effects of a fluid-solid interface,J. Acoust. Soc. Am., 98, 2801-2808.

Turner J.A., 1998. Scattering and diffusion of seismic waves, Bull. Seism. Soc. Am., 88, 276-283.

Van de Hulst, H.C., 1981. *Light Scattering by Small Particles,* Dover, New-York, 1981.

Weaver, R.L., 1982. On diffuse waves in solid media, J. acoust. Soc. Am., 71, 1608-1609.

Weaver, R.L., 1990. Diffusivity of ultrasound in polycrystals, J. Mech. Phys. Solids, 38, 55-86.

Wu R. and K. Aki, 1985a. Scattering characteristics of elastic waves by an elastic heterogeneity, Geophysics, 50, 582-595.

Wu, R.S. and K. Aki, 1985b. Elastic wave scattering by a random medium and the small-scale inhomogeneities in the lithosphere, J. Geophys. Res., 90, 10261-10273.

Wu, R.S., Z. Xu and X.P. Lie, Heterogeneity spectrum and scale-anisotropy in the upper crust revealed by the German Continental Deep-Drilling (KTB) holes, *Geophys. Res. Lett.*, 21, 911-914, 1994.

Ying, C.F. and R. Truell, 1956. Scattering of a plane longitudinal wave by a spherical obstacle in an isotropically elastic solid, J. Appl. Phys., 27, 1086-1097.

Zeng, Y., 1993. Theory of scattered P-wave and S-wave energy in a random isotropic scattering medium, Bull. Seism. Soc. Am., 83, 1264-1276.

Chapter 5

Synthèse des observations

Seismic wave diffusion in the Earth lithosphere
M. Campillo, L. Margerin, N.M. Shapiro.
Article sous presse dans *NATO Advanced Series Studies, Wave diffusion in complex media,* 1999.

Abstract

This paper is devoted to the study of the time decay of the coda of seismograms. We consider a conceptual model of the Earth upper layers: a diffractive crust overlying an almost homogeneous mantle. We simulate the multiple scattering of the seismic waves using the classical radiative transfer equation in a scalar approximation. We solve the equation using the Monte Carlo method and give a particular attention to the asymptotics of the solution. Under the condition that the ratio mean free path/layer thickness is less than one , we can give an analytical form of the time decay of the coda energy as the solution of a diffusive equation. Otherwise, our transcription of the boundary condition is not valid. The asymptotic form is similar to the one that was proposed by Aki and Chouet (1975) to fit their observations. We checked numerically that, even when the mean free path is larger than the layer thickness, the asymptote of the radiative transfer solution has the same functional form than the one obtained when we are able to compute an analytical solution of the diffusion equation. We show a direct comparison of observations made in Mexico with the results of our model in which we included the effect of a weak absorption. The measurements are well predicted by the model, both for the absolute level of apparent attenuation and for its frequency dependence. We stress the importance of the leakage of diffuse energy in the mantle and propose to define a time of residence of diffuse waves in the crust to characterize the temporal decay of the coda energy. An important aspect of our interpretation is the fact that the coda decay corresponds to the decay of scattered waves in the diffusive regime. To demonstrate the diffuse character of the coda, we look for the energy partitionning that is expected for elastic waves in the diffusive regime. Considering a series of records from earthquakes at different epicentral distances, we show that the equilibration between the two modes (that is the energy partitioning) appears very early in the coda. The ratio between compressional and shear energies is very stable while the energy level changes by several orders of magnitude. The energy ratio is independent of the earthquake considered. This experiment tends to confirm that the seismic coda corresponds to waves in the diffusive regime and therefore supports our interpretation that the decay observed in Mexico at low frequency is strongly governed by the rate of leakage of diffuse energy in the mantle.

5.1 Introduction

The seismograms consist of records of the 3 component motion of the free surface of the Earth during earthquakes. The seismograms begin with a series of arrivals of compressional, shear and surface waves that can be interpreted in terms of the ray theory. The very deep structure of our planet has been explored by using this type of waves. On short period seismograms (in the range 1-10 Hz), after these arrivals the envelope decays slowly to reach the level of seismic noise after a delay that can be currently several tens of times the travel time of direct waves. This long tail is called the seismic coda. The coda consists of waves that are arriving to the receiver from almost all directions (see for example Campillo at al, 1998 for recent references). Applying a frequency-wave number analysis to the data of the NORSAR array, Dainty and Toksoz (1990) have shown that the coda is dominated by waves with apparent velocities less then 4 km/s, that correspond in the Earth crust to the shear elastic waves called S waves in seismology.

In their pioneering work, Aki and Chouet (1975) showed that the time decay of energy in the coda is a regional characteristic, independent of the source depth or magnitude. They measured this constant decay rate after a lapse time that is larger than two times the travel time of direct shear waves. They found that the coda envelope can be fitted by the formula:

$$\rho(f,t) = \frac{S_0(f) g_\pi(f)}{2\pi\beta^2 t^{2\gamma}} \exp\left(-\frac{2\pi f t}{Q_c}\right) , \tag{5.1}$$

where $S_0(f)$ is the shear energy emitted by the source, $g_\pi(f)$ is the backscattering coefficient and β the shear wave velocity. γ is a factor of spreading chosen to be 1 since it is assumed that the coda is made up

of body waves. For large lapse time the decay is governed essentially by the exponential term. Q_c, the "coda quality factor" characterizes the decay rate (through the exponential term) and was introduced by analogy with the classical quality factor associated with absorption.

The parameter Qc (coda Q) has been measured in a large number of regions and the different authors reported essentially the Aki and Chouet conclusions about the stability of the decay rate. Qc appeared to be the easiest amplitude parameter to measure while the peak amplitude or attenuation of direct waves are in most cases very difficult to evaluate in the Earth due to focusing and defocusing effects.

It was found that Qc is increasing with frequency with a rate that is larger when its value is small at low frequency. At high frequency, the values observed are very high almost everywhere while around 1 Hz Q_c exhibits regional variations correlated with the tectonic style.

Aki and Chouet interpreted their result using either the single scattering approximation or the diffusion approximation for scalar waves in a full space. Later, Wu (1985) introduced the stationary radiative transfer equation for scalar waves. Abubikarov and Gusev (1987) and Hoshiba (1991) used the Monte Carlo method to solve the radiative transfer equation for scalar waves in the time domain. In all these studies, a constant background velocity and a homogeneous distribution of scatterers were assumed. The use of this type of model in the interpretation of the observed coda decay rate suggests a strong absorption that would be the dominant process in the apparent attenuation of seismic waves in the crust. On the other hand, the study of the decay of direct waves with distance led to the inverse conclusion (see Campillo and Plantet, 1991): when Qs the quality factor of S waves is small (significantly less than 1000), it has a strong frequency dependence characteristic of the scattering effect on primary waves. The measurements of Qs in tectonically active regions suggest that the scattering effect is dominant over the absorption. This apparent contradiction between these two interpretations can be solved by considering a more realistic model of the Earth structure to interpret the coda decay.

5.2 Radiative transfer in the crust

The major characteristic of the structure of the first tens of kilometers of the solid Earth is the existence of the crust overlying the mantle. The crust and the mantle have very different physical properties and chemical composition. The mantle has a very homogeneous composition with mostly olivine (Mg,Fe)SiO4 while the crust is the result of the differentiation of light elements during the Earth existence. In geologically active provinces, the compositionnal heterogeneity of the crust makes it possible the progressive build up of mechanical heterogeneity during the long history of the deformations associated with the tectonic processes. Besides the mantle has a ductile mechanical behavior while the upper crust is brittle. This results in the development of crack networks in the crust. Experiments of deep reflection seismic soundings in the continental domain provided images of a reflective crust above a transparent mantle (see for example Allmendinger et al., 1987 or Meissner, 1989).

It is therefore reasonable to set up a model in which an upper layer containing numerous scatterers (impedance fluctuations, cracks) overlies a half space that is weakly diffusive. There is another special feature of this structure that cannot be neglected. The wave velocities are significantly higher in the mantle than in the crust (typically $4700m/s$ and $3500m/s$ for S waves). As a consequence, the wavefield produced by a source located in the crust comprises strong guided waves due to post critical reflections on the boundary. This particularity of the Green function has to be incorporated in our treatment of the multiple diffraction. A simple conceptual model that accounts for the specificities of the Earth was studied by Margerin et al. (1998a). The configuration is shown in Fig 5.1. Let us begin with a purely elastic model. Considering the observation that coda waves are mostly S waves, we neglect the compressional P waves and assume that, after a few diffractions the S waves are depolarized. We therefore limit our analysis to a scalar problem. This model may appear too simple but our goal at this stage is to investigate the consequences of the existence of the layering. After a series of numerical studies using Monte Carlo simulation, it was shown that the energy decay in such a model varies with time according to the regime of diffraction.

We present in Fig 5.2 an example of the results for a configuration in which the crustal thickness

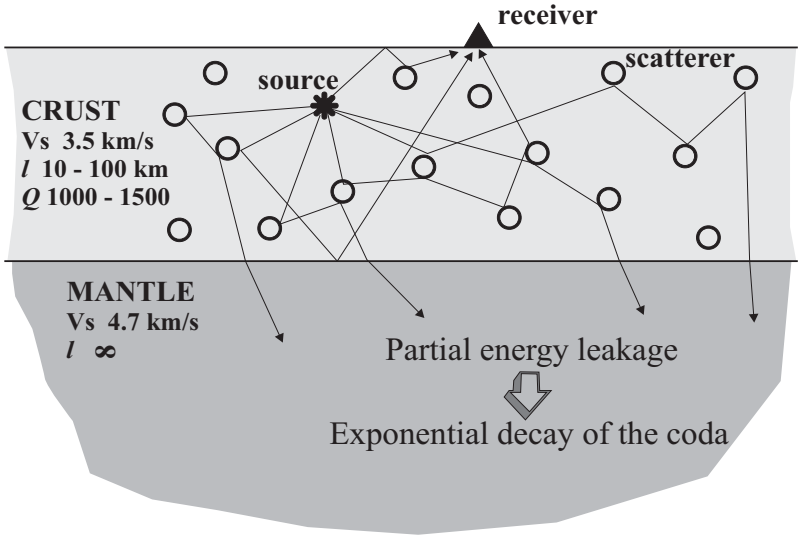

Figure 5.1: Sketch of our simplified model with the physical parameters used in the computations.

is assumed to be 30 km while the mean free path in the crust is 50 km. For very short lapse time, the solution is asymptotic to the single scattering solution. Nevertheless, the divergence of the two curves is almost instantaneous, demonstrating the importance of multiple scattering and the extreme limitation of the single scattering approximation in this problem. Rapidly, the solution of the radiative transfer equation becomes asymptotic to a curve which has the expression proposed by Aki and Chouet from their data analysis. We fit the curve using equation (5.1) with Qc being the free parameter. This result indicates that the simple purely elastic model we propose is able to reproduce this very strong property of the observation, that is the existence of an exponential decay term. Margerin et al. (1998a,b) showed that the fonctional form of the decay is identical for a broad range of mean free path and crustal thickness.

We interpret this exponential behavior as the consequence of the leakage of the diffuse energy from the crust to the mantle. This leakage is nevertheless governed by the reflection coefficient at the base of the crust. In the following we shall use the diffusion approximation to understand this behavior and to give a formal interpretation of Q_c.

5.3 Diffusion equation and asymptotics

The asymptote of the energy envelope of the multiply scattered waves is given, for large lapse times, by the solution of the diffusion equation. Although this is a general statement, the manner of writing the diffusion equation with its initial conditions is far to be obvious. Margerin et al. (1998a) studied explicitely a particular case where the mean free path is smaller than the crustal thickness ($l < H$). The source is assumed to be at the surface. In this case, one can assume that the wavefield is almost diffusive when it reaches the base of the crust. It is therefore possible to write directly a boundary condition for diffuse waves and to solve the diffusion equation analytically. It was checked that, under the condition $l < H$, the agreement between the solution of the diffusion and radiative transfer equations is perfect for large lapse times. The complete solution corresponding to the conceptual model presented above is:

$$\rho(r,t) = \frac{\exp(-\frac{r^2}{4D_1 t})}{2\pi H D_1 t} \sum_n \frac{\sin\xi_n + \frac{t_n\gamma}{H}\cos\xi_n}{(1+\frac{\gamma}{H})\sin\xi_n + \frac{t_n\gamma}{H}\cos\xi_n} \exp(-D_1\frac{\xi_n^2}{H^2}t) \tag{5.2}$$

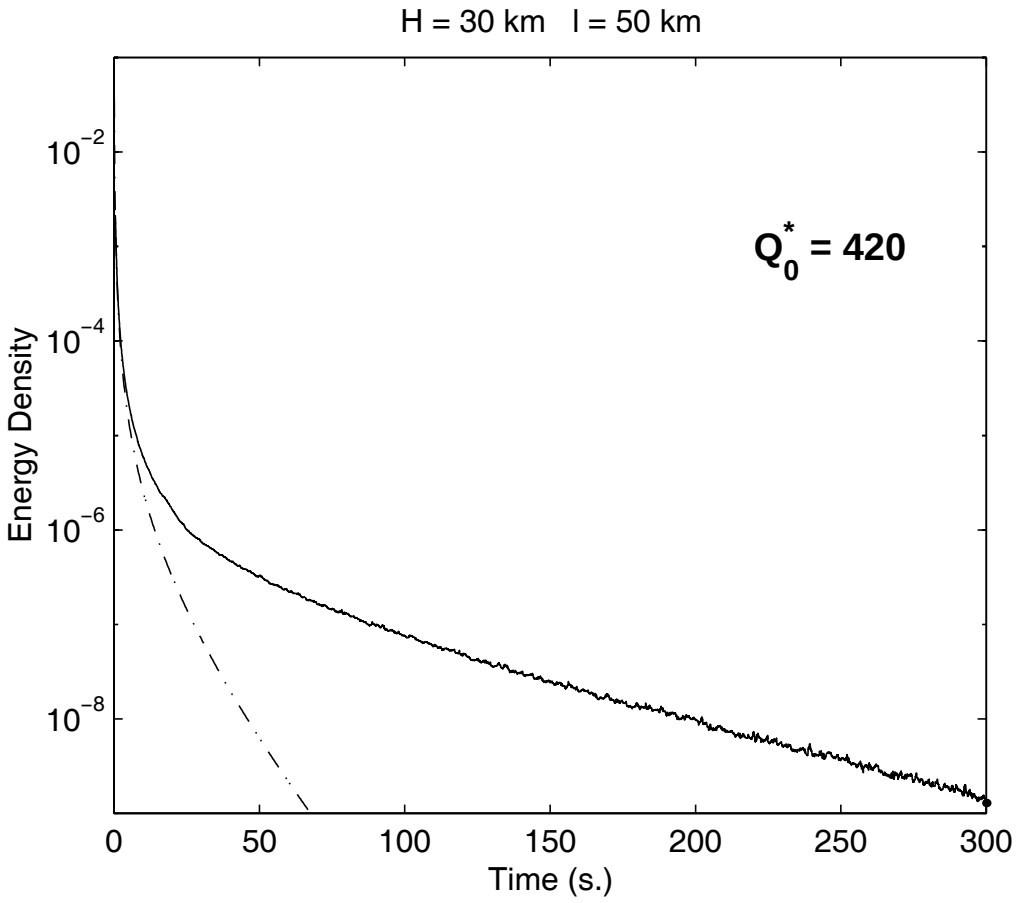

Figure 5.2: Coda decay obtained in our model with $H = 30$ km and the mean free path of the crust l equal to 50 km. Solid lines show the numerical solution of the Radiative Transfer Equation obtained by Monte Carlo modeling. The thin dotted lines shows the result of the single scattering approximation. The black circles indicate an approximation of the radiative transfer solution obtained with the formula $\frac{1}{t}\exp(-\frac{2\pi t}{Q_0^*})$. The $Q_0^\star$ value corresponding to the best approximation is 420. The maximum standard deviation of the $Q_0^\star$ is $\Delta Q_0^\star \approx 30$.

where ρ is the energy density in the coda, t, the time elapsed since the energy release at the source, f, the frequency of waves. The ξ_n are the roots of the equation :

$$\xi_n \tan \xi_n = \frac{H}{\gamma}, \qquad \xi_n \in]n\pi, n\pi + \frac{\pi}{2}[\qquad n \in N. \tag{5.3}$$

In this expression γ is a variable that depends on the differential cross section of the scatterer in the crust, their density and the reflection coefficient at the boundary (Margerin et al, 1998a).

For a configuration where the source and the receiver are close, the leading term of the solution has the form:

$$\rho(t) = \frac{1}{t} \exp(-\frac{t}{\tau_d}) \tag{5.4}$$

and

$$\tau_d = \frac{Q_c^\star}{2\pi f} \simeq \frac{3H^2}{vl\xi^2}, \tag{5.5}$$

where ξ is the root of the equation :

$$\xi \tan \xi = \frac{H}{\gamma}, \qquad \xi \in \left]0, \frac{\pi}{2}\right[. \tag{5.6}$$

$Q_c^\star$ is a parameter that describes the decay rate of the coda in our model. We denote by $Q_0^\star$ the value of $Q_c^\star$ at the frequency $f = 1$ Hz. We maintain in the notation the analogy with the classical quality factor because of the wide practice of this parametrization in experimental seismology. It allows to compare directly the output of our model with the measurements made on actual records. However, the use of τ_d, the time of residence of diffuse energy in the crust would be more appropriate to characterize the leakage effect. Whatever the parametrization chosen, the important result is the fact that the solution of the diffusion equation in a model without absorption gives a functional decay identical to the one that has been observed by Aki and Chouet and widely confirmed later on. The solution of the diffusion equation makes it possible to give an explicit expression of $Q_c^\star$ or τ_d in terms of the physical parameters of the model, again under the condition $l < H$. We are not able to write down a similar problem of diffusion when $l > H$. In this case the field that reaches initially the boundary is not diffusive and therefore we cannot incorporate simply the boundary conditions in our model. Nevertheless, the numerical simulation of the radiative transfer equation for different ratios l/H indicates that the same functional form of the asymptotic decay is expected when $l < H$ or $l > H$ (Margerin et al., 1998b).

5.4 Comparison with observations

In the previous sections we studied a simple conceptual model in which we assume no absorption. Indeed two effects can govern the actual decay of the coda of the seismograms. One is the leakage that we just discussed and another is the anelastic absorption which can be represented by the quality factor Q_i. In order to test the relative importance of these effects, we present a comparison between the decays observed at a series of seismic stations and the results of our simulations using realistic values for the parameters of the model. The stations are located along the Pacific Coast of Mexico, a region which is tectonically active.

We use the records at the seismological stations PNIG, HUIG, CAIG and ZIIG of the Mexican Seismological National Network (see Singh et al., 1997). We consider the records of N earthquakes which occured at epicentral distances between 30 and 150 km. At each station, the decay at a given frequency f is parametrized through the measure of $Q_c(f)$ in the way proposed by Aki and Chouet (1975) (equation 1). The results are shown in Fig 5.3.

Between 1 and 5 Hz, they exhibit a strong frequency dependence as expected from our model. In the region where these data are collected, the crustal thickness is between 20 and 30 km (Kostoglodov et al., 1996). The mean free path is not objectively determined. Therefore, we consider values of l between 20

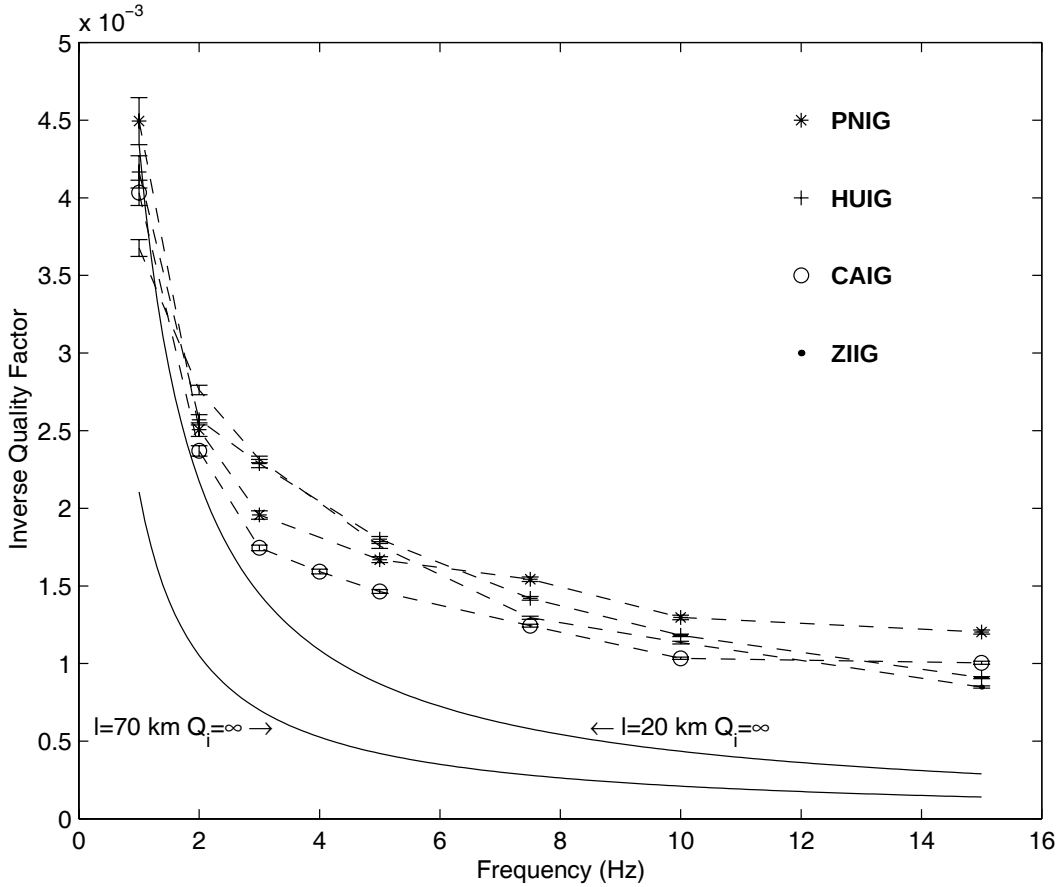

Figure 5.3: The symbols correspond to Q_c as a function of frequency measured at the different stations. The continuous lines correspon d to the solution of the radiative transfer equation in a purely elastic medium for the extreme values of mean free path 20 km and 70 km.

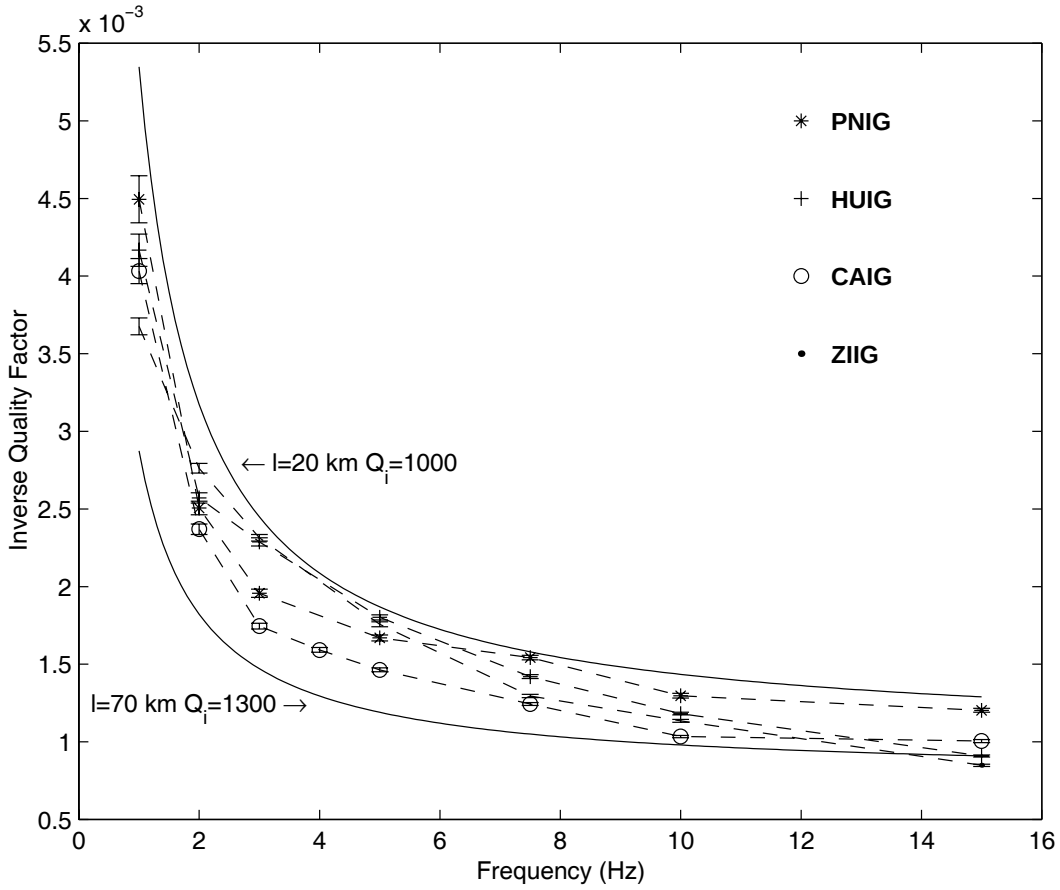

Figure 5.4: A comparison of the measured values of Q_c with the ones deduced from our model including a weak intrinsic absorption.

and 70 km, a range that covers the values proposed for the Earth crust in the frequency range considered here.

The results of the numerical simulations in absence of absorption are plotted in continuous lines in Fig 5.3 for the extreme values of l 20 and 70 km. The results obtained at low frequency (1Hz) are close to the observed values, while at high frequency Q_c is widely overestimated by our purely elastic model. We interpret this discrepancy by the effect of anelasticity. According to laboratory studies, the quality factor inherent to dry rocks is independent of frequency (Johnston, 1981). For crustal rocks at depth and the frequency range considered here, it is difficult to evaluate directly a possible frequency dependence of Q_i. In absence of further evidence, we consider the model with the smallest number of free parameters: a constant Q_i. We add to our model a small absorption term described by $Q_i = 1200$. This value corresponds to the high frequency limit of the measured Q_c. This is a reasonable guess since this value is similar to the one measured in geologically stable regions (Singh and Herrmann, 1983, Hasegawa, 1985) where the crust was not affected by tectonic motions since the early stages of the Earth history and is therefore probably very homogeneous. The apparent attenuation of direct waves measured in these regions is a good evaluation of the intrinsic attenuation of rocks that has to be taken into account in the modelling. After adding to our model a weak attenuation term described by $Q_i = 1200$, we compute again the coda decay parameter $Q_c^\star$ for different frequencies and for the extreme values of l of 20 km and 70 km. The results are compared with the measurements in Fig 5.4.

The numerical results are now in agreement with the observations in the complete range of frequency.

This agreement obtained with a very simple model shows that we catch the essential of the physical processes that govern the coda decay in this example: the leakage of diffuse energy in the mantle, that dominates at low frequency and leads to a linear frequency dependence of $Q_c^\star$ and the intrinsic absorption of rocks that dominates the attenuation in the high frequency limit. Indeed such a simple conceptual model is not expected to represent the various aspects of the Earth structure but it illustrates the importance of the leakage, a process that was neglected in previous interpretations of Q_c. This effect has to be considered in tectonically active regions where the scattering in the crust is strong (l of the order of H) while in stable regions, we expect a weak scattering in the crust (l large) and therefore a predominance of the intrinsic attenuation over the leakage effect in the exponential decay of the coda energy.

In the example of the records in Mexico, the conclusion of our analysis is that the decay rate we measure at low frequency is governed by the leakage into the mantle of diffuse waves of the crust. A strong support to this interpretation should be to demonstrate the diffusive character of coda waves. It is difficult to assess explicitely in what regime is the wavefield from conventional measurements. In the case of seismic waves, we can use the properties of the elastic waves. In the following we use an energy balance property of the elastic waves as a marker of the onset of the diffusive regime.

5.5 Partition of P and S energy

The understanding of the regime of the scattering of seismic waves in the Earth is fundamental for their interpretation in terms of the properties of the Earth materials. Most of previous theoretical studies of the seismic coda (including our study of the effect of the layering) used the acoustic approximation and did not consider the different polarizations of the elastic waves and the mode conversions that occur at each scattering event. As a consequence, the experimental studies were essentially concerned with the measurement of the decay rate of the coda envelopes. However, such kind of measurements is insufficient to distinguish unambiguously between the different scattering regimes.

Recently, the elastic radiative transfer equation has been derived (Weaver, 1982, 1990, Ryzhik et al., 1996; Papanicolaou et al., 1996; Turner, 1998). This equation takes into account the wave polarization and the mode conversion between P and S waves in an infinite elastic body. A fundamental property expected from these studies is that, in the diffusion regime, R, the ratio of energy densities of S and P waves, becomes constant:

$$R = \frac{W_s}{W_p} = \frac{2\alpha^3}{\beta^3} \tag{5.7}$$

where α is the P-wave velocity and β is the S-wave velocity. This property can be regarded simply as a complete randomization of the field in the phase space. For a medium with roughly $\alpha/\beta = \sqrt{3}$, which is the case in the lithosphere, this ratio is 10.39. Therefore, the elastic diffusion approximation predicts that the seismic coda is dominated by S waves as it was observed with actual records. A constant ratio between P and S energy densities is not expected for deterministic arrivals for which this ratio depends on the nature of the source and of the path. The measurement of the repartition of the S and P wave energies and its possible equilibration can give a very strong indication on the regime of seismic wave scattering. The problem is that S and P waves cannot be separated using a record of ground displacement at one point. Particularly in the coda, the wavefield consists of numerous simultaneous arrivals from unknown directions, making the separation between P and S waves impossible using standard signal processing techniques.

Shapiro et al. (1998) present a new approach to separate P and S wave energies. This technique is based on the processing of the data from a small-aperture array. It implies the measurements of the spatial derivatives and the calculation of the curl and divergence of the displacement $\vec{u}$. We have:

$$\vec{curl}\,\vec{u} = 0 \tag{5.8}$$

for P waves and

$$div\vec{u} = 0 \tag{5.9}$$

for S waves. We use these fundamental properties to estimate P and S waves energies separately.

Following Aki and Richards (1980) we can write the density of energy associated with the deformation in elastic medium:

$$W = \frac{1}{2}\sigma_{ij}\chi_{ij} \tag{5.10}$$

where χ is the deformation tensor and σ is the stress tensor. In an isotropic medium, the equation (5.10) can be rewritten as:

$$W = (\frac{\lambda}{2} + \mu)(div\vec{u})^2 + \frac{\mu}{2}(\vec{curl}\,\vec{u})^2 + \mu I \tag{5.11}$$

where

$$I = 2(\frac{\partial u_x}{\partial y}\frac{\partial u_y}{\partial x} + \frac{\partial u_x}{\partial z}\frac{\partial u_z}{\partial x} + \frac{\partial u_y}{\partial z}\frac{\partial u_z}{\partial y}) - 2(\frac{\partial u_x}{\partial x}\frac{\partial u_y}{\partial y} + \frac{\partial u_x}{\partial x}\frac{\partial u_z}{\partial z} + \frac{\partial u_y}{\partial y}\frac{\partial u_z}{\partial z}) \tag{5.12}$$

and λ and μ are Lamé constants. In this study we are looking for a property of a diffuse wavefield, i.e. a random and almost isotropic field. We calculate the average energy $\overline{W}$ in a sufficiently large time window. In this case, average of cross-products of a-priory non correlated functions become zero and we obtain:

$$\overline{I} = 0 \tag{5.13}$$

and

$$\overline{W} = \overline{W_P} + \overline{W_S} \tag{5.14}$$

where:

$$\overline{W_P} = \overline{(\frac{\lambda}{2} + \mu)(div\vec{u})^2} \tag{5.15}$$

$$\overline{W_S} = \overline{\frac{\mu}{2}(\vec{curl}\,\vec{u})^2} \tag{5.16}$$

According to the theory (5.7) of the infinite body, if the wavefield is diffusive, the ratio between these two energies is a constant given by the Lamé parameters, whatever the total energy of the field is and for any type of source. For non-random field, this ratio evolves rapidly according to the arrivals of deterministic waves. For deterministic arrivals, the ratio indeed looses its signification since we neglect the interference term I in the evaluation of energy. We will evaluate this ratio with actual data using the equations (5.15) and (5.16). The direct way to do it would be to install seismic receivers in closely located boreholes at different depths relatively far from the earth surface. This would allow to calculate the partial derivatives with respect to the three spatial coordinates, to estimate the curl and the divergence and hence the S and P wave energies. However, installing numerous seismic stations in bore-holes is extremely expensive and the actual boreholes are not deep enough to allow to neglect the effect of the free surface. So far, there is no theoretical result to describe the equilibration at the surface of a half-space. The problem is indeed more difficult than for the infinite body because the free surface implies deterministic reflection and conversion.

At a depth below the surface larger than the transport mean free path, and because of the scatterings, the reflected wavefield is diffuse and therefore presents the same equilibration between the modes as for the infinite medium. The effect of the surface will be confined to a limit layer. At the surface, the effect of reflection and conversion affects the ratio of energies. This effect is independent of the amplitude of the incident diffuse field. Therefore, as long as an equilibration at a constant ratio occurs in the bulk, a form of equilibration is expected at the free surface. The value of the ratio of the energies at the surface can be different from the one in the bulk. Our goal here is to investigate the existence of the equilibration rather than to discuss the value of the ratio.

We set up an experiment to estimate the S-to-P energy ratio and its temporal evolution using only receivers located at the surface.

We installed a temporary small aperture array close to the city of Chilpancingo (the capital of the Guerrero state, Mexico). The high seismicity rate in Mexico made it possible to record rapidly a series of local earthquakes with magnitudes larger than 4. The location of the array is shown in Fig 5.5.

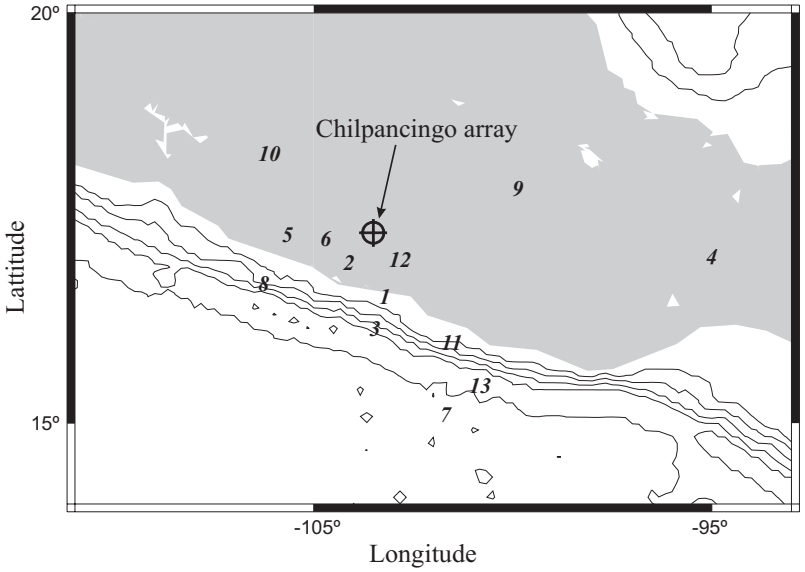

Figure 5.5: Map of Southern Mexico. The crossed circle shows the location of the Chilpancingo array. The italic numbers indicate the epicenters of the events used in this study.

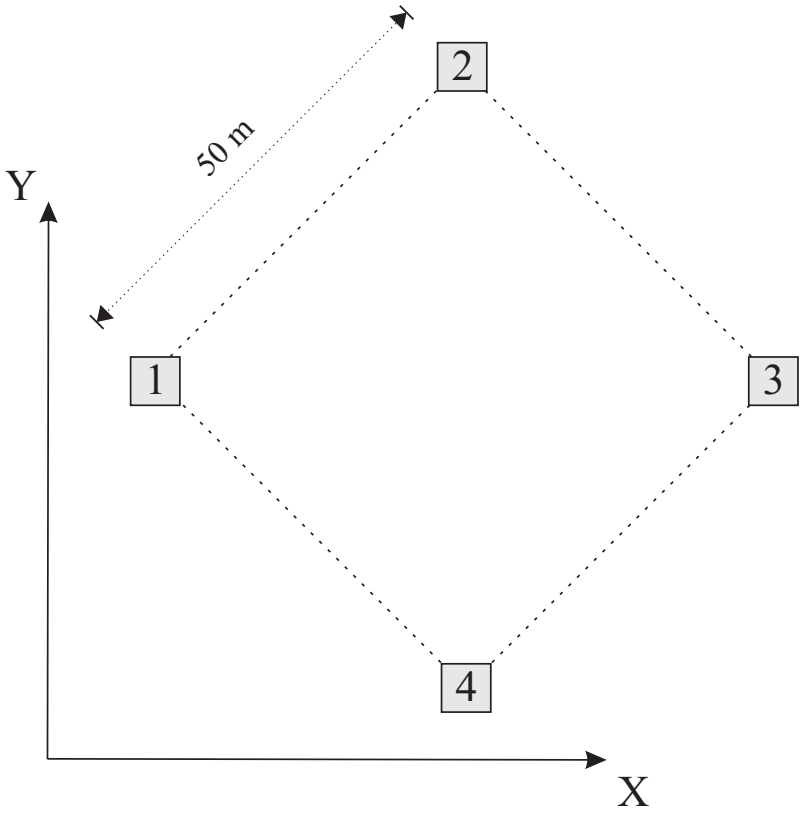

Figure 5.6: Configuration of the Chilpancingo array.

The geometry of the array is a 50 m side square (Fig 5.6). The sensors are CMG-40T seismometers connected to Reftek digitizers. The absolute time was provided by the radio signals of the GPS satellites.

The spatial derivatives of the displacement with respect to horizontal coordinates were estimated by the relations:

$$\frac{\partial u_i}{\partial x} = \frac{u_i^3 - u_i^1}{d} \qquad \frac{\partial u_i}{\partial y} = \frac{u_i^2 - u_i^4}{d} \qquad i = x, y, z \tag{5.17}$$

where u_i^n is the displacement recorded at station n of the array (see Fig 4) and d is the distance between the two stations.

We estimated spatial derivatives of the displacement with respect to the vertical coordinate using the boundary condition at the surface. The free stress condition is:

$$\begin{pmatrix} \sigma_{xx} & \sigma_{xy} & \sigma_{xz} \\ \sigma_{yx} & \sigma_{yy} & \sigma_{yz} \\ \sigma_{zx} & \sigma_{zy} & \sigma_{zz} \end{pmatrix} \begin{pmatrix} 0 \\ 0 \\ 1 \end{pmatrix} = 0 \tag{5.18}$$

In an isotropic medium, it leads to the relations between the derivatives:

$$\begin{cases} \frac{\partial u_y}{\partial z} &= -\frac{\partial u_z}{\partial y} \\ \frac{\partial u_x}{\partial z} &= -\frac{\partial u_z}{\partial x} \\ \frac{\partial u_z}{\partial z} &= -\frac{\lambda}{\lambda + 2\mu}(\frac{\partial u_x}{\partial x} + \frac{\partial u_y}{\partial y}) \end{cases} \tag{5.19}$$

This last equation can be written:

$$\frac{\partial u_z}{\partial z} = (2(\beta/\alpha)^2 - 1)(\frac{\partial u_x}{\partial x} + \frac{\partial u_y}{\partial y}) \tag{5.20}$$

Using equations (5.17), (5.19), and (5.20) we can now estimate the whole set of spatial derivatives of the displacement. We can therefore rewrite equations (5.15) and (5.16) and estimate the ratio of S and P wave energy densities:

$$R = \frac{1}{4}(\frac{\alpha}{\beta})^2 \frac{4\frac{\partial u_z}{\partial x}^2 + 4\frac{\partial u_z}{\partial y}^2 + (\frac{\partial u_x}{\partial y} - \frac{\partial u_y}{\partial x})^2}{(\frac{\partial u_x}{\partial x} + \frac{\partial u_y}{\partial y})^2} \tag{5.21}$$

5.6 Experimental results

During the three months of the experiment we recorded 13 earthquakes located in southern Mexico and with magnitudes large enough to produce a coda with a good signal-to-noise ratio. Event locations are listed in Table 1 and are shown in Fig 5.5.

We selected events not too far away in order to have late arrivals associated with backscattered waves rather than deterministic low velocity guided modes or critical deep reflections. The energy ratio was computed for each record according to equation (5.21). We calculated the average S-to-P energy ratio (R) in a moving window of width 16 s. The results of the processing for two events are shown in Fig 5.7. The two events have different locations. The time window corresponding to the coda with a signal to noise ratio greater than 4 is indicated by grey shading.

The time evolution of the energy ratio shows that the ratio tends to stabilize in the coda. The ratio is widely variable in the noise and at the onset of direct waves. In the coda, in spite of some fluctuations, it is important to note that the ratio varies of about 25% of the mean value for the largest fluctuations while, in the same time, the energy varies by a factor of 10,000. An average value of R for the whole coda window is about 7.5 with a standard deviation of 1. We present in Fig 5.8 the results of essentially the same analysis but limited to the time window corresponding to the arrivals of the body waves.

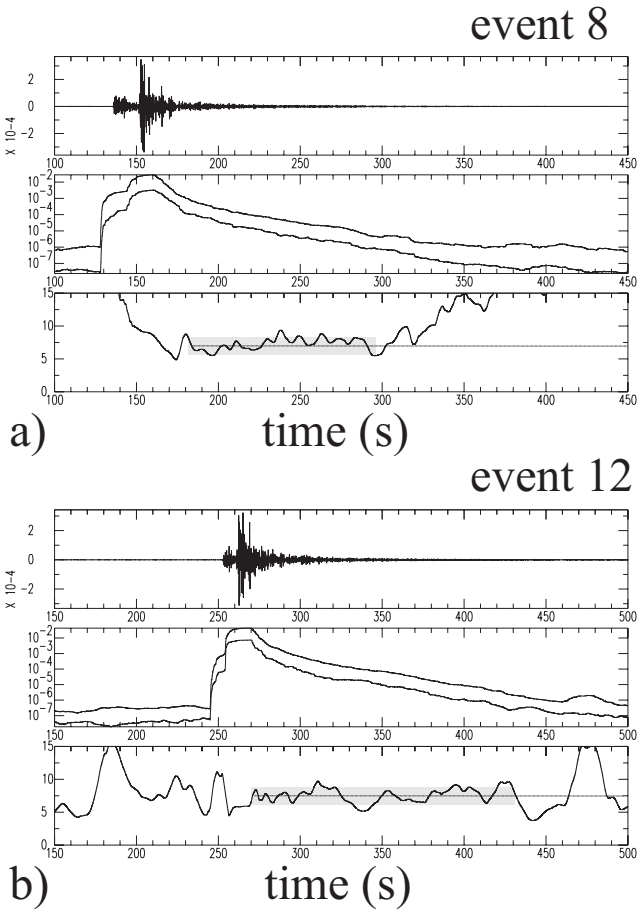

Figure 5.7: Examples of measurements . We selected events with different epicentral distances and backazimuths: a) event 8; b) event 12. For each event, we present the vertical component seismogram band-passed between 1 and 3 Hz (upper part), the P and S energies smoothed in a 16 s moving window (central part) and the S-to-P energy ratio (lower part).

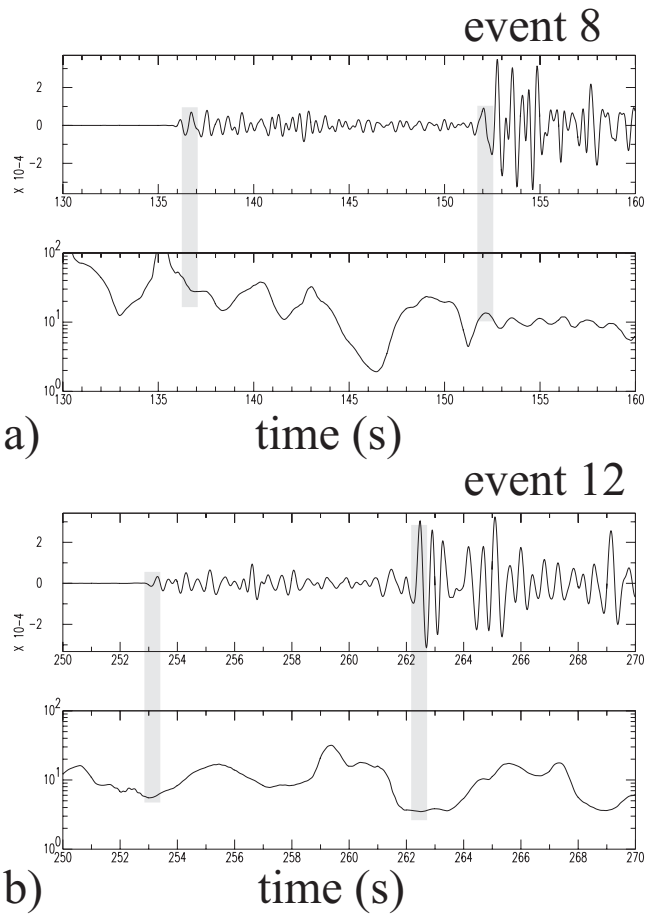

Figure 5.8: Examples of the measurement of the S-to-P energy ratio for direct waves: a) event 8; b) event 12. For each event, we present the vertical component seismogram band-passed between 1 and 3 Hz (upper part), the P and S energies smoothed in a 1 s moving window (central part) and the S-to-P energy ratio (lower part). Note the difference of scale in the plot of the energy ratio with respect to Fig 5.7.

Table 5.1: Parameters of earthquake used in the study. Locations and magnitudes are given by Mexican Seismological Survey.

N	yy:mm:dd	lat	lon	H(km)	M
1	97:06:21	16.47	-99.18	5	4.5
2	97:06:28	16.88	-99.63	7	4.1
3	97:06:29	16.07	-99.30	23	4.4
4	97:06:29	16.96	-95.07	64	4.5
5	97:07:19	17.22	-100.4	56	4.9
6	97:07:21	17.17	-99.92	24	4.5
7	97:07:22	15.02	-98.42	5	5.1
8	97:07:24	16.63	-100.7	16	4.5
9	97:07:28	17.78	-97.51	126	4.0
10	97:07:29	18.21	-100.7	74	4.4
11	97:07:30	15.9	-98.4	?	?
12	97:08:01	16.92	-99.06	35	4.3
13	97:08:03	15.37	-98.05	27	4.7

The grey shading indicates the arrival times of the direct P and S waves. The mean value of the energy ratio R is calculated on 1s intervals. Its evolution is now plotted on a logarithmic scale. The energy ratio shows very rapid and huge variations during the deterministic arrivals. It is expected from the properties of reflection and conversion of body waves at a free surface that the energy ratio has great variations depending upon the angle of incidence and the polarization of the incident wave. The presence of a low velocity layer at the surface provokes strong P to S conversions that can explain the surprisingly high values of R observed at the onset of P waves. We performed the same measurements for the 13 earthquakes. Concerning the coda, we found in every case that the two modes equilibrate very rapidly after the arrival of the direct waves. We extract the values of R for the coda and for the direct P and S waves in order to compare how these measures vary from one event to another. The results of the individual measurements are shown in Fig 5.9. For all events we obtain almost the same R value in the coda: about 7 in average. It means that the S-to-P energy ratio in the coda stabilizes at a values that does not depend on the seismic source nor on the earthquake location. The picture is completely different for direct waves. The ratio is much more variable from an event to the other with mean values which are significantly higher than for the coda.

The stabilization of R in the coda at the same level for all earthquakes is a good indication that the diffusion regime is reached. The theoretical value expected for diffuse waves in an infinite body is given by the equation (5.7). The value which we have observed at the free surface is lower than the one theoretically predicted for the poissonian solid (7 and 10.39, respectively). This difference can be due to the fact that we did not take into account the presence of the reflective surface. Obviously the reflection is a deterministic effect that breaks the isotropy of the diffuse field. This is a fundamental problem that is not yet fully solved as already noticed and we do not know exactly what is the equilibration ratio at the free surface. One can also claim that in a real situation a part of the energy of the P and S waves which are diffuse in the bulk are diffracted into surface waves at the free surface, a process that is not considered in the theory so far. These different arguments show that the important point in our analysis is not the value of the ratio but the equilibration itself which is a marker of the diffusive regime. In this sense, our experiment confirms the results of the analysis of the coda decay for which we found that it follows a law characteristic of the diffusive regime. We need to develop a simulation technique including the proper polarization and coupling effects to give a quantitative interpretation of the value of the ratio and of the short lapse time needed for the waves to equibrate. It is the object of further works. At this present stage, we retain from the results of this experiment that their are in agreement with our

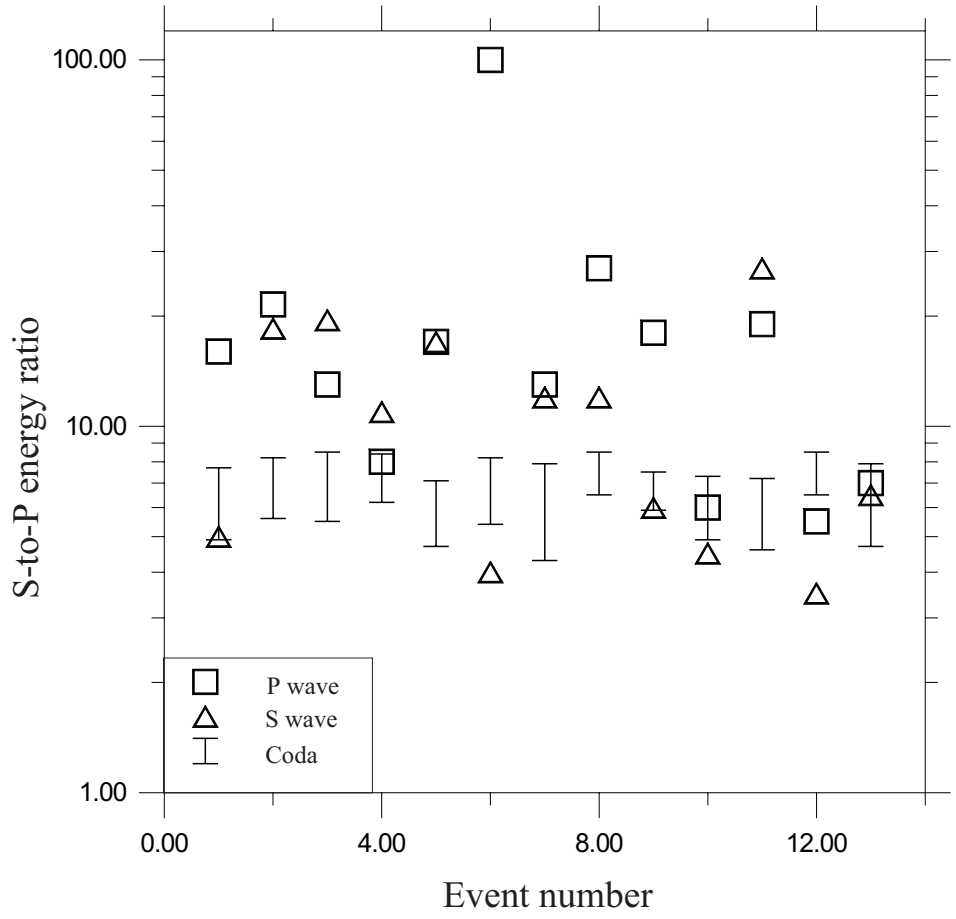

Figure 5.9: S-to-P energy ratios for the 13 events. The squares and the triangles indicate the ratios measured for P and S waves, respectively. Vertical bars show average values plus minus standard deviation of the S-to-P energy ratio measured in the coda window.

conclusion that the decay of the coda energy observed in Mexico is related to the leakage into the mantle of waves which are in the diffusive regime in the crust.

5.7 Conclusion

We studied the time decay of the coda of seismograms. We set up a simplified model of the Earth upper layers: a diffractive crust overlying an almost homogeneous mantle. We used the scalar approximation of the radiative transfer equation to model the multiple scattering of the seismic waves. We solved the equation using the Monte Carlo method. When the ratio mean free path/layer thickness is less than one, we can give an analytical form of the time decay of the coda energy as the solution of a diffusive equation. Otherwise, our transcription of the boundary condition is not valid. The asymptotic form is similar to the one that was proposed by Aki and Chouet (1975) to fit the observations. When the mean free path is larger than the layer thickness, we found numerically that the asymptote of the radiative transfer solution has the same functional form as the one obtained when our diffusion approximation is valid. The decays computed in our model in which we included the effect of a weak absorption are in a very good agreement with the observations. The leakage of diffuse energy into the mantle plays a prominent part at low frequency and controls the frequency dependence of Q_c when, as in our case, the mean free path is of the order of the crustal thickness. We propose to characterize the temporal decay of the coda energy by the time of residence of diffuse waves in the crust. We showed the diffuse character of the coda by looking for the energy partitionning that is expected for elastic waves in the diffusive regime. Considering a series of records from earthquakes at different epicentral distances, we show that the equilibration between the two modes (that is the energy partitioning) appears very early in the coda. The ratio between compressional and shear energies is very stable while the energy level changes by several orders of magnitude. The energy ratio is independent of the earthquake considered. This experiment tends to confirm that the seismic coda corresponds to waves in the diffusive regime and therefore that the decay is strongly governed by the rate of leakage of diffuse energy in the mantle.

We aknowledge financial support from Program "Interieur de la Terre" of INSU/CNRS (France), from the CONACYT project 0974-PT (Mexico) and from the European Union Contract CH*-CT92-0025. We thank B. van Tiggelen, R. Maynard and S.K. Singh for their help and suggestions.

Abubakirov, I.R. and A. A. Gusev, 1990. Estimation of scattering properties of li thosphere of Kamchatka based on Monte-Carlo simulation of record envelope of a n ear earthquake, *Physics of the Earth and Planetary Interior*, **64**, 52 -67.

Aki, K. and B. Chouet, 1975. Origin of coda waves: Source, attenuation, and scattering effects, *J. Geophys. Res.*, **80**, 3322-3342.

Allmendinger, R.W., K.D. Nelson, C.J. Otter, M. Barazangi, L.D. Brown and J.E. Oliver, 1987. Deep seismic reflection characteristics of the continental crust, *Geology*, **15**, 304-310.

Campillo, M. and J.L. Plantet, 1991. Frequency dependence and spatial distribut ion of seismic attenuation in France: experimental results and possible interpretati ons, *Phys. Earth Planet. Interiors*, **67**, 48-64.

Campillo, M., L. Margerin and K. Aki 1998 Seismology, in New Aspects of Electromagnetic and Acoustic Waves Diffusion, POAN Research Group (ed), Springer tracts in modern physics; vol 144, 87-99.

Dainty, A.M. and M.N. Toksoz 1990 Array analysis of seismic scattering, *Bull. Seism. Soc. Am.*, **80**, 2248-2260

Hasegawa, H. S., 1985. Attenuation of *Lg* waves in the canadian shield, *Bull. Seismol. Soc. Am.*, **75**, 1569-1582.

Hoshiba, M., 1991. Simulation of multiple scattered coda wave excitation based on the energy conservation law, *Phys. Earth and Planet. Interiors*, **67**, 123-136.

Johnston, D.H. Attenuation: A state of the art summary. in: Seismic wave attenuation, M.N. Toksoz and D.H. Johnston editors, Geophysics Reprint Series No. 2, Society Of Exploration Geophysicists, Tulsa, 1981.

Kostoglodov, V., Bandy, W., Domingez, J., and Mena, M., 1996. Gravity and seismicity over the Guerrero seismic gap, Mexico. *Geophys. Res. Lett.*, **23**, 3385-3388.

Margerin, L., M. Campillo, B.A. Van Tiggelen, 1998a Radiative transfer and diff usion of waves in a layered medium: a new insight into coda Q, *Geophys. J. Int.*, **134**, 596-612.

Margerin, L., M. Campillo,, N.M. Shapiro and B. van Tiggelen 1998b The time of residence of diffuse waves in the crust and the physical interpretation of coda Q. Application to seismograms recorded in Mexico, submitted to Geophys. J. Int.

Meissner, R., 1989. Rupture, creep, lamellae and crocodiles: happenings in the continental crust, *Terra Nova*, **1**, 17-28.

Papanicolaou, G.C., L.V. Ryzhik and J.B. Keller 1996 Stability of the P to S energy ratio in the diffusive regime, *Bull. Seism. Soc. Am.*, **86**, 1107-1115.

Ryzhik, L.V., G.C. Papanicolaou and J.B. Keller 1996 Tansport equations for elastic and other waves in random media, *Wave Motion*, **24**, 327-370.

Shapiro, N.M., M. Campillo, L. Margerin, S.K. Singh, V. Kostoglodov and J. Pacheco 1998 The energy partitioning between P and S waves and the diffusive character of the seismic coda. submitted to Bull. Seism. Soc. Am.

Singh, S., & Herrmann, R.B., 1983. Regionalization of crustal coda Q in the c ontinental United States, *Journal of Geophysical Research,* **88**, 527-5 38.

Singh, S. K., Pacheco, J., Courboulex, F., and Novelo, D. A. 1997 Source parameters of the Pinotepa Nacional, Mexico, earthquake of 27 March, 1996 (Mw = 5.4) estimated from near-field recording of a single station., *J. Seismology*, **1**, 39-45.

Turner, J.A. 1998 Scattering and Diffusion of Seismic Waves. *Bull. Seism. Soc. Am.*, **88**, 276-283.

Weaver, R.L. 1982 On diffuse waves in solid media. *J. acoust. soc. Am.*, **71**, 1608-1609.

Weaver, R.L. 1990 Diffusivity of ultrasound in polycrystals, *J. Mech. Phys. Solids*, **38**, 55-86.

Wu R.S., 1985 Multiple scattering and energy transfer of seismic wa ves-separation of scattering effect from intrinsic attenuation-I Theoretical modeling. *Geophys. J. R. Astr. Soc*, **82**, 57-80.

Chapter 6

Le Cône de Rétrodiffusion Cohérente

Au chapitre 1, nous avons établi l'équation du transfert radiatif décrivant le transport de l'intensité moyenne dans un milieu inhomogène. L'opération consistant à prendre la moyenne d'ensemble fait disparaître beaucoup d'information. On peut s'en rendre compte en considérant l'équation de transport radiatif dynamique et non statique (comme c'est le cas au chapitre 1). Pour simplifier encore l'explication, nous allons utiliser l'approximation la plus courante de l'équation de transfert radiatif, qui est l'équation de diffusion:

$$\left(\frac{\partial}{\partial t} - D\nabla^2_{\boldsymbol{r}}\right)\rho(\boldsymbol{r},t) = 0 \tag{6.1}$$

Une différence fondamentale qu'on peut noter entre l'équation de diffusion et l'équation d'onde qui nous a servi de premier principe, est l'apparition d'une dérivée partielle première par rapport au temps, à la place d'une dérivée seconde. La conséquence immédiate que l'on en tire est que l'équation de transfert radiatif n'est pas symétrique par renversement du temps, contrairement à l'équation d'onde. Cette propriété importante des ondes a été exploitée en acoustique pour développer les miroirs à renversement temporel. Il a notamment été montré que le renversement du temps est extrêmement stable y compris en régime de diffusion multiple (Derode Roux et Fink, 1995; Fink, 1997).

6.1 Origine du cône de rétrodiffusion cohérente

Le cône de rétrodiffusion cohérente est un autre phénomène spectaculaire qui met en défaut l'équation de transfert radiatif. Il a été l'objet d'études expérimentales et théoriques approfondies en optique. Nous allons dans un premier temps expliquer qualitativement comment le cône est observé et à quel phénomène physique il correspond. Ensuite, nous mentionnerons comment, en complétant l'équation de transfert radiatif, on peut y faire apparaître le cône. Enfin, nous présenterons notre calcul numérique et la comparaison avec un résultat analytique obtenu par Van Tiggelen (1997).

6.1.1 Une approche expérimentale

Le principe d'observation du cône de rétrodiffusion cohérente est illustré sur la figure 6.1. Une onde (plane) est envoyée sur un milieu inhomogène où se produit de la diffusion multiple. On mesure l'intensité rétrodiffusée par l'échantillon en fonction de l'angle Θ par rapport à la direction incidente. Lorsqu'on fait (expérimentalement) la moyenne sur les réalisations du milieu ("configurational averaging"), on voit émerger autour de la direction incidente une amplification du niveau d'intensité par rapport au niveau de base. C'est ce qu'on appelle le "cône de rétrodiffusion cohérente". Expérimentalement, le contraste d'indice entre l'échantillon et le milieu extérieur est très faible de façon à récupérer le maximum d'intensité. Remarquons que dans certains systèmes multi-diffuseurs, tels que des suspensions colloïdales, la moyenne d'ensemble est assurée par le mouvement brownien des particules dans l'eau. Mentionnons aussi que dans le cadre de la théorie du transport radiatif, l'intensité mesurée autour de la direction incidente doit

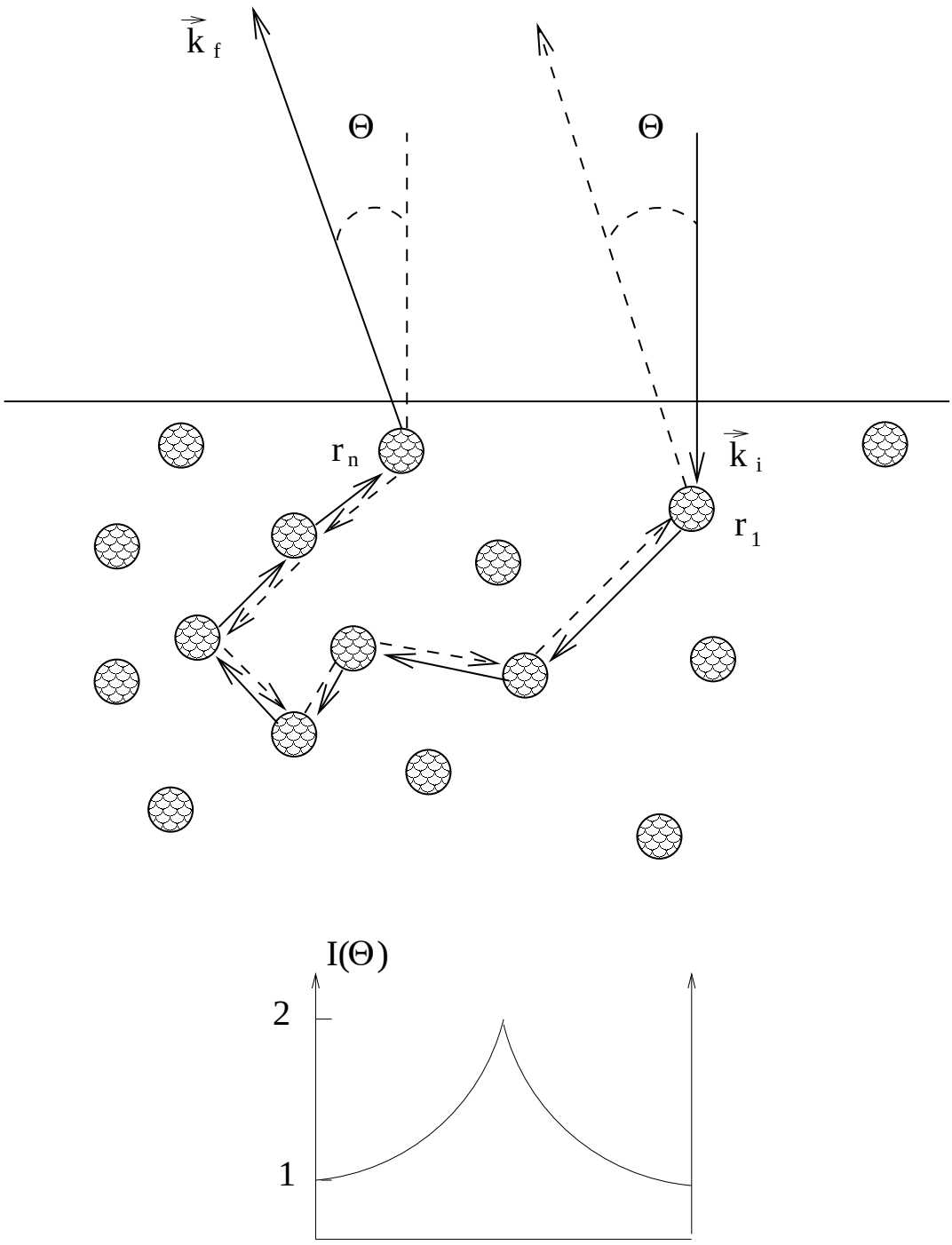

Figure 6.1: Situation typique pour l'observation du cône. Une onde collimatée (et approximativement plane) est envoyée sur un échantillon contenant des diffuseurs. On mesure l'intensité rétrodiffusée par l'echantillon en champ lointain en fonction de l'angle Θ mesuré par rapport à la direction d'incidence. L'intensité mesurée autour de la direction incidente présente un facteur d'amplification par rapport au niveau de base (ici normalisé à 1). Idéalement, le facteur d'amplification vaut 2.

être constante. Pour comprendre l'origine de cet effet, on peut se rappeler l'analogie qu'il existe entre l'équation de Boltzmann régissant la distribution des particules dans un gaz et l'équation de transfert radiatif. Or, il existe une différence fondamentale entre des particules classiques et des photons, car ces derniers peuvent interférer. Sur la figure 6.1, nous avons représenté deux chemins réciproques, l'un en trait plein, l'autre en pointillé. La différence de phase entre ces deux trajets provient de la position relative du premier et du dernier diffuseur. Plus précisément, le déphasage $\Delta\phi$ entre les deux trajets, s'écrit:

$$\Delta\phi = (\vec{k}_f + \vec{k}_i) \cdot (\boldsymbol{r}_n - \boldsymbol{r}_1) \tag{6.2}$$

Par conséquent lorsque le vecteur d'onde incident est exactement opposé au vecteur d'onde sortant ($\vec{k}_i = -\vec{k}_f$), on obtient $\Delta\phi = 0$; les deux trajets réciproques sont parfaitement en phase et il se produit une interférence constructive qui double l'intensité par rapport à la description "classique". Ceci montre que même en régime de diffusion multiple des effets d'interférence peuvent persister.

Nous allons maintenant préciser sous quelles conditions peuvent se produire les interférences et en déduire les paramètres qui contrôlent le cône de rétro-diffusion. Nous allons considérer le cas où la source et la détection sont en champ lointain. Ceci permet que l'onde incidente et l'onde arrivant au détecteur soient essentiellement planes. D'autre part, nous supposerons que le milieu est suffisamment diffusant pour que la première et la dernière diffusion aient lieu au voisinage de la surface, c'est à dire que le libre parcours moyen l est petit par rapport aux dimensions caractéristiques de l'échantillon. Dans ce cas, on a:

$$\Delta\phi = 2Rk \sin\Theta/2, \tag{6.3}$$

où R est la distance entre le premier et le dernier diffuseur, Θ l'angle entre direction sortante et incidente, et $k = 2\pi/\lambda$ est le nombre d'onde. Finalement, comme expérimentalement Θ est petit, on a:

$$\Delta\phi = k\Theta R \tag{6.4}$$

Nous allons maintenant supposer, qu'à l'intérieur du milieu, l'équation de transfert radiatif dans l'approximation de diffusion décrit correctement l'évolution spatio-temporelle de l'énergie. Dans ce cas, la distance quadratique moyenne entre le premier et le dernier diffuseur est donnée par:

$$\langle R^2 \rangle = 2dDt \tag{6.5}$$

où d est la dimension de l'espace, D, la constante de diffusion des ondes dans le milieu et t, le temps. La condition d'interférence est traduite par:

$$\Delta\phi \ll 2\pi.$$

En effet, si la différence de phase des ondes qui interfèrent peut prendre n'importe quelle valeur sur $[0, 2\pi]$, alors les intensités sont à nouveau additives. En utilisant l'approximation de diffusion, on obtient:

$$\frac{\sqrt{6Dt}\Theta}{\lambda} \ll 1 \tag{6.6}$$

On peut donc définir un angle critique Θ_c, au-delà duquel, l'interférence entre ondes incidentes et sortantes disparaît:

$$\Theta_c \approx \frac{\lambda}{\sqrt{6Dt}} \tag{6.7}$$

Cette formule nous apprend que la largeur du cône, dans une expérience dynamique telle que nous la décrivons, diminue avec la racine carrée du temps. On peut exprimer ceci différemment en disant que les chemins de diffusion multiple les plus longs contribuent pour les écarts angulaires Θ les plus faibles. D'autre part on peut définir une largeur maximale pour le cône, en prenant pour t le temps libre moyen de transport, à partir duquel l'approximation de diffusion est applicable. Ceci nous donne une largeur maximale:

$$\Theta_{max} \sim \frac{\lambda}{l^\star}. \tag{6.8}$$

Il a été montré par Tourin et al. (1997) que ce résultat est transposable dans le cas d'une expérience réalisée directement dans le domaine spatial. Pour plus de détails sur l'approche heuristique du cône de rétrodiffusion cohérente, on peut citer l'article de Corey, Kissner et Saulnier (1995) ainsi que le cinquième chapitre du livre de Sheng (1995).

6.1.2 Une approche "théorique"

Nous allons brièvement essayer d'expliquer, comment on peut modifier la théorie du transport de telle sorte que le cône soit inclus. En fait, il a été montré par Akkermans et al. (1988), qu'à chaque diagramme en échelle contenant au moins deux diffuseurs, correspond un diagramme de même poids cyclique ou encore "maximally-crossed" qui s'écrit diagrammatiquement de la façon suivante:

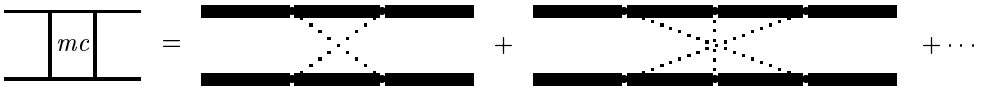

(6.9)

La prise en compte de ces diagrammes dans l'équation de Bethe-Salpeter permet de faire apparaître deux termes pour l'intensité: l'un est l'intensité incohérente correspondant à la solution classique de l'équation de transfert radiatif et l'autre est l'intensité dite cohérente qui tient compte de l'effet d'interférence. Physiquement les diagrammes "maximally-crossed" représentent le trajet de deux ondes qui voient les mêmes diffuseurs mais en sens opposé: ce sont les trajets réciproques pour la fonction de Green et sa complexe conjuguée. Ceci correspond bien à l'image qu'on avait donné plus haut du cône de rétrodiffusion. Dans ce qui suit, nous allons incorporer le terme dit cohérent et expliquer comment il est possible de calculer ce terme dans le cadre d'une simulation Monte Carlo. Les résultats numériques seront comparés avec une formule analytique obtenue dans l'approximation de diffusion.

6.2 Le cône de rétro-Diffusion cohérente en champ proche

6.2.1 Description qualitative

En ce qui concerne le cône de rétrodiffusion cohérente, la sismologie présente une situation un peu particulière par rapport aux autres domaines de la physique où il a été observé comme l'optique ou l'acoustique. En premier lieu les expériences sismologiques sont intrinsèquement dynamiques car les petits tremblements de Terre peuvent être assimilés à des fonctions δ en temps (et aussi en espace). D'autre part, la détection des signaux est toujours réalisée en champ proche car les détecteurs sont à la surface du milieu. La configuration pour le calcul du cône est donc assez particulière. Pour simplifier le problème, nous nous plaçons dans l'approximation acoustique avec une source isotrope et un détecteur à la surface d'un demi-espace. On confondra aussi l et $l^\star$ en considérant des diffuseurs isotropes (ce qui correspond au régime de Rayleigh pour les ondes acoustiques). Nos conventions pour le calcul du cône sont données sur la figure 6.2. Notons d'abord que la géométrie du problème impose des conditions sévères sur la position du premier et du dernier diffuseur. Le détecteur étant à la surface, seuls les trajets tels que $|\boldsymbol{r}-\boldsymbol{R}_1| \leq l$ et $|\boldsymbol{r}-\boldsymbol{R}_n| \leq l$ vont contribuer à l'intensité cohérente car le champ décroît exponentiellement entre la dernière diffusion et le détecteur. D'autre part, les premières collisions ont lieu en majorité dans une sphère de rayon l autour de la source. Si l'on réunit ces conditions, on obtient très grossièrement que la position entre le premier et le dernier diffuseur est telle que: $|\boldsymbol{R}_1 - \boldsymbol{R}_n| \leq l$. On peut noter ici la différence avec l'expérience que nous avons décrite précédemment où $|\boldsymbol{R}_1 - \boldsymbol{R}_n|$ croît avec le temps. Nous allons déterminer maintenant la dimension caractéristique du cône.

6.2.2 Calcul numérique.

Dans cette partie, nous allons utiliser les principes fondamentaux du calcul d'intégrales par méthode de Monte-Carlo introduits au chapitre 2. Nous montrerons ensuite comment la méthode peut-être appliquée

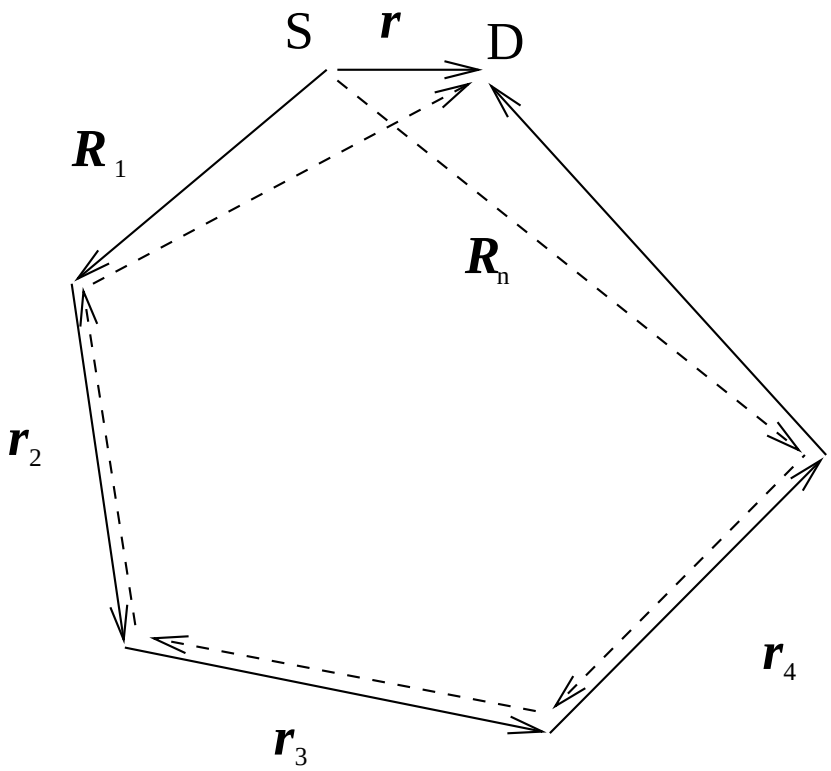

Figure 6.2: Geometry for the calculation of the CBS.

au calcul du cône dans le cas statique, l'extension au cas dynamique étant directe.

Calcul du cône de rétrodiffusion. L'expression de l'intensité cohérente est donnée par Akkermans et al. (1988), et Tsang et Ishimaru (1985):

$$I_{coh}(\boldsymbol{r}) = \iint \psi(\boldsymbol{R}_1)\psi^\star(\boldsymbol{R}_n)P(\boldsymbol{R}_1,\boldsymbol{R}_n)G(\boldsymbol{R}_n,\boldsymbol{r})G^\star(\boldsymbol{R}_1,\boldsymbol{r})d^3R_1 d^3R_n, \tag{6.10}$$

où l'on a introduit les notations suivantes:

$\boldsymbol{r}, \boldsymbol{R}_1, \boldsymbol{R}_n$ indiquent la position du détecteur, de la première et de la dernière diffusion, respectivement (voir figure 6.2);

ψ est le champ *moyen* émis par la source;

G est la fonction de Green *moyenne* pour l'amplitude de l'onde;

P est le propagateur de l'intensité dans le milieu. Autrement dit, P est la solution de l'équation de transfert radiatif pour une source en $\boldsymbol{R}_1$ et un détecteur en $\boldsymbol{R}_n$.

Dans le cas d'une source isotrope, on obtient:

$$\begin{aligned} I_{coh}(\boldsymbol{r}) &= \iint \frac{\exp(-R_1/2l)\exp(ikR_1)}{4\pi R_1}\frac{\exp(-R_n/2l)\exp(-ikR_n)}{R_n}P(\boldsymbol{R}_1,\boldsymbol{R}_n)\times \\ &\times \frac{\exp(-|\boldsymbol{r}-\boldsymbol{R}_n|/2l)\exp(ik|\boldsymbol{r}-\boldsymbol{R}_n|)}{4\pi|\boldsymbol{r}-\boldsymbol{R}_n|}\frac{\exp(-|\boldsymbol{r}-\boldsymbol{R}_1|/2l)\exp(-ik|\boldsymbol{r}-\boldsymbol{R}_1|)}{|\boldsymbol{r}-\boldsymbol{R}_1|}d^3R_1 d^3R_n. \end{aligned} \tag{6.11}$$

k est le nombre d'onde dominant de la source. Nous allons maintenant transformer l'expression de I_{coh}, pour lui donner une forme similaire à celle que nous avons obtenu pour l'intensité dite incohérente au chapitre 2:

$$\begin{aligned} I_{coh}(\boldsymbol{r}) &= \int\cdots\int \frac{\exp(-R_1/l)}{l}\frac{sin\theta_1 d\theta_1 d\phi_1}{4\pi}\cdots\frac{\exp(-r_i/l)}{l}h_{coh}(\boldsymbol{R}_1,\boldsymbol{R}_n,\boldsymbol{r})\frac{sin\theta_i d\theta_i d\phi_i}{4\pi} \\ h_{coh}(\boldsymbol{R}_1,\boldsymbol{R}_n,\boldsymbol{r}) &= \exp ik(R_1 - R_n + |\boldsymbol{r}-\boldsymbol{R}_n| - |\boldsymbol{r}-\boldsymbol{R}_1|)\times \\ &\quad \times \frac{\exp\left[-(|\boldsymbol{r}-\boldsymbol{R}_1| + |\boldsymbol{r}-\boldsymbol{R}_n| + R_n - R_1)/2l\right]}{\frac{4\pi R_n|\boldsymbol{r}-\boldsymbol{R}_n||\boldsymbol{r}-\boldsymbol{R}_1|}{R_1}}. \end{aligned} \tag{6.12}$$

Dans cette dernière équation, on a posé: $\boldsymbol{R}_n = \boldsymbol{R}_1 + \sum_2^n \boldsymbol{r}_i$ (voir figure 6.2). Nous obtenons donc l'estimateur de l'intensité cohérente h_{coh}, où persiste un terme de phase en raison de la différence de trajet entre les deux chemins qui interfèrent. On peut noter que l'expression de I_{coh} et de l'intensité incohérente établie au chapitre 2 ne diffèrent que par l'estimateur de l'intensité, le reste des intégrales étant rigoureusement identique.

6.2.3 Calcul analytique.

Pour le calcul analytique du cône de rétrodiffusion, on rappelle l'expression de l'intensité cohérente:

$$I_{coh}(\boldsymbol{r},t) = \iint \psi(\boldsymbol{R}_1)\psi^\star(\boldsymbol{R}_n)P(\boldsymbol{R}_1,\boldsymbol{R}_n,t)G(\boldsymbol{R}_n,\boldsymbol{r})G^\star(\boldsymbol{R}_1,\boldsymbol{r})d^3R_1 d^3R_n, \tag{6.13}$$

où toutes les notations sont identiques à l'équation (6.12), et où nous précisons explicitement la dépendance du propagateur de l'intensité dans le milieu par rapport au temps. Le principe du calcul analytique consiste à prendre, pour ce propagateur, la fonction de Green de l'équation de diffusion. Dans le cas le plus simple d'un espace infini, on obtient:

$$P(\boldsymbol{R}_1,\boldsymbol{R}_n,t) = \frac{1}{(4\pi Dt)^{3/2}}\exp(-(\boldsymbol{R}_n-\boldsymbol{R}_1)^2/4Dt), \tag{6.14}$$

où l'on a introduit la constante de diffusion du milieu $D = vl/3$, et v la vitesse de transport (qu'on peut confondre avec la vitesse des ondes pour des diffuseurs Rayleigh). Comme nous l'avons discuté précédemment, la géométrie du milieu impose que $(\boldsymbol{R}_n - \boldsymbol{R}_1)^2 \leq l^2$ et donc pour $\sqrt{Dt} \gg l$, le terme exponentiel vaut approximativement 1 et l'on obtient:

$$I_{coh}(\boldsymbol{r},t) \approx \frac{1}{(4\pi Dt)^{3/2}}\left|\int \psi(\boldsymbol{R}_1)G^\star(\boldsymbol{R}_1,\boldsymbol{r})d^3R_1\right|^2 \tag{6.15}$$

Il reste donc à évaluer analytiquement cette intégrale, dans laquelle on a:

$$\psi(\boldsymbol{R}_1) = \frac{\exp(ikR_1 - R_1/2l)}{4\pi R_1} \tag{6.16}$$

$$G(\boldsymbol{R}_1,\boldsymbol{r}) = \frac{\exp(ik|\boldsymbol{r}-\boldsymbol{R}_1| - |\boldsymbol{r}-\boldsymbol{R}_1|/2l)}{4\pi|\boldsymbol{r}-\boldsymbol{R}_1|} \tag{6.17}$$

Nous ne détaillerons pas les calculs. Par transformation de Fourier et application du théorème des résidus, on montre que:

$$\int \psi(\boldsymbol{R}_1)G^\star(\boldsymbol{R}_1,\boldsymbol{r})d^3R_1 = \pi l\exp(-r/2l)\frac{\sin kr}{kr} \tag{6.18}$$

Le calcul de l'intensité incohérente est tout à fait similaire et on obtient la forme analytique asymptotique du cône:

$$\frac{I_{coh}}{I_{inc}} \approx \exp(-r/l)\left(\frac{\sin kr}{kr}\right)^2 \tag{6.19}$$

Par conséquent, on s'attend à ce que la largeur typique du cône soit la longueur d'onde. D'autre part, dans la mesure où, en sismologie, on s'attend à ce que le libre parcours moyen soit un ordre de grandeur plus grand que la longueur d'onde, l'exponentielle n'influence pas fondamentalement la forme du cône.

6.2.4 Comparaison entre résultats numériques et analytiques.

La figure 6.3 montre la construction du cône de rétrodiffusion autour de la source. Chaque sous-figure est un instantané de la dépendance spatiale de la fonction $(I_{coh} + I_{inc})/I_{inc}(r)$. Comme on peut le constater sur la figure 6.3, l'effet d'interférence est localisé sur une longueur d'onde autour de la source comme l'avait prédit le calcul analytique. Néanmoins, la formation du cône n'est pas instantanée. En effet, dans le calcul numérique complet, nous incluons dans l'intensité incohérente le terme de diffusion simple pour lequel il n'existe pas de chemin réciproque. Par conséquent, bien qu'il y ait interférence constructive complète en $r = 0$, on n'obtient pas immédiatement le facteur 2 d'amplification. Celui-ci est atteint uniquement lorsque la diffusion simple (qui décroît exponentiellement) est dominée par les termes de diffusion multiple dont la somme décroît algébriquement. Après environ 5 temps libres moyens, on peut constater que le cône est stabilisé.

Nous montrons sur la figure 6.4, l'évolution temporelle de la fonction $(I_{coh} + I_{inc})/I_{inc})(t)$ en $r = 0, \lambda/8, \lambda/4, 3\lambda/4, \lambda$. On peut constater la convergence de la solution complète vers les valeurs prédites asymptotiquement par le calcul analytique. On peut aussi remarquer que l'amplification d'un facteur 2 en $r = 0$ est atteinte avant que le cône soit devenu parfaitement indépendant du temps. Ceci signifie que l'évolution temporelle du cône est gouvernée aussi par la diffusion multiple, même si cet effet est beacoup plus faible. Nous pouvons en conclure qu'à partir de la solution dynamique, on peut déduire le libre parcours moyen du milieu. La difficulté majeure réside dans la mesure expérimentale du cône de rétrodiffusion en sismologie.

Enfin, nous montrons sur la figure 6.5, la forme du cône atteinte après 15 temps libres moyens dans la simulation. La comparaison avec le calcul analytique est très bonne. Ceci nous indique que, bien que le problème soit intrinsèquement dépendant du temps, le cône devient parfaitement stable. Ceci s'explique par le fait que l'essentiel du phénomène se produit dans une sphère de rayon l autour de la source et du détecteur. Or on sait que le processus de diffusion multiple tend à uniformiser la répartition spatiale d'énergie. Une fois que cette homogénéisation a eu lieu, l'effet d'interférence devient complètement immuable, bien que la valeur *absolue* de l'énergie puisse diminuer sur plusieurs ordres de grandeur.

Bibliographie

Akkermans, E., P.E. Wolf, R. Maynard and G. Maret, 1988. Theoretical study of the coherent backscattering of light by disordered media, J. Phys. France, 49, 77-98.

Corey, R., M. Kissner and P. Saulnier, 1995. Coherent backscattering of light, Am. J. Phys., 63, 560-564.

Derode, A., P. Roux and M. Fink, 1995. Phys Rev. Lett., 75, 4206.

Fink, M, 1997. In Phys. Today, 50, 34.

Sheng P., 1995. *Introduction to wave scattering, localization and mesoscopic phenomena*, Academic Press, San Diego.

Tourin, A., A. Derode, P. Roux, B.A. van Tiggelen and M. Fink, 1997. Time-dependent coherent backscattering of acoustic waves, Phys. Rev. Let., 79, 3637-3639.

Tsang, L. and A. Ishimaru, 1985. Theory of backscattering enhancement of random discrete scatterers based on the summation of all ladder and cyclical terms, J. Opt. Soc. Am.,A 2, 1331-1338.

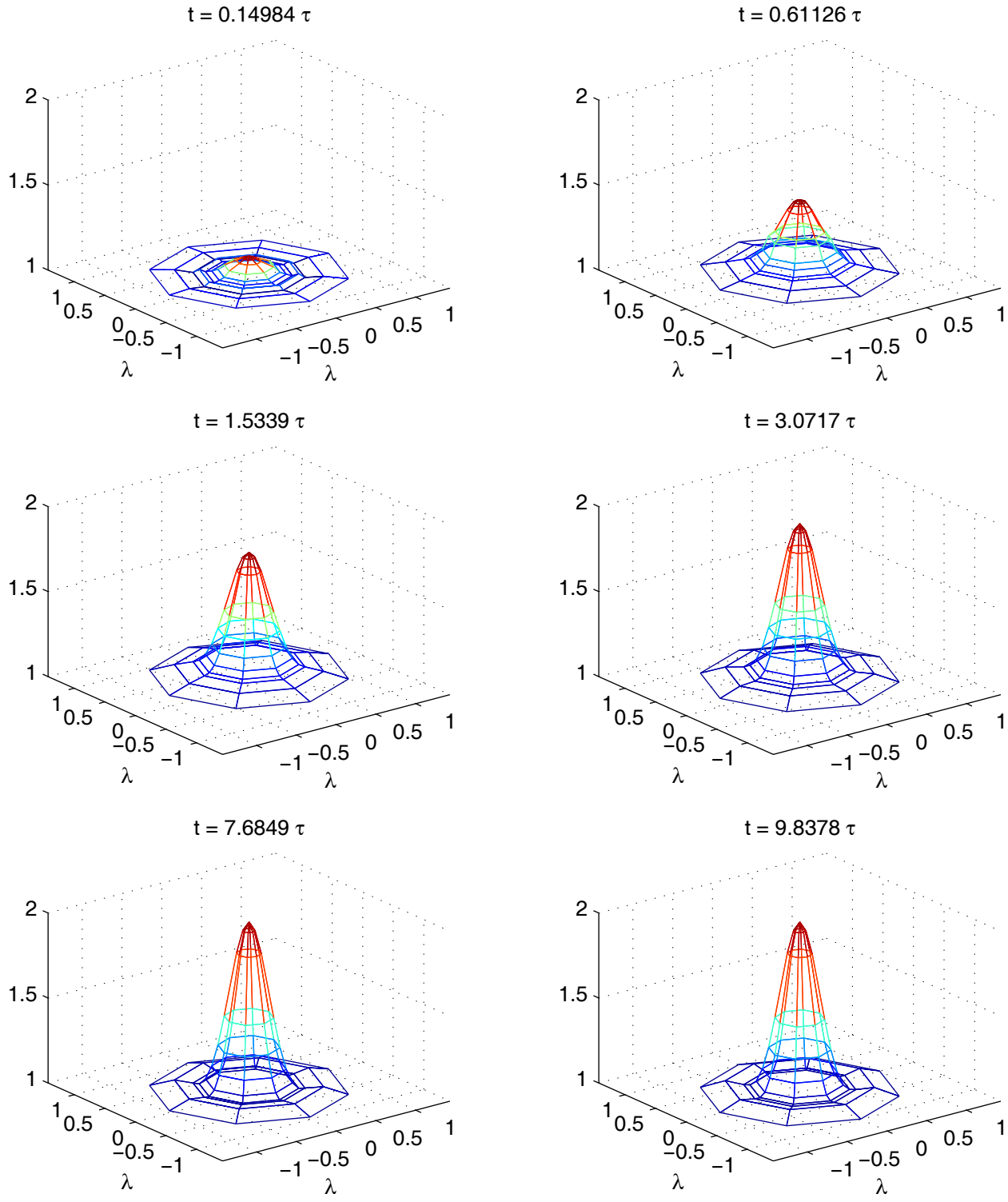

Figure 6.3: Evolution spatio-temporelle du cône de rétrodiffusion. Sur l'axe vertical: $(I_{coh} + I_{inc})/I_{coh}$; axes horizontaux: distance par rapport à la source exprimée en longueur d'onde. Le temps est exprimé en fonction du temps libre moyen au-dessus de chaque figure.

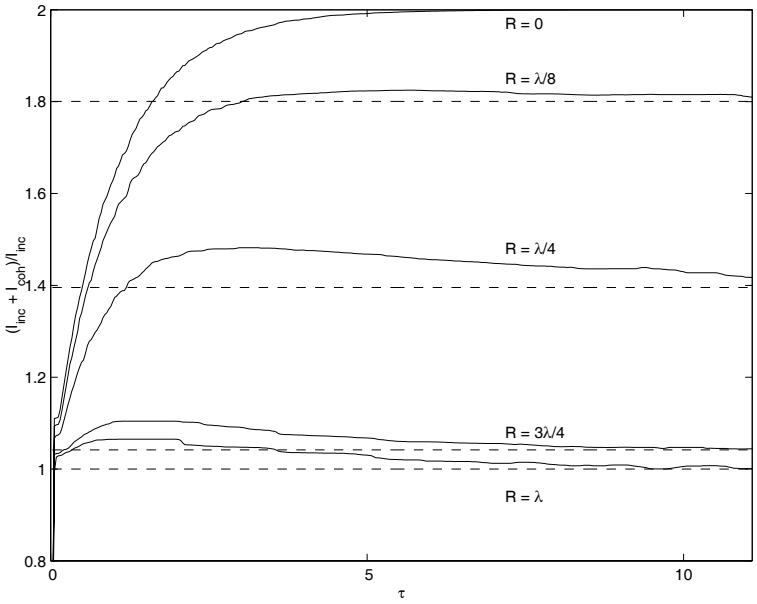

Figure 6.4: Comparaison entre les solutions numériques et analytiques à différentes distances R entre source et récepteur, exprimées en nombre de longueur d'onde. La solution numérique (en pointillé) évolue asymptotiquement vers la valeur prédite par la solution analytique (trait plein).

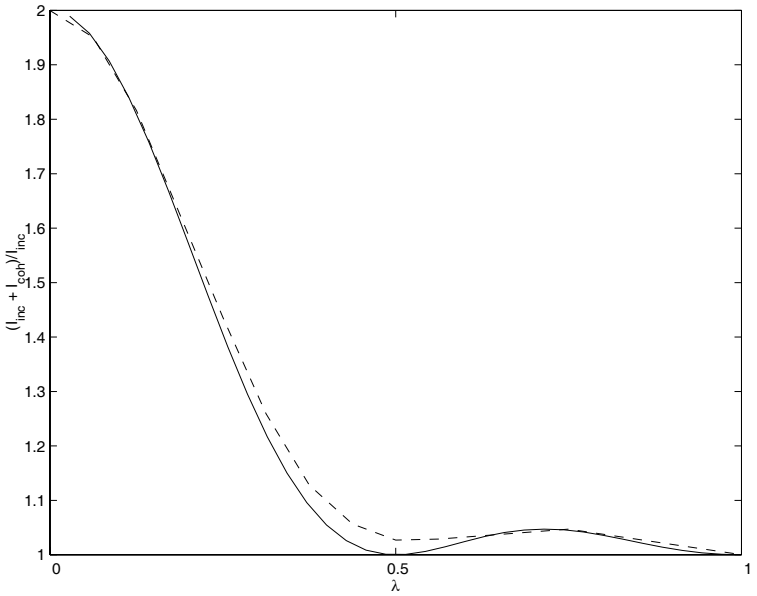

Figure 6.5: Comparaison entre la forme du cône obtenue par simulation Monte-Carlo (pointillé) après 15 temps libres moyens et la prédiction asymptotique analytique. La distance par rapport à la source est exprimée en abscisse en fonction de la longueur d'onde

Chapter 7

Conclusions.

Au cours de cette thèse, nous avons essayé de développer des modèles plus réalistes de propagation des ondes courtes périodes dans la croûte. Du point de vue méthodologique, nous avons proposé des méthodes de simulation Monte-Carlo permettant de résoudre l'équation de transfert radiatif pour des milieux stratifiés, dans l'approximation acoustique. Puis, nous avons levé l'approximation acoustique en développant une simulation complète, incluant le couplage des ondes P et S, l'anisotropie de la diffusion ainsi qu'une description précise de la polarisation des ondes S, pour un milieu infini. Nous avons ensuite montré comment inclure un bord réflechissant dans la simulation élastique. Enfin, nous avons présenté une méthode permettant de tenir compte des effets d'interférence persistant en régime de diffusion multiple. Autant que possible, nous avons comparé nos résultats à des solutions analytiques de l'équation de transfert radiatif dans l'approximation de diffusion. Nous avons porté une attention particulière à l'établissement des conditions de bord pour l'équation de diffusion et avons discuté son domaine de validité. Nous avons souligné l'influence de ces conditions de bord sur la forme analytique des solutions. Les deux approches (transport et diffusion) sont complémentaires, l'approximation de diffusion étant particulièrement efficace pour les milieux très hétérogènes où le temps libre moyen est très petit par rapport au temps de trajet des ondes.

Pour modéliser la décroissance de la coda, nous avons proposé un modèle simple. La croûte est représentée par une couche hétérogène et faiblement anélastique; le manteau est représenté par une couche homogène non rétrodiffusante. Dans ce modèle, il apparaît que la décroissance exponentielle de la coda à des fréquences proches de 1 Hz est liée non pas à l'anélasticité, mais aux pertes d'énergie diffuse à la base de la croûte. Ce phénomène de perte ("leakage") d'énergie constitue une interprétation physique alternative du facteur de qualité de la coda. Nous montrons que cet effet est particulièrement marqué dans la gamme de fréquence 1-5 Hz, et qu'au delà, l'atténuation intrinsèque devient le facteur dominant de décroissance de la coda. L'étude de l'effet de perte nous amène à considérer l'épaisseur de la croûte comme un paramètre physique fondamental pour expliquer les mesures du facteur de qualité. La coda est donc possiblement contrôlée par trois paramètres: épaisseur de la croûte, libre parcours moyen et atténuation intrinsèque. Notre modèle est appliqué à un ensemble de données du Mexique et rend compte de façon satisfaisante de la dépendance fréquencielle du facteur de qualité de la coda. Nous trouvons qu'un facteur de qualité intrinsèque supérieur à 1000 et ne dépendant pas ou peu de la fréquence permet de rendre compte des observations.

Nous avons d'autre part étudié l'importance des couplages entre ondes P et S en simulant la diffusion multiple des ondes élastiques. Nous montrons que le mode S est rapidement dominant dans la coda, quelque soit le type de source. La convergence du rapport d'énergie des modes P et S vers une valeur d'équilibre ne dépendant que des vitesses de propagation des modes P et S est montrée numériquement. D'autre part nous mettons en évidence que la vitesse de convergence vers l'équilibre dépend fortement du rapport entre la longueur d'onde et la taille caractéristique des inhomogénéités. En particulier lorsqu'elles sont du même ordre de grandeur, l'équilibre est atteint après quelques temps libres moyens. Nous concluons que l'équilibre entre les modes P et S est un marqueur possible du régime de diffusion multiple.

L'effet de la surface libre est étudié. Nous montrons qu'il ne doit pas affecter l'équilibre entre les modes P et S. Nous rapportons également des observations d'équilibration entre les modes P et S dans la coda au Mexique. L'ensemble des observations sur la coda (décroissance et équilibration) nous amène à conclure qu'au Mexique, la coda est probablement constituée d'ondes diffusives.